

University of Windsor

Scholarship at UWindor

Electronic Theses and Dissertations

Theses, Dissertations, and Major Papers

2011

Plasmon-Enhanced Raman and Resonance Raman Scattering and Single Molecule Detection in Langmuir-Blodgett Monolayers

Golam Moula
University of Windsor

Follow this and additional works at: <https://scholar.uwindsor.ca/etd>

Recommended Citation

Moula, Golam, "Plasmon-Enhanced Raman and Resonance Raman Scattering and Single Molecule Detection in Langmuir-Blodgett Monolayers" (2011). *Electronic Theses and Dissertations*. 395.
<https://scholar.uwindsor.ca/etd/395>

This online database contains the full-text of PhD dissertations and Masters' theses of University of Windsor students from 1954 forward. These documents are made available for personal study and research purposes only, in accordance with the Canadian Copyright Act and the Creative Commons license—CC BY-NC-ND (Attribution, Non-Commercial, No Derivative Works). Under this license, works must always be attributed to the copyright holder (original author), cannot be used for any commercial purposes, and may not be altered. Any other use would require the permission of the copyright holder. Students may inquire about withdrawing their dissertation and/or thesis from this database. For additional inquiries, please contact the repository administrator via email (scholarship@uwindsor.ca) or by telephone at 519-253-3000ext. 3208.

Plasmon-Enhanced Raman and Resonance Raman Scattering and Single Molecule Detection in Langmuir-Blodgett Monolayers

by

Golam Moula

A Dissertation

Submitted to the Faculty of Graduate Studies

Through Chemistry and Biochemistry

in Partial Fulfillment of the Requirements for

the Degree of Doctor of Philosophy at the

University of Windsor

Windsor, Ontario, Canada

2011

© 2011, Golam Moula

**Plasmon-Enhanced Raman and Resonance Raman Scattering and Single
Molecule Detection in Langmuir-Blodgett Monolayers**

by

Golam Moula

APPROVED BY

Dr. Elder De la Rosa, External Examiner
Centro de Investigaciones en Optica, Mexico

Dr. Elena Maeva
Department of Physics

Dr. S. Holger Eichhorn
Department of Chemistry & Biochemistry

Dr. Zhuo Wang
Department of Chemistry & Biochemistry

Dr. R. F. Aroca, Advisor
Department of Chemistry & Biochemistry

Dr. K. Tepe, Chair of Defense
Department of Electrical and Computer Engineering

19 January, 2011

Declaration of Co-Authorship / Previous Publication

I. Co-Authorship Declaration

I hereby declare that this thesis incorporates material that is result of joint research, as follows:

This thesis incorporates the outcome of research undertaken in material and surface science group in chemistry and biochemistry at the University of Windsor, Ontario, Canada under the supervision of Dr. Ricardo Aroca. The work in collaboration with Dr. N. P. W. Pieczonka and Adam R. Skarbek under the supervision of Dr. Aroca is presented in part of chapter 3 and 5, and all the remaining chapter are comprised with the works exclusively done by the author himself. In all cases, the key ideas, primary contributions, experimental designs, data analysis and interpretation, were performed by the author.

I am aware of the University of Windsor Senate Policy on Authorship and I certify that I have properly acknowledged the contribution of other researchers to my thesis, and have obtained written permission from each of the co-authors to include the above materials in my thesis.

I certify that, with the above qualification, this thesis, and the research to which it refers, is the product of my own work.

II. Declaration of Previous Publication

This thesis includes five original papers that have been previously published/submitted for publication in peer reviewed journals, as follows:

Thesis Chapter	Publication title/full citation	Publication status
Chapter 3 and 5	Nicholas P.W. Pieczonka; G. Moula; Adam R. Skarbek; Ricardo F. Aroca, "Single Molecule and Trace Detection by SERS", Surface Enhanced Raman Spectroscopy; Analytical, Biophysical and Life Science Applications, Chap 4, <i>Wiley Publishers</i> , 2010.	Published
Chapter 4	G. Moula; R. F. Aroca, "Surface-Enhanced Raman Scattering (SERS) of Phospholipids in Langmuir-Blodgett Films", <i>Journal of Physical Chemistry</i> , 2010.	In final Review
Chapter 5	G. Moula; R. F. Aroca, "Plasmon enhanced resonance Raman scattering and fluorescence in Langmuir-Blodgett Monolayers", <i>Journal of Analytical Chemistry</i> , 2010	Published
Chapter 5	N.P.W. Pieczonka; G. Moula; R. F. Aroca, "SERRS for Single-Molecule Detection of Dye Labeled Phospholipids in Langmuir-Blodgett Monolayer", <i>Langmuir</i> , 2009.	Published
Chapter 6	G. Moula; R. F. Aroca, "Controlled surface plasmon by Self-assembly of Silver Nanoparticles on Silanized Surface and SERS in Langmuir-Blodgett (LB) Monolayer", <i>Journal of Nanotechnology</i> (Manuscript in Preparation)	In Preparation
Chapter 7	G. Moula; R. F. Aroca "Single-Molecule Detection of PTCD in Langmuir-Blodgett Monolayers using shell coated nanoparticle enhanced fluorescence and resonance SERS", <i>Journal of Analytical Chemistry</i> (Manuscript in preparation).	In Preparation

I certify that I am copyright owner to include the above published material(s) in my thesis. I certify that the above material describes work

completed during my registration as graduate student at the University of Windsor.

I declare that, to the best of my knowledge, my thesis does not infringe upon anyone's copyright nor violate any proprietary rights and that any ideas, techniques, quotations, or any other material from the work of other people included in my thesis, published or otherwise, are fully acknowledged in accordance with the standard referencing practices. Furthermore, to the extent that I have included copyrighted material that surpasses the bounds of fair dealing within the meaning of the Canada Copyright Act, I certify that I have obtained a written permission from the copyright owner(s) to include such material(s) in my thesis.

I declare that this is a true copy of my thesis, including any final revisions, as approved by my thesis committee and the Graduate Studies office, and that this thesis has not been submitted for a higher degree to any other University or Institution.

ABSTRACT

The present work explores vibrational Raman spectroscopy. Vibrational Raman and vibrational infrared are the most commonly used spectroscopies for detection and identification of molecules with their *vibrational fingerprint*. Under certain conditions, molecules display unique fluorescence and Raman scattering behavior when they are close to metal nanostructures sustaining localized surface plasmon resonances (LSPR), giving rise to surface-enhanced Raman scattering (SERS) and surface-enhanced resonance Raman scattering (SERRS).

The utilization of LSPR in metallic nanoparticles, in particular silver and gold nanostructures, is a remarkable means of improving the efficiency of Raman scattering enhancing optical signals in SERS and SERRS. Correspondingly, the fabrication and characterization of silver and gold island films are first presented, and SERS signals enhancement of an organic dye on these metal nanostructured films are demonstrated. The excitations are characterized by UV-Vis absorption spectroscopy, while the morphology is revealed by atomic force microscopy (AFM).

To control the surface coverage of the metal nanostructures, the Langmuir-Blodgett (LB) technique is used to coat the SERS substrate with monomolecular layers of several target systems, such as dyes and phospholipids.

The most important results in this work are in the field of single molecule detection (SMD) using two spectroscopic approaches: LB-SERRS and LB-SERS. LB-SERRS improves the scattering efficiency from the electronic resonances (resonance Raman) of dye using silver island film with a plasmon absorption

overlapping the molecular absorption. Several experiments are designed to the statistical average of LB-SERRS spectra, and the statistical breakdown observed in spectral characteristics when SMD is approached.

The development of other SERS-substrates was attempted to control plasmonic using LSPR. A convenient method was pursued using a self-assembly of silver colloidal nanoparticles on a silanized glass surface. The SERS spectral evidence is presented to validate the substrate development.

Surface-enhanced fluorescence (SEF) was also used for single molecule studies. Shell-isolated nanoparticles (SHINs) are used to produce SEF that named SHINEF. Using mixed LB monolayers of perylene tetracarboxylic (*PTCD*) derivatives, we report single molecule fluorescence and single molecule SERRS. In addition, overtones and combinations of fundamental vibrational modes are seen with atypical relative intensity in the LB-SERRS spectra of PTCDs.

For my parents, my wife & my sons

ACKNOWLEDGEMENTS

I would like to express my sincere gratitude and thanks to my research advisor, Dr. Ricardo Aroca. His guidance, patience and continuous encouragement are highly appreciated. He introduced me to the exciting world of nanoscience. I enjoyed my projects a lot.

I would like to thank my committee members Dr S. Holger Eichhorn, Dr. Zhuo Wang and Dr. Elena Maeva. Also, I wish to thank to Dr. Elder De la Rosa for agreeing to be my External Examiner.

The Department of Chemistry and Biochemistry is munificent to provide me both financial support and the resources to conduct my research works. I also thank the members of the Material and Surface Science Group: Nik, David, Goulet, Daniel, Ariel, Grace, Aldo, Chindo, Case, Salwen, Haider, Pape, Igor, Romolo, Teo and friends and others who made my stay in Windsor enjoyable and enriched my life.

Lastly, the acknowledgement to my parents for their desire to take me in a way for higher studies and also my wife whom patience, encouragement and perseverance throughout my study made my graduation possible.

TABLE OF CONTENTS

DECLARATION OF CO-AUTHORSHIP/PREVIOUS PUBLICATIONS.....	iv
ABSTRACT.....	vii
DEDICATIONS.....	ix
ACKNOWLEDGEMENTS.....	x
LIST OF TABLES.....	xvi
LIST OF FIGURES.....	xvii
LISTS OF ABBREVIATIONS.....	xxii
CHAPTER 1.....	1
1. INTRODUCTION.....	1
1.1 Overview.....	2
References.....	9
CHAPTER 2.....	13
2. BACKGROUND.....	13
2.1 Introduction.....	14
2.2 Raman spectroscopy.....	14
2.2.1 <i>Molecular origin of Raman spectroscopy</i>	17
2.2.2 <i>Raman scattering</i>	20
2.2.2.1 <i>Classical treatment of RS</i>	22
2.2.2.2 <i>Quantum Mechanical theory of RS</i>	25
2.2.2.3 <i>Polarizability, Raman scattering and Intensity</i>	28
2.2.2.4 <i>Raman cross section</i>	32
2.2.2.5 <i>Weak “cross section” in RS needs enhancement</i>	34
2.3 SERS / SERRS.....	35
2.3.1 <i>Plasmon enhanced Raman</i>	36
2.3.2 <i>Changes in polarizability</i>	39
2.3.3 <i>Origin of localized surface plasmon resonance</i>	41
2.3.3.1 <i>Controlling LSPR in SERS experiments</i>	43
2.3.3.1.1 <i>LSPR size dependent</i>	43

2.3.3.1.2	<i>LSPR shape dependent</i>	45
2.3.3.1.3	<i>LSPR environment dependent</i>	46
2.3.3.1.4	<i>LSPR distance dependent</i>	47
2.3.4	<i>Surface selection rules in SERS</i>	48
2.4	Metal island films by vacuum deposition.....	51
2.5	Langmuir Blodgett films.....	53
2.5.1	<i>Langmuir monolayer formation</i>	54
2.5.2	<i>Surface Pressure(π)-Area (A) isotherm</i>	55
2.5.3	<i>Langmuir monolayer deposition</i>	58
2.5.4	<i>LB – Brewster angle microscopy</i>	60
2.6	Atomic force microscopy.....	61
2.6.1	<i>Contact mode AFM</i>	64
2.6.2	<i>Tapping mode AFM</i>	64
2.7	UV-Vis absorption.....	65
	References.....	67
CHAPTER 3.....		72
3. METAL NANOSTRUCTURES PREPARATIONS AND LANGMUIR- BLODGETT (LB) APPROACH TO SERS / SERRS.....		72
3.1	Background.....	73
3.2	Preparation of metal nanostructures.....	75
3.2.1	<i>Introduction</i>	75
3.2.2	<i>Experimental</i>	75
3.2.3	<i>Results and Discussions</i>	77
3.2.3.1	<i>Particle size variation in a silver island films</i>	77
3.2.3.2	<i>Film thickness and plasmon absorption</i>	78
3.2.3.3	<i>Temperature of substrate and plasmon absorption</i>	79
3.2.3.4	<i>Comparison of plasmon absorption in Ag and Au films</i>	81
3.2.3.5	<i>Gold films and Ag/Au mixed films</i>	82
3.3	SERS demonstration using benzene thiol.....	83

3.3.1	<i>Introduction</i>	83
3.3.2	<i>Experimental</i>	85
3.3.3	<i>Results and Discussions</i>	87
3.3.3.1	<i>SERS of benzene thiol on silver island films</i>	87
3.3.3.2	<i>SERS of benzene thiol on gold island film</i>	88
3.4	Langmuir-Blodgett (LB) approach to SERS.....	91
3.4.1	<i>Introduction</i>	91
3.4.2	<i>Langmuir-Blodgett (LB) monolayer approach-SERS</i>	92
	References.....	95
CHAPTER 4	99
4. SURFACE ENHANCED RAMAN SCATTERING OF PHOSPHOLIPID BILAYERS IN LANGMUIR-BLODGETT FILMS	99
4.1	Background.....	100
4.2	Introduction.....	103
4.3	Experimental.....	105
4.4	Results and Discussion.....	108
4.4.1	<i>UV-Vis absorption</i>	108
4.4.2	<i>Langmuir surface pressure Area Isotherm</i>	109
4.4.3	<i>Vibrational Raman spectra of phospholipids-DMPC & DPPC</i> ..	110
4.4.4	<i>Surface-enhanced Raman scattering of DMPC and DPPC</i>	112
4.4.4.1	<i>SERS effects on LB multilayers</i>	114
4.4.4.2	<i>Bilayers LB-SERS reproducibility by mapping</i>	117
4.4.5	<i>SERS of phospholipid in gold film compare to silver film</i>	119
4.5	Conclusions.....	120
	References.....	121
CHAPTER 5	123

5. SINGLE MOLECULE DETECTION OF DYE TAGED PHOSPHOLIPIDS IN LANGMUIR BLODGETT MONOLAYERS ON SILVER ISLAND FILM.....	123
5.1 Single molecule detection- Background.....	124
5.2 Single molecule detection by SERS.....	126
5.2.1 <i>Enhancement factor in metal island film</i>	128
5.2.2 <i>Raman instrumentation and SMD</i>	132
5.2.3 <i>Langmuir-Blodgett approach to SM-SERRS</i>	137
5.3 LB-SERRS of dye tagged phospholipids for SMD.....	138
5.4 Experimental	141
5.5 Results and Discussion.....	145
5.5.1 <i>Absorption and Fluorescence</i>	145
5.5.2 <i>LB-SERS and reference spectra</i>	147
5.5.3 <i>SERRS mapping and ensembled averaged spectra</i>	151
5.5.4 <i>Trace detection with SERRS and spectrum of the single molecule</i>	154
5.5.5 <i>Single molecule (SM) SERRS spectra</i>	155
5.6 Conclusions.....	159
References.....	160
CHAPTER 6.....	164
6. CONTROLLED SURFACE PLASMON RESONANCES BY SELF-ASSEMBLY OF SILVER NANOPARTICLES ON SILANIZED SURFACES.....	164
6.1 Overview.....	165
6.2 Self assembly of Ag nanoparticles.....	167
6.3 Experimental.....	169
6.4 Results and Discussion.....	173
6.4.1 <i>Absorption</i>	173
6.4.2 <i>Reference and LB-SERRS spectra of R18</i>	175
6.4.3 <i>LB-SERRS substrate</i>	176
6.5 Conclusions.....	180

References.....	181
CHAPTER 7.....	186
7. SINGLE MOLECULE DETECTION OF PERYLENE TETRACARBOXYLIC DERIVATIVES IN LANGMUIR-BLODGETT MONOLAYERS USING SURFACE ENHANCED RESONANCE RAMAN SCATTERING AND SHELL ISOLATED NANOPARTICLE ENHANCED FLUORESCENCE (SHINEF).....	186
7.1 Overview.....	187
7.2 Experimental.....	192
7.3 Results and Discussion	196
7.3.1 Absorption and resonance Raman scattering.....	196
7.3.2 Ensemble average SERRS spectra.....	198
7.3.3 The spectrum of the single molecule.....	200
7.3.4 Fluorescence of LB stock solutions.....	205
7.3.5 SHINEF in concentrated LB films	206
7.3.6 Single-molecule detection by SHINEF.....	208
7.4 Conclusions.....	210
References	211
CHAPTER 8 CONCLUSIONS	214
8.1 Conclusions.....	215
8.2 Future Work.....	218
VITA AUCTORIS.....	221

LIST OF TABLES

Table 2.1	Excitation Lasers.....	16
Table 2.2	Typical values for cross sections σ for various possible interactions of molecules with incident electromagnetic radiation.....	34
Table 4.1	Characteristic vibrational Raman modes of DPPC and DMPC. Solids and LB-SERS data.....	116
Table 5.1	Excitation Lasers.....	132
Table 5.2	Spectral Resolution for Grating-Laser combinations	134
Table 5.3	List of Objectives and Spot Sizes	136
Table 5.4	Probe Molecule to AA “Ratios” with the approximate number of molecules in $1 \mu\text{m}^2$	143
Table 5.5	Observed band (1650 cm^{-1}) parameters in SM-SERRS spectra of TRITC and TEXAS RED in LB monolayer.....	158

LIST OF FIGURES

Figure 2.1	Raman spectrometers. Ramanscope 2000 and Invia.....	15
Figure 2.2	Potential Energy Diagram for Vibrations of a Diatomic Molecule	18
Figure 2.3	Raman Spectrum of CCl ₄ excited by laser radiation wavenumber $\omega_0 = 20,492 \text{ cm}^{-1}$	21
Figure 2.4	Energy level diagram for Raman (S as Stoke, R as Resonance and AS as anti-Stokes), Resonance Raman and Fluorescence.....	26
Figure 2.5	Polarization of a diatomic molecule in an electric field.....	28
Figure 2.6	The vector component of the excitation source polarization that is parallel to the changing polarizability of the molecule drives the scattering process.....	29
Figure 2.7	Illustration of the single sphere model: (a) a molecule at a distance d from the metal nanosphere and (b) a molecule attached to the nanosphere or chemical adsorption model	37
Figure 2.8	Energy level diagram of the couple molecule-adsorbent system in SERS.....	40
Figure 2.9	The Origin of surface plasmon resonance, (a) at the interface of thin metal film and a dielectric, and (b) in nanoparticles.....	42
Figure 2.10	Cartoon representing EM enhancement from a single particle and two body interaction. The incident wave is polarized along z axis.....	47
Figure 2.11	Cartoon of a molecular orientation in an electric field.....	49
Figure 2.12	The Total System for Metal Evaporation	52
Figure 2.13	Nima Langmuir Trough and Monolayer of Arachidic Acid.....	55
Figure 2.14	Surface Pressure – Area Isotherm	56
Figure 2.15	Deposition of monolayer by vertical substrate movement	58
Figure 2.16	Set up of Nima LB trough with MicroBAM2 for monolayer.....	61
Figure 2.17	(a) SPM Microscope, (b) essential elements of an AFM and (c) an AFM image	62

Figure 2.18	Illustration of the principles of AFM imaging	63
Figure 2.19	The cantilever oscillation during tapping mode imaging.....	65
Figure 2.20	Cary UV-Vis spectrometer.....	66
Figure 3.1	Illustration of metal deposition using vacuum evaporation technique.....	76
Figure 3.2	AFM image of nanoparticle size variation profile (section analysis) in 6 nm silver island film	77
Figure 3.3	Surface plasmon absorption of Ag island films (thickness variation).....	78
Figure 3.4	Surface plasmon absorption of Ag island films(temperature variation)...	79
Figure 3.5	Particle size distribution analysis for silver island films of 9 nm at 100 ⁰ C and 200 ⁰ C.....	80
Figure 3.6	Surface plasmon absorption of Ag and Au island films.....	81
Figure 3.7	Surface plasmon absorption of Au and mixed Ag/Au island films.....	83
Figure 3.8	Absorption spectra of Benzene thiol solution, Ag and Au island films.....	86
Figure 3.9	Deposition of Benzene thiol onto metal island films by vertical dipping...	87
Figure 3.10	Raman spectra acquisition for Benzene Thiol on silver film and glass surface.....	88
Figure 3.11	Raman spectra acquisition for Benzene Thiol on gold film and glass surface	89
Figure 3.12	SERS spectra of Benzene Thiol on Ag film at 514 nm, 633 nm and 785 nm.....	90
Figure 3.13	SERS - Benzene Thiol on Au island film at 514 nm, 633 nm and 785 nm	90
Figure 4.1	Illustration of a Phospholipid Bilayer model in cell membranes.....	101
Figure 4.2	Illustration for chemical structures of the Phospholipids.....	105
Figure 4.3	UV-visible absorption of 9 nm Silver island film and Phospholipid-DPPC.....	108
Figure 4.4	Surface-pressure area isotherm for DPPC on water, AFM of the Ag nanostructures, the BAM image of monolayer morphology, and the arrow shows the surface pressure for monolayer transfer.....	110

Figure 4.5	Raman scattering of phospholipids solid-DMPC and DPPC	111
Figure 4.6	LB-SERS of monolayer and bilayers and Raman of solid, a) DMPC and b) DPPC.....	114
Figure 4.7	Illustration of DPPC spectra, a) comparison of adding monolayers on SIF and glass and b) raw spectrums of bilayers and trilayers on SIF.....	115
Figure 4.8	LB-SERS point-by-point mapping a) DMPC and b) DPPC.....	118
Figure 4.9	LB-SERS DPPC monolayer in silver and gold.....	119
Figure 5.1	Illustration for EM Field variation on a SIF surface.....	129
Figure 5.2	A graphical representation of interplay between the intrinsic Raman cross section of a molecule and the required enhancement factor needed for SMD.....	130
Figure 5.3	Illustration of location for a molecule adsorbed on metal nanostructured surface.....	131
Figure 5.4	Renishaw's precision diffraction grating stage.....	133
Figure 5.5	Spectra of CCl ₄ taken with standard and high resolution inVia Raman microscopes (spectra offset for clarity).....	135
Figure 5.6	Illustration of SM-SER(R)S experiment.....	137
Figure 5.7	Molecular structures of Dye tagged Phospholipids, a) TRITC-DHPE and b) Texas Red.....	140
Figure 5.8	Experimental set-up for single molecule approach in LB_SERRS of TRITC-DHPE and TEXAS RED.....	142
Figure 5.9	Solution Absorption and Fluorescence spectra a) 10 ⁻⁵ M TRITC and b) 10 ⁻⁵ M TEXAS RED.....	146
Figure 5.10	LB-SERRS, LB-RRS and Reference Spectra a) TRITC and b) TEXAS RED.....	148
Figure 5.11	Illustration of LB-SERRS and LB-SERS spectra a) TRITC and b) TEXAS RED.....	150
Figure 5.12	Ensemble SERRS map of LB film fabricated on SIF and excited at 514.5 nm and ~20 μW. Step sizes were 2 μm x 2 μm, and the map was constructed from 1651 collected spectra. An intensity map was generated from the integrated area of the 1650 cm ⁻¹ band. The inset	

	shows the likely orientation of probe molecules with respect to the metal surface. a) TRITC and b) TEXAS RED.....	152
Figure 5.13	Ensemble average breaking in LB-SERRS spectra a) TRITC and b) TEXAS RED.....	154
Figure 5.14	Single molecule LB-SERRS maps, excited at 514 nm with a step size $2\ \mu\text{m} \times 2\ \mu\text{m}$ and power $\sim 20\ \mu\text{W}/\mu\text{m}^2$. The intensity map images were generated from correlation to the reference ensemble spectrum. a) TRITC and b) TEXAS RED.....	156
Figure 6.1	Surface silanization of glass and preparation of silver metal film by self-assembly of silver nanoparticle on silanized surface.....	171
Figure 6.2	Experimental set up for LB monolayer deposition on silver metal film...	172
Figure 6.3	Surface plasmon absorption of citrate silver colloid dispersion and molecular absorption of $1.34 \times 10^{-4}\ \text{M}$ octadecyl rhodamine B chloride R18.....	174
Figure 6.4	Plasmon absorption spectra of silver films made by 2 hrs, 6 hrs, 10 hrs and 14 hrs of deposition.....	175
Figure 6.5	The LB-SERRS and reference resonance Raman (solid) spectrum of octadecyl rhodamine B chloride R18.....	176
Figure 6.6	SERRS mapping spectra from a self assembly silver film made by 2 hrs deposition, mapping image and AFM image of the Ag.....	177
Figure 6.7	SERRS mapping spectra from a self assembly silver film made by 14 hrs deposition, mapping image and AFM image of the Ag film.....	178
Figure 6.8	SERRS spectra and mapping images from self assembly silver films made by 2 hrs, 6 hrs, 10 hrs and 14 hrs deposition.....	179
Figure 7.1	LB monolayers of arachidic acid mixed with PTCs fabricated on SIF and glass for SMD by SERRS and SHINEF.....	193
Figure 7.2	Schematic of coating the LB monolayers on glass by SHIN particles and experimental for SHINEF.....	195
Figure 7.3	Absorption spectra of silver island film, Bis(ndodecyl imido) perylene solution and Bis(3,4 dichloro benzylimido) perylene solution.....	197
Figure 7.4	The ensemble average spectra, SERRS and RRS, of PTCs at laser excitation of 514 nm and power 10-20 μW . a) Bis (ndodecyl imido) perylene and b)	

Figure 7.5	Bis (3,4 dichloro benzylimido) perylene.....199 SMD in LB-SERRS of PTCDs. laser excitation of 514.5 nm and power 10-20 μ W, a) Bis (ndodecyl imido) perylene and b) Bis (3,4 dichloro benzylimido) perylene.....201
Figure 7.6	SMD spectra (LB-SERRS) of Bis (3,4 dichloro benzylimido) perylene acquired at different spots by mapping with a laser excitation of 514.5 nm and power 10-20 μ W.....204
Figure 7.7	The solution fluorescence spectra of PTCDs mixed with AA excited at 514.5 nm a) Bis (ndodecyl imido) perylene and b) Bis (3,4 dichloro benzylimido) perylene.....205
Figure 7.8	Fluorescence and SHINEF spectra of concentrated LB-PTCDs at 514.5 nm excitation a) Bis (ndodecyl imido) perylene and b) Bis (3,4 dichloro benzylimido) perylene.....207
Figure 7.9	Single molecule - SHINEF spectra of LB-PTCDs at laser 514.5 nm excitation a) Bis (ndodecyl imido) perylene and b) Bis (3,4 dichloro benzylimido) perylene.....209

LIST OF ABBREVIATIONS

AA	Arachidic Acid
AFM	Atomic Force Microscopy
APTES	3-aminopropyltriethoxysilane
BAM	Brewster Angle Microscopy
BPE	Trans-1,2-bis(4-pyridyl)ethylene
CM	Centre of Mass
CT	Charge Transfer
CCD	Charged Coupled Device
DMPC	1,2-dimyristoyl-sn-glycero-3-phosphocholine
DPPC	1,2-Dipalmitoyl-sn-glycero-3-phosphocholine
EBL	Electron-beam Lithography
EF	Enhancement Factor
EM	Electromagnetic
FWHM	Full Width at Half Maximum
HOMO	Highest Occupied Molecular Orbit
LB	Langmuir-Blodgett
LL	Laser Line
LSPR	Localized Surface Plasmon Resonance
LUMO	Lowest Unoccupied Molecular Orbit
NA	Numerical Aperture
NIR	Near Infra Red
NSL	Nanosphere Lithography

ODA	Octadecylamine
PC	Phosphatidylcholine
PTCD	Perylene Tetracarboxylic Derivatives
PTFE	Polytetrafluoroethylene
PZT	Piezoelectric Scanning Tube
SEF	Surface-enhanced Fluorescence
SERS	surface-enhanced Raman scattering
SERRS	surface-enhanced resonance Raman scattering
SHIN	Shell Isolated Nanoparticle
SHINEF	Shell Isolated Nanoparticles-enhanced Fluorescence
SIF	Silver Island Film
SMD	Single Molecule Detection
SMF	Single Molecule Fluorescence
SPM	Scanning Probe Microscopy
STM	Scanning Tunneling Microscopy
RRS	Resonance Raman Scattering
RS	Raman Scattering
SPR	Surface Plasmon Resonance
Texas Red	1,2-dihexadecanoyl- <i>sn</i> -glycero-3-phosphoethanolamine
TFA	Trifluoroacetic Acid
TM	Target Molecule
TMCL	Tetramyristoyl Cardiolipin
UV-Vis	Ultraviolet-Visible

CHAPTER 1

INTRODUCTION

1.1 Overview

Raman spectroscopy is a vibrational spectroscopic technique that measures inelastic light-scattering and provides specific spectroscopic fingerprints of molecular structures. This technique offers a powerful analytical tool in material science.¹ As Raman scattering is a second-order process, it has a very low cross section. In absence of any resonance in the Raman process, the Raman cross sections are typically less than 10^{-29} cm² molecule⁻¹, whereas the cross section for fluorescence could be about 10^{-16} cm² molecule⁻¹.²⁻³ Hence, the signal-to-noise ratio (S/N) of the surface Raman signal expected for a monolayer of adsorbate is below the detection limit. The inherently small Raman scattering cross-section or intensity of the Raman signal from molecules can be significantly improved by the surface-enhanced Raman scattering effect.⁴⁻⁶ In the mid-1970s, SERS was discovered which impacted surface science and spectroscopy because of its extremely high surface sensitivity.⁷ Most chemical sensors rely on properties such as mass, fluorescence, or a refractive index, which are often not specific for the substance in question. In contrast, Raman spectroscopy offers rich molecular information, and thus provides unequivocal identification of chemical and biological materials of interest. The discovery of SERS has triggered many highly sensitive detection technology development in analytical chemistry,⁸ biomedical engineering, and life sciences.⁹⁻¹⁰

Surface-enhanced Raman scattering (SERS) is based on the localized surface plasmon resonance phenomenon, which can greatly increase the Raman scattering cross-section of molecules located in the vicinity of a metallic

nanostructure.¹¹ This enormous signal amplification can be explained by an electromagnetic (EM) mechanism of SERS that is the defining feature of the effect and can provide enhancement of several orders of magnitude. Another important source of Raman signal enhancement is the molecular resonance effect, which is employed by laser excitation that falls within the envelope of an electronic transition of the molecular system, called resonance Raman scattering (RRS).¹²⁻¹³ In SERS experiments, enhancements typically up to 10^6 in the Raman signal can be obtained for molecules adsorbed on nanostructures of copper, silver, and gold.⁷

Because SERS activity critically depends not only on the nature of the metal but also on architectures of metal nanostructures; and the preparation of substrates is central to gain a higher SERS activity. Different types of nanoparticles give rise to different Raman enhancement characteristics,¹⁴⁻¹⁵ as the amplification of Raman signals depends on the molecular coupling with localized electromagnetic excitation on the surface of metal nanostructures. Hence, optimizing and tuning of the SERS characteristics require an appropriate control of SERS substrates: size, shape, spacing between nanoparticles, functionalization of nanoparticles and the dielectric environment.¹⁶⁻¹⁷

Most surface-enhanced Raman scattering (SERS) is done on large ensembles of molecules adsorbed onto metallic nanostructures, where good signal to noise ratios are achieved. We call this reproducible SERS signal “average SERS”.¹⁸ When the statistics are lost and we approach single-molecule SERS, the SERS signal fluctuates at room temperature, and correspondingly, the

spectral features may change from one spatial location to another.¹⁹⁻²⁰ In recent years, the development of single molecule detection²¹⁻²² (SMD) techniques has opened up a new era of life science and a great deal of activity in analytical chemistry and biology.²³⁻²⁵ The dynamic properties of biomolecules, and the unique operations of molecular machines, which were hidden in averaged ensemble measurements, can be unveiled. The SMD techniques have rapidly been expanding in a wide range of life sciences,²⁶ which includes molecular motors, DNA sequencing, enzyme reactions, protein dynamics, and cell signaling. The advent of single molecule fluorescence studies was an important development, but required that the molecules under study must be intrinsically fluorescent. The discovery that Raman spectroscopy could also be extended to single molecules, by exploiting surface-enhancement, is an enormous advance, since vibrational spectra contain vibrational fingerprints for structural information that can be used to identify molecules and interactions. In the case of surface-enhanced resonance Raman scattering, where both of these resonance (plasmon and molecular) conditions are fulfilled, the two enhancement mechanisms are multiplicative and can lead to large enhancement factors that often make a easier way to detect a single molecule.²⁷⁻³³ The greatest challenge in SERS is the preparation of SERS-active substrates with the highest electromagnetic enhancement factor. On a SERS-active substrate, some spots or sites exhibit much higher SERS activity than other areas. Moskovits, Shalaev and their coworkers have investigated this phenomenon, especially from the theoretical point of view, and named the highly active spots as “hot spots”.³⁴⁻³⁵ In

this case, it is believed that the greatest enhancements ($\sim 10^{10}$) that enabled single-molecule detection only occurred at specific sites (junctions or gaps between two or more closely spaced nanoparticles) termed hot spots.³⁶⁻³⁸ Single molecule detection, using SERS/SERRS, has been reported only with silver or gold nanoparticles.²¹⁻⁴⁰ In this work, the Langmuir-Blodgett (LB) approach was employed to control the fabrication of a one molecule thick film of analyte on a nanostructured metal surface (mainly Ag island films) used to detect SERS/SERRS.

The mapping of the Raman intensity obtained with variable sub-monolayer coverage of the analyte is consistent with signals being dominated by molecules at junctions in nanoparticle aggregates, where the electromagnetic field is localized. The fabrication of SERS substrates containing hot spots usually relies on the random aggregation of metal nanoparticles. In general, the poor reproducibility of the fabrication, as well as the broad distribution in terms of size, shape and space for the nanoparticles, imposes many challenges for effectively correlating the detected SERS signals to the specific attributes of a hot spot, although progress is being made⁴¹⁻⁴². Hence, developing a fabrication method yielding reproducible, reliable, and stable SERS nanostructures/substrates is critical for predictable and reproducible SERS performance. The most commonly used techniques for fabricating SERS substrates are: oxidation reduction cycling on a metal electrode, metal island films by physical evaporation deposition, reduction of Au or Ag with various chemicals,⁴³ and a sol-gel process.⁴⁴ The activity of SERS substrates with ordered and an appropriate surface

nanostructure is also being tested. It is of special interest to extend the SERS substrate from randomly rough surfaces to ordered nanostructures. Several approaches to preparing ordered periodic arrays of nanoparticles for SERS have been made that include electron beam lithography,⁴⁵ self-assembly of metal colloids⁴⁶⁻⁴⁷ and nanosphere lithography⁴⁸⁻⁴⁹. One of the most significant approaches has been proposed and developed by Natan and co-workers based upon the self-assembled monolayer technique.⁵⁰⁻⁵¹ It allows one to prepare regularly arranged monodispersed colloidal gold and silver particles on functionalized metal or glass substrates, producing SERS with good reproducibility and stability.⁵⁰⁻⁵² Another important property of this method is to control the particle size and density, and the space between the particles, thus tuning the electromagnetic characteristics of the surface for a systematic study of the SERS enhancement.

In SERS, the basic components involved are a molecule, a metal nanostructure and electromagnetic radiation. The SERS complexities may arise from: 1) the molecule interacting with nanostructure; 2) the layout of the molecules adsorbed on the metal surface; 3) the photoreactions of the molecules induced by the incident photon of electromagnetic radiation; 4) the dielectric function of the metallic nanostructures changes due to the adsorbed molecules. SERS is commonly obtained by excitation with visible or near infrared light. As a result, spatial spectroscopic tuning is an application of SERRS that exploits both the enhanced field in SERS and the molecular specificity of the enhancement when exciting in resonance (RRS). To maximize SERS, a profound

understanding of the experiment is required, along with the possibilities and limitations. Questions also come up about how to achieve the highest enhancement from SERS substrates, how to optimize experimental parameters when the ensemble average breaks down, what the characteristics of single molecule detection are. Ironically, a very simple SERS measurement may require a very challenging spectral interpretation.

In this work, an effort has been made to obtain SERS/SERRS and at the same time to control some of the variables. The thesis “Plasmon Enhanced Raman and Resonance Raman Scattering (SERS/SERRS) and Single Molecule Detection (SMD) in Langmuir Blodgett (LB) Monolayers” has the LB technique at the centre of the experimental part, in order to control the coating of the SERS-active substrate with well organized molecular layers. In Chapter 2, the fundamentals of Raman scattering, the origin of surface-enhanced Raman scattering (SERS), and the surface-enhanced resonance Raman scattering (SERRS) have been discussed, followed by the details of Langmuir-Blodgett (LB) technique for monomolecular film fabrication, and the atomic force microscopy (AFM), and the UV-Vis spectroscopy for characterization purposes are introduced and discussed.

In Chapter 3, the preparation of Ag, Au and mixed Ag/Au island films by the vacuum evaporation technique, and their characterization using UV-Vis absorption spectroscopy and AFM are discussed, which is the main nanostructured substrate for SERS experiments. It is shown that the Langmuir-

Blodgett (LB) technique, although limited in the scope of molecular systems, is one of the best choices for SERS investigation.

Chapter 4 presents the use of one molecule thick LB monolayers for the SERS studies of phospholipids, which mimic lipid bilayers in cell membranes. The success of the phospholipid bilayer SERS is established in this investigation.

Single molecule identification and studies of its behavior are the priority in analytical analysis. In Chapter 5, the ensemble averaged LB-SERRS, the breakdown of the average and characteristics of single molecule LB-SERRS are examined and discussed. Two dye tagged phospholipids are used in this study, which opens the door to extract information about biomolecules through LB-SERRS.

In Chapter 6, a method of preparation for SERS substrate to attain controlled plasmon, by means of electromagnetic enhancement, using a surface silanization technique to deposit Ag colloidal nanoparticles by self-assembly, is presented. This survey is performed using a rhodamine B dye coating the newly developed SERS-active substrate by a LB technique.

In Chapter 7, single molecule studies of Perylene tetracarboxylic (*PTCD*) derivatives by shell isolated nanoparticle enhanced fluorescence (SHINEF) and surface-enhanced resonance Raman scattering (SERRS) are presented. The overtones and combinations of the *PTCD* are also observed in SERRS experiments, which is the rare molecular structural identification.

Finally, the main conclusions of this thesis and probable future track of study are discussed in Chapter 8.

References

- (1) Raman, C. V.; Krishnan, K. S. *Nature (London, U. K.)* **1928**, *121*, 501-2.
- (2) Kneipp, K.; Kneipp, H.; Itzkan, I.; Dasari, R. R.; Feld, M. S. *Chemical Reviews* **1999**, *99*, 2957-2975.
- (3) Garrell, R. L. *Analytical Chemistry* **1989**, *61*, 401A-411A.
- (4) Fleischmann, M.; Hendra, P. J.; McQuillan, A. J. *Chemical Physics Letters* **1974**, *26*, 163-166.
- (5) Albrecht, M. G.; Creighton, J. A. *Journal of the American Chemical Society* **1977**, *99*, 5215-5217.
- (6) Jeanmaire, D. L.; VanDuyne, R. P. *Journal of Electroanalytical Chemistry* **1977**, *84*, 1-20.
- (7) Moskovits, M. *Rev. Mod. Phys.* **1985**, *57*, 783-826.
- (8) Graham, D.; Goodacre, R. *Chem Soc Rev* **2008**, *37*, 883-4.
- (9) Anker, J. N.; Hall, W. P.; Lyandres, O.; Shah, N. C.; Zhao, J.; Van Duyne, R. P. *Nature Materials* **2008**, *7*, 442-453.
- (10) Camden, J. P.; Dieringer, J. A.; Zhao, J.; Van Duyne, R. P. *Accounts of Chemical Research* **2008**, *41*, 1653-1661.
- (11) Le Ru, E. C.; Etchegoin, P. G. *Chemical Physics Letters* **2006**, *423*, 63-66.
- (12) Shorygin, P. P.; Krushinskij, L. L. *J. Raman Spectrosc.* **1997**, *28*, 383-388.
- (13) Myers, A. B. *J. Raman Spectrosc.* **1997**, *28*, 389-401.
- (14) Willets, K. A.; Van Duyne, R. P. *Annual Review of Physical Chemistry* **2007**, *58*, 267-297.

- (15) Rubim, J. C.; Aroca, R. F. *Physical Chemistry Chemical Physics* **2008**, *10*, 5412-5418.
- (16) Nordlander, P.; Oubre, C.; Prodan, E.; Li, K.; Stockman, M. I. *Nano Letters* **2004**, *4*, 899-903.
- (17) Noguez, C. *Journal of Physical Chemistry C* **2007**, *111*, 3806-3819.
- (18) Aroca, R. *Surface-enhanced Vibrational Spectroscopy*; John Wiley & Sons: Chichester, 2006.
- (19) Le Ru, E. C.; Meyer, M.; Blackie, E.; Etchegoin, P. G. *J. Raman Spectrosc.* **2008**, *39*, 1127-1134.
- (20) Pieczonka, N. P. W.; Aroca, R. F. *Chem. Soc. Rev.* **2008**, *37*, 946-954.
- (21) Kneipp, K.; Wang, Y.; Kneipp, H.; Perelman, L. T.; Itzkan, I.; Dasari, R. R.; Feld, M. S. *Phys. Rev. Lett.* **1997**, *78*, 1667-1670.
- (22) Nie, S.; Emory, S. R. *Science (Washington, D. C.)* **1997**, *275*, 1102-1106.
- (23) Kneipp, J.; Kneipp, H.; Kneipp, K. *Chemical Society Reviews* **2008**, *37*, 1052-1060.
- (24) Kneipp, K.; Kneipp, H. *Applied Spectroscopy* **2006**, *60*, 322A-334A.
- (25) Pieczonka, N. P. W.; Moula, G.; Aroca, R. F. *Langmuir* **2009**, *25*, 11261-11264.
- (26) Moerner, W. E. *J. Phys. Chem. B* **2002**, *106*, 910-927.
- (27) Bravo-Vasquez, J.-P.; Fenniri, H. *J. Phys. Chem. C FIELD Full Journal Title:Journal of Physical Chemistry C* **2009**, *113*, 12897-12900.
- (28) Cho, H.; Baker, B. R.; Wachsmann-Hogiu, S.; Pagba, C. V.; Laurence, T. A.; Lane, S. M.; Lee, L. P.; Tok, J. B. H. *Nano Lett. FIELD Full Journal Title:Nano Letters* **2008**, *8*, 4386-4390.

- (29) MacAskill, A.; Crawford, D.; Graham, D.; Faulds, K. *Anal. Chem. (Washington, DC, U. S.) FIELD Full Journal Title:Analytical Chemistry (Washington, DC, United States)* **2009**, *81*, 8134-8140.
- (30) Pieczonka, N. P. W.; Moula, G.; Aroca, R. F. *Langmuir FIELD Full Journal Title:Langmuir* **2009**, *25*, 11261-11264.
- (31) Sabatte, G.; Keir, R.; Lawlor, M.; Black, M.; Graham, D.; Smith, W. E. *Anal. Chem. (Washington, DC, U. S.) FIELD Full Journal Title:Analytical Chemistry (Washington, DC, United States)* **2008**, *80*, 2351-2356.
- (32) Smith, W. E. *Pharm. Appl. Raman Spectrosc. FIELD Full Journal Title:Pharmaceutical Applications of Raman Spectroscopy* **2008**, 65-84.
- (33) Yoshida, K.-i.; Itoh, T.; Biju, V.; Ishikawa, M.; Ozaki, Y. *Physical Review B: Condensed Matter and Materials Physics* **2009**, *79*, 085419/1-085419/6.
- (34) Tsai, D. P.; Kovacs, J.; Wang, Z.; Moskovits, M.; Shalaev, V. M.; Suh, J. S.; Botet, R. *Phys. Rev. Lett.* **1994**, *72*, 4149-52.
- (35) Haslett, T. L.; Tay, L.; Moskovits, M. *J. Chem. Phys.* **2000**, *113*, 1641-1646.
- (36) Kang, T.; Yoon, I.; Jeon, K.-S.; Choi, W.; Lee, Y.; Seo, K.; Yoo, Y.; Park, Q. H.; Ihee, H.; Suh, Y. D.; Kim, B. *J. Phys. Chem. C FIELD Full Journal Title:Journal of Physical Chemistry C* **2009**, *113*, 7492-7496.
- (37) Le Ru, E. C.; Etchegoin, P. G. *J. Chem. Phys. FIELD Full Journal Title:Journal of Chemical Physics* **2009**, *130*, 181101/1-181101/4.
- (38) Lee, S. J.; Morrill, A. R.; Moskovits, M. *J. Am. Chem. Soc. FIELD Full Journal Title:Journal of the American Chemical Society* **2006**, *128*, 2200-2201.

- (39) Michaels, A. M.; Nirmal, M.; Brus, L. E. *J. Am. Chem. Soc.* **1999**, *121*, 9932-9939.
- (40) Eggeling, C.; Schaffer, J.; Seidel, C. A. M.; Korte, J.; Brehm, G.; Schneider, S.; Schrof, W. *J. Phys. Chem. A* **2001**, *105*, 3673-3679.
- (41) Stockman, M. I. *Nature* **2010**, *467*, 541-542.
- (42) Stranahan, S. M.; Willets, K. A. *Nano Letters* **2010**, DOI: 10.1021/nl102559d.
- (43) Kovacs, G. J.; Loutfy, R. O.; Vincett, P. S.; Jennings, C.; Aroca, R. *Langmuir* **1986**, *2*, 689-94.
- (44) Volkan, M.; Stokes, D. L.; Vo-Dinh, T. *Appl. Spectrosc.* **2000**, *54*, 1842-1848.
- (45) Liao, P. F.; Bergman, J. G.; Chemla, D. S.; Wokaun, A.; Melngailis, J.; Hawryluk, A. M.; Economou, N. P. *Chem. Phys. Lett.* **1981**, *82*, 355-9.
- (46) Yu, H.-Z.; Zhang, J.; Zhang, H.-L.; Liu, Z.-F. *Langmuir* **1999**, *15*, 16-19.
- (47) Maxwell, D. J.; Emory, S. R.; Nie, S. *Chem. Mater.* **2001**, *13*, 1082-1088.
- (48) Deckman, H. W.; Dunsmuir, J. H. *Appl. Phys. Lett.* **1982**, *41*, 377-9.
- (49) Halteen, J. C.; Van Duyne, R. P. *J. Vac. Sci. Technol., A* **1995**, *13*, 1553-8.
- (50) Nicewarner-Pena, S. R.; Freeman, R. G.; Reiss, B. D.; He, L.; Pena, D. J.; Walton, I. D.; Cromer, R.; Keating, C. D.; Natan, M. J. *Science* **2001**, *294*, 137-41.
- (51) Keating, C. D.; Kovaleski, K. K.; Natan, M. J. *J. Phys. Chem. B* **1998**, *102*, 9414-9425.
- (52) Huang, X.; Huang, H.; Wu, N.; Hu, R.; Zhu, T.; Liu, Z. *Surf. Sci.* **2000**, *459*, 183-190.

CHAPTER 2
BACKGROUND

2.1 Introduction

In this chapter, an overview of elemental concepts involved in the research work of this thesis is discussed. A brief discussion of the fundamentals of Raman spectroscopy¹⁻² is given, followed by the description of SERS/SERRS prop up by Localized Surface Plasmon Resonance (LSPR). Surface Enhanced Raman Scattering (SERS) and Surface Enhanced Resonance Raman Scattering (SERRS)³⁻⁷ are the main techniques used in this research to achieve trace molecular detection below the femtomole concentrations. In addition, the experimental details on the fabrication of metal island films by Vacuum Deposition Technique, Langmuir Blodgett (LB) films using the LB technique to deposit molecular monolayers are discussed. Finally, Atomic Force microscopy (AFM) and UV-Vis absorption spectroscopy, which are important tools for characterizing plasmons in metal island films and electronic transitions in the analyte (solid state and solutions), are also described.

2.2 Raman spectroscopy

Raman spectroscopy is a highly versatile analytical tool, carrying fingerprint information of molecular moieties, requiring little sample preparation, making it ideal for a wide range of applications in material science. Recent years have seen an explosion in the use of Raman spectroscopy for biological purposes such as blood analyte detection and cellular examination, pharmaceutical product design and production processes. In addition in forensic sciences for the unambiguous identification of unknown substances, it has also

biomedical applications to demonstrate the sensitivity to distinguish between cancerous, pre-cancerous and normal tissues; and its sensitivity to changes in cell metabolites and protein structures etc., which elevate it above competing spectroscopic techniques.⁸ Raman is an interesting option for several reasons, including the sensitivity to small structural changes, non-invasive sampling capability, minimal sample preparation and high spatial resolution. Furthermore, the laser lines of modern instruments make the Raman spectrum available in the entire UV-visible and near infrared part of the electromagnetic spectrum.⁹ The spatial resolution of Raman micro spectroscopy in the low micrometer scale and its ability to probe samples *in vivo* conditions allow new insights into single cells without the need for fixatives, markers or stains.¹⁰ The output of Raman spectroscopy can now be used for structural imaging from “vibrational fingerprints” of a molecular moiety. This is a unique technique that identifies the chemical structure of the analyte.

To exploit this spectroscopic technique, the Raman spectrometers used for the work contained within this thesis were bench top systems manufactured by Renishaw (Renishaw, UK.). These are the “InVia” and the “System 2000”,



Figure 2.1: Raman spectrometers. Ramanscope 2000 (left) and InVia (right)

shown in Figure 2.1.

The most important facets of these Micro-Raman systems are: (1) the proper choice of objectives that allows for high spatial resolution and control of probe volumes, which is vital for trace detection down to single molecule level and (2) these systems have optical configurations that maximize throughput and are equipped with high sensitivity detectors. This is a type of spectrometer where the Raman spectra follow the excitation laser line. A wide range of laser lines allow working with any class of materials. The laser lines used in these spectrometers are given in Table 2.1.

Table 2.1: Excitation Lasers

Laser Type	Wavelength ¹¹	Output Power (mW)
HeCd (Coherent)	442, 325	20
Tunable Ar ⁺ (Lexar)	488, 514	10 – 100
Ar ⁺		
HeNe	633	18
Solid State Diode	785	19

An appropriate plasma-rejection line filter was used in each laser line at the entrance beam path to allow the laser light to pass through a set of neutral density filters for the purpose of controlling the laser light intensity at the sample. The reduction of intensity was achievable from 100% to 50%, 10%, 5%, 1% and gradually down to 0.000005%.

2.2.1 Molecular origin of Raman spectroscopy

Molecular detection and characterization techniques have evolved as one of the most active research areas in science with vast applications from biology to astronomy. Depending on the energy scale probed, molecular spectroscopy can be classified into three categories: Electronic, Rotational and Vibrational spectroscopy. The energy of a molecule can be separated into three components associated with (1) the motion of electrons in the molecule, (2) the vibrations of the constituent atoms, and (3) the rotation of the molecule as a whole:

$$E_{\text{total}} = E_{\text{el}} + E_{\text{vib}} + E_{\text{rot}} \text{ ----- (2.2.1)}$$

The basis for this separation lies in the fact that electronic transitions occur on a much shorter timescale and rotational transitions occur on a longer time scale than vibrational motions. The translational energy of the molecule may be ignored as it is essentially not quantized. The electronic spectroscopy investigates the electronic energy states of a molecule, which can be probed by ultraviolet or visible radiation. The *vibrational energy states* can be explored either by infrared absorption or *Raman scattering (RS)*. Vibrational Raman spectroscopy is an effective method to study the structure and dynamics of molecules, irrespective of the environment in which they are present. Every molecule has its characteristic vibrational spectrum which can be used as a fingerprint.¹²⁻¹⁴ A molecule can exist in the ground electronic state and also a series of excited electronic states.¹³ There are several vibrational and rotational energy levels at each electronic state. The rotational energy can be probed by microwave radiation. A simplest potential energy curve for inter-nuclear

vibrations of a diatomic molecule at its electronic ground state is presented in Figure 2.2.¹²⁻¹³

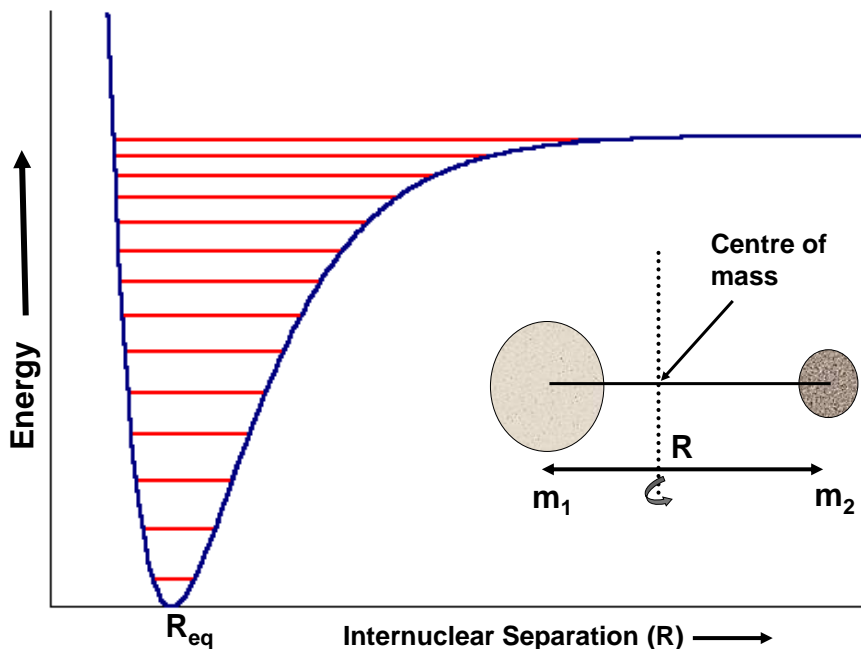


Figure 2.2: Potential Energy Diagram for Vibrations of a Diatomic Molecule

This model shows that the motion of a diatomic molecule creates harmonic oscillations which describe the vibrations of the two atoms along the bond direction and the rigid rotor which approximates the rotation of the molecule in space.¹³ The energy levels for the vibrations of the chemical bond by applying Quantum Mechanics to the simple harmonic oscillations.¹⁴

$$\epsilon(v) = hv\left(v + \frac{1}{2}\right) \quad (2.2.2)$$

dividing by hc , we have

$$G(v) = \omega\left(v + \frac{1}{2}\right) \quad (2.2.3)$$

Where ω is the wavenumbers (cm^{-1}), v is the quantum number having values

$\nu = 0, 1, 2, 3 \dots$ i.e. the number of vibrational states and h is Planck's constant, ν is the vibrational frequency (in Hz) which is given by

$$\nu = \frac{1}{2\pi} \sqrt{\frac{k}{\mu}} \quad (2.2.4)$$

Where μ is the reduced mass of the diatomic molecule, equal to $(m_1 m_2)/(m_1 + m_2)$ and k is the force constant of the bond in units of N m^{-1} or dynes cm^{-1} . The vibrational frequency is often expressed in units of cm^{-1} (wavenumber), rather than Hz, through the relation, $\omega c = \nu$, where c is the speed of light.

In diatomic molecules, the vibration occurs only along the chemical bond connecting the nuclei. In polyatomic molecules, the situation is complicated because all the nuclei perform their own harmonic oscillations. However, any of these complicated vibrations of a molecule can be expressed as a superposition of a number of "normal modes of vibration" which are completely independent of each other.¹⁴ The theoretical modeling of vibrations for a polyatomic molecule of N atoms can be viewed as N objects connected through a set of mass-less springs. So the system has $3N$ degrees of freedom to move in the 3 Cartesian directions (x, y, z) to describe its motions and fix the origin of the system of coordinates in the centre of mass (CM) of the molecule (the location of the heavy nuclei by fix nuclei approximation). The molecule is considered as complete system. The motion of the CM in space is described by 3 degrees of freedom, which accounts for translational movement. So there are $3N-3$ degrees of freedom for the fixed molecule at the centre of mass. The molecule can also rotate; to describe this rotation of a nonlinear molecule needs 3 degrees of

freedom and 2 degrees of freedom for a linear molecule. The remaining vibrational degrees of freedom to describe the vibrational motions of a polyatomic molecule are $3N-6$ (or $3N-5$ for a linear molecule). Each vibration is called “normal mode” based on the harmonic approximation for each vibrational motion. The spatial arrangement of the atoms in a molecule is called its equilibrium configuration or structure. This configuration is invariant under a certain set of geometric operations that form the symmetry point group.¹⁴⁻¹⁵

2.2.2 Raman scattering

When a molecular system is illuminated with a beam of monochromatic light of wavenumber ω_0 , an instantaneous exchange of energy between a monochromatic light source and a molecule may occur, causing polarization of the Raman active molecule, resulting in two different types of photon scattering. The majority is Rayleigh scattering, a form of elastic scattering, retaining the original wavenumber ω_0 without changing the frequency of incident photons. The inelastic scattering of photons by the molecule, Raman scattering, is also observed with much smaller cross section, resulting in the production of photons with different wavenumber from that of the incident light, i.e., $\omega_0 \pm \omega_i$.

In the case of vibrational Raman of a molecular system, the wavenumber ω_i lies in the range associated with transition between vibrational energy levels. Two types of energy shifts, Stokes and anti-Stokes, are possible, and these are related to the vibrational energy spacing in the extant electronic state of the

molecule.^{2,16} A Raman spectrum of CCl_4 is shown in Figure 2.3, which represents the spectrum generated from both types of scattering processes.

The absolute intensity of the Stokes shifted light is stronger than the anti-Stokes shifted light at room temperature. The incident photon transfers energy into the oscillations of the molecule, resulting in lower photon energy, and therefore a lower frequency being scattered. In the case of anti-Stokes scattering, the incident photon instantaneously extracts energy from the oscillations of a molecule, resulting in scattering of higher frequency. Because anti-Stokes scattering requires the molecule to begin in a vibrationally excited state, this type of scattering is statistically less likely than Stokes scattering.

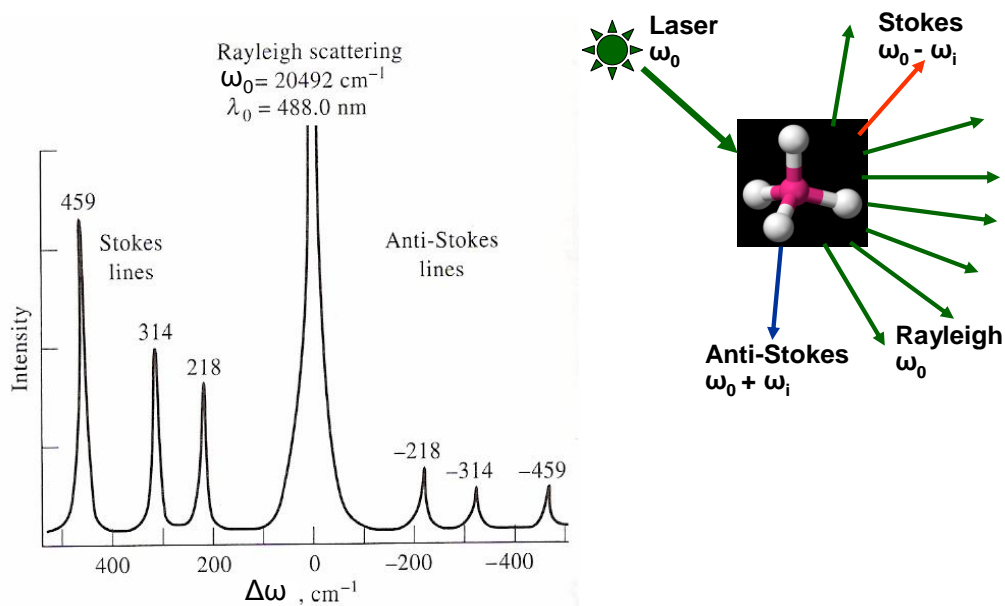


Figure 2.3: Raman Spectrum of CCl_4 excited by laser radiation of wavenumber $\omega_0 = 20,492 \text{ cm}^{-1}$

2.2.2.1 *Classical treatment of RS*

Two theoretical approaches can be employed in linear optics as well as in laser physics. The first is the semi-classical theory and the second is the quantum electrodynamical theory. The most essential feature of the semi-classical theory is that the media composed of atoms or molecules is described by the theory of quantum mechanics, while the light radiation is described by the classical Maxwell's theory. The key issue of semi-classical theory in linear optics is to give the expression of macroscopic linear electric polarization for optical media. Raman scattering or scattered radiation arises from an oscillating electric dipole induced in a scattering molecule by the oscillating electric field associated with the incident monochromatic electromagnetic radiation. Using classical theory, the magnitude of the induced electric dipole p is linearly related to the magnitude of the incident electric field strength E , expressed by a scalar relationship:

$$p = \alpha E \quad (2.2.5)$$

where α is the polarizability associated with the molecule. The intensity of the radiation emitted by the oscillating dipole is proportional to p^2 . The polarizability measures the perturbation of the electron density in a molecule by an electric field. If the electric field of frequency ω_0 is given by, $E = E_0 \cos(\omega_0 t)$, then the equation 2.2.5 becomes

$$p = \alpha \cdot E_0 \cdot \cos(\omega_0 t) \quad (2.2.6)$$

The polarizability is a function of the frequency of excitation and the vibrational coordinates. If a scattering system is a molecule which is free to vibrate in a space around its fixed equilibrium configuration; then the components of

polarizability for any vibration of the molecule can be expanded as a Taylor series about the equilibrium geometry as:

$$\alpha = \alpha_0 + \left(\frac{\partial \alpha}{\partial q} \right)_0 q + \frac{1}{2} \left(\frac{\partial^2 \alpha}{\partial q^2} \right)_0 q^2 \dots \dots \dots \quad (2.2.7)$$

where α_0 is the value of α at the equilibrium configuration and q represents the normal coordinate of vibration deviated from equilibrium coordinate q_0 and this is associated with molecular vibrational frequency ω_i . Then the q can be expressed as: $q = q_0 \cos(\omega_i t)$. For a polyatomic molecule, the vibrational motions are complex and are summations are over all normal coordinates.

The first derivative, $\alpha' = \left(\frac{\partial \alpha}{\partial q} \right)_0$, is responsible for determining the observation of

vibrational fundamentals in the Raman spectrum. So the equation 2.2.7 becomes:

$$\alpha = \alpha_0 + \alpha' q_0 \cos(\omega_i t) \quad (2.2.8)$$

and the induced dipole moment becomes:

$$p = \alpha_0 \cdot E_0 \cdot \cos(\omega_0 t) + \alpha' E_0 q_0 \cos(\omega_0 t) \cos(\omega_i t) \quad (2.2.9)$$

Using the trigonometric identity, $\cos a \cdot \cos b = \frac{1}{2} [\cos(a + b) + \cos(a - b)]$, the induced

dipole moment expression is

$$p = \alpha_0 \cdot E_0 \cdot \cos(\omega_0 t) + \alpha' E_0 q_0 \cos(\omega_0 - \omega_i)t + \alpha' E_0 q_0 \cos(\omega_0 + \omega_i)t \quad (2.2.10)$$

The first term of equation 2.2.10 is for the elastic Rayleigh scattering, the second term for the inelastic Stokes Raman scattering and the third one is for inelastic anti-Stokes Raman scattering.^{52,55} Raman scattering active mode foundation is based on the selection rule that the polarizability during the motion of vibration:

$$\alpha' = \left(\frac{\partial \alpha}{\partial q} \right)_0 \neq 0 \quad (2.2.11)$$

Polarizability is response function when a molecule is placed in an electric field (laser light) and represents the volume and shape of the molecular electronic cloud. Polarizability is a tensor consisting of three components in x, y and z directions and p and E are vectors. So equation 2.2.5 must be written as

$$\begin{aligned} p_x &= \alpha_{xx} E_x + \alpha_{xy} E_y + \alpha_{xz} E_z \\ p_y &= \alpha_{yx} E_x + \alpha_{yy} E_y + \alpha_{yz} E_z \\ p_z &= \alpha_{zx} E_x + \alpha_{zy} E_y + \alpha_{zz} E_z \end{aligned} \quad (2.2.12)$$

In matrix form, it is written as

$$\begin{bmatrix} p_x \\ p_y \\ p_z \end{bmatrix} = \begin{bmatrix} \alpha_{xx} & \alpha_{xy} & \alpha_{xz} \\ \alpha_{yx} & \alpha_{yy} & \alpha_{yz} \\ \alpha_{zx} & \alpha_{zy} & \alpha_{zz} \end{bmatrix} \begin{bmatrix} E_x \\ E_y \\ E_z \end{bmatrix} \quad (2.2.13)$$

The first matrix in the right hand side is the polarizability tensor. In normal Raman scattering, this tensor is symmetric; $\alpha_{xy} = \alpha_{yx}$, $\alpha_{xz} = \alpha_{zx}$ and $\alpha_{yz} = \alpha_{zy}$.

So for a symmetric tensor, each vibration has six probabilities to be observed in Raman spectrum. Also it can be said that for a vibrational transition to be allowed in the Raman spectrum, at least one of the six components of the derivative tensor must be different from zero.¹⁴

Although classical theory of Raman scattering explains the origin of Stokes and anti-Stokes line, they do not account for their differences in intensities. The classical theory cannot provide information about how α' is related to the properties of the scattering molecule, in particular its characteristic

transition frequencies, and to the frequency of the incident radiation. The quantum mechanical theory will provide this information and forms the basis for a complete treatment of all aspects of Raman scattering.

2.2.2.2 *Quantum Mechanical theory of RS*

The quantum theory of radiation in the regime of quantum electrodynamics treats the medium and optical field as a combined and quantized system. According to the basic principles of quantum mechanics, the energy associated with electronic, vibrational and rotational degrees of freedom of a molecule can assume the values only from a discrete set, namely the quantized energy levels correspond the possible stationary states of the molecule. In this case, the key issue is to determine the probability of state change of the combined system due to interaction between the photon field and the medium. These energy states are characterized by specific set of quantum numbers and a corresponding wave function. In electrodynamics, the quantum theory of radiation can be perfectly used to explain any kind of effects and phenomena related to the interaction of radiation field with matter in both qualitative and quantitative ways. The most important feature of quantum theory of radiation is that a concept of virtual energy can be introduced, which represents an intermediate quantum state occupied by the combined system of the photon field and the medium.

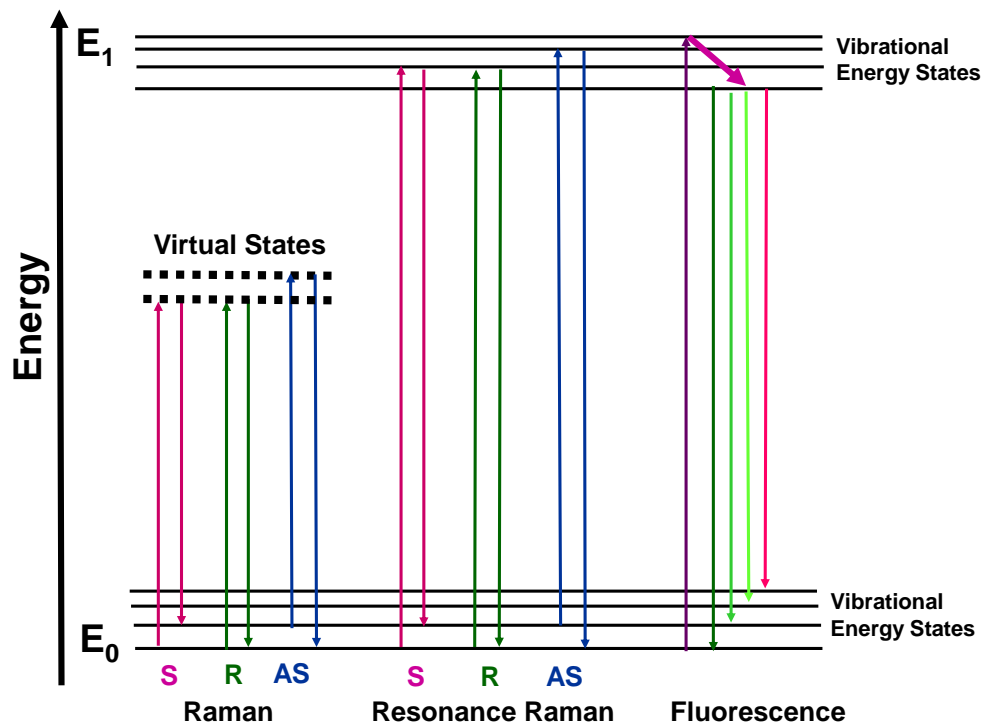


Figure 2.4: Energy level diagram for Raman (S as Stoke, R as Resonance and AS as anti-Stokes), Resonance Raman and Fluorescence

Based on the concept of virtual energy level or intermediate state, the principles and mechanism of linear optical effects can be consistently interpreted and clearly illustrated by an energy-level diagram involving the transitions via virtual energy levels.² The energy level diagram of Raman scattering, Resonance Raman scattering and Fluorescence is presented in Figure 2.4. *Resonance Raman scattering* (RRS) makes use of an excitation source with frequency close to a molecular electronic absorption frequency. Under these conditions a resonance occurs which may enhance the intensities of the Raman lines by several orders of magnitude.¹⁷⁻¹⁸ Fluorescence occurs when the molecule is excited to a discrete level of the electronic excited state, finally, fluorescence

spectrum may not be observed if the excited state molecule decays to lowest vibrational level via radiationless transitions.

In the quantum mechanical treatment of light scattering phenomena, the interacting molecule in the material system is treated quantum mechanically and the incident electromagnetic radiation used to produce perturbations is treated classically. The main concerns are the permitted transitions between the states of the molecule and the frequency dependent transition moments associated with such transitions. In the quantum mechanical treatment, the induced electric dipole of the classical theory is replaced by the transition electric dipole associated with a transition in the molecule from an initial state, i , to a final state, f , which has been induced by the incident electric field frequency ω_i . Thus the total induced transition electric dipole vector,

$$(p)_{fi} = (p^{(1)})_{fi} + (p^{(2)})_{fi} + (p^{(3)})_{fi} + \dots \quad (2.2.14)$$

where $(p^{(1)})_{fi}$ is linear in E , $(p^{(2)})_{fi}$ is quadratic in E and $(p^{(3)})_{fi}$ is cubic in E and so on. Then it is expected that any direct transition between two energy levels is accompanied by emission or absorption of radiation. If the total transition electric dipole $(p)_{fi}$ is nonzero,

$$(p)_{fi} = \langle \psi_f' | \hat{p} | \psi_i' \rangle \neq 0 \quad (2.2.15)$$

Where ψ_f' and ψ_i' are the time-dependent perturbed wave functions of the initial and final states of the molecule respectively and \hat{p} is the electric dipole moment operator.

2.2.2.3 Polarizability, Raman scattering and Intensity

When a molecule is placed in an electric field (laser beam), it suffers distortion, since the positively charged nuclei are attracted toward the negative pole and electrons toward positive pole. This is shown in Figure 2.5.

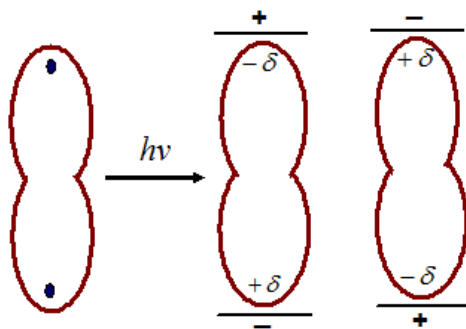


Figure 2.5: Polarization of a diatomic molecule in an electric field

This charge separation produces induced dipole moment p , which causes molecular polarization α , by shifting of chemical bond from its equilibrium position. To determine whether the vibration is active in the IR or Raman spectra, the selection rules must be applied to each normal vibration. According to quantum mechanics, a vibration is IR active if the dipole moment is changed during the vibration and is Raman active if the polarizability is changed during the vibration.

The force that the electric field of light can apply to an electron cloud is in the plane perpendicular to the direction of light is travelling. The direction of that force in the plane can be represented by a vector whose amplitude oscillates sinusoidally between positive and negative values. The direction in which this vector points is called the polarization of the light. Unpolarized light can be polarized by passing through a filter, called polarizer, which transmits only light

polarized in one direction. An external electric field can push the electron cloud of the chemical bond away from its equilibrium position. Light can therefore cause the position of the electron cloud in a chemical bond to oscillate. This emission of the light from the light-induced oscillation in the electron cloud is the scattering. The polarization of the Raman scattered light for a particular molecular vibration will be in the same direction as the change polarizability of the electron cloud caused by that vibration. When light induced-movement of the electron cloud is in the same direction as the polarization of the incident light, the scattered light will have the same polarization as the incident light. If, however, the incident light induces a movement of the electron cloud (induced dipole) in a different direction, the scattered light will have a polarization different from the incident light. An example of this situation is shown in figure 2.6.

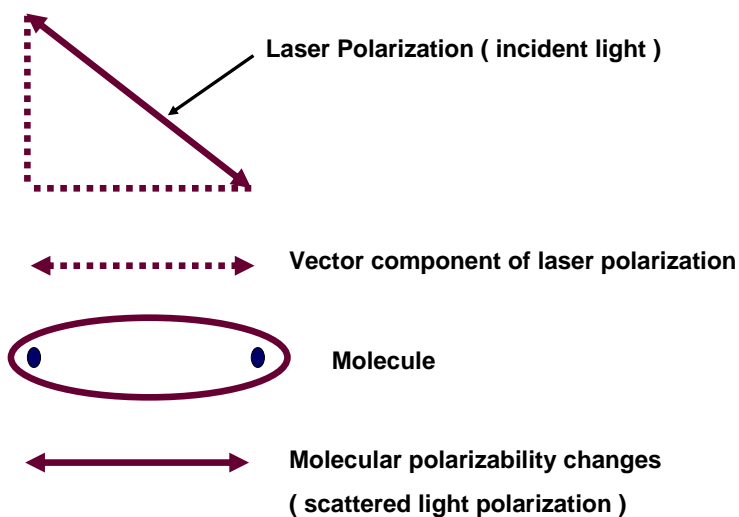


Figure 2.6: The vector component of the excitation source polarization that is parallel to the changing polarizability of the molecule drives the scattering process

The description of Raman scattering so far has only considered a single molecule fixed in space and its spectrum depends generally on the relative orientation of the molecular axis with respect to the polarization of the incident light and the polarization of the detected Raman light. Completely disordered molecules, such as tumbling liquids or gases, have all possible orientations with equal probability. However, when there is a molecular orientation as in solids, adsorbate or films, the scalar product $j \langle \psi_{v'} | p | \psi_v \rangle$ along the direction E_j of light polarization becomes the most important tool in the spectral interpretation of the observed intensities, where $\psi_{v'}$ and ψ_v represent the energy level between vibrational transitions.

Vibrations having spherical symmetry will have their induced dipole in the same direction as the polarization of the incident light regardless of the molecular orientation. As a result, Raman scattering from these vibrations will always have the same as the incident light. Raman scattering from vibrations that lack this symmetry will have an orientation dependent polarization. The summed Raman scatter from the entire sample will therefore be mostly depolarized. A useful measure of the polarization properties of a given vibration is the depolarization ratio ρ , is given by:

$$\rho = \frac{I_{\perp}}{I_{\parallel}} \quad (2.2.16)$$

Where I_{\perp} = Raman scattered intensity whose polarization is perpendicular to the
of plane of incidence

I_{\parallel} = Raman scattered intensity whose polarization is parallel to the

plane of incidence.

The polarizability of the electron cloud may change as the positions of the atoms held together by the chemical bond change. The intensity of the scattered light is proportional to the amount of electron cloud displacement. A quantum-mechanical modification to the model for Raman scattering described first by Placzek.¹⁹ One form of the derived resulting expression for the Raman scattering intensity from a sample, I_{RS} , is given by

$$I_{RS} = \frac{2^4 \pi^3}{45 \cdot 3^2 \cdot c^4} \cdot \frac{h I_L N (\nu_0 - \nu)^4}{\mu \nu (1 - e^{-h\nu/T})} \left[45 (\alpha'_a)^2 + 7 (\gamma'_a)^2 \right] \quad (2.2.17)$$

where c = Speed of light

h = Plank's constant

I_L = Excitation intensity

N = Number of scattering molecules

ν = Molecular vibrational frequency in Hertz

ν_0 = Laser excitation frequency in Hertz

μ = reduced mass of the vibrating atoms

k = Boltzmann constant

T = Absolute temperature

α'_a = Mean value invariant of the polarizability tensor

γ'_a = Anisotropy invariant of the polarizability tensor

Equation 2.2.17 shows that the Raman scattering intensity is proportional to the number of molecules illuminated, the intensity of incident light and to $(\nu_0 - \nu)^4$.²⁰

The Raman intensity can therefore be increased by increasing the incident light intensity or by using incident light of higher frequency, ν_0 (shorter wavelength).

2.2.2.4 Raman cross section

The efficiency of Raman scattering processes is determined by Raman cross section. The relationship between Raman scattered radiation from a single molecule, I_{RS} and the irradiance ϕ of the incident radiation has the general form:

$$I_{RS} = \sigma' \phi \quad (2.2.18)$$

Where, σ' is the proportionality constant.

Rearranging equation 2.2.18 gives the following expression:

$$\sigma' = \frac{I_{RS}}{\phi} \quad (2.2.19)$$

Where, σ' has the unit $\text{cm}^2 \cdot \text{sr}^{-1} \cdot \text{molecule}^{-1}$.

Then introducing the quantity σ which is define by

$$\sigma = \int_0^{4\pi} \sigma' d\Omega \quad (2.2.20)$$

Where, $d\Omega$ is an element of solid angle (unit: steradian, which is dimensionless).

The quantity σ has the unit $\text{cm}^2 \text{ molecule}^{-1}$ and termed as the total Raman scattering cross section per molecule and σ' is the first differential Raman scattering cross section per molecule. Integration of the differential cross section σ' , over all directions (4π steradians) in space, gives the total cross-section. If the scattered intensity varies across a range of wavenumbers around a central

wavenumber, then it is required to introduce σ'' , the second differential cross section per molecule, per unit wavenumber interval, defined by

$$\sigma'' = \frac{\partial \sigma'}{\partial \omega} = \frac{\partial^2 \sigma}{\partial \omega \cdot d\Omega} \quad (2.2.21)$$

Where, σ'' has the unit $\text{cm sr}^{-1} \text{molecule}^{-1}$ when frequency ω has the unit cm^{-1} .⁵⁵

As σ has dimensions of $\text{cm}^2 \text{molecule}^{-1}$, it may say that the radiation scattered over 4π steradians by a molecule with a scattering cross section σ corresponds to the incident radiation on the area σ . The Raman cross section σ is proportional to the square of the polarizability derivative for the $i \rightarrow j$

vibrational transition, $\alpha' = \left(\frac{\partial \alpha}{\partial q} \right)_0$ and the fourth power of the scattering frequency

ω_s expressed as

$$\sigma = C \omega_s^4 |\alpha_{ij}|^2 \quad (2.2.22)$$

where C contains numerical constants.

Optical efficiencies of different spectroscopic processes are determined by the function “cross section”, which is the meeting point of experiments with theory. The approximate order of magnitude for cross-sections σ (per molecule) for various possible processes in spectroscopy is listed in Table 2.2.

Table 2.2. Typical values for cross sections ‘ σ ’ for various possible interactions of molecules with incident electromagnetic radiation.

Process	Cross section of	$\sigma(\text{cm}^2)$
Absorption	Ultra Violet	10^{-18}
Absorption	Infrared	10^{-20}
Emission	Fluorescence	10^{-19}
Scattering	Rayleigh scattering	10^{-26}
Scattering	Raman scattering	10^{-29}
Scattering	Resonance Raman	10^{-24}
Scattering	SERRS	10^{-17}
Scattering	SERS	10^{-19}

2.2.2.5 Weak “cross section” in RS needs enhancement

In general, Raman scattering is extremely weak; typical cross sections are 10^{-29} to 10^{-31} $\text{cm}^2/\text{molecule}$. This optical quality is not enough for lower detection limits in analytical applications. Raman scattering is a two-photon process occurring at a time scale of ca. 10^{-12} s; and the cross section of a molecule for such a process is about 10^8 and 10^{10} times smaller than those of infrared and fluorescence processes, respectively. Therefore, Raman spectroscopy has intrinsically low detection sensitivity. This detection sensitivity was significantly improved in the early 1960s, when the laser was invented and then used as an ultra intense light source for Raman spectroscopy. In the seventies, a discovery was made that the Raman cross section of a material may be increased by a

factor of 10^7 or more by the presence of metal colloid or roughened metal surface.^{11, 21-22} This effect is called surface enhanced Raman scattering (SERS). Silver and gold are usually used because they yield the largest enhancement. SERS has also been demonstrated using copper and several other metals like indium and the alkali metals. Both visible and near-infrared excitation can be used for SERS on silver. Red or near-infrared excitation is required for SERS on gold or copper. By combining SERS enhancement with resonance enhancement (surface enhanced resonance Raman scattering - SERRS), Raman cross section has been increased by a factor of 10^{11} , making single molecule Raman scattering possible. In 1997, by using SERS, single molecules on nanoparticles were successfully detected.²³⁻²⁴ The enhancement factor (EF) may be defined by

$$EF = \frac{\sigma_{SERS}}{\sigma_{RS}} \quad (2.2.23)$$

Where, σ_{SERS} is the Raman scattering cross section due to SERS results and σ_{RS} is the normal Raman scattering cross section.

2.3 SERS / SERRS

The intensity of normal Raman scattering from free molecules is determined by the first order transition electric dipole, which depends on the transition polarizability of the molecule and the electric field strength of the exciting radiation. The origin of surface enhanced Raman scattering (SERS) must therefore be sought in enhancement either of the transition polarizability or of the electric field strength experienced by the molecules when adsorbed on certain types of surface.²⁵ Classical electromagnetic theory indicates that the

molecule at the metal surfaces will experience a local electromagnetic field that is larger than that of the incident radiation. The extent of the enhancement depends on a number of factors, including the dielectric properties of the metal, the distance of the molecule from the surface, the orientation of the molecule, the wavelength of the exciting radiation, the morphology of the surface and the size and geometry of the nanostructure. The polarizability can also be changed as a result of electronic interaction between the molecule and the metal. In some cases, charge transfer may be observed, leading to resonances different from that of the target molecule. The optical response of a chemisorbed molecule may differ from that of a free molecule, which may result in wavenumber shifts of those modes involving atoms bound to the metal surface. The maximum enhancement will be expected with SERRS, when the wavenumber of exciting radiation approaches to both an electronic transition of the molecule and the plasmon absorption wavenumber of the metal for LSPR to be excited.^{4, 26-28}

2.3.1 Plasmon enhanced Raman

The SERS phenomenon is a direct correspondence with the localized surface plasmon resonance (LSPR) producing an intense local electromagnetic (EM) field on the SERS-active nanostructures. SERS is primarily a phenomenon associated with the enhancement of the electromagnetic field surrounding a small metal objects optically excited near an intense and sharp dipole resonance. The enhanced re-radiated dipolar fields excite the adsorbate, and if the resulting molecular radiation remains at or near resonance with the enhancing object, the

scattered radiation will again be enhanced. So under appropriate circumstances, accumulated two-fold of electromagnetic enhancement will scale as E^4 as:

$$E^{EM} = |A(\nu_L)|^2 \cdot |A(\nu_S)|^2 \cdot I(\nu_L) \quad (2.3.1)$$

Where, $A(\nu_L)$ and $A(\nu_S)$ represent the enhancement factors for an excited source of intensity $I(\nu_L)$ and Raman scattered fields respectively. The total SERS enhancement, E^{SERS} is then given by;

$$E^{SERS} = N \cdot \sigma_{ads}^R |A(\nu_L)|^2 \cdot |A(\nu_S)|^2 \cdot I(\nu_L) \quad (2.3.2)$$

Where, σ_{ads}^R is the Raman cross-section of the molecule in contact with the nanostructure, and N is the number of molecules involved in the SERS process. The physical meaning of the mechanisms can be illustrated by the basic and the most simplest model “ the spherical model ” shown in Figure 2.7

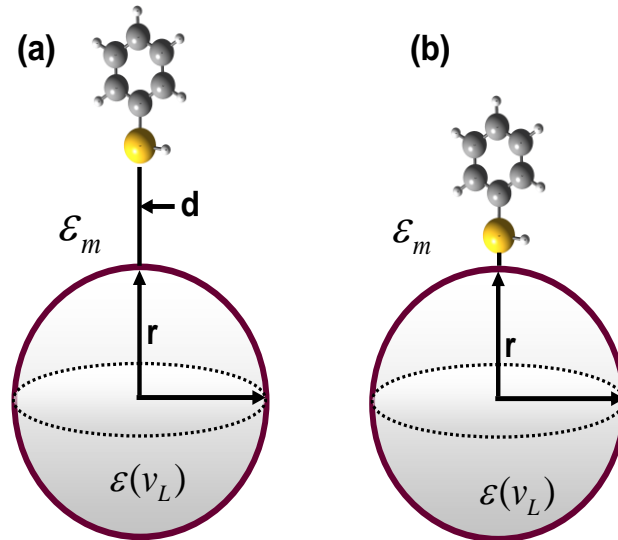


Figure 2.7: Illustration of the single sphere model: (a) a molecule at a distance d from the metal nanosphere and (b) a molecule attached to the nanosphere or chemical adsorption model

This model considers single metal nanosphere – single molecule SERS at the surface of the spherical particle with dielectric function $\varepsilon(\nu_L)$ embedded in a medium of dielectric constant ε_m . A molecule at distance d from a metal sphere of radius r (where $r \ll \lambda$, the excitation wavelength) is exposed to a field E_M , which is the superposition of the incident field E_0 and the field of a dipole E_{SP} induced in the metal sphere. The field enhancement factor $A(\nu_L)$ is the ratio of the field at the position of the molecule and the incident field:

$$A(\nu_L) = \frac{E_M(\nu_L)}{E_0(\nu_L)} \approx \frac{\varepsilon(\nu_L) - \varepsilon_m}{\varepsilon(\nu_L) + 2\varepsilon_m} \left(\frac{r}{r+d} \right)^3 \quad (2.3.3)$$

The isolated sphere is polarized when illuminated in an EM field owing to collective displacement of the electrons with respect to the nuclei and provide maximum enhancement at resonant condition ($\varepsilon(\nu_L) = -2\varepsilon_m$) i.e. at plasmon resonance.

The Raman scattered field is enhanced in the same manner, but with ν_S instead of ν_L . Referring back to equation (2.3.2), the EM enhancement contribution can then be written as:

$$|A(\nu_L)|^2 \cdot |A(\nu_S)|^2 \approx \left| \frac{\varepsilon(\nu_L) - \varepsilon_m}{\varepsilon(\nu_L) + 2\varepsilon_m} \right|^2 \left| \frac{\varepsilon(\nu_S) - \varepsilon_m}{\varepsilon(\nu_S) + 2\varepsilon_m} \right|^2 \left(\frac{r}{r+d} \right)^{12} \quad (2.3.4)$$

So the significant implications from this equation are:

(1) The enhancement is the fourth power of the local field near the metallic nanostructure and mainly strong when the scattered and the plasmon field are in resonance.²⁹

(2) The EM enhancement is a distance dependent mechanism. The

enhancement decays following the relation $\left(\frac{r}{r+d}\right)^{12}$.

2.3.2 Changes in polarizability

The intensity of Raman scattering is proportional to the square of the induced dipole moment, $p = \alpha.E$; any changes in the spectra must come from perturbations in the α (molecular polarizability). Molecules directly adsorbed on to the metal surface may have specific interaction with the nanoparticles leading to the formation of a surface complex. In some case, charge transfer (CT) from the adsorbate into the empty levels on the metal surface or from the occupied surface levels to the adsorbate may be observed. This interaction is shown in Figure 2.8. This effect is mainly attributed to electronic coupling between metal and molecule, when the frequencies of the incident laser become nearly resonant with the CT excitation of the adsorbate (molecule)–absorbent (metal) coupled system, resonance Raman is observed.³⁰

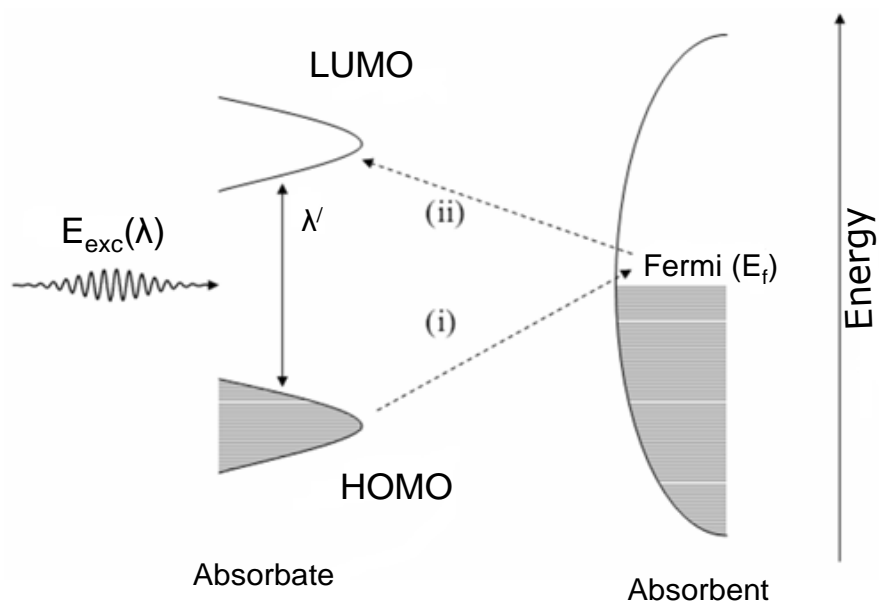


Figure 2.8: Energy level diagram of the couple molecule-adsorbent system in SERS

The principle is to create electron-hole pairs at particular sites or excitations. Once initiated, it interacts strongly with the molecules adsorbed at this site and can be in resonant intermediate states in Raman scattering. If a resonant negative state is formed by transformation of an electron between the metal and the adsorbate, the Raman scattering cross-section may be substantially changed. The CT interaction encompasses the following steps; (a) an incident photon with energy λ induces an intraband transition creating a hole; (b) an electron transfer between the metal and the excited electron level of the adsorbate via tunnelling for physisorbed adsorbates and via hybridizing for chemisorbed adsorbates, and (c) photon emission with energy λ' occurs as this electron recombines with the hole somewhere below the Fermi energy. Since the highest occupied molecular orbit (HOMO) and lowest unoccupied molecular orbit

(LUMO) of the adsorbate may be symmetrically disposed in energy with respect to Fermi energy of metal, the general case of CT phenomena involves transfer of an electron from the Fermi level of the metal to the LUMO or vice versa.³¹

2.3.3 Origin of localized surface plasmon resonance

Metal nanoparticles having a size much smaller than the wavelength of light exhibit intense colors, which are quite different than the bulk metal. Dispersion of colors observed by metal nanoparticles, like ruby red for gold nanoparticles and yellow for silver, was explained by Gustav Mie in 1908 using classical electromagnetic theory.³²⁻³³ The origin of the intense color was attributed to strong absorption and scattering of light by dispersion of metal nanoparticles. Noble metal (i.e. gold, silver, copper) nanoparticles show a strong absorption band in the visible to near infra-red region of electromagnetic spectrum, arising from a resonance of collective oscillation of conduction electrons with incident electromagnetic radiation.^{27,34} Metal nanoparticles are assumed to comprise of positive ions surrounded by a 'sea of electrons'. The incoming field induces polarization of conduction electrons as compared to those of heavier ions, which results in the formation of electric dipoles.

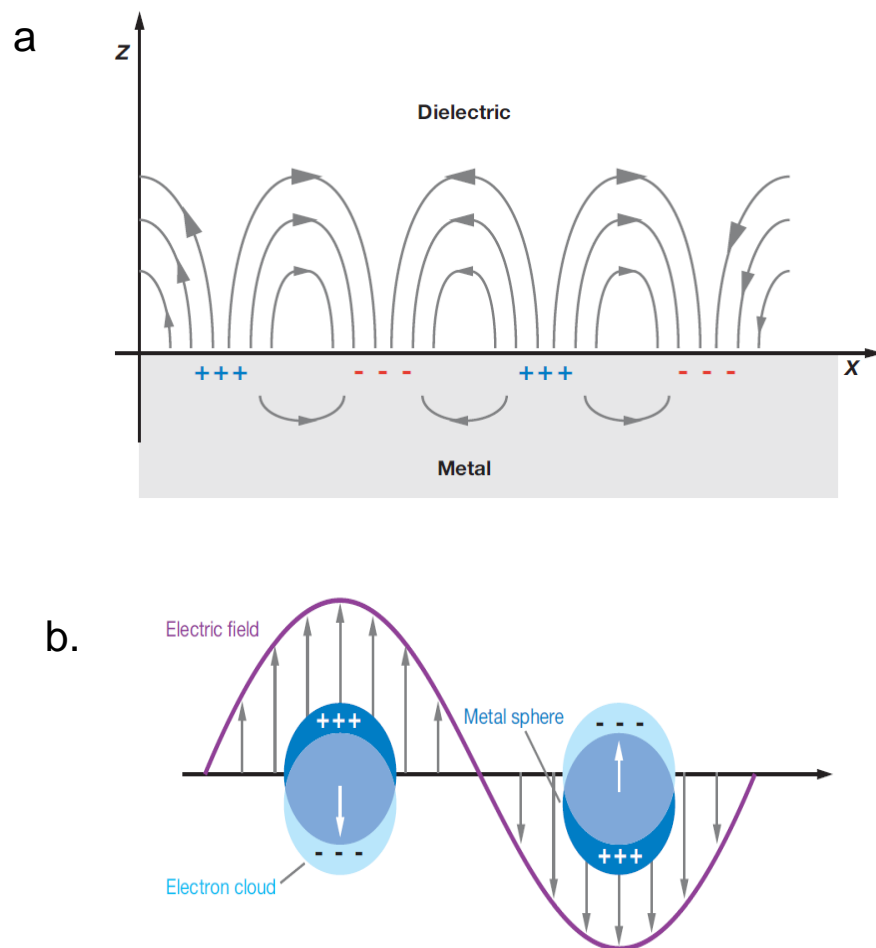


Figure 2.9: The Origin of surface plasmon resonance, (a) at the interface of thin metal film and a dielectric, and (b) in nanoparticles.

The resonance between frequency of oscillation of electrons and frequency of incident photon of the plasmon resonance (PR), characterized by a strong absorption band.³⁵⁻³⁶ As the net charge difference is left at the surface of a nanoparticle, the resonance is also called the “Surface Plasmon Resonance (SPR)”. A pictographic representation of SPR in a nanoparticle and on the interface of a thin metal film with a dielectric is shown in Figure 2.9.

SPR associated with metal nanoparticles within a size range 20-100 nm is a “Localized Surface Plasmon Resonance (LSPR)”; whereas SPR associated with

a metallic thin film of thickness in the range 20-100 nm can travel across the interface with a dielectric, which is called propagating SPR.³⁷⁻³⁸

A large number of studies have shown the LSPR resonance position to be highly tunable across a wide spectroscopic range by only varying the size and the shape of the nanoparticle.^{32-33, 39-40}

2.3.3.1 Controlling LSPR in SERS experiments

The LSPR is responsible for the electromagnetic-field enhancement that leads to surface-enhanced Raman scattering (SERS) and other surface-enhanced spectroscopic processes. The outcome of SERS results depends on the quality of the LSPR. The LSPR is a sensitive function of material dielectric properties, the nanoparticle's shape, size, and interparticle distance and the local environment.³⁹⁻⁴² Materials that possess a negative real and small positive imaginary dielectric constant are capable of supporting a surface plasmon resonance (LSPR) in the visible region of the spectrum. This resonance is a coherent oscillation of the surface conduction electrons excited by electromagnetic (EM) radiation. Surface plasmons can be excited in small metal particles or surface protrusions; however, they cannot be directly excited on a flat metal surface.

2.3.3.1.1 LSPR size dependent

In 1908, Mie³²⁻³³ presented a rigorous solution to Maxwell's equations that described the excitation spectra (extinction = scattering + absorption) of a plane

monochromatic wave by homogeneous spheres of arbitrary size. The extinction cross-section is therefore the sum of the scattering and the absorption cross-section:

$$\sigma_{ext} = \sigma_{sca} + \sigma_{abs} \quad (2.3.5)$$

Extinction scattering cross-section is the measure of optical response in LRPR and is useful when the concentration of the nanoparticles is low i.e. the nanoparticles acts as independent scattering centers. Using Mie theory, extinction cross-section σ_{ext} is given by,⁴³

$$\sigma_{ext} = \frac{24\pi^2 r^3 \varepsilon_m^{3/2}}{\lambda} \cdot \frac{\varepsilon''(\omega)}{(\varepsilon' + 2\varepsilon_m)^2 + \varepsilon''^2} \quad (2.3.6)$$

Where, λ is the wavelength of the incident light at angular frequency ω , $\varepsilon'(\omega)$ and $\varepsilon''(\omega)$ are the real and imaginary parts of the relative permittivity $\varepsilon(\omega)$ of the nanoparticles, ε_m is the relative permittivity of the ambient medium and r is the nanoparticle radius. When a spherical nanoparticle of radius r is irradiated by z-polarized light of wavelength λ , the magnitude of the electric field appears static around the nanoparticle from the solution of Maxwell's equations using a quasi-static approximation³ is given by ,

$$E_{out}(x, y, z) = E_0 \hat{Z} - \left[\frac{\varepsilon(\omega) - \varepsilon_m}{\varepsilon(\omega) + 2\varepsilon_m} \right] r^3 E_0 \left[\frac{\hat{Z}}{a^3} - \frac{3z}{a^5} (x\hat{X} + y\hat{Y} + z\hat{Z}) \right] \quad (2.3.7)$$

Where, 'a' is the distance from the nanoparticle surface to the adsorbate.

Extinction would be maximum when $\varepsilon' = -2\varepsilon_m$, which gives rise to a strong LSPR peak and also electric field would be maximum when $\varepsilon(\omega) = -2\varepsilon_m$. In the case of

silver and gold, this situation is met in the visible region of the spectrum, which is important condition for SERS.

Experimentally the LSPR bandwidth and band position depend on the nanoparticle size. Drude and Sommerfield included the size dependence of relative permittivity of the nanoparticle: $\varepsilon(\omega, r)$ in lieu of $\varepsilon(\omega)$.^{39,44} The real and the imaginary parts of the modified relative permittivity are given by:

$$\varepsilon'(\omega) = \varepsilon^\infty - \frac{\omega_p^2}{\omega^2 + \omega_d^2} \quad (2.3.8)$$

and

$$\varepsilon''(\omega) = \frac{\omega_p^2 \omega_d}{\omega(\omega^2 + \omega_d^2)} \quad (2.3.9)$$

where, ε^∞ is the high-frequency limit of $\varepsilon(\omega)$ arising from response of the core electrons, ω_d is the relaxation or damping frequency which represents collisions of electrons with the lattice(phonons) and defects, and ω_p is the bulk plasmon frequency defined as

$$\omega_p^2 = 4\pi n e^2 / m \quad (2.3.10)$$

Where 'n' is the electron density in metal, 'e' the electronic charge and 'm' the effective mass of electron. The dependence of the relative permittivity on the particle radius r was introduced by the assumption that the particle size is smaller than the mean free path of conduction electrons.

2.3.3.1.2 LSPR shape dependent

The shape of a nanoparticle has a prominent effect on LSPR band. A change in shape produces much larger shifts in the LSPR band, compare to the

change in size of the nanoparticle. For instance, in a rod, a short-wavelength plasmon resonance (transverse) corresponds to the oscillations of electrons along any minor axis, while the longer-wavelength plasmon resonance band (longitudinal) corresponds to the oscillations of electrons along the major axis. The shorter-wavelength band is insensitive to the nanoparticle's aspect ratio and coincides with the LSPR band of spherical nanoparticle; but the longer-wavelength plasmon resonance band can be tuned up to infra-red regime by increasing the aspect ratio.⁴⁵ The term $\varepsilon' + 2\varepsilon_m$ in the equation of optical extinction cross-section can be changed to $\varepsilon' + \chi\varepsilon_m$ for shape modified particles, where χ is a parameter for shape factor; which is equal to 2 for a sphere and increases with aspect ratio. When the shape changes from spherical to acirculate (i.e. rod-like), a broad plasmon absorption band splits into two plasmon bands. The peak at the shorter wavelength is due to the transverse plasmon resonance, whereas the peak at the longer wavelength is due to the longitudinal plasmon resonance.

2.3.3.1.3 LSPR environment dependent

The wavelength of the LSPR peak also depends on the refractive index of the surrounding environment and its expression⁴³ is given by,

$$\lambda^2 = \lambda_p^2 (\varepsilon^\infty + 2\varepsilon_m) \quad (2.3.11)$$

where $\lambda_p = 2\pi c / \omega_p$ (2.3.12)

and c is the speed of light in free space. Equation 2.3.11 suggests a red-shift in the LSPR band with the increase in the refractive index $\sqrt{\epsilon_m}$ of the environment.

2.3.3.1.4 LSPR distance dependent

As a rule experimental studies suggest that the SERS enhancement is substantially increased when a molecule resides in the junction between two nanoparticles.⁴⁶⁻⁴⁷ As two nanoparticles approach each other, the near-field of one particle interacts with the electrons in the adjacent particle, coupling the plasmon oscillations together. This coupling yields a significantly stronger near-field in the junction compared to that which exists around a single particle.⁴⁸⁻⁵⁰ In the case of close packing and proper polarization (E field is polarized along the inter-particle axis), higher enhancement is achieved with a two-body interaction than that from a single particle. This is shown in a cartoon in Figure 2.10.

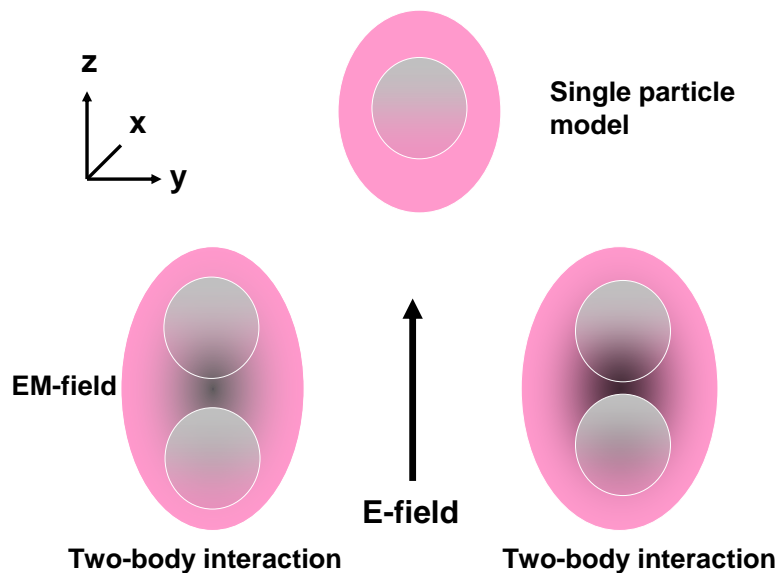


Figure 2.10: Cartoon representing EM enhancement from a single particle and two body interaction. The incident wave is polarized along z axis.

SERS from isolated particles are seldom reported because of their lower enhancement. In the cartoon, spheres are used for an example to show this two-body interaction. The EM field enhancement increases as the distance between the two particles is reduced. At the interstice region between two particles, plenty of opposite charges gather at the two sides, which in turn form a strong capacitive field across the interstice. The mutual interaction of the two nanoparticles also leads to an increase of the surface plasmon resonance, which contains two components: the inner particle resonance and the inter-particle resonance. In other words, the induced dipole arises from the incident light as well as the partner particle. As a result, there is an amplification of polarization. With the length of the interstice increasing about ten nanometers or more, the inter-particle resonance will diminish almost completely, and the enhancement falls rapidly to the level of that from isolated particles. The two-body interaction is not limited to spherical particles. Particles with other shapes, e.g. rod, triangle, cube, also have such two-body interaction with exactly the same principle, as long as they are closely-packed and are polarized along the direction of inter-particle axis.

2.3.4 Surface selection rules in SERS

When molecules are adsorbed on metal surface, they may have specific orientations with respect to the normal of the surface. Therefore, for a fixed orientation, the directions of the polarizability tensor in the adsorption geometry can be probed using polarized light. A fixed molecular orientation of the adsorbed molecule and the polarization properties of the light at the metal surface will lead

to SERS spectra that can be interpreted using the “surface selection rules” or propensity rules.⁴

Consider a molecule placed on the flat metal surface at a distance d shown in Figure 2.11 and illuminated by two beams (direct and reflected) which superimpose coherently at the molecule.

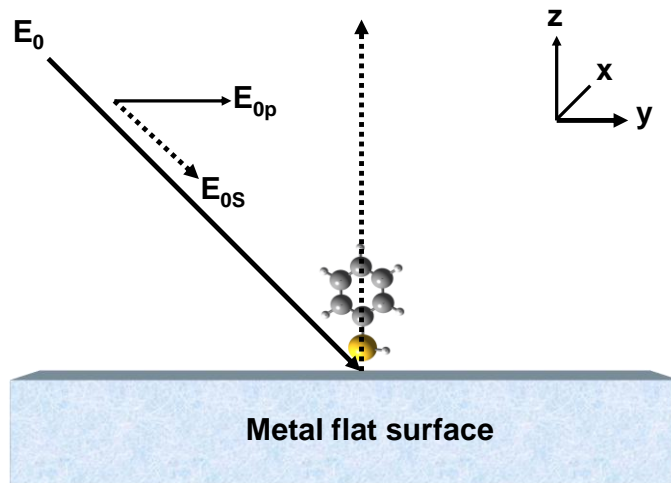


Figure 2.11: Cartoon of a molecular orientation in an electric field.

The d is taken as zero for simplicity, i.e. the molecule is placed right on the surface. The components of electric field in the molecule are:

$$E_x = (1 + r_s)E_{0s},$$

$$E_y = (r_p - 1)\cos\phi E_{0p}, \quad (2.3.13)$$

$$E_z = (r_p + 1)\sin\phi E_{0p}$$

Where, r_s and r_p are the Fresnel reflection coefficients at the ambient-metal interface for s-polarized (normal to the plane of incidence) and p-polarized

(parallel to the plane of incidence) light, E_{os} and E_{op} are the magnitude of the electric field components of incidence light and ϕ is the angle of incidence. The scattered radiation at a specific angle of incidence will be superimposed of two coherent waves given by:

$$E'_s = (1+r'_s)p_x \quad (2.3.14)$$

$$E'_p = (1-r'_p)p_y \cos \phi' + (1+r'_p)p_z \sin \phi' \quad (2.3.15)$$

Where primes indicate the scattered light, r'_s and r'_p are their respective Fresnel reflection coefficients calculated for ϕ' , the angle of scattered light.⁵

Four intensity components may be defined in Raman experiments referring to the polarization states of incident and scattered light.⁶¹ Labelling the quantities as SS, PS, SP and PP, where the first and second letters refer to the directions of the electric vectors in the incident and scattered light, respectively. The expressions of the intensity components are as follows:

$$SS \propto |\alpha_{xx}(1+r_s)(1+r'_s)|^2, \quad (2.3.16)$$

$$PS \propto |\alpha_{xy}(-1+r_p)(1+r'_s)\cos \phi + \alpha_{xz}(1+r_p)(1+r'_s)\sin \phi|^2, \quad (2.3.17)$$

$$SP \propto |\alpha_{yx}(1+r_s)(1-r'_p)\cos \phi' + \alpha_{zx}(1+r_s)(1+r'_p)\sin \phi'|^2 \quad (2.3.18)$$

$$PP \propto |[\alpha_{yy}(1-r_p)\cos \phi + \alpha_{yz}(1+r_p)\sin \phi](1-r'_p)\cos \phi' + [\alpha_{zy}(-1+r_p)\cos \phi + \alpha_{zz}(1+r_p)\sin \phi](1+r'_p)\sin \phi'|^2 \quad (2.3.19)$$

If the metal surface is very good reflecting i. e. total reflecting, the above equations reduce to

$$SS = 0 \quad (2.3.20)$$

$$PS = 0 \quad (2.3.21)$$

$$SP = 0 \quad (2.3.22)$$

$$PP = \left|_{zz}(1+r_p)(1+r_p')\right|^2 \sin^2 \phi \sin^2 \phi' \quad (2.3.23)$$

This result is interesting that the SS component, which is the strongest for normal Raman scattering, is zero and the component PP, which is not usually measured in ordinary Raman scattering, is the one which survives. This should be keeping in mind that when the surface is not highly reflective, certain intensity components may vanish for symmetry reasons. Notice that the latter discussion is for 90 degree geometry.

2.4 Metal island films by vacuum deposition

Metal island films can be produced by vacuum deposition and are broadly used as SERS substrates. In this thesis work, mainly the vacuum deposition technique has been used to create metal nanostructures of silver (Ag), gold (Au) or mixed Ag/Au films. Vacuum deposition was performed at about 10^{-6} Torr (1 Torr= 133.322Pa) using thermal evaporation Ag or Au by the passing of a high current through a tungsten boat, which holds the metal. The vacuum evaporation system used in this work is shown in Figure 2.12.



Figure 2.12: The Total System for Metal Evaporation

The processes for the metal film formation include the physical stages: 1) transformation of the solid metal into gaseous phase by thermal evaporation, 2) metal atoms stick to the substrate placed in the vacuum chamber and 3) nanoparticle formation onto the substrate under the proper conditions of surface diffusion (temperature of the substrate). This method is applicable to almost any solid substrate to form high purity films of specific mass thickness.⁵²

The magnitude of surface enhancement in SERS is critically dependent on the metal film morphology. The film structure can be controlled by deposition thickness, deposition rate, substrate temperature during deposition, substrate roughness and annealing after deposition to activate grain growth. The LSPR is tuned by maintaining these parameters to access the required SERS experimental conditions. In this work, the Ag and Au films were deposited with 5-

10 nm mass thickness onto the substrate (mostly corning quartz glass slides), maintaining its temperature between 100° and 200° C, and a deposition rate 0.30-0.50 $\text{Å}^0/s$. Finally, annealing of the films was done from 30 to 60 minutes after deposition.

2.5 Langmuir-Blodgett films

Langmuir films are formed by spreading a small number of molecules in volatile solutions onto the water subphase in a Langmuir trough.⁵¹⁻⁵² After the evaporation of the solvent, the floating molecules are compressed by barriers forming a monolayer at the air/water interface, i.e. the Langmuir film. A stable Langmuir monolayer can be formed from the amphiphilic molecules at the air-water interface with their hydrophobic part (e.g. alkyl chains) oriented toward the air and the polar moieties embedded in the water. The intermolecular interactions between the polar moieties and the water subphase as well as the van der Waals interactions between the alkyl chains are the requisite to hold together the molecules of the ordered Langmuir monolayers. The Langmuir-Blodgett (LB) films⁵¹⁻⁵² are produced by transferring the Langmuir monolayers from the water surface to solid substrates. During transfer, the surface pressure is kept constant, and the substrate is immersed and withdrawn by means of a dipper into the water subphase. When the Langmuir film is transferred only during the upstrokes, the LB films are referred to as Z-type. These LB films have been used for a wide variety of scientific experimentation. An LB monolayer can be considered as a two-dimensional film of material having a thickness of only one molecule.

The growing aspects of nanotechnology concern the controlled elaboration of nanoscale systems. Nanobiotechnology requires the organization of atoms and molecules in a two- or three-dimensional space. The efficient nanofabrication strategy employed by LB monolayer deposition allows a direct characterisation of molecular organization. When all parameters are optimized, this technique corresponds to one of the most promising for preparing thin films of amphiphilic molecules, since it enables (i) an accurate control of the thickness and of the molecular organization,²⁵ (ii) an homogeneous deposition of the monolayer over large areas compared to the dimension of the molecules, (iii) the possibility to transfer monolayers on almost any kind of solid substrates and (iv) to elaborate bilayer structures with varying layer compositions.⁵³⁻⁵⁴

2.5.1 Langmuir monolayer formation

Nima Langmuir trough (Model 302M) made of Polytetrafluoroethylene (PTFE) material, which will not contaminate the subphase, was used to fabricate the monolayer of amphiphilic molecules on nanostructured metal films discussed in this thesis. The subphase for the monolayer was ultra pure water from Millipore system (Water resistivity 18.2 MΩ cm). The LB trough and monolayer formation are shown in Figure 2.13.

The Langmuir-Blodgett technology is based on the particular properties of organic molecules like lipids, phospholipids or dye tagged with long hydrocarbon chain to orient themselves at an air/water interface between the gaseous and the liquid phase to minimise their free energy and form an *insoluble monolayer* called *Langmuir film*.

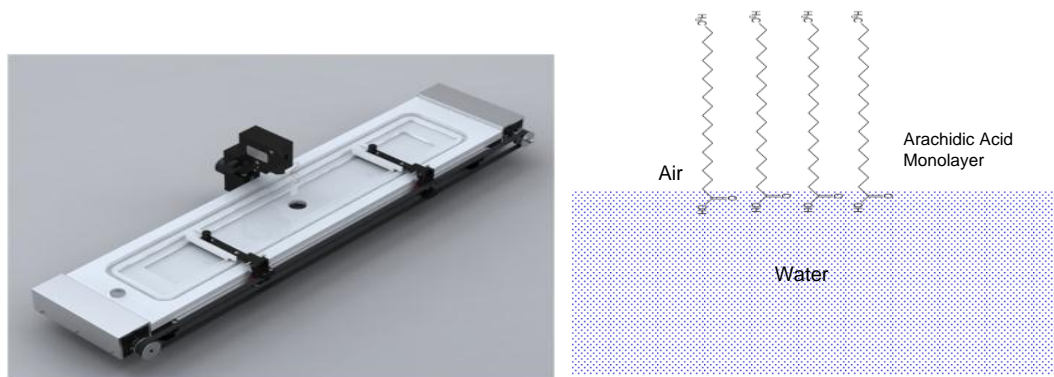


Figure 2.13: Nima Langmuir Trough and Monolayer of Arachidic Acid

The classical materials forming Langmuir monolayers are insoluble amphiphiles, composed of two distinct molecular regions: a hydrophilic (“water loving”) head group which is easily soluble in water, and a hydrophobic (“water-hating”) tail which is soluble in nonpolar solvents. When drops of a dilute solution of amphiphilic molecules in volatile and water-immiscible solvent, such as chloroform, are applied to a pure water surface, they rapidly spread over the interface to cover all the available area. After solvent evaporation, the interfacial film results in a monomolecular layer of one-molecule thick, with the head groups immersed in the water and the tail groups remaining outside (pointing towards the gas phase). This specific orientation is dictated by the amphiphilic nature of the molecules, since they are located at the air/water interface.

2.5.2 Surface pressure (π) – area (A) isotherm

The surface pressure (π) - Area (A) isotherm is a plot of the change in surface pressure as a function of the area available to each molecule on the aqueous subphase surface. This isotherm is the most common indicator of the monolayer

formation and monolayer properties of an amphiphilic material. The isotherm is measured at constant temperature by continuously compressing the monolayer while monitoring the surface pressure. As the film is compressed, the area per molecule in the monolayer is reduced with the increasing of surface pressure, which results in monolayer phase transition as gas phase – liquid expanded – liquid condensed – solid phase, that creates an isotherm.⁵⁵⁻⁵⁶ A typical isotherm of a phospholipid at 25^o C is shown in Figure 2.14.

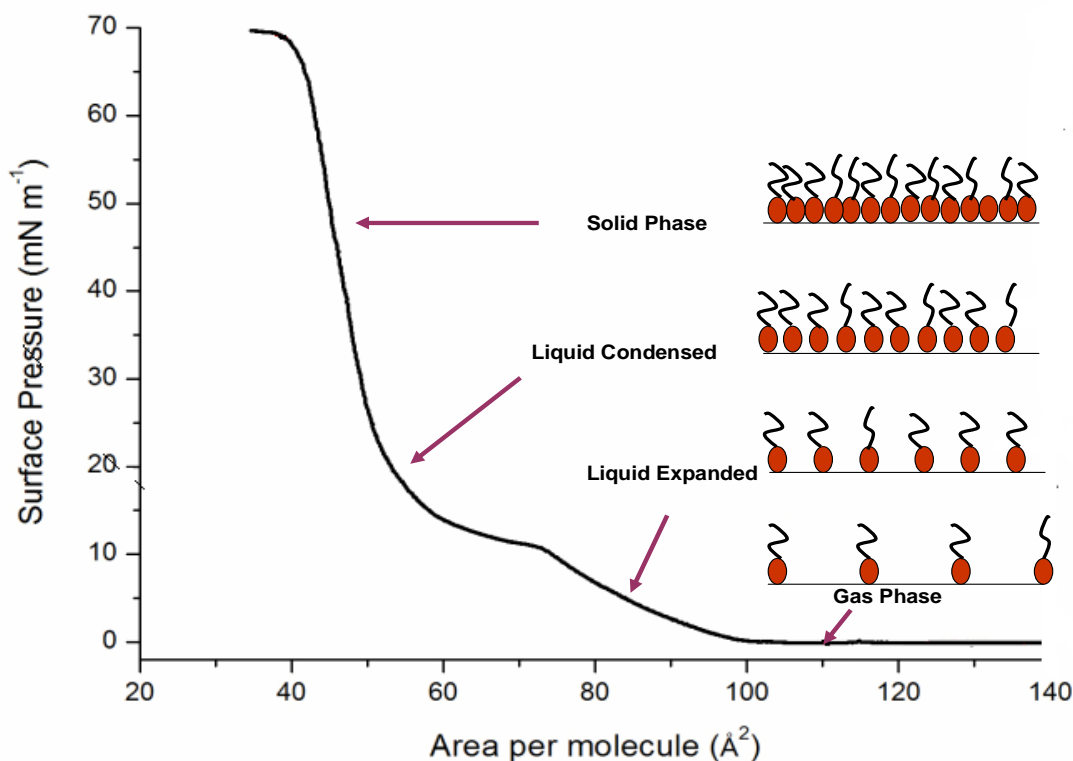


Figure 2.14: Surface Pressure – Area Isotherm

The surface tension can be viewed as a negative pressure due to the attractive interactions of the water molecules at the interface, which will be lowered by accumulation of the amphiphiles at the air/liquid interface. When the area of surface available to the interfacial film is large and the amount of

molecules sufficiently low to limit the interactions between adjacent amphiphile molecules, the monolayer has a minimal effect on the liquid surface tension. If the available surface area to the monolayer is reduced by a compression of the mobile barriers, the intermolecular distance decreases and the surface tension is lowered due to interaction of the adjacent molecules. The amphiphile molecules (mainly their hydrocarbon chains) start to interact and exert a repulsive effect on each other. The force exerted by the film per unit length, corresponding to a two-dimensional analogue of a pressure, is called *surface pressure* (π).

It is equal to the reduction of the pure liquid surface tension by the presence of the interfacial film, as in equation 2.5.1.

$$\pi = \gamma_0 - \gamma \quad (2.5.1)$$

In equation 2.5.1, γ_0 is the surface tension of the pure liquid and γ is the surface tension of the film-covered surface. It results from this equality that the maximum surface pressure for a monolayer on water surface at 20°C is 72.8 mN/m. The Nima trough used the Wilhelmy plate to measure the surface pressure in the interfacial film during the monolayer compression at the air-water interface. The Wilhelmy plate method is based on an absolute measurement of the force due to the surface tension on a plate, which is made of filter paper (ashless hatmanChromatographypaperChr1), partially immersed in the subphase. The measurement is first performed on a clean surface and subsequently on the same surface covered by the monolayer. The variation due to the alteration in the surface tension is then converted into surface pressure with the help of the dimensions of the plate.

2.5.3 Langmuir monolayer deposition

When the surface pressure is sufficiently high (usually in solid phase) to ensure lateral cohesion in the interfacial film, the floating monolayer can be transferred from the water surface onto a solid substrate. There are a number of different ways in which the monolayer may be transferred. The vertical movement of a solid substrate through the monolayer/air interface to deposit single monolayer, was used in the work. This is accomplished by successively dipping a solid substrate up and down through the monolayer, while simultaneously keeping the surface pressure constant by a computer controlled feedback system between the electrobalance measuring the surface pressure and the barrier movement mechanism.

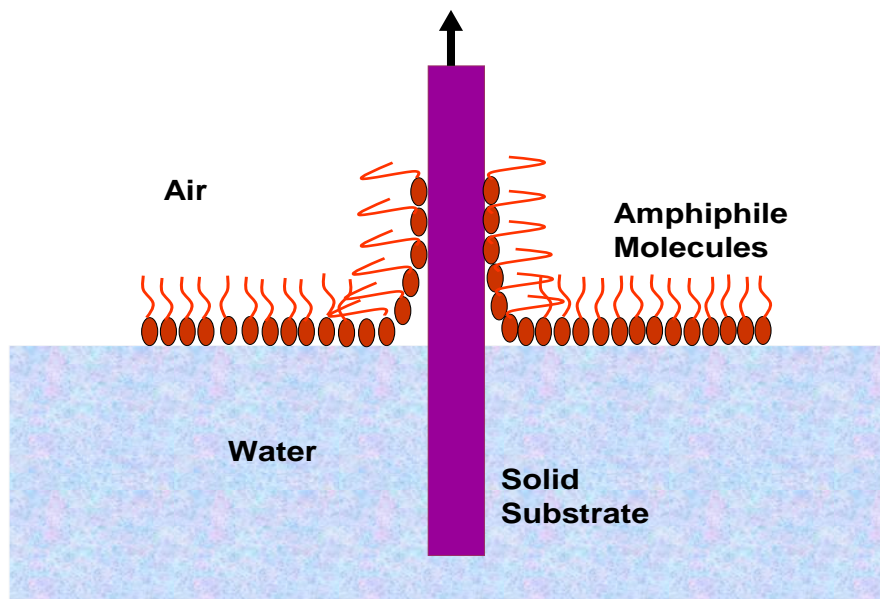


Figure 2.15: Deposition of monolayer by vertical substrate movement

Consequently the floating monolayer is transferred to the solid substrate.⁵⁷

This mechanism is shown in Figure 2.15

In this way multilayer structures can be produced. These multilayer structures are commonly called Langmuir-Blodgett or simply LB films. There are several parameters that affect on what type of LB film is produced. These are the nature of the spread film, the subphase composition and temperature, the surface pressure during the deposition, the deposition speed and the type and nature of the solid substrate. Depending on the behaviour of the molecule and the solid substrate, different kind of LB multilayers or monolayer can be produced and/or obtained by successive deposition of monolayers on the same substrate. The most common one is the Y-type multilayer, which is produced when the monolayer deposits to the solid substrate in both up and down directions. When the monolayer deposits only in the up or down direction, the multilayer structure is called either Z-type or X-type respectively.

The transfer of the monolayer onto a solid substrate is usually characterised by the *deposition* in terms of *transfer* ratio. To be quantitatively transferred, the monolayer must be held at a constant surface pressure during the deposition process. To achieve this, the barrier advance compensates the surface pressure decrease. This allows the measurement of the *transfer ratio*, which is used as an indicator of the quality of the transfer. The transfer ratio is defined as the decrease in the area occupied by the monolayer on the water surface divided by the coated area of the solid substrate. The transfer is most efficient when the transfer ratio equals one. Such a transfer ratio of unity is often taken as a criterion for good deposition; and under most circumstances the

orientation of the molecules on the substrate would be expected to be very similar to their orientation on the water surface.

2.5.4 LB – Brewster angle microscopy

The Langmuir–Blodgett (LB) technique offers the possibility of controlling, in a very precise fashion, the organization in organic thin films. Specific substitution of hydrophilic and hydrophobic moieties, surface pressure, subphase p^H , temperature etc may lead to a particular ordering of the molecules within the floating monolayer. Visualization of monolayer films can be attained using Brewster Angle Microscopy (BAM). This is a useful tool for observing the homogeneity of compressed monolayer films, domain sizes, shapes and packing behaviors. The Nima MicroBAM2 was employed in this work to detect changes in the refractive index of the water surface in the presence of Langmuir monolayer, which is shown in Figure 2.16. When p-polarized light impinges at the air-water interface at the Brewster angle (53°), no light is reflected from the interface between the two media with different refractive indices. At the same angle of incidence, the introduction of a Langmuir monolayer modifies the Brewster angle conditions, and light is now reflected, which is used for recording and imaging by CCD camera.

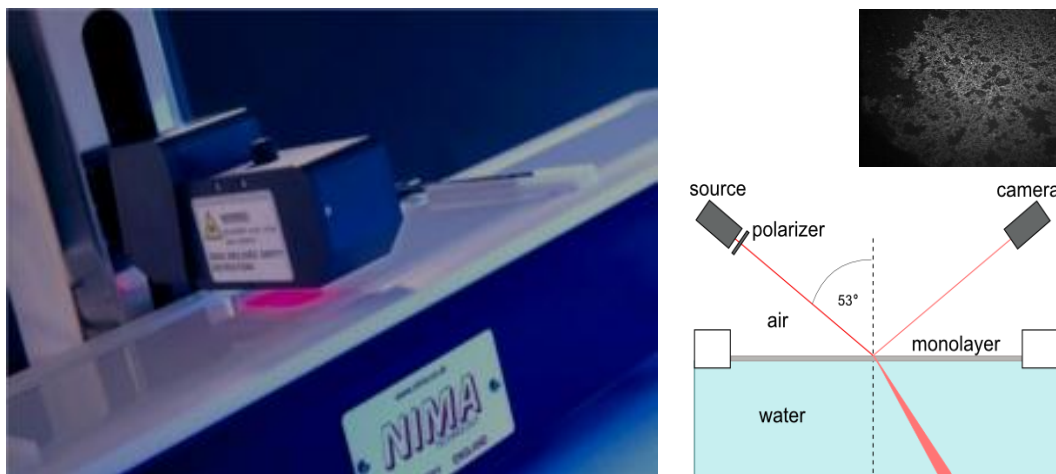


Figure 2.16: Set up of Nima LB trough with MicroBAM2 for monolayer

With the MicroBAM2, the transparent materials can be imaged with high contrast at an effective magnification of 40x. The sampling area is 4.0 x 3.6mm, displayed as a greyscale image of 640 x 480 pixels. One of the main problems with Langmuir films is the optical anisotropy of the film, due to which one can not assume a single refractive index. In this case, the background is eliminated and the contrast arises due to the monolayer that has a different refractive index from that of bulk subphase water. Different domain shapes are usually observed during BAM measurements, which are related to either different phases of the monolayer, such as liquid-expanded, liquid-condensed and solid phases that are accompanied by domain growth, or to the formation of three-dimensional crystallites which is seen as cracks or fractures.⁵⁵⁻⁵⁸

2.6 Atomic force microscopy

Scanning probe microscopes (SPMs) are instruments that measure morphology of surfaces with nanometric precision. They include atomic force

microscopes (AFMs) and scanning tunnelling microscopes (STMs). The scanning tunnelling microscopes were the first to produce real-space images of atomic arrangements on flat surfaces. The atomic force microscope was developed to overcome a basic drawback with STM - that it can only image conducting or semiconducting surfaces. The AFM, however, has the advantage of imaging almost any type of surface, including polymers, ceramics, composites, glass, and biological samples.

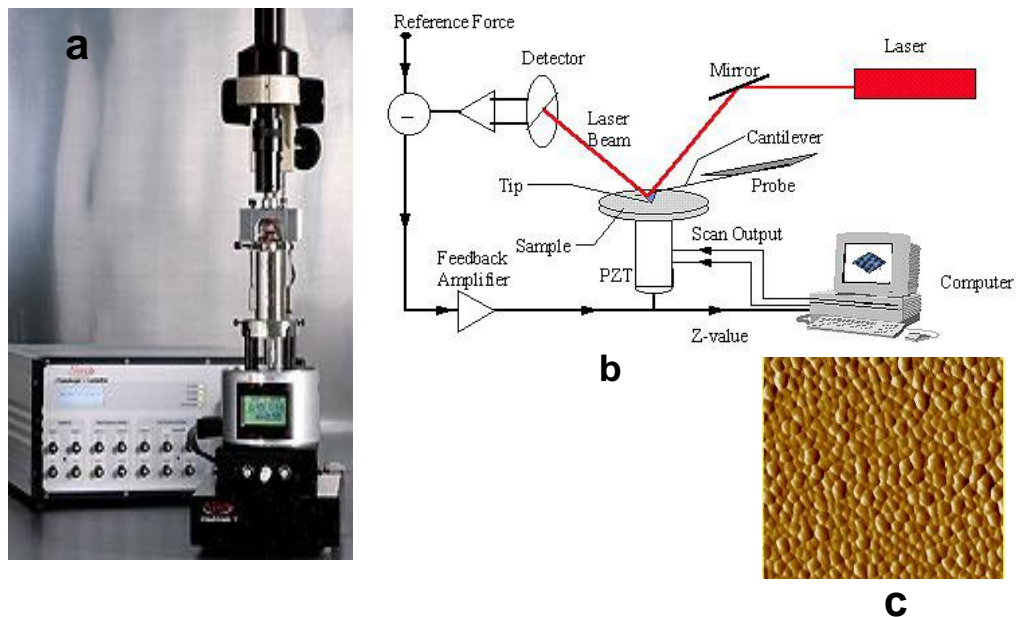


Figure 2.17: (a) SPM Microscope, (b) essential elements of an AFM and (c) an AFM image

Atomic force microscopy (AFM) has become a standard technique, both to visualize surface topography and microstructure very precisely from angstrom-to-micrometer scale. The Veeco Digital Multi Mode SPM used for the AFM images in this research work and the diagram showing the essential elements of an AFM are presented in Figure 2.17. This technique is based on the principle that when

a tip, which is integrated to the end of a spring cantilever, is brought within the interatomic separations of a surface, interatomic potentials will be developed between the atoms of the tip and the atoms of the surface. As the tip travels across the surface, the interatomic potentials will then force the cantilever to bounce up and down with the contours of the surface. Therefore, by measuring the deflection of the cantilever, the topographical features of the surface can be mapped out. The forces between the sample and the tip are measured using a laser and detector, which monitors the cantilever motion.⁵⁹ The negative feedback loop moves the sample up and down via a piezoelectric scanning tube (PZT) so as to maintain the interaction force to a preselected level (Reference Force). A three dimension image can finally be constructed by recording the cantilever motion in Z direction as a function of the sample's X and Y position. Most AFMs use a laser beam deflection system, introduced by Meyer and Amer, where a laser is reflected from the back of the reflective AFM lever and onto a position-sensitive detector. AFM tips and cantilevers are microfabricated from Si or Si₃N₄. Typical tip radius is from a few to 10s of nm.

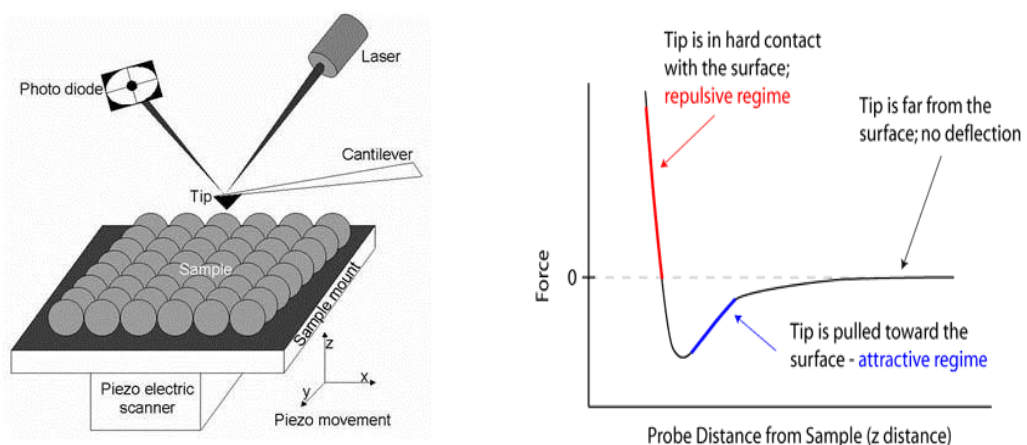


Figure 2.18: Illustration of the principles of AFM imaging

A number of AFM imaging modes are available. The most widely used AFM imaging modes, the contact mode and the non-contact mode “Tapping Mode™”, were used in the work presented in this thesis.

2.6.1 Contact mode AFM

In contact mode AFM, the sharp tip at the end of the microfabricated AFM cantilever is in perpetual contact with the sample surface, while monitoring the change in cantilever deflection with a split photodiode detector. In constant force mode, the tip is constantly adjusted to maintain a constant deflection, and therefore constant height above the surface, which result in images for changes in height, friction and deflection. A feedback loop maintains a constant deflection between the cantilever and the sample surface by vertical movement of the scanner at each (x, y) data point to maintain a set point deflection. Soft sample is not appropriate for the contact mode as the tip dragged on the surface that can scratch the sample. So tapping mode is required as a non-contact mode of imaging.⁶⁰

2.6.2 Tapping mode™ AFM

In tapping mode, the cantilever is oscillated near the resonance frequency using piezoelectric actuators, and touches the surface periodically, producing a scan without scratching the surface. As the cantilever oscillation amplitude is maintained constant by a feedback loop, when the tip passes over a bump in the surface, the cantilever has less room to oscillate and the amplitude of oscillation decreases; conversely, when the tip passes over a depression, the cantilever has

more room to oscillate and the amplitude increase.^{8,31} This results in changing the amplitude, frequency and phase of the oscillation shift depending on the interaction between the tip and the surface, and thus in turn provides AFM images. The cantilever oscillates at or near its resonance frequency with amplitude ranging typically from 20 nm- 100 nm, which presented in Figure 2.19.

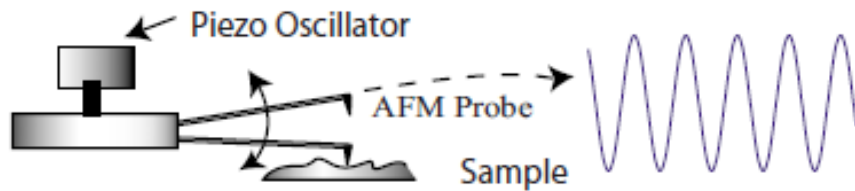


Figure 2.19: The cantilever oscillation during tapping mode imaging

Owing to its ability to significantly minimize lateral forces associated with scanning, tapping (or intermittent contact) mode AFM has become an increasingly important experimental technique in studying soft, easily damaged, nanoscale structures.⁶¹⁻⁶²

2.7 UV-Visible absorption

Ultraviolet and visible (UV-Vis) absorption spectroscopy is the measurement of the attenuation of a beam of light after it passes through a sample or after reflection from a sample surface. Ultraviolet and visible light are energetic enough to promote outer electrons to higher energy levels. The UV-Vis spectra have broad features that impose limitation for sample identification, but are very useful in quantitative measurements. All plasmons of nanostructured

silver island films (SIFs) and molecular solutions in this work were characterized by UV-Vis absorption with the Cary 50 UV-Vis single beam spectrometer, which is presented in Figure 2.20.



Figure 2.20: Cary UV-Vis Spectrometer

The Cary 50 used a Xenon flash lamp that offers many advantages over traditional UV-Vis spectrophotometers. The maximum scan rate is 2400 nm per minute. That means, it can scan the whole wavelength range of 190-1100 nm in less than 3 seconds. The light beam in the Cary 50 sample compartment is very narrowly focussed and extremely intense. This design ensures that approximately 80% of the beam passes through the small aperture of a 40 μ L micro cell. With this much energy available, the data produced are much smooth and more precise.

REFERENCES

- (1) Diem, M. *Modern Vibrational Spectroscopy*; John Wiley & Sons: New York, **1993**.
- (2) Long, D. A. *The Raman Effect*; John Wiley & Sons, Ltd: Chichester, **2001**.
- (3) Schatz, G. C.; Young, M. A.; Van Duyne, R. P. *Top. Appl. Phys.* **2006**, *103*, 19-46.
- (4) Moskovits, M. *Rev. Mod. Phys.* **1985**, *57*, 783-826.
- (5) Aroca, R. *Surface-enhanced Vibrational Spectroscopy*; John Wiley & Sons: Chichester, **2006**.
- (6) Moskovits, M. *Reviews of Modern Physics* **1985**, *57*, 783-826.
- (7) Schatz, G. C.; Van Duyne, R. P. In *Handbook of Vibrational Spectroscopy*; Griffiths, J. M. C. a. P. R., Ed.; John Wiley & Sons, Ltd, **2002**; Vol. Volume 1.
- (8) Baena, J. R.; Lendl, B. *Current Opinion in Chemical Biology* **2004**, *8*, 534-539.
- (9) Ryder, A. G. *Current Opinion in Chemical Biology* **2005**, *9*, 489-493.
- (10) Kiefer, W. *Journal of Raman Spectroscopy* **2009**, *40*, 1766-1779.
- (11) Jeanmaire, D. L.; VanDuyne, R. P. *Journal of Electroanalytical Chemistry* **1977**, *84*, 1-20.
- (12) Herzberg, G. *Molecular Spectra and Molecular Structure. II Infrared and Raman Spectra of Polyatomic Molecules*; D. Van Nostrand Co., Inc.: Princeton, N.J., **1945**.
- (13) Herzberg, G. *Molecular Spectra and Molecular Structure. I Spectra of Diatomic Molecules.*; 2nd. ed.; D. Van Nostrand Co., Inc: Princeton, N.J., **1950**.
- (14) Wilson Jr, E. B.; Decius, J. C.; Cross, P. C. *Molecular Vibrations; The Theory Of Infrared And Raman Vibrational Spectra*; McGraw-Hill: New York, **1955**.

- (15) Ferraro, J. R.; Nakamoto, K.; Brown, C. W. *Introductory Raman Spectroscopy, Second Edition*, **2003**.
- (16) Laserna, J. J.; Editor *Modern Techniques in Raman Spectroscopy*, **1996**.
- (17) Myers, A. B. *J. Raman Spectrosc.* **1997**, 28, 389-401.
- (18) Shorygin, P. P.; Krushinskij, L. L. *J. Raman Spectrosc.* **1997**, 28, 383-388.
- (19) 'Rayleigh-Streuung and Raman-Effekt'; Placzek, G., Ed.: Leipzig., **1934**; Vol. VI.
- (20) Pelletier, M. J. *Applied Spectroscopy* **2003**, 57, 20A-42A.
- (21) Albrecht, M. G.; Creighton, J. A. *Journal of the American Chemical Society* **1977**, 99, 5215-5217.
- (22) Fleischmann, M.; Hendra, P. J.; McQuillan, A. J. *Chemical Physics Letters* **1974**, 26, 163-166.
- (23) Nie, S. M.; Emery, S. R. *Science* **1997**, 275, 1102-1106.
- (24) Kneipp, K.; Wang, Y.; Kneipp, H.; Perelman, L. T.; Itzkan, I.; Dasari, R. R.; Feld, M. S. *Physical Review Letters* **1997**, 78, 1667.
- (25) Schatz, G. C. *Accounts of Chemical Research* **1984**, 17, 370-376.
- (26) Camden, J. P.; Dieringer, J. A.; Zhao, J.; Van Duyne, R. P. *Accounts of Chemical Research* **2008**, 41, 1653-1661.
- (27) Willets, K. A.; Van Duyne, R. P. *Annual Review of Physical Chemistry* **2007**, 58, 267-297.
- (28) Le Ru, E. C.; Meyer, M.; Blackie, E.; Etchegoin, P. G. *J. Raman Spectrosc.* **2008**, 39, 1127-1134.

- (29) Baker, G. A.; Moore, D. S. *Analytical and Bioanalytical Chemistry* **2005**, 382, 1751-1770.
- (30) Lombardi, J. R.; Birke, R. L. *Acc. Chem. Res.* **2009**, 42, 734-742.
- (31) Lombardi, J. R.; Birke, R. L. *Accounts of Chemical Research* **2009**, 42, 734-742.
- (32) Mie, G. *Physik. Z.* **1908**, 8, 769.
- (33) Mie, G. *Greifswald. Ber. physik. Ges.* **1908**, 5, 492-500.
- (34) Zhang, X.; Yonzon, C. R.; Van Duyne, R. P. *J. Mater. Res.* **2006**, 21, 1083-1092.
- (35) Jain, P. K.; El-Sayed, M. A. *Journal of Physical Chemistry C* **2007**, 111, 17451-17454.
- (36) Jain, P. K.; Lee, K. S.; El-Sayed, I. H.; El-Sayed, M. A. *Journal of Physical Chemistry B* **2006**, 110, 7238-7248.
- (37) Welford, K. *Optical and Quantum Electronics* **1991**, 23, 1-27.
- (38) Sherry, L. J.; Chang, S. H.; Schatz, G. C.; Van Duyne, R. P.; Wiley, B. J.; Xia, Y. N. *Nano Letters* **2005**, 5, 2034-2038.
- (39) Noguez, C. *Journal of Physical Chemistry C* **2007**, 111, 3806-3819.
- (40) Pinchuk, A. O.; Schatz, G. C. *Applied Physics B: Lasers and Optics* **2008**, 93, 31-38.
- (41) Nordlander, P.; Oubre, C.; Prodan, E.; Li, K.; Stockman, M. I. *Nano Letters* **2004**, 4, 899-903.
- (42) Xu, H.; Kall, M. *Physical review letters* **2002**, 89, 246802.
- (43) Mulvaney, P. *Langmuir* **1996**, 12, 788-800.
- (44) Link, S.; El-Sayed, M. A. *The Journal of Physical Chemistry B* **1999**, 103, 4212-4217.

- (45) Haes, A. J.; Haynes, C. L.; McFarland, A. D.; Schatz, G. C.; Van Duyne, R. R.; Zou, S. L. *Mrs Bulletin* **2005**, *30*, 368-375.
- (46) Michaels, A. M.; Jiang; Brus, L. *The Journal of Physical Chemistry B* **2000**, *104*, 11965-11971.
- (47) Lee, S. J.; Morrill, A. R.; Moskovits, M. *Journal of the American Chemical Society* **2006**, *128*, 2200-2201.
- (48) Hossain, M. K.; Ozaki, Y. *Current Science* **2009**, *97*, 192-201.
- (49) Brus, L. *Accounts of Chemical Research* **2008**, *41*, 1742-1749.
- (50) Xu, H.; Aizpurua, J.; Käll, M.; Apell, P. *Physical Review E* **2000**, *62*, 4318.
- (51) Roberts, G. *Langmuir-Blodgett Films*; Plenum Press: New York, 1990.
- (52) Petty, M. C. *Langmuir-Blodgett Films: An Introduction*; Cambridge University Press: Cambridge, **1996**.
- (53) Takahashi, M.; Kobayashi, K.; Takaoka, K.; Takada, T.; Tajima, K. *Langmuir* **2000**, *16*, 6613-6621.
- (54) Pevenage, D.; Van der Auweraer, M.; De Schryver, F. C. *Langmuir* **1999**, *15*, 8465-8473.
- (55) Dynarowicz-Latka, P.; Dhanabalan, A.; Oliveira, O. N. *Advances in Colloid and Interface Science* **2001**, *91*, 221-293.
- (56) Kimura, H.; Watanabe, S.; Shibata, H.; Azumi, R.; Sakai, H.; Abe, M.; Matsumoto, M. *The Journal of Physical Chemistry B* **2008**, *112*, 15313-15319.
- (57) Petrov, J. G.; Petrov, P. G. *Langmuir* **1998**, *14*, 2490-2496.
- (58) Vila-Romeu, N.; Nieto-Suarez, M.; Dynarowicz-Latka, P. *The Journal of Physical Chemistry B* **2005**, *109*, 14965-14970.

- (59) Rosa, L. G.; Liang, J. *Journal of Physics-Condensed Matter* **2009**, *21*.
- (60) Bresson, B.; Portigliatti, M.; Salvant, B.; Fretigny, C. *Journal of Applied Polymer Science* **2008**, *109*, 602-607.
- (61) Horng, T. L. *Applied Surface Science* **2009**, *256*, 311-317.
- (62) Dankowicz, H.; Zhao, X. P.; Misra, S. *International Journal of Non-Linear Mechanics* **2007**, *42*, 697-709.

CHAPTER 3

METAL NANOSTRUCTURES PREPARATION, AND LANGMUIR-BLODGETT (LB) APPROACH TO SERS/SERES

3.1 Background

Recently, there has been an increasing interest in optical nano-sensors based on the optical properties of nanometer-sized metallic nanostructures. When metal nanoparticles are excited by electromagnetic radiation and the frequency of the incident photon is in resonant with the collective oscillation of the conduction electrons of the nanoparticles, the resulting response is the localized surface plasmon resonance (LSPR).¹⁻³ Within the broad spectrum of applications, the LSPR of metal nanoparticle systems, particularly those of Ag and Au, LSPRs are the best known source of the local electromagnetic field enhancement in SERS and SERRS.⁴⁻⁵ The main optical signature of metallic nanoparticles of Ag, Au and Cu is a strong UV-VIS-NIR plasmon absorption and scattering bands. The wavelength corresponding to the extinction maximum, λ_{\max} , of the LSPR is highly dependent upon the size and shape of the nanoparticles, the interparticle spacing and dielectric constant of both the metal and the surrounding environments.^{2-3,6} As the size or shape of the nanoparticle changes, the observed color also changes. Gold spheres have a characteristic red color, while silver spheres are yellow. The oscillation frequency is usually in the visible region for gold and silver giving rise to the strong surface plasmon resonance absorption. Distribution of the nanoparticles, their aggregates and interparticle separation also affects the plasma oscillation frequency.⁷ The primary consequences of LSPR excitation are selective photon absorption, scattering, and local electromagnetic field enhancement.⁸ To predict and manipulate the LSPR of metal nanoparticle systems is advantageous in all

technological applications. Controlling size, shape and the formation of the aggregates of metallic nanostructures becomes a main task for experimental SERS/SERRS.

The excitation of surface plasmons by an incident photon produces an electromagnetic wave propagating along the surface. The corresponding local EM field localizes spatially at the edge, corner or fracture of the noble metal nanoparticle, or at the junction of the noble metal nano aggregate. Thus, the confined EM field polarizes the adsorbed molecules nearby through dipole–dipole coupling. At the same time, the Raman scattered light is within the envelope of the plasmon absorption and scattering, and this is the basis for the $|E|^4$ enhancement factor that has been repeatedly discussed in the SERS literature.^{1,9} If the incident photon is in resonant with the molecular electronic transition, the additional resonance Raman scattering (RRS) enhancement is at work. Therefore, in SERRS (= SERS +RRS) the observed intensity is determined by the two main factors: (1) resonance of incident light with an LSPR, and (2) resonance of incident light with the electronic transition in the molecular system. The factors affecting the pattern of the observed spectra in SERS or SERRS, have been listed in details in reference four.⁴ Notably, SERS and SERRS will be observed at a distance from the metal surface, and this property has been used recently to developed SHINERS, a technique where very thin coated (2 nm) gold nanoparticles are used to produce SERS avoiding the metal-molecule interaction.¹⁰⁻¹¹

3.2 Preparation of metal nanostructures

3.2.1 Introduction

There has been significant interest in the design of a variety of nanostructures for surface-enhanced Raman scattering sensing applications. Since the discovery of SERS in the mid-1970s, remarkable effort has been directed to design and fabricate highly active substrates for molecular sensing. Since the LSPRs are extremely size and shape sensitive, the particles with shapes beyond solid spheres are very interesting for SERS applications. In particular, shapes with high local curvature, presence of sharp points, protrusions, and large aspect ratio, cubes, disks, nanorods, nanoshells, prisms, and multipods can effectively amplify the local electric field. Very large enhancement in nano domains, or high concentration of the electromagnetic EM field, is called a “hot spots”. They are, most often found in nanoscale junctions and interstices in metal nanostructures such as nanoparticles dimers and aggregates.¹²

Diverse SERS architectures have been developed including roughened metal surfaces, colloids, island films, self-assembled nanoparticles and arrays of nanoellipsoids. In our research group, the silver and gold colloids as well as metal island films are prepared and used as SERS substrates.

3.2.2 Experimental

Metal island films of Ag and Au used in this thesis were fabricated by vacuum evaporation technique as described in section 2.4, chapter 2. A cartoon

representing the schematic diagram of metal deposition system used is shown in Figure 3.1.

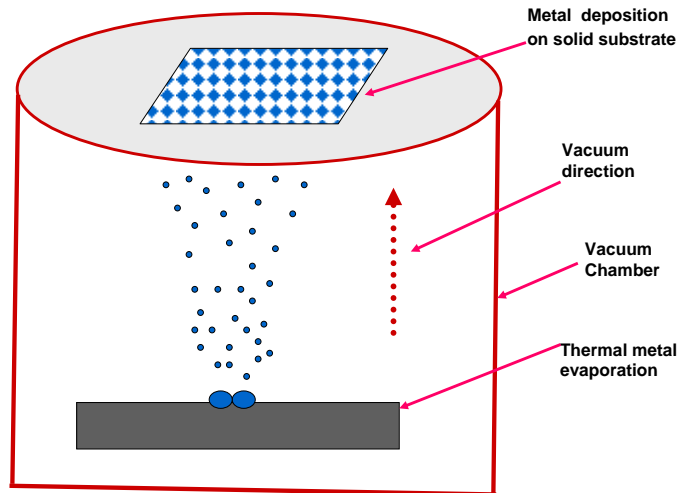


Figure 3.1: Illustration of metal deposition using vacuum evaporation technique

This type of deposition produces non-uniform or inhomogeneous metal coverage with a distribution of shapes and sizes of nanoparticles and their aggregates. It is important to control the kinetic factors influencing the particle distribution, in order to tune the plasmon absorption and ensure reproducibility. During the fabrication of nanometric metal films, the following experimental parameters were optimized: thickness of the metal island films, the temperature of the substrate (usually glass slides) upon which evaporated metal deposited, the deposition rate, vacuum pressure in the evaporation chamber, and curing or annealing the metal film after deposition. The plasmon absorption dependence on these parameters is discussed in the following sections.

3.2.3 Results and Discussion

3.2.3.1 Particle size variation in a silver island film

The vacuum evaporation technique produces a wide range of nanoparticle sizes and shapes in the metal island film. An AFM image of 9 nm thick Ag film is shown in Figure 3.2. The section analysis illustrates how the particle sizes varied on the metal film. Figure 3.2 (a) illustrates a section analysis of the film for the variation of the particle width, which is $\sim 70 \text{ nm} \pm 20 \text{ nm}$ and figure 3.2(b) is a section analysis of the same film for the particle height variation which is about $\sim 6 \text{ nm} \pm 3 \text{ nm}$. The AFM image also shows particle aggregation adding to the inhomogeneity of the nanometric film. To achieve the most reproducible film with reliable plasmon absorption, the film thickness, temperature of the substrate for metal deposition, the deposition rate and the curing after deposition are fixed for a particular SERS/SERRS application.

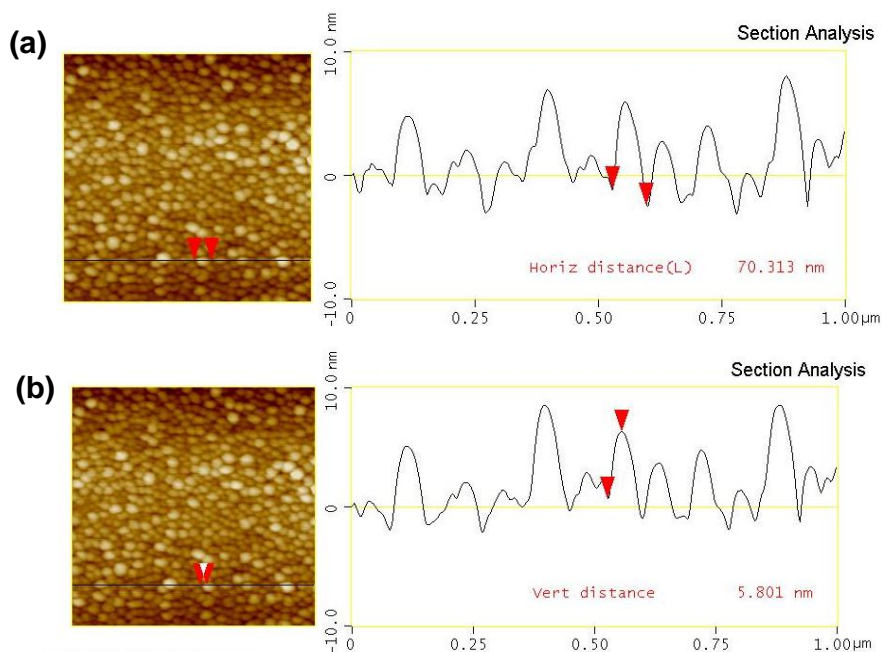


Figure 3.2: AFM image of nanoparticle size variation profile (section analysis) in 6 nm silver island film

3.2.3.2 Film thickness and plasmon absorption

The change in surface plasmon absorption as the film mass thickness of the Ag island film changes is shown in Figure 3.3. The films were prepared at the same temperature, $100^0 \pm 2^0$ C and the deposition rate was $0.4 - 0.5 \text{ \AA} / \text{sec}$.

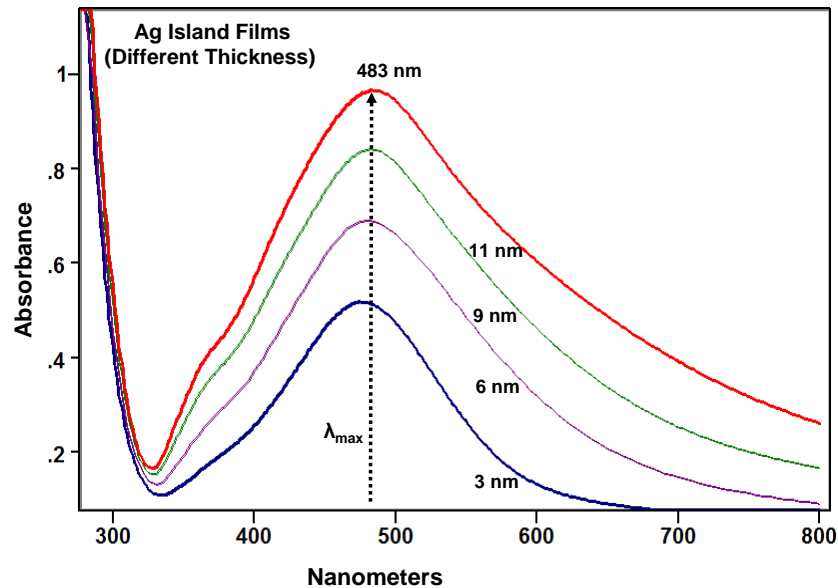


Figure 3.3: Surface plasmon absorption of Ag island films (thickness variation)

The heating after deposition, 1 hour and cooling, 30 minutes were maintained constant for all fabrications. The plasmon absorption reveals that absorbance intensity increases with the increase in film mass thickness that raised gradually from 3 nm to 11 nm, and, at the same time, the FWHM (full width at half maximum) of the absorbance bands is also increasing in a proportionate order. However, the absorbance wavelength maxima, λ_{max} , remain almost constant. This indicates that the particle size grows as more deposition was made to attain a higher film mass thickness, and the plasmon interaction results in band broadening. As the particle sizes increased, the plasmon coupling increases due

to dipole-dipole interaction and more particle-particle aggregation also takes place. The only explanation for similar absorbance maxima could be in the formation of nanoparticles of similar shape with increasing film mass thickness.

3.2.3.3 Temperature of the substrate and plasmon absorption

In Figure 3.4, three surface plasmon absorption spectra of Ag island films of same thickness, 9 nm, are shown. The films were prepared at three different temperatures (100°C , 150°C and 200°C) and maintained all other parameters identical. The FWHM of the plasmon absorption spectra decreases as the temperature increases from 100°C to 200°C and the absorbance wavelength maxima, λ_{max} , shifted from red to blue region.

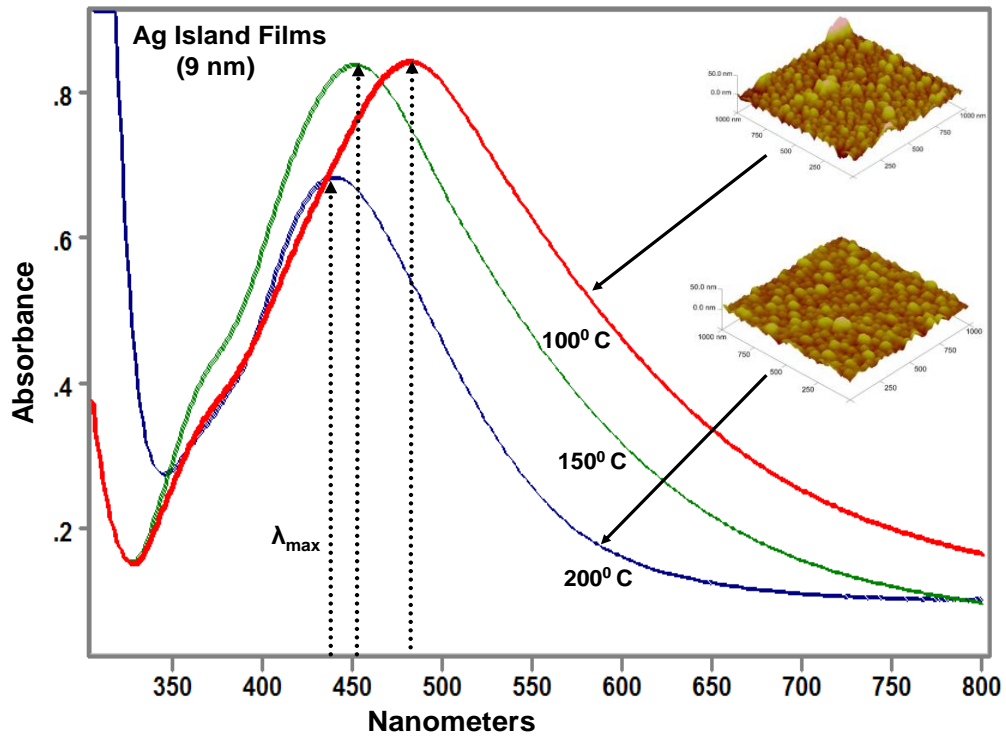


Figure 3.4: Surface plasmon absorption of Ag island films (temperature variation)

The 3D surface plots of AFM images from 100⁰ C and 200⁰ C are also shown in Figure 3.4. The decrease in the FWHM with increasing temperature, shifting of wavelength maximum to the blue, could be due to a more narrow particle size distribution, less particle-particle aggregation and comparatively smaller particle sizes due to a higher degree of particle mobility on the surface upon heating of the film at 200⁰ C.

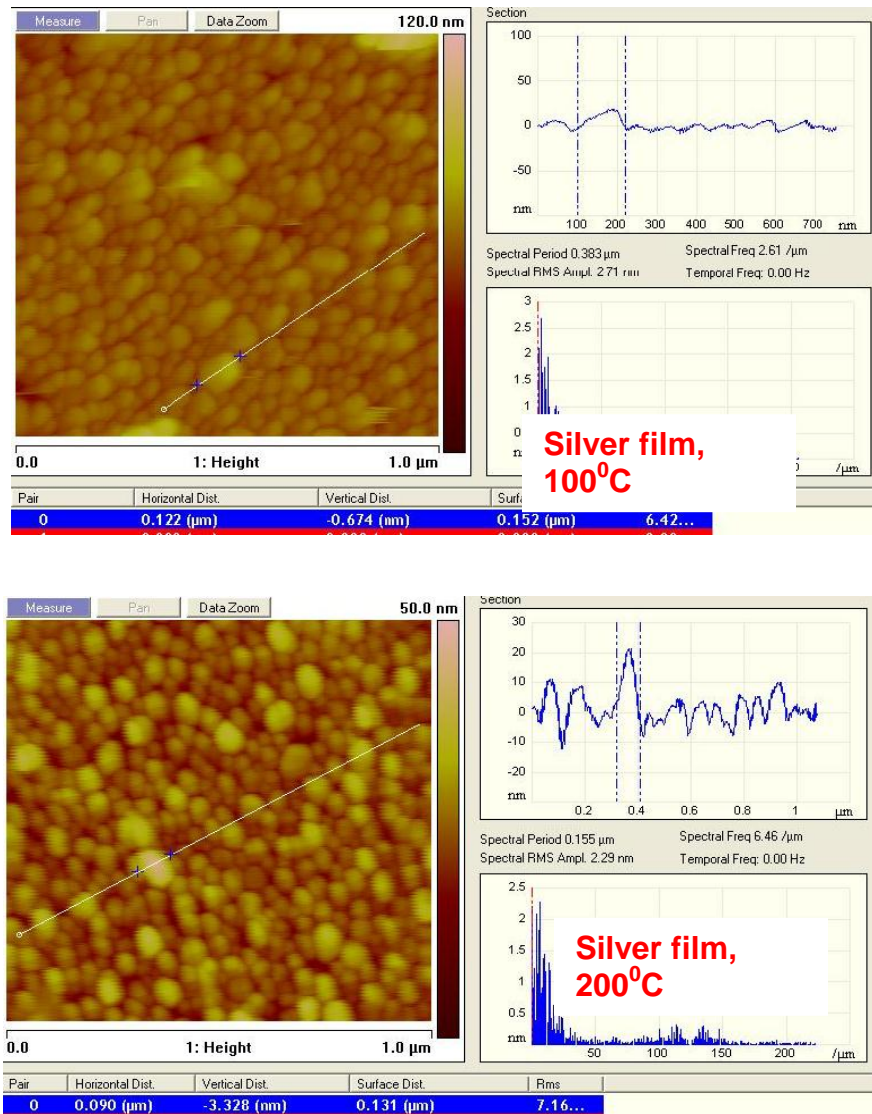


Figure 3.5: Particle size distribution analysis for silver island films of 9 nm mass thickness at 100⁰C and 200⁰C

In Figure 3.5 is shown the particle size distributions of silver island films of same thickness, 9 nm. The larger particle sizes and more aggregates are evident in case of the film prepared at 100⁰ C compared to the film prepared at 200⁰ C.

3.2.3.4 Comparison of plasmon absorption in Ag and Au film

For comparison, the absorption spectra of Ag and Au are shown in Figure 3.6. Both films were fabricated with the same experimental protocol.

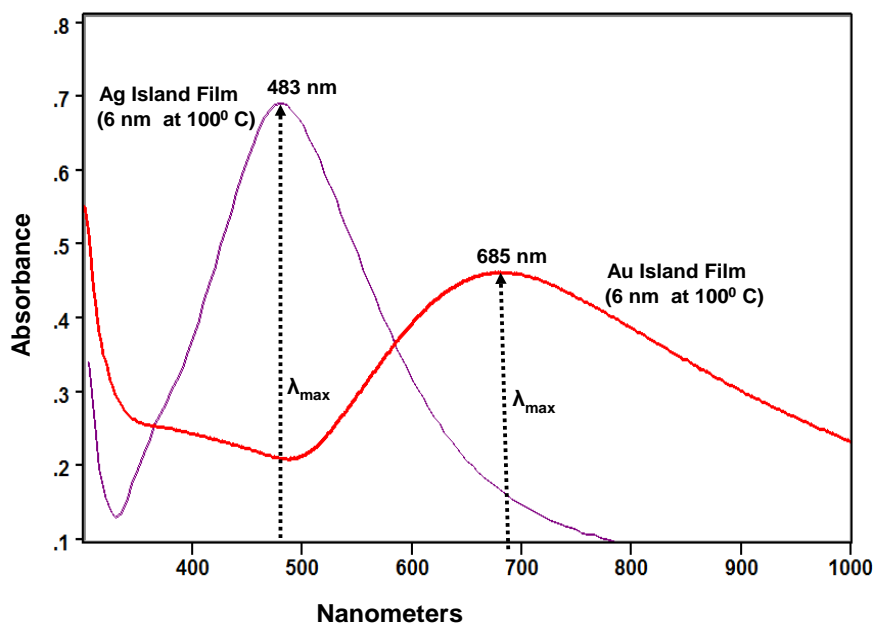


Figure 3.6: Surface plasmon absorption of Ag and Au island films

As can be seen in Figure 3.6, that the plasmon absorption wavelength maxima, λ_{max} , for Ag is 483 nm and that of Au is 685 nm, a characteristic of the optical properties of each metal in that region of the electromagnetic spectrum.

These results provide a direct pathway in selecting a laser line excitation for SERS/SERRS experiments: Ag island films in the blue-green and Au island films in the red. In addition, the choice of Ag or Au could be determined by the

potential photochemistry at the surface; silver is more reactive than gold. In the case of gold, not only the surface is less reactive; but the SERS/SERRS excitation can be achieved with lower energy light (near-infrared) avoiding photobleaching or photodissociation. A different option is to fabricate mixed film of Ag and Au with required mixing ratio by changing film thickness or temperature of deposition to attain an effective SERS/SERRS substrate.¹³

3.2.3.5 Gold films and Ag/Au mixed films

The plasmon absorption of gold films and Ag/Au mixed films are presented in Figure 3.7. In Figure 3.7 (a) and 3.7 (b), the 10 nm gold film and 6 nm gold film respectively, were prepared keeping the temperature of the substrate at 100⁰ C. The plasmon absorptions show the similar behaviour to that seen in silver film, and the FWHM increases with the mass thickness. Also the band maximum is a bit shifted towards near infra-red (NIR). Similarly, the effect of substrate temperature in gold film fabrication (thickness 6 nm) is shown in Figure 3.7 (b) and (c), made at 100⁰ C and 200⁰ C. As in the case of silver, higher substrate temperature during film formation shifts the plasmon towards blue region. In Figure 3.7 (d) and (e), the mixed films having the same mixing ratio, 7 nm Ag: 3 nm Au, were made at 100⁰ C and 150⁰ C respectively. Their plasmon absorptions also indicate the similar nature of blue shifting towards the blue region.

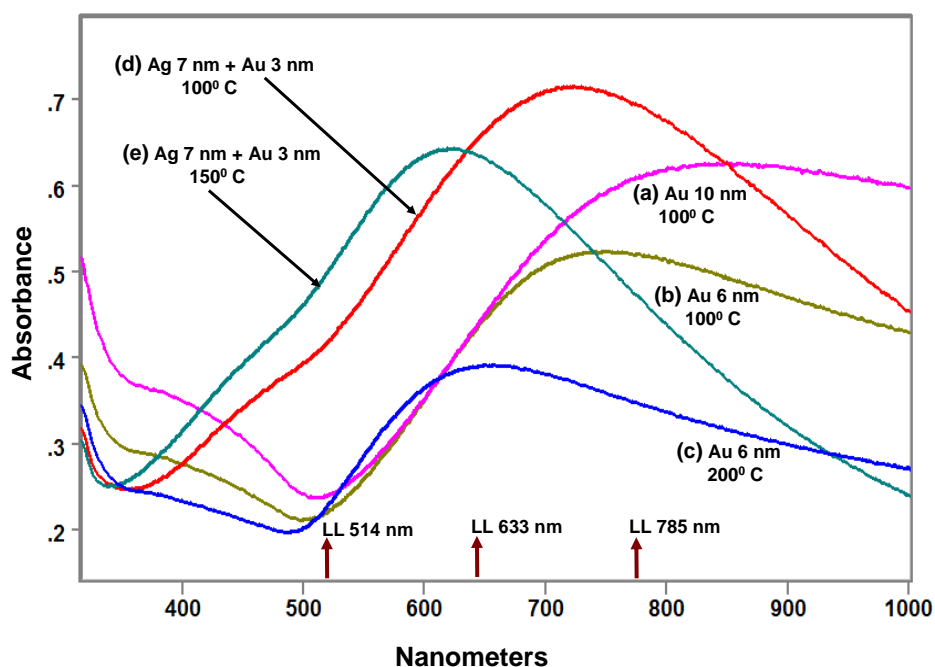


Figure 3.7: Surface plasmon absorption of Au and mixed Ag/Au island films

By changing the mixing ratio of Ag and Au, it is straightforward to tune the plasmon absorption region.

3.3 SERS demonstration using benzene thiol

3.3.1 Introduction

The surface-enhanced Raman scattering increases the normal Raman scattering cross section, thus enabling sensitive detection of analytes that are attached to or at a short distance (up to 10 nm) from the surface of the SERS active substrate. Raman scattering cross sections are generally small, on the order of 10^{-29} $\text{cm}^2 \text{molecule}^{-1} \text{sr}^{-1}$, 12 orders of magnitude less than those of fluorescence. This limited scattering power compensated by the SERS enhancement factor (EF)¹⁴. SERS is characterized by large EFs in the effective

Raman cross-section (typically 10^5 - 10^8) of analytes spatially confined within the near electromagnetic field (viz., 0-10 nm) generated upon excitation of the localized surface plasmon resonance of metal nanostructures. This EM enhancement^{1,8}, that has been discussed and explained in the literature. The total observed plasmonic enhancement can be seen in terms of two factors. The excitation of localized surface plasmon resonances leads to a substantial enhancement in the electromagnetic fields on the surface of the SERS substrates, E_{loc} . Therefore, the first factor enhancement in the vicinity of the SERS substrates containing Raman-active molecules is due to the enhanced local field,

$$EF_{loc} = \frac{|E_{loc}|^2}{|E_0|^2}, \text{ where } E_{loc} \text{ is the actual field feel by the molecule.}^9 \text{ The latter is}$$

directly related to the induced Raman dipole. The near field enhancement decreases away from the surface, thereby putting a requirement on the location of the Raman-active analyte molecule relative to the metallic SERS substrate.

The second factor comes from the field emitted by the induced dipole (with a

$$\text{Raman frequency } \omega_{Raman}) \text{ and scattered by the nanostructure; } EF_{Raman} = \frac{|E_{sca}|^2}{|E_0|^2}.$$

When the frequency of the incident radiation and the Stokes frequency of the emitted Raman signal are not spectrally far from each other, the total classical EM enhancement of the SERS signals has been described to be approximately proportional to the fourth power of the enhancement of the localized electric field in the vicinity of metallic nanostructures.⁹ The total enhancement factor is then given by;

$$EF_{total} = EF_{loc}(\omega_0) \times EF_{Raman}(\omega_{Raman}) \quad (1)$$

where ω_0 is the laser frequency and ω_{Raman} is $(\omega_0 - \Delta\omega_{Raman,shift})$. To estimate the Raman enhancement effect using experimentally measured parameters such as: intensities (I^{SERS}), the normal Raman intensities (I^R), the following approximation may be used;

$$EF = \frac{I^{SERS}}{I^R} \cdot \frac{N^R}{N^{SERS}} \cdot \frac{P^R}{P^{SERS}} \cdot \frac{t^R}{t^{SERS}} \quad (2)$$

Where, N^{SERS} and N^R correspond to the number of molecules illuminated by the laser on the SERS substrate and without SERS substrate, respectively, and P is the laser power and t is the exposure time.

3.3.2 Experimental

The materials used here are benzene thiol, C_6H_5SH , dichloromethane, silver and gold acquired from Aldrich. Both silver island film of 9 nm (mass thickness) and gold island film of 6 nm (mass thickness) have been used as the SERS active substrate in this work. The metal island films used in this study were produced by evaporating Ag or Au onto glass substrates (Corning 2048 glass slides). The 9 nm Ag island films were prepared by vacuum evaporation at a pressure of $\sim 10^{-6}$ Torr, and a temperature of $+100^0$ C with a deposition rate of ~ 0.5 A⁰/s. The 6 nm Au island films prepared keeping the substrate temperature during deposition at 200^0 C. These films were then heated at the same temperature for 1 hour after evaporation and left to cool for 1 more hour under vacuum. The absorption spectra of 1.36×10^{-4} M solution of benzene thiol in

dichloromethane, Ag island film of 9 nm and Au island film of 6 nm are seen in Figure 3.8.

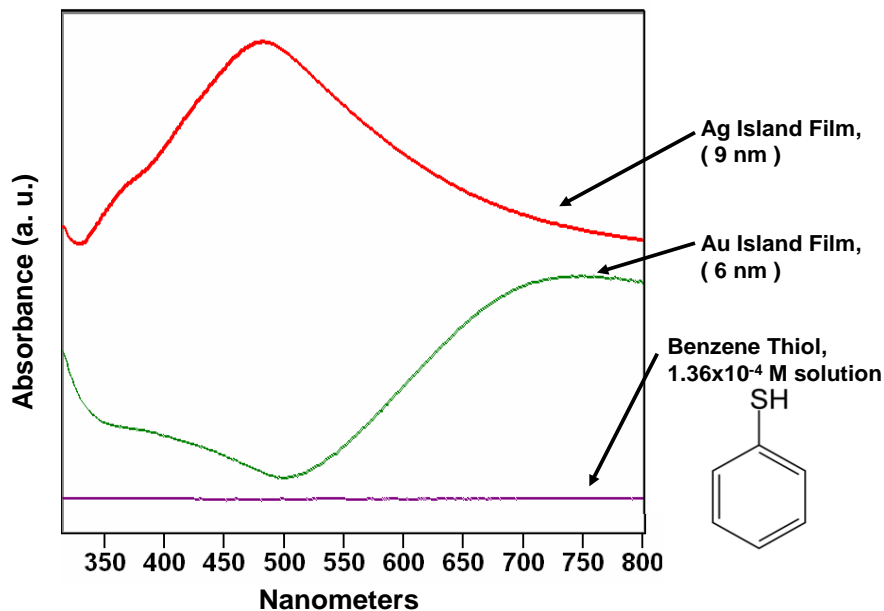


Figure 3.8: Absorption spectra of benzene thiol solution, Ag and Au island films

After preparing the metal island films, the deposition of benzene thiol on the films was performed using vertical deposition technique, which is shown in Figure 3.9. The metal island films were dipped in a solution of 1.36×10^{-4} M benzene thiol in dichloromethane at an ambient temperature. The benzene thiol molecules, adsorbed on the surface of metal island film and glass slide, were then probed by Raman spectroscopy.

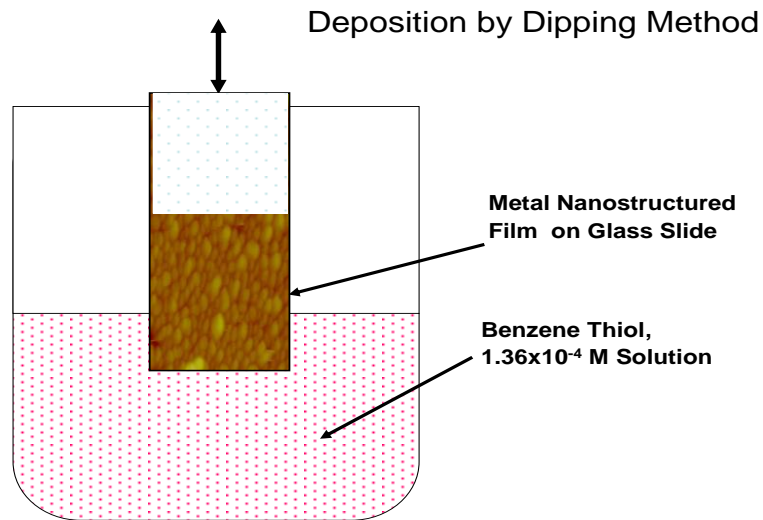


Figure 3.9: Deposition of benzene thiol onto metal island films by vertical dipping

3.3.3 Results and Discussion

3.3.3.1 SERS of benzene thiol on silver island film

The Raman spectra of benzene thiol adsorbed on Ag island film and glass surface obtained by using a laser line of 514 nm excitation can be seen in Figure 3.10. The Raman spectrum from the nanostructured silver island film is strong and evident, while the spectrum on the glass surface did not show any Raman bands. These spectra were recorded using the same experimental conditions, equal laser power and exposure time. Using the Raman band at 1577 cm⁻¹ to estimate the enhancement factor due to the LSPR effect from silver island film, an SERS enhancement factor $\sim 10^6$ is observed compare to RS spectrum on glass.

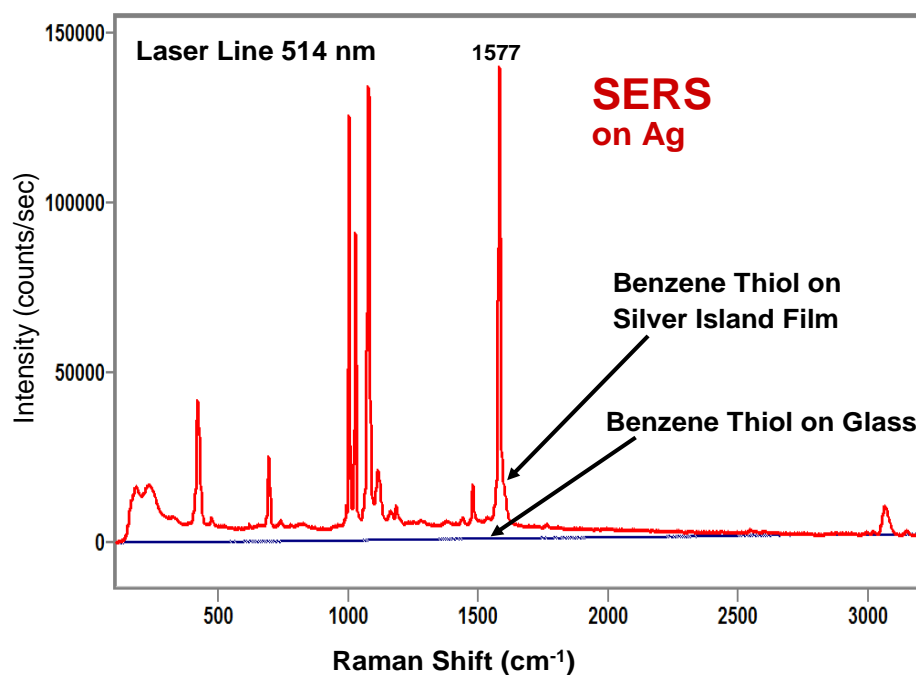


Figure 3.10: Raman spectra acquisition for benzene thiol on silver film and glass surface

3.3.3.2 SERS of benzene thiol on gold island film

The SERS spectra of benzene thiol on gold island film and Raman spectra for the same compound on glass surface can be seen in Figure 3.11. The laser line, 633 nm, with same laser power and exposure time has been used in both acquisitions of the Raman spectra. If the Raman band at 1577 cm⁻¹ is taken as to assess the SERS enhancement compare to Raman spectra on bare glass substrate, the Raman band intensity enhancement is estimated to be $\sim 10^4$. The enhancement effect for gold film is 100 fold lower than that on silver island film.

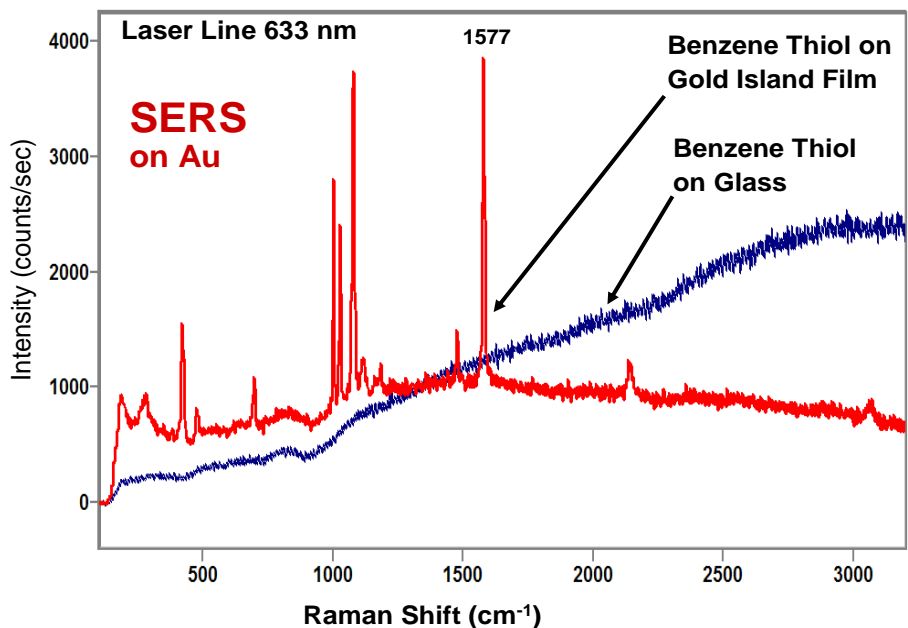


Figure 3.11: Raman spectra acquisition for benzene thiol on gold film and glass surface

The SERS spectra of the benzene thiol adsorbed on silver island film were recorded using laser lines: 514 nm, 633 nm and 785 nm. These spectra are shown in Figure 3.12. Minor differences in the relative intensity are observed due to CCD response. However, the SERS enhancement is observed with all three lines in agreement with broad plasmon absorption of the silver island film. However, SERS of the benzene thiol on Au island film is mainly observed with only the red laser lines: 633 nm and 785 nm as shown in Figure 3.13, which is in correspondence with the location of the Au film plasmon absorption.

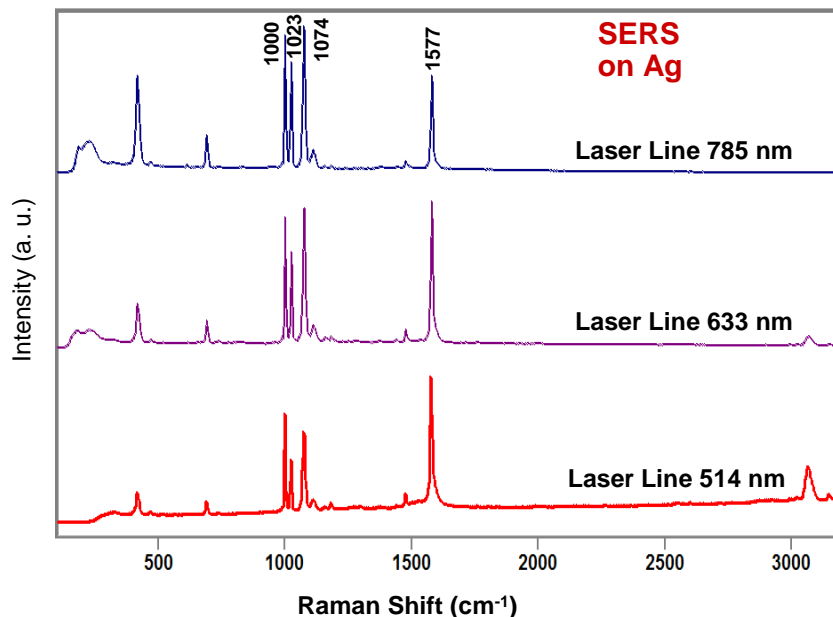


Figure 3.12: SERS spectra of benzene thiol on Ag film at 514 nm, 633 nm and 785 nm

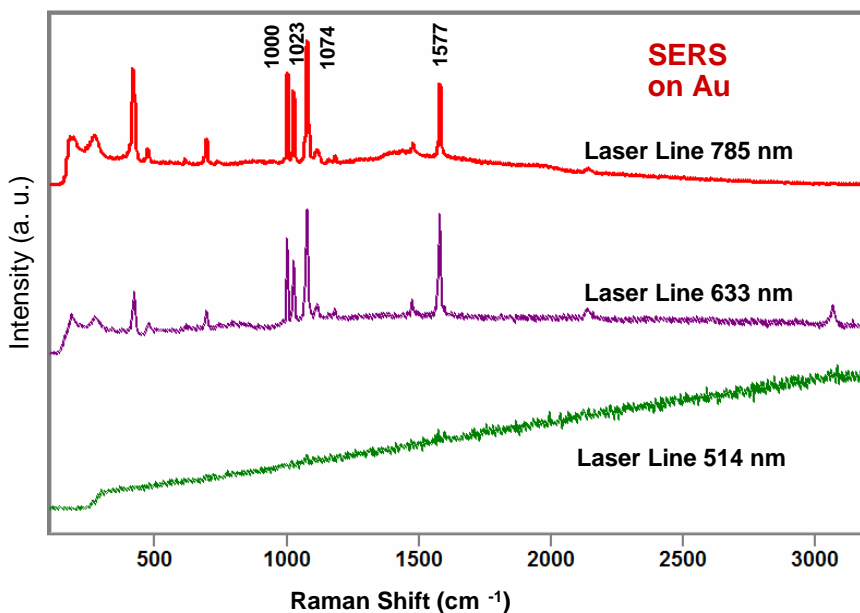


Figure 3.13: SERS - benzene thiol on Au island film at 514 nm, 633 nm and 785 nm

The enhancement of the Raman scattering signals is due to the enhanced electromagnetic field at or near the metal surface that would strongly modify the molecular polarizability in the region of excitation.

3.4 Langmuir Blodgett (LB) approach to SERS

3.4.1 Introduction

In SERS, the basic components involved are a molecule, a metal nanostructure and electromagnetic radiation. The incident radiation is defined in terms of its monochromaticity, polarization and intensity, which are under control by experimental set up of the Raman experiment. The metal nanostructures are fabricated to provide the LSPR. Raman spectrum in gas phase involved only the molecule and the incident radiation. Since there is a random orientation of the molecules in gas phase, directionality is not a concern in the spectral interpretation and polarization properties; and this refer entirely to the spatial orientation of the electric field of the incident light. However, for a molecule in solid phase or adsorbed onto solid substrate, the observed intensity of the Raman modes are modulated by the polarization of the incident electric field and a spatial molecular orientation. The spectra can be explained by application of surface selection rules that emphasizes the dependence of the Raman intensities on the orientation properties of the molecule and light polarization on the surface.¹

In SERS, the close proximity of the molecules to the metal surface provides the highest enhanced Raman intensities. The plasmonic enhancement arising from LSPR decreases as the molecules move apart from the surface of SERS active substrate. Because the field enhancement around a small metal sphere decays with d^{-3} , using the E^4 approximation, the overall distance dependence should scale with d^{-12} (referring chapter 2, section 2.3.1 and

equation 2.3.4). Taking into account the increased surface area scales with d^2 for shells of molecules at an increased distance from the nanoparticle, then the d^{-10} distance dependence could be observed;⁶

$$I_{SERS} = \left(\frac{d+r}{r} \right)^{-10} \quad (3.4.1)$$

Where, I_{SERS} is the intensity of the Raman mode, r is the average size of the field-enhancing features on the surface, and d is the distance from the surface to the adsorbate.¹⁵

The intensities of Raman scattering for a given band can be simply written

as:
$$I_{RS} = I_0 \sigma_{RS} N \quad (3.4.2)$$

Where, I_{RS} , the Raman intensity (photons sec^{-1}) is proportional to the incoming flux of photons, I_0 (photons $\text{sec}^{-1} \text{cm}^{-2}$) and N , the number of scatterers or molecules. The proportionality constant, σ_{RS} , is the Raman cross section and is a function of the frequency of excitation.

3.4.2 Langmuir Blodgett (LB) monolayer approach –SERS

The Langmuir-Blodgett (LB) technique is one of the most powerful tools to form organic ultrathin films with molecular organization¹⁶. This LB technology is an appropriate technique allowing the manipulation of materials at the molecular level and the fabrication of ultra thin and highly ordered organic films. In the LB method, a thin molecular layer spread at the air/water interface (Langmuir monolayer) is transferred onto a solid substrate, a process that can be repeated

several times with the same substrate to form multilayer films, providing one of the most elegant approaches to fabricate organic films of thickness at the molecular level. This simple way of getting a well defined and organized surface coverage of the adsorbed organic molecules on SERS substrate can be utilized to create model system for SERS studies. The molecular orientations are tuneable by controlling mainly the temperature and composition of LB subphase and surface pressure of the monolayer. The surface coverage or the number of molecules adsorbed per unit area of the SERS active surface could be determined when area per molecule is known from the solid phase of the LB isotherm of the respective compound. The LB monolayer formation, its deposition on solid substrate and isotherm behaviours are explained in details in chapter 2 and section 2.5. The study of distance dependence of the molecules from the surface is also possible when a monolayer of inert molecule of known thickness is used as a spacer layer between the molecules and SERS substrate. When all parameters are optimized, this technique corresponds to one of the most promising for preparing thin films of amphiphilic molecules as it enables 1) an accurate control of the thickness and of the molecular organization, 2) an homogeneous deposition of the monolayer over large areas compared to the dimension of the molecules, 3) the possibility to transfer monolayers on almost any kind of solid substrate and 4) to elaborate bilayer structures with varying layer compositions. Based on the self-assembled properties of amphiphilic biomolecules at the air/water interface, LB technology offers the possibility to prepare biomimetic layers suitable for immobilisation of bio-active molecules.

One of the highest important aspects to comprehend the SERS results is the surface coverage dependence of the SERS intensity and the enhancement factor (EF). The SERS intensity as a function of surface coverage can be elucidated in terms of LSPR active sites that are responsible for the enhancement on a metal surface. After the saturation of these sites by the adsorbed molecular species, the SERS intensity should reach a plateau. The electromagnetic model of SERS intensity may be achievable by a quantitative approach for the interpretation of the surface coverage effect on SERS. A maximum SERS intensity enhancement is observed in submonolayer coverage.²⁴⁻²⁵ The Langmuir-Blodgett deposition for molecules that can form LB films or mixed LB films (LB-SERS), permits very good control over the surface molecular coverage concentrations,²⁶⁻²⁷ allowing to compare SERS substrates and to estimate the enhancement factor for the target molecule. A fair quantitative approach to expound SERS results, a controlled diluted monomolecular film and well-defined molecular spatial distribution provided by the LB technique is crucial for SERS understanding and development of theoretical and experimental SERS studies. In contrary, SERS can also be applied to study a variety of LB film properties, such as to determine the molecular organization and/or molecular aggregation²⁸⁻³⁴, to distinguish dye monomer and aggregates³⁵ and in molecular recognition.³⁶⁻³⁷ Single-molecule-SERS and resonance SERS (SERRS) are the emergent field of single molecule spectroscopy³⁸. The use of the LB technique has played an important role in the observation of SERS/SERRS spectra of a single molecule and has contributed to validate single molecule detection in

several experiments using doped LB monolayers with an average of one molecule in the field of view of the Raman-microscope.³⁹⁻⁴⁰ The potential and advantages of the 2D LB structures to explore the spectral properties in the transition from the average SERS/SEERS spectra to the single molecule regime is possible with a large amount of data collection for a single LB on metal island films.

References

- (1) Moskovits, M. *Reviews of Modern Physics* **1985**, *57*, 783-826.
- (2) Noguez, C. *Journal of Physical Chemistry C* **2007**, *111*, 3806-3819.
- (3) Willets, K. A.; Van Duyne, R. P. *Annual Review of Physical Chemistry* **2007**, *58*, 267-297.
- (4) Aroca, R. *Surface-enhanced Vibrational Spectroscopy*; John Wiley & Sons: Chichester, **2006**.
- (5) Le Ru, E. C.; Etchegoin, P. G. *Principles of Surface Enhanced Raman Spectroscopy (and related plasmonic effects)*; Elsevier: Amsterdam, **2009**.
- (6) Baker, G. A.; Moore, D. S. *Analytical and Bioanalytical Chemistry* **2005**, *382*, 1751-1770.
- (7) Pinchuk, A. O.; Schatz, G. C. *Applied Physics B: Lasers and Optics* **2008**, *93*, 31-38.
- (8) Schatz, G. C.; Van Duyne, R. P. In *Handbook of Vibrational Spectroscopy*; Griffiths, J. M. C. a. P. R., Ed.; John Wiley & Sons, Ltd, **2002**; Vol. Volume 1.
- (9) Le Ru, E. C.; Etchegoin, P. G. *Chemical Physics Letters* **2006**, *423*, 63-66.

- (10) Li, J. F.; Huang, Y. F.; Ding, Y.; Yang, Z. L.; Li, S. B.; Zhou, X. S.; Fan, F. R.; Zhang, W.; Zhou, Z. Y.; Wu, D. Y.; Ren, B.; Wang, Z. L.; Tian, Z. Q. *Nature* **2010**, *464*, 392-395.
- (11) Moskovits, M. *Nature* **2010**, *464*, 357.
- (12) Lee, S. J.; Morrill, A. R.; Moskovits, M. *Journal of the American Chemical Society* **2006**, *128*, 2200-2201.
- (13) Goulet, P. J. G.; Aroca, R. F. *Canadian Journal of Analytical Sciences and Spectroscopy* **2007**, *52*, 172-177.
- (14) Le Ru, E. C.; Blackie, E.; Meyer, M.; Etchegoin, P. G. *Journal of Physical Chemistry C* **2007**, *111*, 13794-13803.
- (15) Kneipp, K.; Kneipp, H. *Applied Spectroscopy* **2006**, *60*, 322A-334A.
- (16) Roberts, G. *Langmuir-Blodgett Films*; Plenum Press: New York, 1990.
- (17) Constantino, C. J. L.; Duff, J.; Aroca, R. *Spectrochimica Acta Part a-Molecular and Biomolecular Spectroscopy* **2001**, *57*, 1249-1259.
- (18) Constantino, C. J. L.; Aroca, R. F. *Journal of Raman Spectroscopy* **2000**, *31*, 887-U3.
- (19) Aroca, R.; Jennings, C.; Kovacs, G. J.; Loutfy, R. O.; Vincett, P. S. *Journal of Physical Chemistry* **1985**, *89*, 4051-4054.
- (20) Tao, A.; Kim, F.; Hess, C.; Goldberger, J.; He, R. R.; Sun, Y. G.; Xia, Y. N.; Yang, P. D. *Nano Letters* **2003**, *3*, 1229-1233.
- (21) Goulet, P. J. G.; Pieczonka, N. P. W.; Aroca, R. F. *Analytical Chemistry* **2003**, *75*, 1918-1923.

- (22) Bernard, S.; Felidj, N.; Truong, S.; Peretti, P.; Levi, G.; Aubard, J. *Biopolymers* **2002**, *67*, 314-318.
- (23) Dynarowicz-Latka, P.; Dhanabalan, A.; Oliveira, O. N. *Advances in Colloid and Interface Science* **2001**, *91*, 221-293.
- (24) Aroca, R.; Kovacs, G. J. *In Vibrational Spectra and Structure*; Durig, J., Ed.,; Elsevier; Amsterdam, Vol. 18, **1989**.
- (25) Moscovits, M. *Rev. Mod. Phys.* **1985**, *57*, 783.
- (26) M. C. Petty. *Langmuir-Blodgett Films: An Introduction*. Cambridge University Press, Cambridge, **1996**.
- (27) G. Roberts. *Langmuir-Blodgett Films*. Plenum Press, New York, **1990**.
- (28) A. K. Maiti, R. Aroca, Y. Nagao. *Journal of Raman Spectroscopy* **1993**, *24*, 351-356.
- (29) J. Souto, R. Aroca, J. A. DeSaja. *Journal of Raman Spectroscopy* **1991**, *22*, 349-353.
- (30) C. J. L. Constantino, P. A. Antunes, E. C. Venancio, N. Consolin, F. J. Fonseca, L. H. C. Mattoso, R. F. Aroca, O. N. Oliveira, Jr., A. Riul, Jr. *Sensor Letters* **2004**, *2*, 95-101.
- (31) C. J. L. Constantino, R. F. Aroca. *Journal of Raman Spectroscopy* **2000**, *31*, 887-890.
- (32) C. J. L. Constantino, R. F. Aroca, J. A. He, V. Zucolotto, L. Li, O. N. Oliveira, Jr., J. Kumar, S. K. Tripathy. *Applied Spectroscopy* **2002**, *56*, 187-191.

- (33) C. J. L. Constantino, R. F. Aroca, S. Yang, V. Zucolotto, L. Li, O. N. Oliveira, Jr., A. L. Cholli, J. Kumar, S. K. Tripathy. *Journal of Macromolecular Science, Pure and Applied Chemistry* **2001**, A38, 1549-1557.
- (34) C. Heywang, M. S.-P. Chazalet, M. Masson, J. Bolard. *Spectrosc. Biol. Mol.: New Dir., Eur. Conf., 8th*, **1999**, 339-342.
- (35) U. Guhathakurta-Ghosh, R. Aroca, R. O. Loutfy, Y. Nagao. *Journal of Raman Spectroscopy* **1989**, 20, 795-800.
- (36) J. Huang, C. Li, Y. Liang. *Langmuir* **2000**, 16, 3937-3940.
- (37) C. Li, J. Huang, Y. Liang. *Langmuir* **2000**, 16, 7701-7707.
- (38) W. E. Moerner. *J. Phys. Chem. B* **2002**, 106, 910-927.
- (39) C. J. Constantino, T. Lemma, P. A. Antunes, R. Aroca. *Analytical chemistry* **2001**, 73, 3674-3678.
- (40) P. J. G. Goulet, R. F. Aroca. *Analytical Chemistry* **2007**, 79, 2728-2734.

CHAPTER 4

SURFACE ENHANCED RAMAN SCATTERING OF PHOSPHOLIPID BILAYERS IN LANGMUIR-BLODGETT FILMS

4.1 Background

The use of phospholipids as mimetic systems for studies involving the cell membrane is a well-known approach. In this context, the Langmuir-Blodgett (LB) technique¹ is used to produce ordered layers of phospholipids structured as mono- or bilayer². The basic structure of cell membranes is formed by a phospholipids' bilayer. The structure of this bilayer determines its properties and, crucially important for the living organism, its functions. The importance of phospholipids as biological building blocks is becoming increasingly apparent. Phospholipids' membranes serve as encapsulators of cells and organelles and are integral participants in the control of molecular transport into and out of cells and in cell communication. Lipid malfunction is implicated in several diseases. Research on lipid structure and its dynamics is vital in understanding the cell membrane and membrane-bound protein behaviour is a key factor in drug development. A schematic diagram of a cell membrane and phospholipids bilayer is shown in Figure 4.1. Phospholipids, the building blocks of the cell membranes, are both hydrophilic and hydrophobic.

A lipid bilayer is a thin film of lipids two molecules thick, arranged so that the hydrophilic phosphate heads face the surface on either side of the bilayers, while the hydrophobic tails point "in" to the core of the bilayer. This arrangement results in two "leaflets" where each one is a single molecular layer.

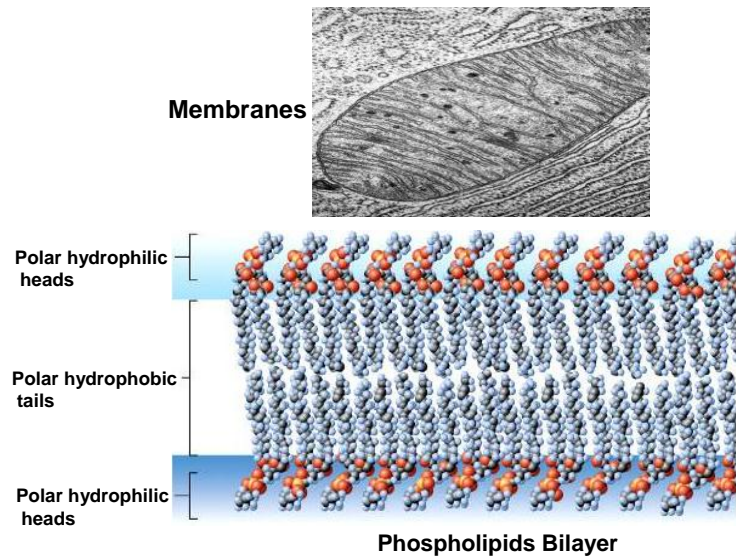


Figure 4.1: Illustration of a Phospholipid Bilayer model in cell membranes

Lipids self-assemble into this structure because of the hydrophobic effect, which creates an energetically unfavourable interaction between the hydrophobic lipid tails and the surrounding water when forming the Langmuir monolayer. Thus, an LB lipid bilayer is typically held together by entirely non-covalent forces that do not involve formation of chemical bonds between individual molecules.²⁻⁶

Organic thin films like monomolecular thick monolayer offer an attractive method of designing molecular materials for various applications. The properties of such films arise not only from the specific characteristics of the molecules but also from their arrangement within the film. Phospholipids' monolayers provide suitable model systems for biological membranes. Therefore they have traditionally been used for studying the competitive interactions between polar hydrophilic headgroups and hydrophobic chains connected to the glycerol backbone. Langmuir-Blodgett films of phospholipids' model the cellular systems nicely because the molecules in these films are ordered and interactions among

the molecules are similar to that found in cells. Thus, studies of LB films have become increasingly important for understanding cellular membrane dynamics.^{3,7-11}

The change of the inter- and intramolecular order of lipid molecules during the transitions into the cell membrane can be determined using Raman spectroscopy. The Raman spectrum of a cell represents an intrinsic biochemical fingerprint, containing molecular-level information about all cellular biopolymers, including DNA, RNA, proteins, lipids, and carbohydrates. The main advantages of Raman micro spectroscopy over conventional techniques include its capability for rapid, non-invasive sensing, high spatial resolution, and the weak Raman scattering of aqueous media enables the in vitro analysis of living cells in the absence of fixatives or labels

Nanostructured metals such as gold and silver are particularly interesting as platforms for supporting phospholipids' bilayers because they enable the use of electrochemical and optical techniques. These techniques provide in situ complementary information about interaction and transport of different molecules, biomolecules or nanomaterials in self-assembled molecular layers in contact with electrolytes. SERS is a very sensitive technique that employs different types of nanostructured substrates to enhance the Raman signal produced by adsorbed and immobilized species, which is otherwise too weak to be detected with conventional Raman spectroscopy.⁸⁻¹¹

4.2 Introduction

Practical applications of Surface-enhanced Raman scattering (SERS) as a reliable and rapid biosensing technique face several challenges. i) The fabrication of reproducible SERS substrates with an average enhancement factor (EF) of at least four orders of magnitude or more.¹²⁻¹³ ii) Organic biomolecules that do not contain aromatic rings or bulky “soft” atoms (such as sulphur), with electronic absorptions in the UV, normally present a poor scattering cross section, placing the strain on the SERS enhancement factor for ultrasensitive detection. iii) In order to take advantage of the maximum value of the EF (first layer effect), optimization of the adsorption to the enhancing nanostructure becomes a very important issue. At the same time, the photochemistry that may take place at the first layer (photodissociation or “bleaching”),¹⁴ leads to the formation of carbon in many biomolecules, and it may hinder the SERS applications. Therefore, the task of reporting reproducible SERS spectra for ultra sensitive detection is of primary importance, and it should be the anticipated achievement for SERS of biomolecular systems. In this chapter, exploring the SERS technique using single monolayers and bilayers of common phospholipids is reported, and also the SERS spectra of trilayers is discussed. The final aim is to provide reproducible and characteristic SERS spectra for the analytical detection of phospholipids as bilayers, a subject of interest for fundamental studies in membrane biophysics. Phospholipid Langmuir-Blodgett (LB) films are a good representation for biomembranes used in a variety of immobilization studies.¹⁵⁻¹⁶ The spectroscopic characterization of phospholipids using molecular vibrational fingerprints leads to

either infrared or Raman techniques. In particular, the high spatial resolution and the “in-situ” possibilities of micro-Raman spectroscopy are very attractive.¹⁷ In addition, SERS offers high sensitivity with low detection limits. However, the Raman cross section of phospholipids is very small and achieving reproducible SERS spectra of this important class of molecules has been elusive. In fact, there are no reports on SERS of phospholipids. The phospholipids in SERS reports have mainly been the silent matrix during the detection of others moieties with larger Raman cross sections.¹⁸ Our own work on single molecule detection has been achieved with tagged phospholipids and surface-enhanced resonance Raman scattering.¹⁹ Dai et al.²⁰ have reported the SERS spectra of mixed Langmuir monolayers of octadecylamine (ODA) monolayers and egg phosphatidylcholine (PC) on silver colloidal nanostructures. However, they pointed out that “...we cannot find any signal of PC monolayer in the spectrum”. A very good example of using LB phospholipids as a silent SERS overlayer is given in the report of Bernard et al.¹⁸ where reproducible SERS spectra of trans-1,2-bis(4-pyridyl)ethylene (BPE) with excitation at 632.8 nm is achieved on gold nanostructures coated with an LB monolayers of synthetic tetramyristoyl cardiolipin (TMCL). Here the SERS spectra of bilayers of 1,2-Dipalmitoyl-sn-glycero-3-phosphocholine (DPPC) and 1,2-dimyristoyl-sn-glycero-3-phosphocholine (DMPC) fabricated by the Langmuir–Blodgett (LB) technique onto silver nanostructures evaporated on glass substrates are reported. The chemical structures of DMPC and DPPC are shown in Figure 4.2.

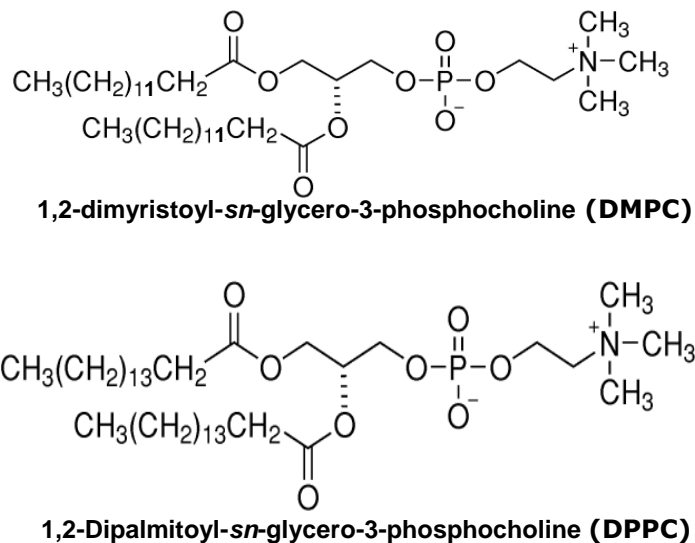


Figure 4.2: Illustration for chemical structures of the Phospholipids

The SERS spectra were obtained with two different lines: 514.5 nm and 632.8 nm, both in full resonance with the localized surface plasmons of the silver nanostructures. The issue of SERS reproducibility is particularly sensitive in the plasmon enhanced spectra of biomolecules,²¹ and the SERS spectra of bilayers reported here (with the 632.8 nm excitation) are reproducible over the LB surface area, as demonstrated by mapping with micrometer spatial resolution.

4.3 Experimental

Material and sample preparation. The amphiphilic phospholipids, 1,2-Dipalmitoyl-*sn* glycero-3-phosphocholine (C₄₀H₈₀NO₈P or DPPC) and 1,2-dimyristoyl-*sn*-glycero-3-phosphocholine (C₃₆H₇₂NO₈P or DMPC), ultra pure Ag shots and chloroform were purchased from Aldrich. All were used without further purification. The phospholipids solutions were prepared using spectroscopic grade chloroform as the solvent. Silver island films (SIF) of 9 nm mass thickness

used as a SERS substrate were prepared by vacuum evaporation. The SIF was deposited on Corning-2048 glass microscope slides at a pressure of $\sim 10^{-6}$ Torr, while the substrate temperature was kept at 100 °C during evaporation (and maintained for 1 hour after evaporation was completed).

Langmuir-Blodgett (LB) film deposition. Langmuir-Blodgett monolayer of Phospholipids was prepared at the air-water interface of a Lauda Langmuir film balance (model 302M) with dimensions 414 x 70 mm², and transferred onto the SIF. Prior to deposition, the trough was cleaned by chloroform. The subphase was distilled deionized water. The subphase was ultrapure Milli-Q water (18.2 M Ω cm) at a constant temperature of 25 °C. After filling the trough with the subphase, the pressure sensor was calibrated using the cross and weight set provided by Lauda. Langmuir monolayer of DMPC or DPPC was prepared at the air-water interface of a Lauda film balance, in order to study the surface pressure area isotherm. The phospholipid solution was spread drop to drop on the aqueous surface using a microsyringe held very close to the aqueous surface and then the solvent was allowed to evaporate completely over a period of time at least 25 minutes. The monolayer was then compressed at a fixed barrier speed of 10 cm²/min until the monolayer breaks to record the surface pressure – area per molecule (π -A) isotherm, which is shown in Figure 4.3. The surface pressure (π) was measured by a Wilhelmy paper plate pressure sensor in mN m⁻¹. After knowing the surface pressure – area per molecule (π -A) isotherm, the phospholipid monolayer was prepared at water-air interface in the Lauda film balance at the same conditions of isotherm; and film transfer onto SIF was

carried out using Z-deposition with a Lauda Film Lift FL-1 electronically controlled dipping device at a constant surface pressure of 25 mN m^{-1} , that corresponding to the condensed phase of the Langmuir monolayer, with transfer ratio near unity.

UV-visible absorption spectra were recorded for all solutions and 9 nm Ag nanoparticle films in a Cary 50 scan UV-visible spectrophotometer. Atomic force microscopy (AFM) images were recorded using a Digital Instruments NanoScope IV, operating in tapping mode with an n+- silicon tip. All images were collected with high resolution (512 lines per scan) at a scan rate of 0.5 Hz. Topographical (height) images were used for analysis of the surface morphology of the films. The data were collected under ambient conditions, and each scan was duplicated to ensure that any features observed were reproducible. Micro-Raman scattering experiments were carried out using a Renishaw InVia system with laser excitation at 514.5 nm and 632.8 nm and powers of 10-20 μW at the sample to avoid the possibility of photodegradation. All measurements were made in a backscattering geometry, using a 50x microscope objective with a numerical aperture value of 0.75, providing scattering areas of ca. $1 \mu\text{m}^2$ for the 514.5 nm laser line and ca. $2 \mu\text{m}^2$ for the 632.8 nm laser line. Single point spectra were recorded with 4 cm^{-1} resolution and 10-second accumulation times, while 2D SERRS mapping results were collected through the rastering of a computer controlled 2-axis encoded (XY) motorized stage, with a step of $2 \mu\text{m}$.

4.4 Results and Discussion

4.4.1 UV-vis absorption

In Figure 4.3, the surface plasmon absorption spectrum of a 9 nm mass thickness silver island film is shown. The FWHM of this band covers a large section of visible spectral region, indicating that the film encloses of a broad distribution of particle sizes and shapes. It also implies that there is a high degree of particle-particle interaction in the film. A typical height image (3D) of AFM results of the silver film used in this work is also shown in Figure 4.3. This plasmon width facilitates the use different laser excitations for Raman in the visible region.

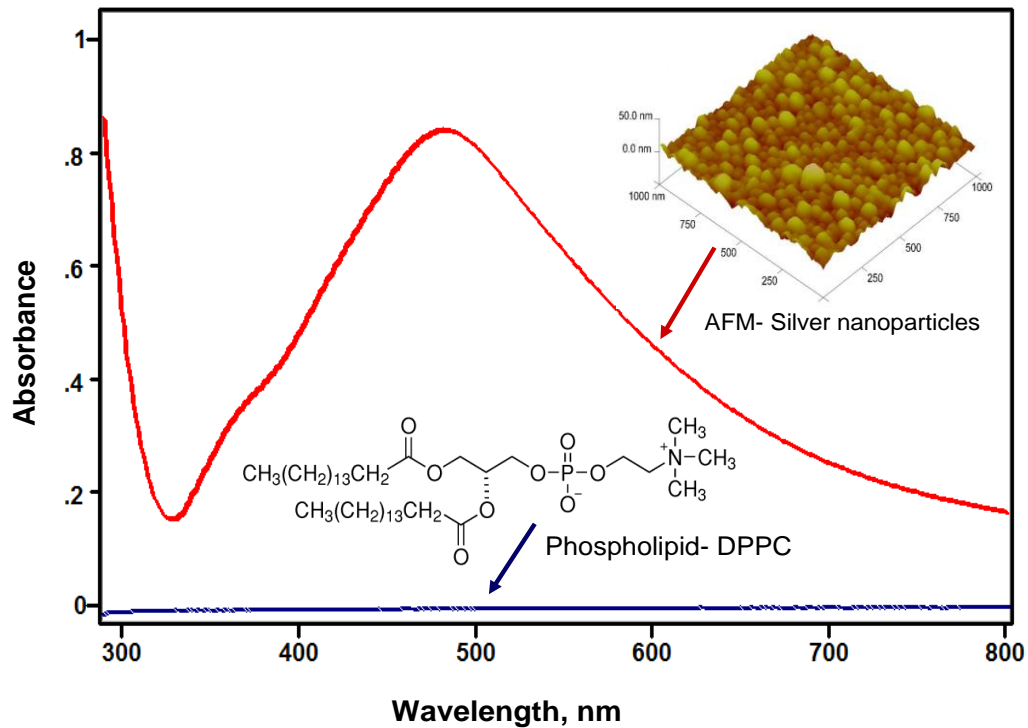


Figure 4.3: UV-visible absorption of 9 nm Silver island film and Phospholipid-DPPC

The absorption spectra of the DPPC solution of 10^{-4} M in chloroform is also shown in Figure 4.3, which indicates that phospholipids have no absorption in the visible, and thereby, there no electronic resonance, and SERRS is not significant in this investigation.

4.4.2 Langmuir-Blodgett surface pressure area isotherm

The surface-pressure area isotherm of Langmuir monolayer DPPC is given in Figure 4.4. The DPPC solution of 10^{-4} M in chloroform was spread over the water surface of the trough at a constant subphase temperature of 25 °C. Two phase transitions can be seen in the surface-area isotherm; a gas-liquid transition with a limiting area ca. 85 \AA^2 per molecule, and the formation of a condensed phase in the monolayer with a limiting area of ca. 40 \AA^2 per molecule, indicating that the smaller polar section of the molecule is interacting with the water surface (head-on organization). The molecular organization at the interface is illustrated with the cartoon in Figure 4.4, where the hydrophobic part (two alkyl chains) is floating away from the water surface and the polar part is interacting with the water. Our results, as well as the work of Wang et al.,²² indicate that the surface pressure dependent chain-conformational organization is preserved during the transfer of the monolayers (onto the silver island film to form the LB monolayer, bilayers and trilayers).

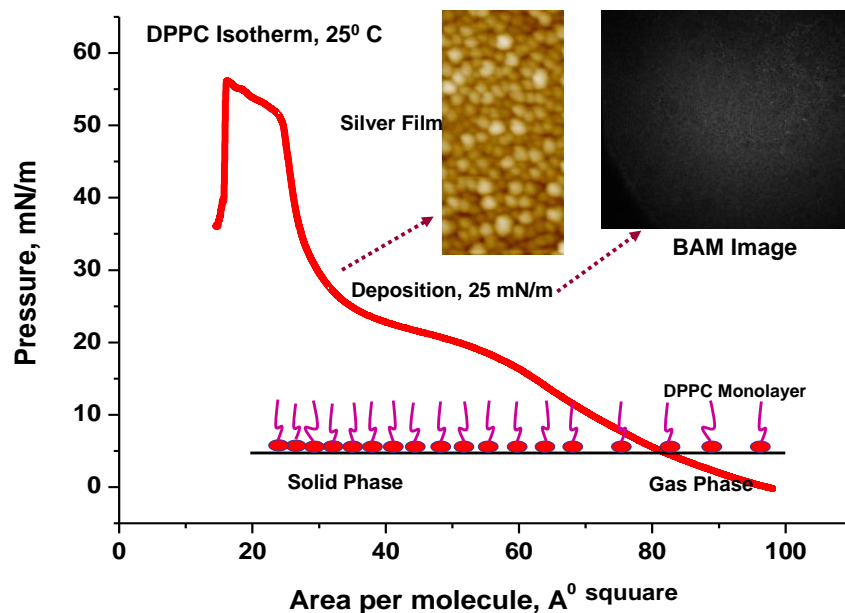


Figure 4.4: Surface-pressure area isotherm for DPPC on water, AFM of the Ag nanostructures, the BAM image of monolayer morphology, and the arrow shows the surface pressure for monolayer transfer.

The metal film image (2D) of silver nanostructures and BAM image of the phospholipid monolayer at the deposition surface pressure are also shown in Figure 4.4. The arrow in Figure 4.4, points to the surface-pressure used for monolayer deposition. The transfer ratio for both phospholipid monolayers is close to unity. As expected, identical results were found for DMPC monolayers (not shown in the Figures).

4.4.3 Vibrational Raman spectra of phospholipids – DMPC and DPPC

At the beginning, the Raman spectra of neat powder phospholipids, both DMPC and DPPC, were recorded with several laser lines (442, 514.5 and 632.8 nm). There is minimal dispersion in this spectral region and the representative

spectrums DMPC and DPPC are shown in Figure 4.5 for the 442 nm laser excitation.

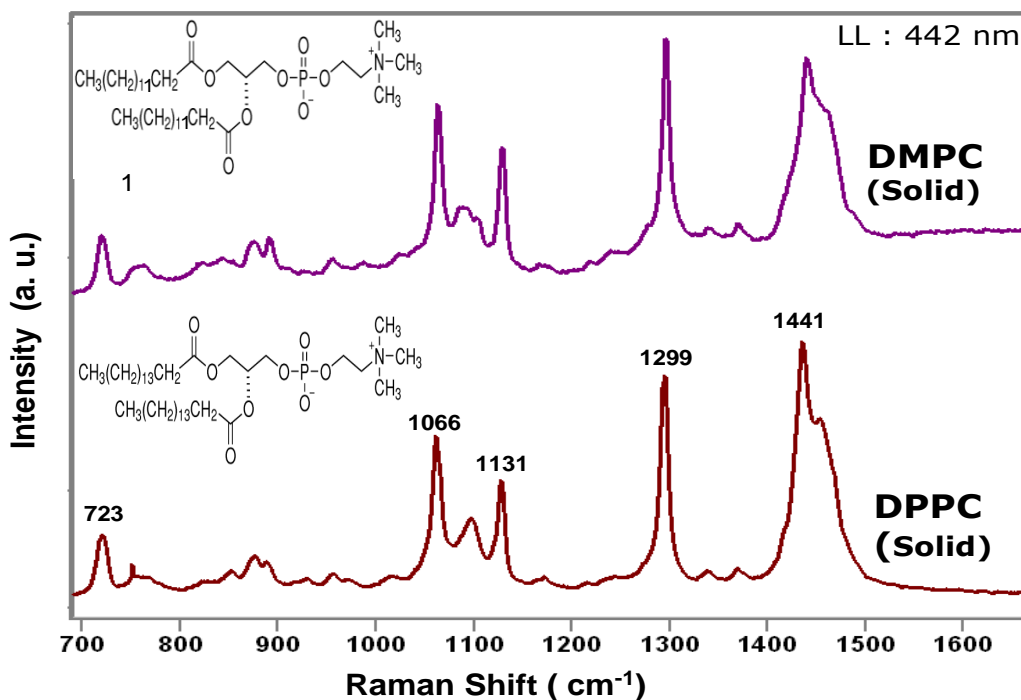


Figure 4.5: Raman scattering of phospholipids solid-DMPC and DPPC.

Both phospholipids produced similar spectrum, since their chemical structures are identical except two more alkyl groups in the chain of DPPC. The effect of alkyl chains will be shown in the following section in Figure 4.6 in their extended Raman spectrum. The Raman scattering cross section for the vibrational modes in the spontaneous inelastic Raman scattering of the phospholipids is low (likely $\sim 10^{-29}$ cm² per molecule), i.e., the absolute intensity is low. DPPC has two more alkyl groups [CH₃(CH₂)₁₃CH₂-] than that of DMPC [CH₃(CH₂)₁₁CH₂-], and the Raman spectrum is completely dominated by the methylene vibrational modes, and this is also valid for DMPC (See Figure 4.6.a). The relative intensity of the C-H stretching modes (28 CH₂) is the highest, as can be seen in Figure 4.6.b, and

the spectrum is quite simple for such a large molecular system, and in complete agreement with published DMPC and DPPC Raman obtained at 647.1 nm excitation.^{17,23} The characteristic anti-symmetric stretch methylene vibration is seen at 2888 cm^{-1} , and symmetric stretch at 2848 cm^{-1} . Correspondingly, the CH_2 scissoring modes are seen at 1462 and 1441 cm^{-1} with high relative intensity. The other three bands of large relative intensity at: 1299 , 1131 , and 1066 cm^{-1} can be assigned to the CH_2 twisting mode and two C-C stretching modes of the methylene groups. Specific studies directed to the identification of the choline moiety in phospholipids have identified the C-N symmetric stretching of the quaternary ammonium group at 720 cm^{-1} .²⁴ This characteristic vibration is seen at 723 cm^{-1} in DPPC and 720 cm^{-1} in DMPC. The Raman spectra of DMPC and DPPC bilayers obtained using total internal reflection is also in agreement with the spectra presented in Figure 4.6.²⁵

4.4.4 Surface-enhanced Raman scattering of DMPC and DPPC

The surface-enhancement Raman scattering (SERS) experiment was carried out by transferring a monomolecular thick LB-monolayer of DPPC and DMPC film onto SIF as a monolayer, bilayers or trilayers. It should be pointed out that using micro-Raman and the typical objective of 50x, the illuminated area is about 1 micron squared for the 514.5 nm laser line or $2\text{ }\mu\text{m}^2$ for the 632.8 nm laser line, and the number of DPPC or DMPC molecules are of the order of 2.5×10^6 or 5×10^6 molecules, respectively, in the probed surface area, i.e., about 4 to 8 attomole of the phospholipid, when monolayer film is used in SERS experiment.

The first set of experiments was performed in LB-SERS on SIF for monolayer and bilayers of both DMPC and DPPC. Using SIF and very low laser power (microwatts of the 514.5 nm laser line) SERS spectra are observed; though, the stability and reproducibility of these results is not satisfactory due to photoinduced changes at the silver surface. However, when a bilayer of DPPC is transferred to a SIF, reproducible SERS spectra are obtained as can be seen in Figure 6. b. Similar results are obtained for DMPC illustrated in Figure 6.a. Since the electromagnetic enhancement extends to at least 100 Å above the metal surface, the second layer also contributes to the enhancement and helps to obtain reproducible SERS spectra. The best results were obtained with the 632.8 nm laser line. The 514.5 nm laser line causes significant degradation of the sample, even very low energy densities.

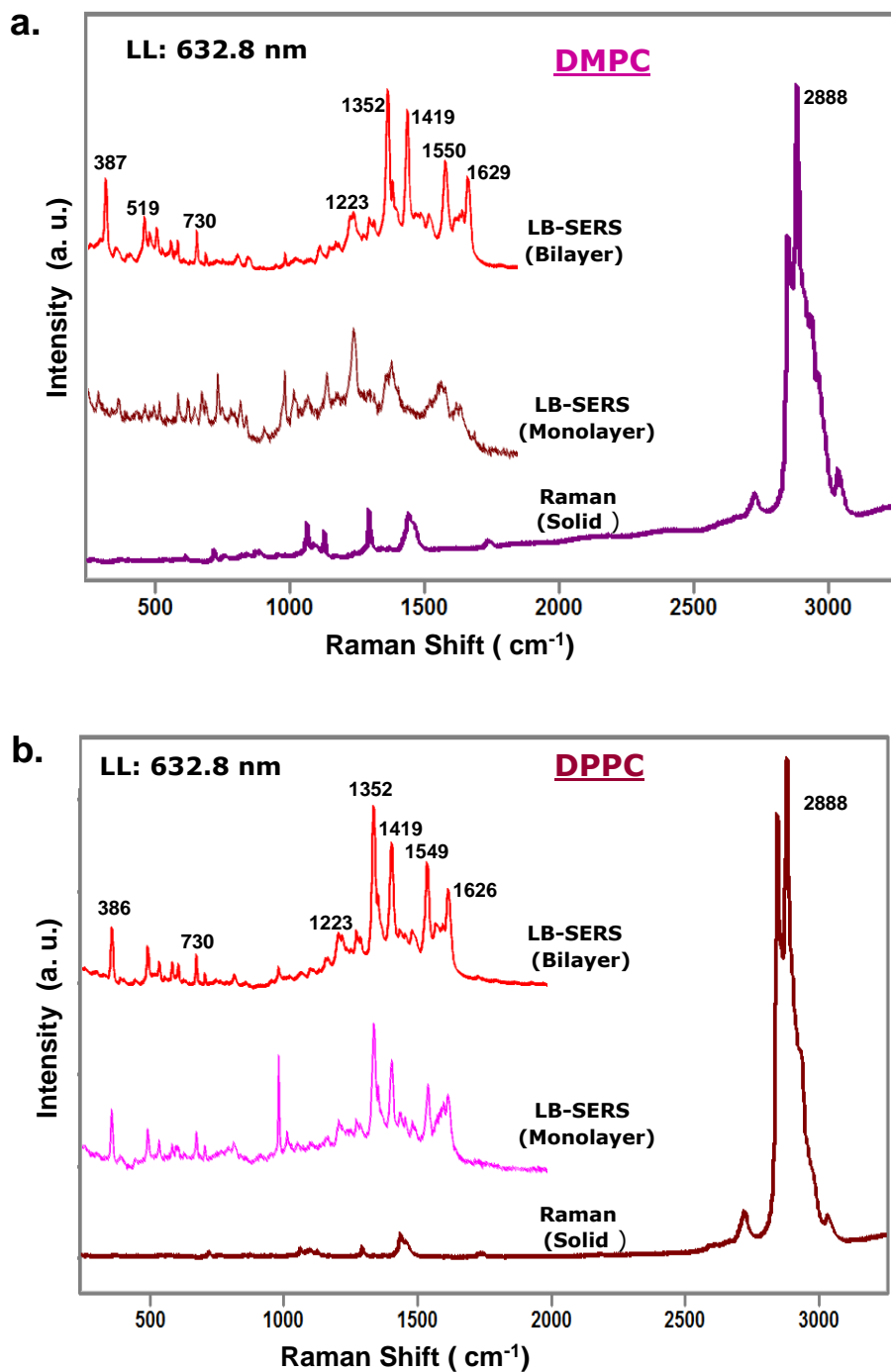


Figure 4.6 LB-SERS of mololayer and bilayers and Raman of solid, a) DMPC and b) DPPC.

4.4.4.1 SERS effects in LB multilayers

The SERS spectrums for LB monolayer, bilayers and trilayers of DPPC are shown in Figure 4.7.a. The Raman spectrum of LB monolayer on uncovered

glass is also presented in the same Figure, which shows no band at all due the poor Raman scattering cross-section of the DPPC. In order to further confirm the results, a DPPC sample with three monolayers was fabricated (trilayer) onto SIF.

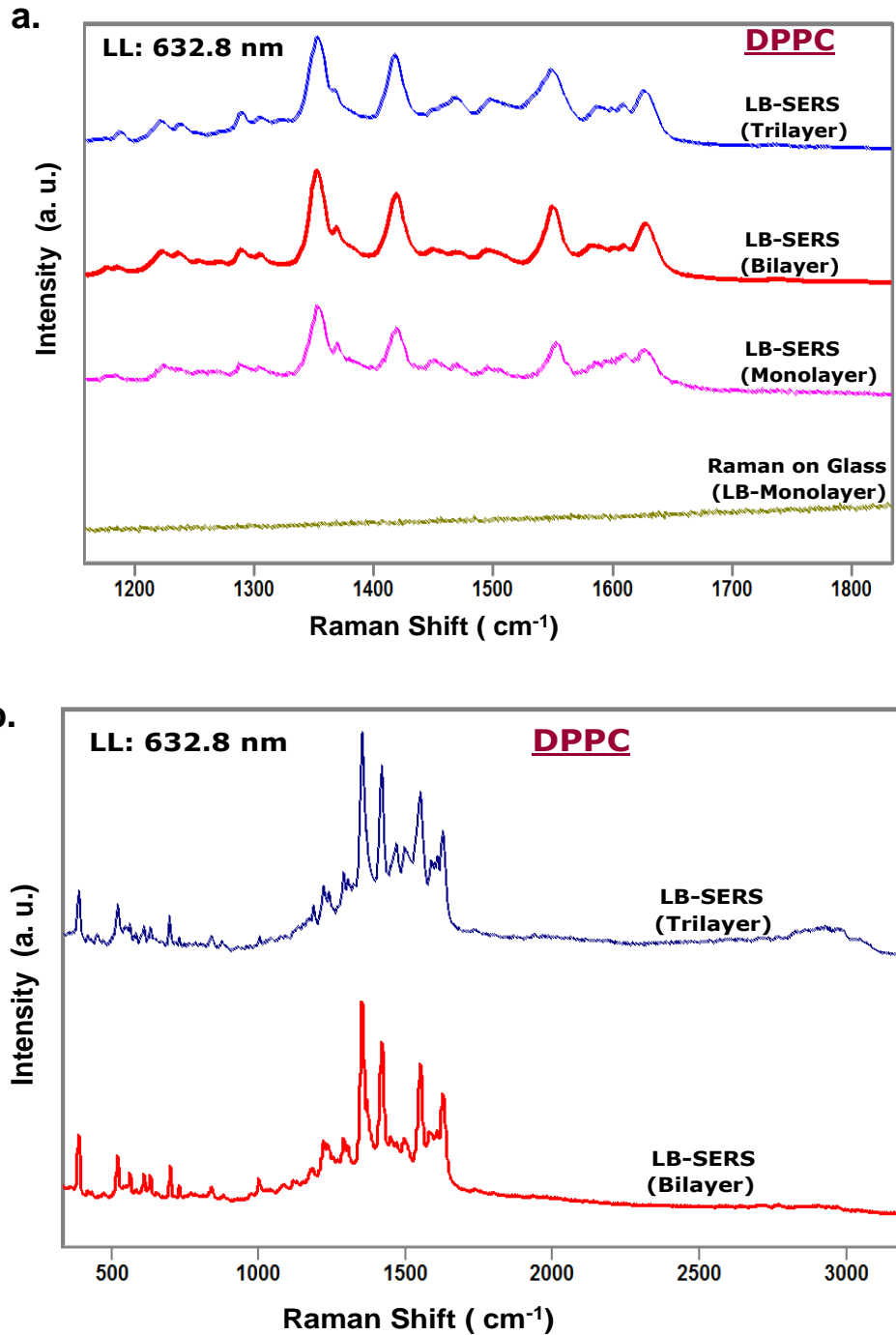


Figure 4.7: Illustration of DPPC spectra, a) comparison of adding monolayers on SIF and glass and b) raw spectrums of bilayers and trilayers on SIF.

The raw SERS spectra of the bilayer and the trilayer are presented in Figure 4.7.b. The spectral range includes the C-H stretching modes to illustrate their low relative intensity. It should be pointed out that the EM enhancement achieved with the bilayer does not increase any further in the trilayer sample. The Raman scattering for DPPC and DMPC is the characteristic spectrum of a polymethylene (see Figures 4.6). Correspondingly, the SERS spectra are the same for both DPPC and DMPC.

Table 4.1: Characteristic vibrational Raman modes of DPPC and DMPC. Solids and LB-SERS data.

Solid (cm ⁻¹)		LB SERS (cm ⁻¹)		Literature	Assignment
DPPC	DMPC	DPPC	DMPC		
		1626	1629		-COO-C stretching
		1549	1550		-COO-C stretching
1462	1466			1468 ²⁶	CH ₂ scissor
1441	1441	1419	1419	1440 ²⁶	CH ₂ scissor
1374	1369	1352	1352		CH ₃ deformation
1299	1295	1289	1289	1295 ²⁶	CH ₂ twist
		1223	1223		C-O stretch
1131	1128			1131 ²⁶	C-C stretch
1066	1063			1061 ²⁶	C-C stretch
723	720	730	730	720 ²⁷	C-N sym. stretch (choline)
		631	631		C=O bending
		609	609	598 ²⁹	PO ₄ deformation
		561	563		PO ₄ deformation
		518	519	537 ³⁰ 514 ²⁹	PO ₂ rock
374		386	387	389 ³⁰	P-OH deformation

In addition, the relative intensity of the C-H stretching is very low, a result that supports the idea that the alkyl chain is away from the surface. The characteristic SERS spectra contain molecular wavenumbers from the groups close to the surface; the phosphate (386 cm^{-1}), the quaternary ammonium moiety (1352 cm^{-1}) and the carboxylate (1626 cm^{-1}). A summary of the characteristic wavenumbers found in the SERS spectra and the corresponding assignment is given in Table 4.1, where the characteristic wavenumbers are in bold type.

4.4.4.2 Bilayer LB-SERS reproducibility by mapping

A key problem for the analytical application of SERS, and especially for the characterization of biological samples, is to attain reproducible signals. To demonstrate the high degree of reproducibility, repeat SERS spectra were collected from different spots of the biofilm. The best proof of reproducibility is the point-by-point SERS mapping. Spectral maps for the bilayer sample of both DPPC and DMPC were recorded with the 632.8 nm laser line for a surface area of 80 by 80 micrometers with a step of 2 micrometers. The point-by-point mapping is a set of static measurements that include a small spectral window; the window is shown in Figures 4.8. The light coloration in these figures indicates higher counts on the detector for the vibrational modes selected for the mapping. The information provided by the maps indicates that the same vibrational bands (reproducible spectrum) are detected, with different absolute intensity for different regions of the SIF coated with the phospholipid bilayer. The results for DPPC and DMPC shown in Figures 4.8 confirm that the fingerprint SERS spectrum is observed everywhere, with variations reflecting the distribution

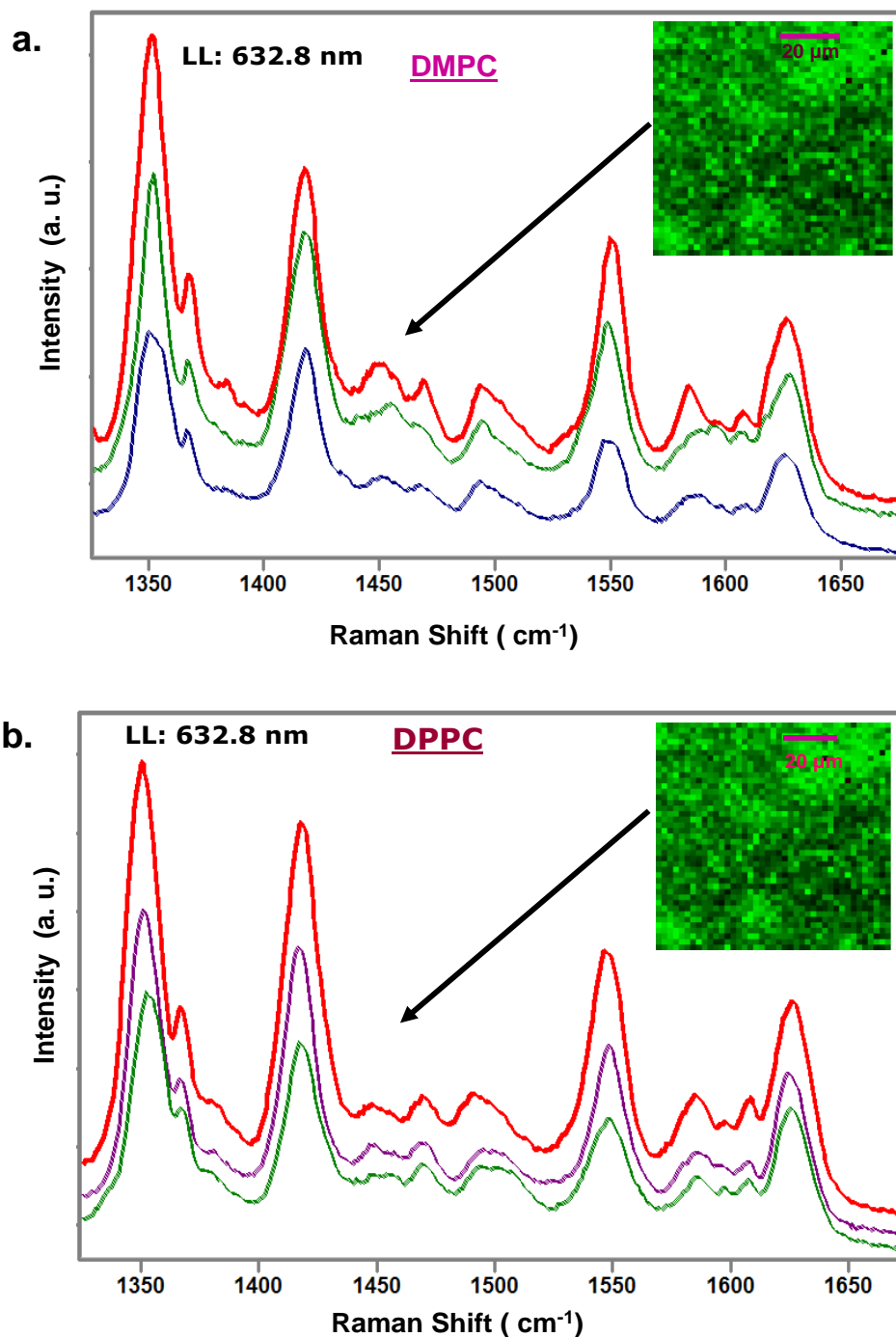


Figure 4.8 LB-SERS point-by-point mapping a) DMPC and b) DPPC.

of the average enhancement factor on the surface of the silver nanostructures. The reference spectrum for the maps is the main spectral window from the extended SERS spectrum of the bilayer shown in Figures 4.7.b. The working

assumption is that these wavenumbers are characteristic of the SERS spectra, and indeed they are observed everywhere on the surface of the silver island film coated with a phospholipid bilayer (or trilayer).

4.4.5 SERS of Phospholipid in Gold film compare to Silver film

For the purpose of comparison for SERS in gold island film, a LB monolayer of DPPC was fabricated on gold coated silver island film. The mixed island film was prepared by first depositing 6 nm mass thickness silver on glass at 100^o C and a vacuum pressure of $\sim 10^{-6}$ Torr, and then a gold film of 4 nm mass thickness was deposited on top of that silver island film at 150^o C with a same vacuum pressure. The SERS spectrums of DPPC in LB monolayer on SIF as described in section 4.3.4 and that of on this gold film are shown in Figure 4.9.

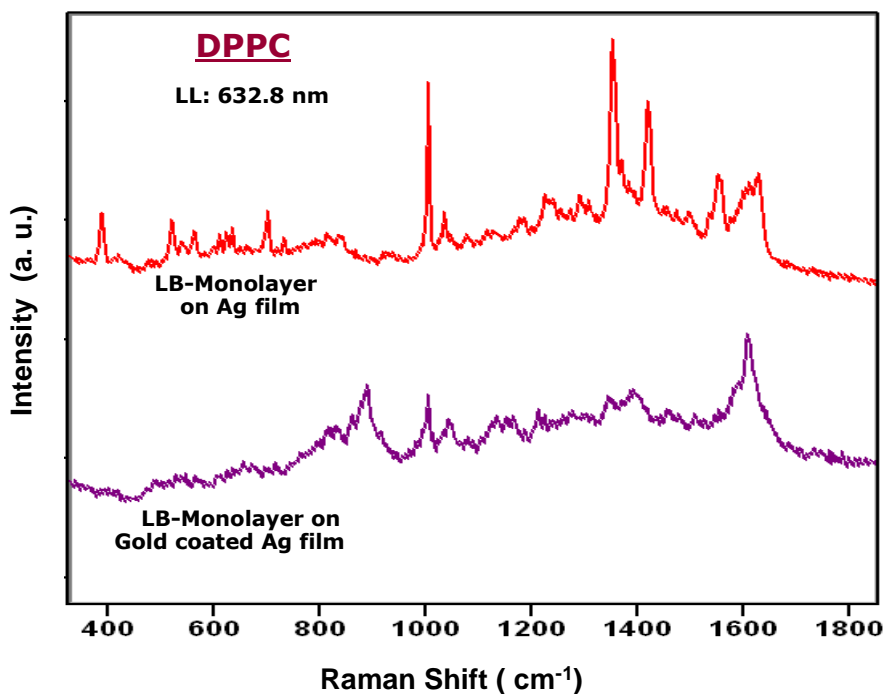


Figure 4.9 LB-SERS DPPC monolayer in silver and gold

This is evident that the SERS effect on gold is lower compared to that on silver. Since the scattering cross-section of the phospholipid is very small and the enhancement factor of gold is smaller than that of silver, we cannot claim that SERS of DPPC on gold has been successful.

4.5 Conclusions

Using a LB technique, two monolayers of DMPC or DPPC were transferred from air-water interface onto the SIF. This approach allowed forming the bilayer at the controlled surface pressure, providing a well-defined thin solid film. Reproducible SERS spectra of Langmuir–Blodgett of DPPC and DMPC phospholipid bilayers, that transferred to silver nanostructures evaporated onto glass substrates (SIF), have been obtained for the 632.8 nm laser line excitation. The reproducibility is demonstrated using point-by-point mapping proving that characteristic SERS wavenumbers are detected on large surface area (80 by 80 micrometers) of the bilayers on Ag. The detection of the LB-SERS with the Raman microscopy is of attomole quantities. SERS of a single monolayer on SIF is also observed; but the variation in the SERS spectra from point to point indicates that the dynamic at the surface (photodegradation) hinders SERS reproducibility. The addition of third layer (trilayer) does not contribute to the enhancement, and the results simply confirm the bilayer SERS.

References

- (1) Petty, M. C. *Langmuir-Blodgett Films: An Introduction*; Cambridge University Press: Cambridge, **1996**.
- (2) Nielsen, L. K.; Bjornholm, T.; Mouritsen, O. G. *Langmuir* **2007**, *23*, 11684-11692.
- (3) Kamilya, T.; Pal, P.; Talapatra, G. B. *Journal of Physical Chemistry B* **2007**, *111*, 1199-1205.
- (4) Leporatti, S.; Bringezu, F.; Brezesinski, G.; Mohwald, H. *Langmuir* **1998**, *14*, 7503-7510.
- (5) Solletti, J. M.; Botreau, M.; Sommer, F.; Brunat, W. L.; Kasas, S.; Duc, T. M.; Celio, M. R. *Langmuir* **1996**, *12*, 5379-5386.
- (6) Zawisza, I.; Bin, X. M.; Lipkowski, J. *Langmuir* **2007**, *23*, 5180-5194.
- (7) Aoki, P. H. B.; Alessio, P.; Rodríguez-Méndez, M. L.; De Saja Saez, J. A.; Constantino, C. J. L. *Langmuir* **2009**, *25*, 13062-13070.
- (8) Fox, C. B.; Uibel, R. H.; Harris, J. M. *Journal of Physical Chemistry B* **2007**, *111*, 11428-11436.
- (9) Heywang, C.; Saint-Pierre-Chazalet, M.; Masson, M.; Bolard, J. *Langmuir* **1997**, *13*, 5634-5643.
- (10) Meuse, C. W.; Niaura, G.; Lewis, M. L.; Plant, A. L. *Langmuir* **1998**, *14*, 1604-1611.
- (11) Millone, M. A. D.; Vela, M. E.; Salvarezza, R. C.; Creczynski-Pasa, T. B.; Tognalli, N. G.; Fainstein, A. *Chemphyschem* **2009**, *10*, 1927-1933.

- (12) Le Ru, E. C.; Blackie, E.; Meyer, M.; Etchegoin, P. G. *The Journal of Physical Chemistry C* **2007**, *111*, 13794-13803.
- (13) Graham, D.; Faulds, K. *Chem. Soc. Rev.* **2008**, *37*, 1042-1051.
- (14) Pieczonka, N. P. W.; Aroca, R. F. *Chemphyschem* **2005**, *6*, 2473-2484.
- (15) Nobre, T. M.; de Sousa e Silva, H.; Furriel, R. P. M.; Leone, F. A.; Miranda, P. B.; Zaniquelli, M. E. D. *The Journal of Physical Chemistry B* **2009**, *113*, 7491-7497.
- (16) Caseli, L.; Crespilho, F. N.; Nobre, T. M.; Zaniquelli, M. E. D.; Zucolotto, V.; Oliveira, O. N. *Journal of Colloid and Interface Science* **2008**, *319*, 100-108.
- (17) Fox, C. B.; Horton, R. A.; Harris, J. M. *Analytical Chemistry* **2006**, *78*, 4918-4924.
- (18) Bernard, S.; Felidj, N.; Truong, S.; Peretti, P.; Levi, G.; Aubard, J. *Biopolymers* **2002**, *67*, 314-318.
- (19) Pieczonka, N. P. W.; Moula, G.; Aroca, R. F. *Langmuir* **2009**, *25*, 11261-11264.
- (20) Dai, S. X.; Zhang, X. T.; Du, Z. L.; Huang, Y. B.; Dang, H. X. *Colloids and Surfaces B-Biointerfaces* **2005**, *42*, 21-28.
- (21) Ivleva, N. P.; Wagner, M.; Horn, H.; Niessner, R.; Haisch, C. *Analytical Chemistry* **2008**, *80*, 8538-8544.
- (22) Wang, L.; Cruz, A.; Flach, C. R.; Pérez-Gil, J.; Mendelsohn, R. *Langmuir* **2007**, *23*, 4950-4958.
- (23) Fox, C. B.; Myers, G. A.; Harris, J. M. *Applied Spectroscopy* **2007**, *61*, 465-469.
- (24) Akutsu, H. *Biochemistry* **1981**, *20*, 7359-7366.
- (25) Lee, C. S.; Bain, C. D. *Biochimica Et Biophysica Acta-Biomembranes* **2005**, *1711*, 59-71.

CHAPTER 5

SINGLE MOLECULE DETECTION OF DYE TAGED PHOSPHOLIPIDS IN LANGMUIR BLODGETT MONOLAYERS ON SILVER ISLAND FILM

5.1 Single Molecule Detection – Background

Since the early 1990s, the optical spectrum of a single molecule has been detected and single-molecule spectroscopy has swiftly grown into an important research field. Single-molecule detection (SMD) represents the ultimate goal in analytical chemistry and is of great scientific interest in several fields.¹⁻² In particular, activity monitoring by SMD in fixed and living cells has become the most fascinating topic within a wide variety of research activities.³ Many of the initial applications of SMD have been in the area of extremely sensitive imaging and analytical detection. The more intriguing aspects of SMD stretch out into the investigation of dynamics and spectroscopy of single molecule and interactions with their molecular environments, by monitoring of the chemical and structural changes of individual molecules.³⁻⁴ These investigations at the single molecule level have the potential of offering important perspectives and provide fundamental information of intercellular processes. The advantage of single-molecule measurement is to provide information free from ensemble averaging. It allows the examination of individual molecules in a complicated system so that the differences in structure or functionality of each molecule can be identified and related to its specific molecular environment. The distribution of a given molecular property among the members of the system, rather than the statistical ensemble-averaged property, can be revealed. Ultimately, the SMD has the potential of providing spatial and temporal distribution information, which enable in vivo monitoring of dynamic movements of single molecules like in intercellular space and the observation of their behaviour over an extended period of time.

Single-molecule detection allows extracting information on a molecule hidden deep within a condensed phase sample. This corresponds to detection at the crucial sensitivity level of $\sim 1.66 \times 10^{-24}$ moles of the molecule of interest (~ 1.66 yoctomole), or a quantity of moles equal to the inverse of Avogadro's number.⁵ Detection of the single molecule of interest may be done in the company of billions host molecules and in the presence of noise from the measurement itself. The standard ensemble measurements, which yield the average value of a parameter for a large number of (presumably identical) copies of the molecule of interest, permit the quantitative analysis using spectroscopic measurements. By contrast, SM completely removes the ensemble averaging, which allows construction of a frequency histogram of the actual distribution of values i.e., the probability distribution function for an experimental parameter and the distribution contains other information than the average value alone. A single molecule can be a local reporter of its "nano-environment," that is, of the exact constellation of functional groups, atoms, ions, electrostatic charges and/or other sources of local fields in its immediate vicinity.

SMD techniques have mostly involved fluorescence, and more recently, surface-enhanced (resonance) Raman scattering (SERS/SERRS). The former suffers from either a lack of molecular specificity, perturbation of the sample by intrusive labelling by fluorescent probes, or destructive processes such as cell fixation or lysing. SERS/SERRS is a novel and noninvasive method based on a vibrational spectroscopy that can directly probe the molecular scale structure of a live biological sample, enabling acquisition of data in the company of high

chemical specificity without perturbing the natural state of the sample. SERS offers high spatial resolution subcellular chemical analysis of an individual cell. It relies on the scattering of photons by molecules, which yields chemical information about the chemical structure and conformations in the sample. It has been an increase of its use for advanced research because it offers many attractive features. This method is able to probe living samples both in-vitro and in-vivo in a non-invasive and non-destructive manner in different environments, which can provide new insights into the biology of living cells without incorporating fixatives, markers or stains which may alter the cellular biology. In addition, using low energy density at the sample, or near infrared radiation, Raman can avoid photobleaching of the signal allowing for live cells to be probed for long time periods, when monitoring dynamic behaviour.⁶⁻⁷

5.2 Single molecule detection by SERS

The applications of surface-enhanced Raman scattering (discovered⁸⁻¹⁰ in 1974, and explained in 1977), have busted to become a major surface diagnostic and analytical technique. SERS is widely used as a high sensitive analytical tool for molecular detection and characterization. Single molecule surface-enhanced Raman scattering (SM-SERS) is growing side by side with single molecule fluorescence.¹¹⁻¹² The relevance of Raman scattering is obvious since it applies to fluorescent and non-fluorescent molecules, and provides the vibrational molecular fingerprints for spectral characterization. SM-SERS is expected to extend and complement fluorescence studies. Fluorescent measurements do not

provide detailed molecular information and photobleaching often limits the number of photons obtainable from a single molecule. These limitations could be overcome by Raman scattering, and allow the detection, identification and dynamic studies of single molecule, which provide highly resolved vibrational information and avoid rapid photobleaching.

Normal Raman scattering is an extremely weak process, with molecular cross-sections in the range 10^{-29} cm² per molecule (for comparison, a good fluorescence cross-section is 10^{-17} cm² per molecule). The scattering cross-section of ordinary Raman scattering is much smaller than that of fluorescence by a factor of 10^{-12} or more.² So to achieve single molecule detection sensitivity, the normal efficiency of Raman scattering must be enhanced by 10^{12} fold. The local field enhancement in SERS and SERRS may be observed with cross-sections on the order of 10^{-17} cm² enabling optical detection of single molecules. For target molecules showing no electronic transitions at the excitation wavelength, this requires SERS enhancement factors on the order of 10^{12} . For a strong resonance-Raman contribution of the target molecule in SERRS, the requirements for the local field enhancement for single-molecule Raman detection could be reduced to 10^7 . For example, “normal” resonance-Raman scattering can be observed with RRS cross-sections to a level of about 10^{-24} cm² per molecule. So, two cases can be explored in single molecule detection. One exploits a favourable superposition of local field enhancement and resonance Raman enhancement of the analyte molecule. The latter can be attained using excitation wavelengths within the molecular absorption band of the analyte and

also in resonance with the plasmon absorption. The second one is based solely on the enhancement factor provided by the local field at the nanostructure. Particularly giant enhancements are observed for dye molecules that shows a strong absorption in the visible spectrum. In this respect, high levels of enhancement are always related to specific morphologies of nanostructures. Almost all reports on single molecule Raman scattering rely on clusters or aggregates formed by individual silver or gold nanoparticles.¹³⁻¹⁴

5.2.1 Enhancement factor in metal island films

There is an increasing number of reports for single molecule detection using SERS/SERRS.^{11,13,15} Experimentally, it is found that the largest signals in single molecule SERS/SERRS comes from junctions between nanoparticles formed by aggregation. On a solid surface like silver island films which are used in this research work, it is known that not all sections of the film are equivalent in activity of the local field enhancement. The locations of highest local field enhancement are dubbed “Hot Spots”, and they create the maximum intensity of the detected Raman signal. Most of the reports of SM-SERS detection have involved the use of metal colloids in suspensions. Typically quoted values of the SERS enhancement factor i.e., the ratio between a measured Raman cross section in the presence and in the absence of a metal nanostructured surface, range between 10^3 and 10^6 in the case of silver colloid.¹⁵⁻¹⁶ However, recent single-molecule SERS experiments on Ag and Au colloids have indicated that a much larger enhancement factor, 10 orders of magnitude or more are obtained, to compensate for the intrinsically small Raman cross section.^{11,13,17-18} The

immobilized nanoparticles of metal island films of Ag or Au are also sustained hot spots to make accessible single molecule detection.¹⁹⁻²⁰ The critical factor in these milestone studies has been the development of exceptional SERS substrates. The highest priority need for SMD is controlled fabrication of reproducible nanostructures with a known quantity of spatial locations of high electric field enhancement or “hot spots”.

In this research work, vacuum evaporated silver island films (SIFs) were used as SERS active substrate for the single molecule detection. A 3D AFM image of a SIF with arbitrary variations of enhancement factor on its surface is illustrated in Figure 5.1.

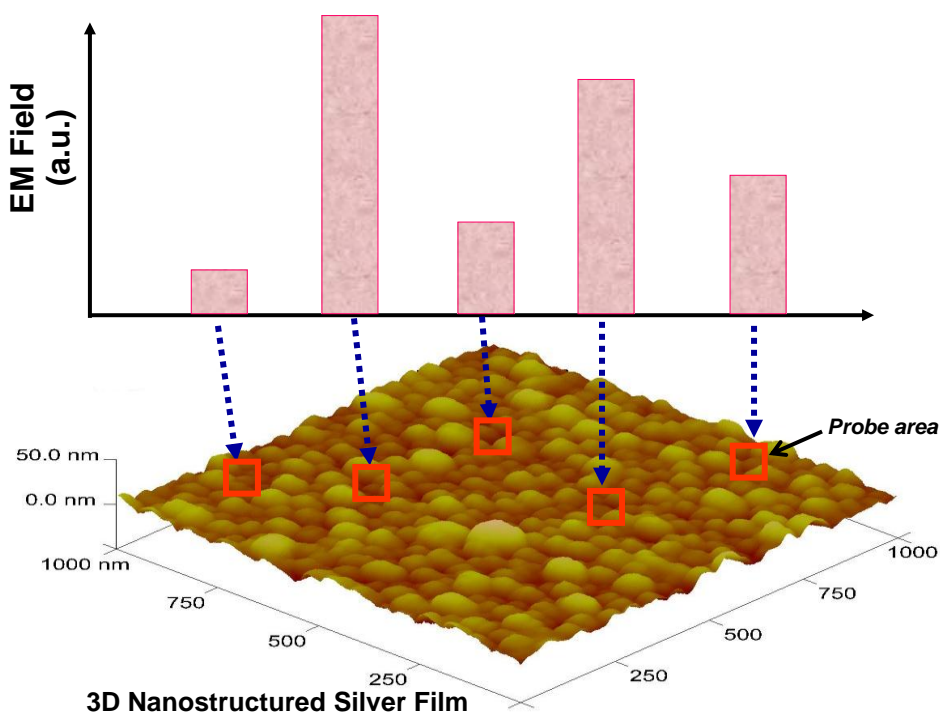


Figure 5.1: Illustration for EM Field variation on a SIF surface

From the AFM shown in this Figure, it can be seen that shape, sizes and

aggregations of the nanoparticles all over the surface are inhomogeneous. From the results of this work we can anticipate that SIF contains hot spots in several spatial locations, where, most likely, the stronger enhancement comes from hot spots as those found in colloidal aggregates or nanocrystal junctions or edges.²¹⁻

²² A cartoon showing the degree of enhancement needed for SM detection is presented in Figure 5.2. Clearly, the requirements of local field enhancement are also strongly dependent on the intrinsic Raman scattering cross section of the target molecule.

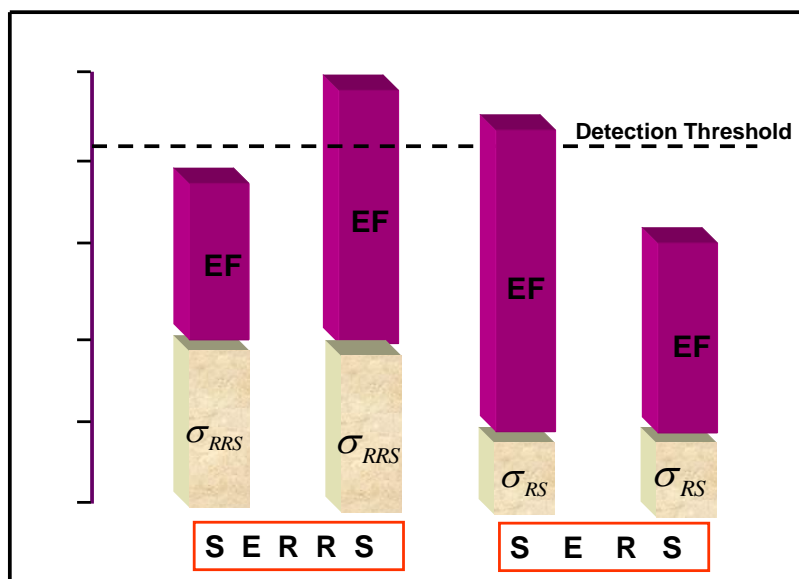


Figure 5.2: A graphical representation of interplay between the intrinsic Raman cross section of a molecule and the required enhancement factor needed for SMD

The EF required to reach the detection threshold of SM varies for two different situations: SERS and SERRS. The latter explain the fact that the majority of the reported SM-SERS is under resonance Raman condition, i.e. it is SM-SERRS. The difference in cross section that can be experienced under resonance conditions can be $\sim 10^6$ times greater than under non-resonance

excitation. Even in SM-SERRS, a relatively large enhancement factor is still required and the evidence to date suggests this only attained from a small number of nanostructures.²³⁻²⁴ Notably, the importance of the intrinsic Raman cross section is exemplified by the fact that SM detection has only been achieved with a small set of molecules. All the reported systems are “soft”, highly polarizable molecules that have relatively large intrinsic Raman cross sections.

The validation of SM-SERS (SERRS) led to a consensus on the idea of hot spots, a point of convergence in the theory of SM-SERS or SM-SERRS: a spatial location in Ag or Au nanostructure aggregates, where the enhancement factor can exceed the SM detection threshold limit. As there is now common belief that hot spots are found in the junctions of aggregated nanostructures such as silver and gold, the rare event of molecule-hot spot coupling in sections of the metals island films represent the probability of single molecule detection. A cartoon is shown in Figure 5.3 illustrating the molecules may adsorb at nanostructure junction, presumably a hot spot, and also on the surface of the nanoparticles.

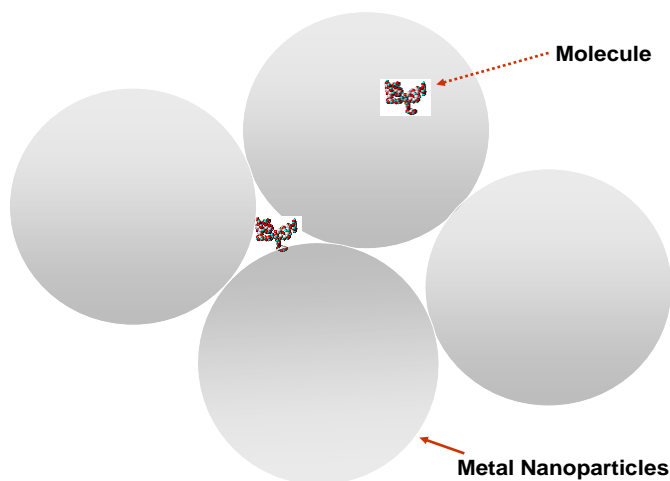


Figure 5.3: Illustration of location for a molecule adsorbed metal nanostructured surface

Unfortunately, the spatial distribution of the hot spots can not be controlled in a metal island film. The single molecule detection is found by mapping the metal island film surface and the chances of finding SMD signals are attributed to the rare spatial coincidence of target analyte molecule and localized electromagnetic- hot spots in the nanostructured metal film.

5.2.2 Raman instrumentation and SMD

In this work, the Renishaw inVia micro-Raman system has been used for acquisition of Raman spectra. This inVia Raman microscope is shown in chapter 2. The inVia Raman microscope combines simplicity of operation with high sensitivity, flexibility and enabling high resolution confocal measurements. The coupling of spectrometer to the microscope provides the ability to achieve high spatial resolution of the probed sample. In particular, micro-Raman has been specially instrumental in the development and realization of SERS experiments and been essential in the application of SERS in detection of single molecule.²⁵⁻²⁶ The microscope supports multiple laser lines, with automatic software switching of excitation wavelength. Three excitation laser lines have been used in this system, which are demonstrated in Table 5.1.

Table 5.1 : Excitation Lasers

Laser Type	Wavelength (nm)	Output Power (mW)
Tunable Ar ⁺ (Lexar)	488, 514	20
HeNe	632.8	18
Solid State Diode	785	19

The available attenuation of the laser power begins with 50%, 10%, 5%, 1% with a value down to 0.00001% of the original power. The selection of laser line and attenuation are predetermined by the requirements of a specific experiment.

The resolution of a spectrograph is its ability to separate adjacent peaks, which is affected by many factors including grating diffraction order, grating diffraction angle (include angle – the angle between incident and diffracted light), spectrometer slit width, detector pixel size, system magnification and focal length. The diffraction grating is an optical component used to spatially separate polychromatic light (white light) into its constituent optical frequencies. A precision diffraction grating stage used in Renishaw's system is shown in Figure 5.4.

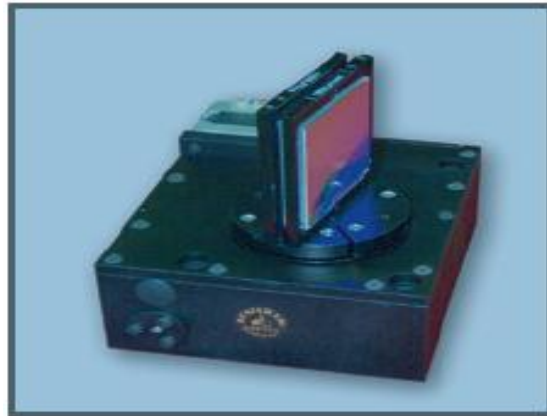


Figure 5.4: Renishaw's precision diffraction grating stage

The scattered light is focussed through a set of slits set to 50 μm for all measurements and then focussed onto a dispersive grating. The gratings used here depending on the excitation laser line and they are summarized in Table 5.2.

Table 5.2: Spectral Resolution for Grating-Laser combinations

Laser Line, nm	Grating, grooves/mm	Resolution, cm^{-1} (50 μm slit)
488	1800	2
514	1800	3
633	1800	2
785	1200	3

The main attribute of concern is the groove density that resolves the effective spectral resolution. The approximate resolution for each laser/grating (based on the measurement of the isotopic splitting in CCl_4) is given in Table 5.2. Spectra of CCl_4 taken with standard and high resolution inVia Raman microscopes are shown in Figure 5.5. Renishaw's precision diffraction grating stage enables to switch rapidly and easily between gratings to tailor spectral range and resolution to match particular analytical requirements. Frequency accuracy is monitored in these investigations, using is 520 cm^{-1} band of silicon as an external standard material.

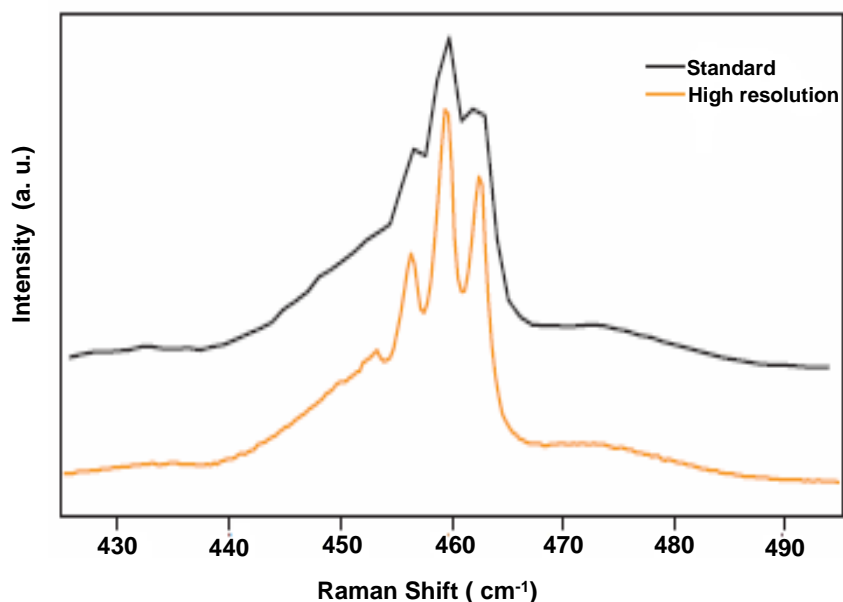


Figure 5.5: Spectra of CCl₄ taken with standard and high resolution inVia Raman microscopes (spectra offset for clarity)

The CCD (Charge Coupled Device) detector used in this instrument consists of an array with 578x385 pixels, and each pixel having dimension of 22 μm x 22 μm . This detector is highly sensitive and provides low electronic background, which is very important for SM experiments as the measured S/N ration have relatively low value.

Vital components in a Raman system are light delivery and collection optics. This is employed by coupling of the spectrometer to a microscope. In micro-Raman system, the 180⁰ backscattering geometry is used and the objective is a key component as it defines both excitation and probe areas.

Table 5.3: List of Objectives and Spot Sizes

Objective	NA	Spot Size, μm^2
5X	0.12	50
20X	0.40	20
50X	0.75	1
100X	0.90	< 1

The objectives are characterized by their Numerical Aperture (NA) value and magnification. Ultimately, they determine the spot size of the exciting laser. The spot sizes for the objectives in the inVia micro-Raman system are listed in Table 5.3. The spot size parameter is a fundamental requirement for SM-SERS studies as the experimental procedure is based on this spatial resolution. The 50x objective has been used in this SM-SER(R)S experimental set-up. An image for spot size acquired by the inVia-Raman system using 50X objective is shown in Figure 5.6.

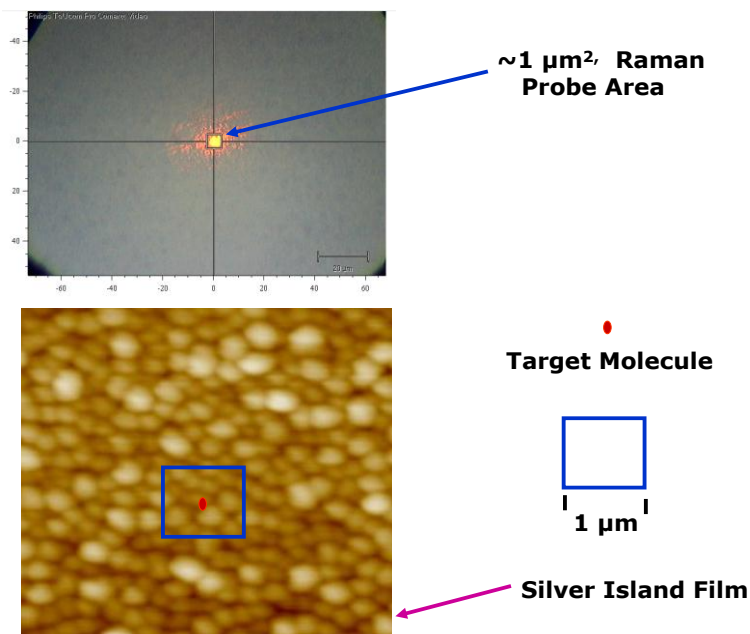


Figure 5.6: Illustration of SM-SER(R)S experiment

In a SM experiment, the Raman probe area is restricted to $1 \mu\text{m}^2$ of the surface covered with a monolayer of one molecule thick film on a SERS active substrate (silver island film in this case).

5.2.3 Langmuir-Blodgett approach to SM-SERRS

The SM detection by SERS/SERRS has been reported using Ag or Au aggregated colloidal nanoparticles that support for LSPR.^{6,27} This approach is based on the ability to dilute the target molecule in a solution down to a level believed to be 1 molecule in the probe volume at the time of acquiring Raman spectra. The weaknesses of this approach are thermodynamically driven, the molecule and nanoparticles are in Brownian motion, and above all, there is no true control of concentration of the analyte.²⁸ The immobilization of the molecules to SERS substrate is the main motivation in this work, in controlling concentration

of molecules in scattering areas, probed by the Raman spectroscopy. Among several techniques of producing organized molecular assemblies, a Langmuir-Blodgett method is one of the most versatile techniques of making well-ordered ultrathin films, wherein molecules are expected to maintain a highly ordered arrangement of unimolecular thickness. This technique has been extensively used in Aroca's group and collaborators. In particular, LB-SERRS has been successfully applied for SM studies.^{20,28-31} There are several advantages when using the LB technique. The LB monolayer changes the Raman 3D probe volume to 2D probe area, in a mixed monolayer of target molecule within an "inert matrix", like fatty acid, could be used to ease control of concentration of target molecules in the probed area. The molecular architecture such as orientation and intermolecular distances are manageable with this technique. Inert matrix can be selected with very low Raman cross section compare to the target molecule. This is the case of arachidic acid used in this work. The apparent restriction of this approach is the limited number of molecules is used in the LB technique. This work will disclose the requirements on how LB-SERS is used to detect the spectrum of a single molecule.

5.3 LB-SERRS of dye tagged phospholipids for SMD

Phospholipid monolayers have traditionally been studied as models of biological membranes, since the lipid fraction of biological membranes is mainly composed of phospholipids. Langmuir-Blodgett (LB) films can be used to mimic a phospholipid monolayer and bilayers or trilayers consist of weakly coupled

monolayers and investigations could be performed on these LB films.³²⁻³³ In the field of chemical biology, molecular recognition has served as a basic concept to understand the construction of biological assemblies and the biological functions. These studies mainly based on the interactions between immobilized biomolecules and drugs or proteins that might be incorporated into artificial membranes. Interface properties such as diffusion, membrane interactions protein folding and DNA sequencing, are often investigated by single-molecule spectroscopy to track the behaviour of individual molecules through the attached chromophores.³⁴⁻³⁵ In this study, SM-SERRS is the spectroscopic technique, used to provide the ultra sensitivity that rivals to the SM-fluorescence.³⁶⁻³⁷ The access to the information rich vibrational Raman spectrum is the main thrust for SM-SERRS in contrast to SM-fluorescence. Single molecule detection in phospholipids using SER(R)S is not possible without attaching chromophore, given the fact that the Raman cross section of phospholipids is very small. SERRS benefits from two resonance enhancements: the resonance Raman scattering effect achieved by tuning the excitation frequency to the electronic absorption band of the chromophore with RRS cross sections as high as 10^{-25} $\text{cm}^2 / \text{molecule}$,³⁸ and the local field enhancement attained by the excitation of the surface plasmons of a metal nanostructure, given approximately and E^4 plasmon enhancement.²⁷

Two dye tagged phospholipids were used for the single molecule detection as target molecules (TM) in this research work, which are shown in Figure 5.7.

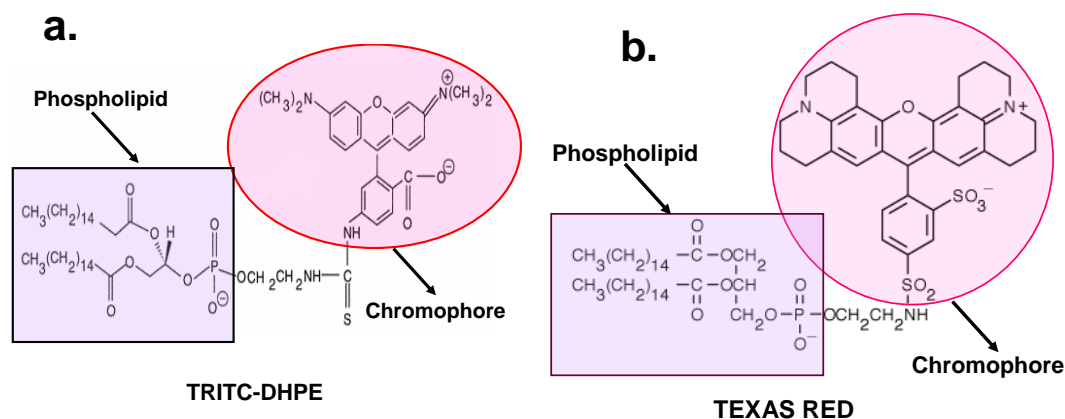


Figure 5.7: Molecular structures of Dye tagged Phospholipids, a) TRITC-DHPE and b) Texas Red

In this work, the chromophore (TRITC) is anchored to a phospholipid (Figure 5.7 a.) and chromophore (Texas red) is also anchored to another similar phospholipid (Figure 5.7 b.). Both are important model systems for membrane research. The phospholipid plays a dual role; being an amphiphilic, it can easily be incorporated into mixed Langmuir films, and its large size makes any chance of aggregation of the attached chromophore at SM level is negligible. The tagged phospholipids systems are: N-(6-tetramethylrhodaminethiocarbamoyl)-1,2-dihexadecanoyl-*sn*-glycero-3-phosphoethanolamine ($C_{62}H_{94}N_4O_{11}PS$) or TRITC-DHPE and 1,2-dihexadecanoyl-*sn*-glycero-3-phosphoethanolamine ($C_{68}H_{101}N_3O_{14}PS_2$) or TEXAS RED, are probes routinely used in SMF studies.^{35,39} The vibrational spectrum of TRITC-DHPE and TEXAS RED provide unique fingerprint.

5.4 Experimental

Arachidic acid (AA), chloroform, and ultra pure Ag shot (1-3 mm) were obtained from Aldrich; and N-(6-tetramethylrhodaminethiocarbamoyl)-1,2-dihexadecanoyl-sn-glycero-3-phosphoethanolamine (TRITC-DHPE) and 1,2-dihexadecanoyl-Sn-glycero-3-phosphoethanolamine (TEXAS RED) were obtained from Molecular Probes. All were used without further purification. All solutions were prepared using spectroscopic grade chloroform as the solvent. Silver nanostructured films of 9 nm mass thickness were vacuum evaporated onto corning glass microscope slides at a pressure of $\sim 10^{-6}$ Torr and keeping the temperature of the substrate at 100° C (maintained for 1 h after evaporation). Arachidic acid Langmuir monolayers doped TRITC or TEXAS RED at various concentrations were prepared at the air-water interface of a Lauda Langmuir film balance and deposited onto the Ag nanoparticle films (shown in Figure 5.8). For these depositions, spreading solutions of AA/TRITC-DHPE or AA/TEXAS RED at different mixing ratios, were prepared from stock solutions of AA and TRITC-DHPE or TEXAS RED so as to achieve 4×10^6 , 10^5 , 10^4 , 10^3 , 10^2 and 1 TRITC or TEXAS RED molecule(s) within the $1 \mu\text{m}^2$, an area corresponds to the scattering area being probed by the laser beam with our Raman experimental setup. The corresponding molar ratios of TRITC-DHPE and TEXAS RED to arachidic acid are mentioned in Table 5.4. The choice of Raman laser spot size, $1 \mu\text{m}^2$ determined by the 50x objective (NA=0.75) is used and maintained in this work. The ratio calculations are based on the area occupied by the arachidic acid.²⁵

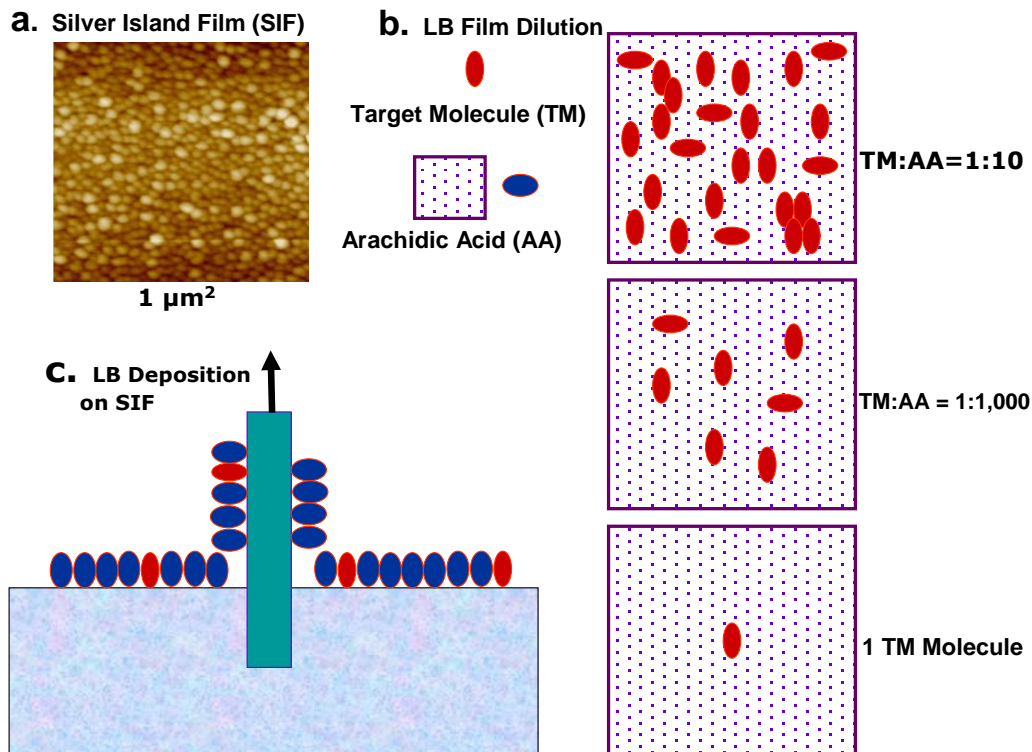


Figure 5.8: Experimental set-up for single molecule approach in LB_SERRS of TRITC-DHPE and TEXAS RED

Experimentally, the area per molecule of arachidic acid is 25 \AA^2 . So, 4×10^6 molecules are required to cover the surface of $1 \mu\text{m}^2$. Out of these molecules, only one molecule will contain the chromophore (marker or probe molecule), and the remaining will be made up by arachidic acid as inert matrix in case of single molecule detection. For the Lauda Langmuir Film Balance used in this work, the number of molecules to be spread on the water subphase is 8.64×10^{16} to start with a gas phase of the LB monolayer. To meet this requirement, it becomes necessary to spread a total of 2.16×10^{10} probe molecules and 8.6399×10^{16} arachidic acid molecules on the trough; and ultimately 1 probe molecule out of

total 4×10^6 molecules per $1 \mu\text{m}^2$ for SMD when the molecules are in a state of close packing. A convenient spreading volume used in this work was 1000 μL . The concentrations of both the probe molecules (TRITC and TEXAS RED) and arachidic acid in the spreading solution were calculated by the equation:

$$C = \frac{N_{\text{molecules}}}{N_A \cdot V_{\text{spreading}}} \quad (5.4.1)$$

The concentrations calculated for a “single molecule” spreading solution of volume 1000 μL from equation 5.4.1 are 3.59×10^{-11} M for probe molecule and 1.43×10^{-4} M for arachidic acid.

Table 5.4: Probe Molecule to AA “Ratios” with the approximate number of molecules in $1 \mu\text{m}^2$

Ratio	Approximate number of molecules in $1 \mu\text{m}^2$	
	Probe Molecule	AA
1 : 9	4,00,000	3,600,000
1 : 99	40,000	3,960,000
1 : 999	4,000	3,996,000
1 : 9,999	400	3,999,600
1 : 3,999,999	1	3,999,999

First, the corning 2049 glass slide coated with 9 nm silver island film, was immersed in the water subphase using a Lauda film lift FL-1 electronically controlled dipping device. The mixed “probe-arachidic acid” solution was then

spread (1000 μL) drop by drop on the water subphase of the LB trough using microsyringe. Pure water (18.2 $\text{M}\Omega\text{ cm}$) in the LB subphase, which contain small amounts of CdCl_2 ($2.5 \times 10^{-4}\text{ M}$) to aid the stability of the monolayer, was maintained at a constant temperature of 15° C . This was employed as the subphase preparation of the Langmuir monolayers. After spread the probe-arachidic acid mix solution, 20-25 minutes time was allowed for solvent evaporation and monolayer film was then begun compressed by the barrier moving at a speed 3.5 cm/min . The film compression was continued till the setting surface pressure 25 mN/m , which is correspondence to the condensed phase of the LB film. Film transfer was then carried out using Z deposition vertically upward on to silver island film (Figure 5.8) with a Lauda film lift FL-1 electronically controlled dipping device at a constant speed of 2 mm/min . All transfers were carried out by Z-deposition and transfer ratios were calculated to be near unity. This way the SERS/SERRS samples were prepared for Raman experiment.

All micro-Raman scattering experiments were conducted using a Renishaw InVia system, with laser excitation at 514.5 nm and 632.8 nm , and powers of 10-20 μW at the sample. The laser 514 nm is appropriate to take full advantage of increased scattering efficiency of resonance Raman scattering. In the single molecule experiments, the laser power was kept low to reduce the chances of photodegradation of the target molecule. All measurements were made in a backscattering geometry, using a 50x microscope objective with a numerical aperture value of 0.75, providing scattering areas of ca. 1 μm^2 . Single

point spectra were recorded with 4 cm^{-1} resolution and 10-second accumulation times over a range (3200 to 200 cm^{-1}) in the continuous mode of the Renishaw system, while 2D SERRS mapping results were collected through the rastering of a computer controlled 3-axis encoded (XYZ) motorized stage, with a step of $2\text{ }\mu\text{m}$ and 2 seconds accumulation time for recording at each spot. UV-visible absorption spectra were recorded for all solutions and 9 nm Ag nanoparticle films employing a Cary 50 scan UV-visible spectrophotometer. Atomic force microscopy (AFM) images were recorded using a Digital Instruments NanoScope IV, operating in tapping mode with an n+- silicon tip. All images were collected with high resolution (512 lines per scan) at a scan rate of 0.5 Hz. Topographical (height), error (amplitude), and phase images were used for analysis of the surface morphology of the films. The data were collected under ambient conditions, and each scan was duplicated to ensure that any features observed were reproducible.

5.5 Results and Discussion

5.5.1 Absorption and Fluorescence

The absorption spectra and fluorescence spectra of 10^{-5} TRITC solution and 10^{-5} TEXAS RED solution are shown in Figure 5.9.a and 5.9.b respectively. The spectra TRITC and TEXAS RED reveal absorption maxima resulting from the π - π^* electronic transitions of the rhodamine chromophore and sulforhodamine 101 acid chromophore.

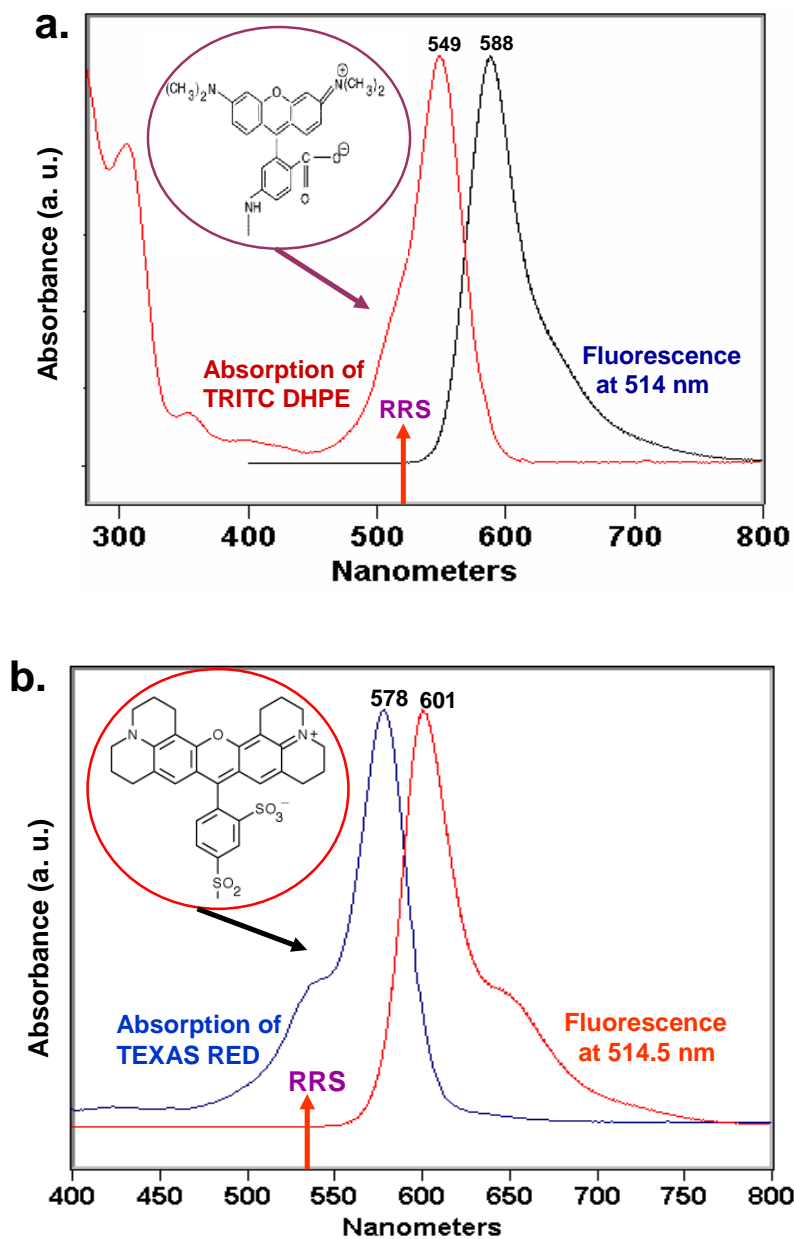


Figure 5.9: Solution Absorption and Fluorescence spectra
a) 10^{-5} M TRITC and b) 10^{-5} M TEXAS RED

The 0-0 transition of TRITC appears at 549 nm and emission peak at 588 nm. For TEXAS RED, the 0-0 transition appears at 578 nm and emission peak at 601 nm. The absorption spectra of both probe molecules reveal that the excitation for Raman spectrum by 514 nm laser line is in resonance with molecular absorption and this excitation is also resonant with the surface plasmon absorption (shown

in Figure 5.9) of the 9 nm mass thick Ag nanoparticle films, that effectively fulfilling the double resonance condition³⁹ of SERRS. The Ag nanoparticle films have a broad extinction spectrum, covering the entire visible range, with a maximum at 501 nm, indicating a relatively large distribution of particle geometries and particle-particle interactions. The morphology of these 9 nm mass thickness films was studied by employing atomic force microscopy (AFM), and a typical image is shown in Figure 5.8.a. The image reveals an inhomogeneous distribution of particles with sizes ranging between ~20 and 80 nm, which are in agreement with surface plasmon absorption results. The fluorescence spectrum of both TRITC and TEXAS solutions is the mirror image of their absorption spectrum indicating that they are stable at the excitation frequency, and photodecomposition is negligible.

5.5.2 LB-SERRS and reference spectra

The SERRS spectra were recorded on mixed LB monolayers with a 1:10 ratio of TRITC or TEXAS: Arachidic acid, deposited on silver island films. The corresponding RRS spectra were taken from the same LB monolayer coated on corning 2049 microscopic glass slide. To obtain the reference RRS spectra of the target molecules, a few drops of 10^{-5} M solutions were casted onto flat copper plate and remove the solvent by evaporation, and then solid films of the compounds were obtained. The resonance effect was attained with laser excitation of 514.5 nm, using 1 accumulation time of 10 s. The LB-SERRS, LB-RRS and reference solid-RRS spectra of TRITC are shown in Figure 5.10.a and the similar results of TEXAS RED are shown in Figure 5.10.b.

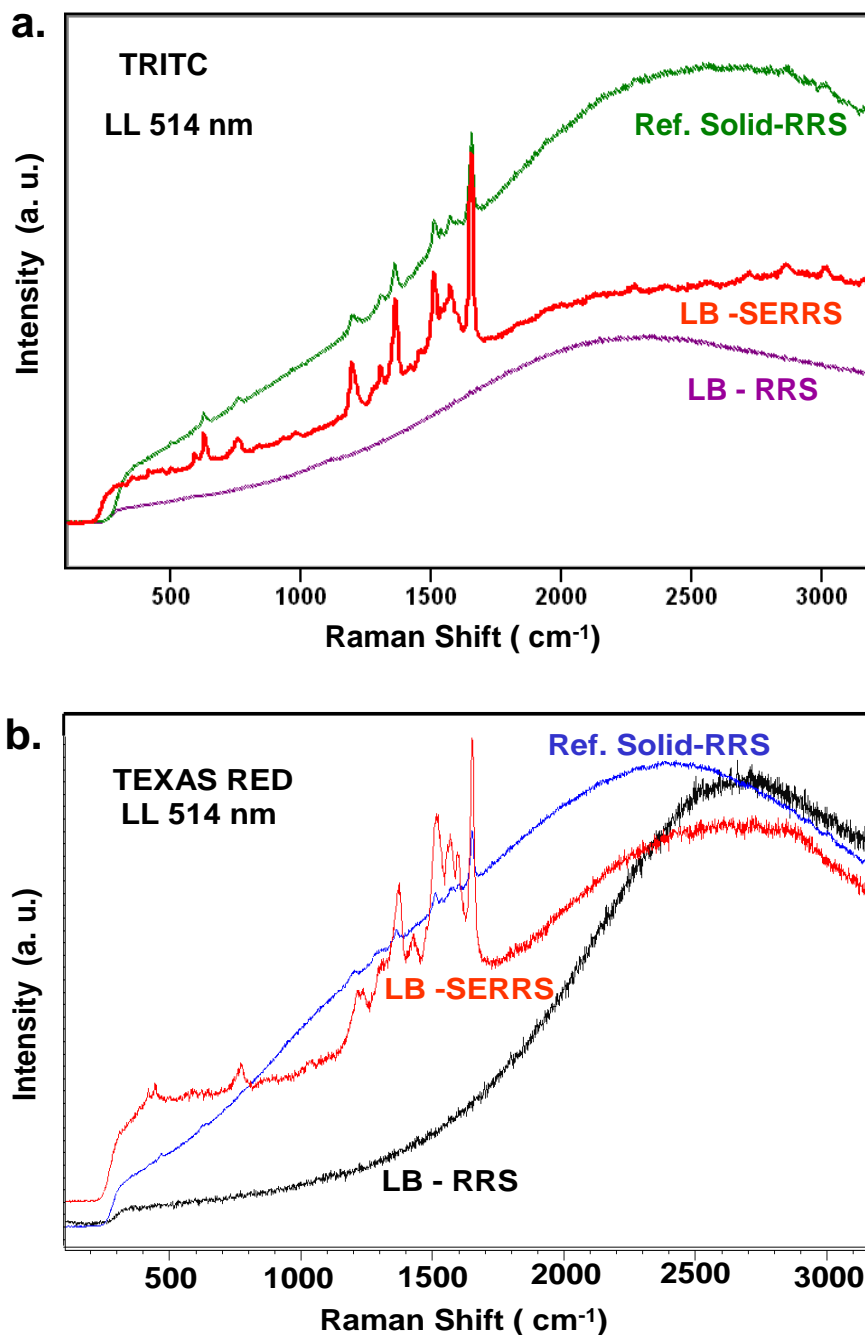


Figure 5.10: LB-SERRS, LB-RRS and Reference Spectra
a) TRITC and b) TEXAS RED

It is noticeable that the LB on glass cannot produce any RRS spectrum, and only fluorescence is seen. On the other hand, LB-SERRS provides clean Raman spectra of both these molecules with high enhancements of the Raman

intensity due to plasmonic support from SIF. The reference solid RRS spectra of both the compounds are in correspondence with the LB-SERRS spectra. The LB-SERRS spectra obtained here are considered the results of an ensemble average, since the mixed LB film composition was in ratio of 1:10 i.e. approximately 4×10^5 molecules per $1 \mu\text{m}^2$ probe area in this investigation.⁴⁰

For a comparison of LB-SERS and LB-SERRS, the Raman spectra were also acquired using 514.5 nm and 633 nm laser lines for excitation in mixed Langmuir-Blodgett (LB) monolayers of TRITC and TEXAS RED at the ratio 1:10, which were fabricated on 9 nm silver island film. The obtained spectra shown in Figure 5.11.a and 5.11.b for TRITC and TEXAS RED respectively. The molecular absorption and plasmon absorption of the SIF used in these experiments are also displayed in inset of both Figures. The combined absorption spectra clearly show that the laser 514 nm is within the region of double resonance with the LSPR of the SIF as well as the probe molecule and provides the SERRS spectrum with highest signal enhancement; whereas the laser 633 nm exploits only resonance with the plasmon absorption and could produce SERS spectrum with lower signal enhancement.

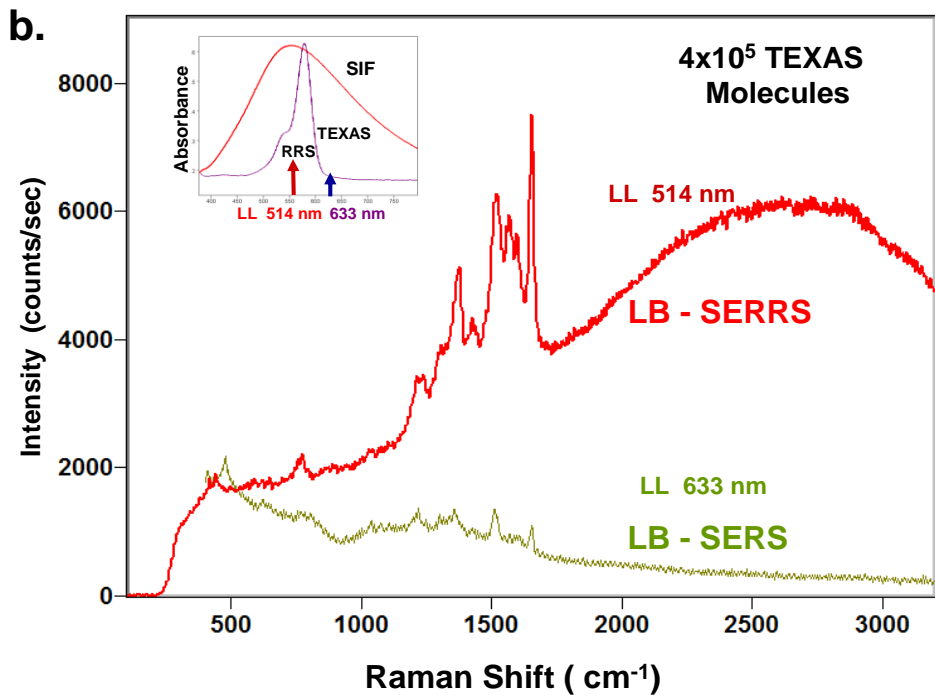
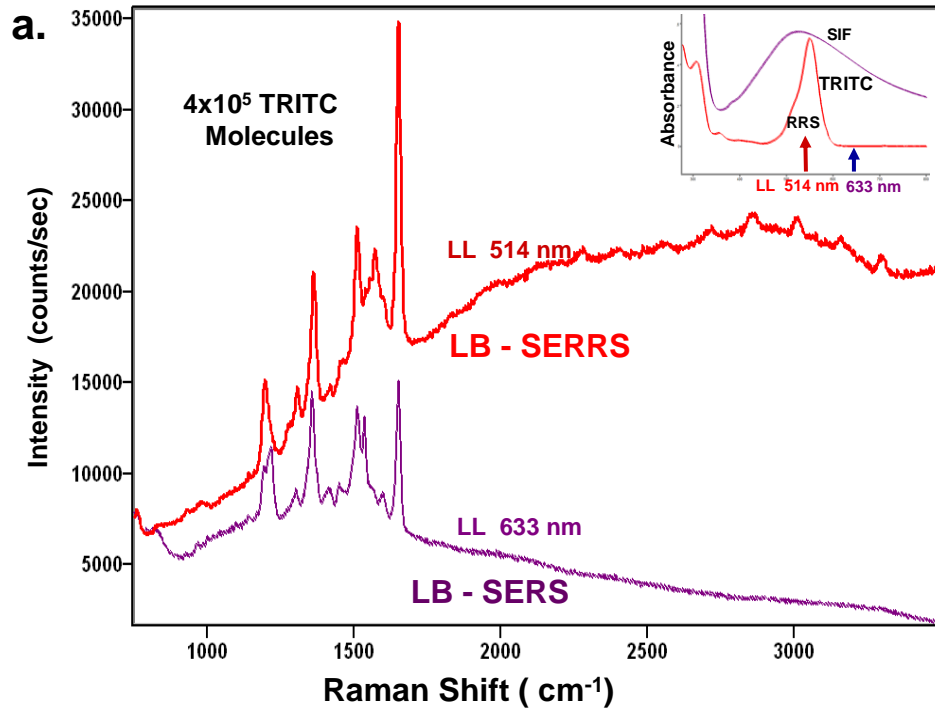


Figure 5.11: Illustration of LB-SERRS and LB-SERS spectra
a) TRITC and b) TEXAS RED

Clearly, the Raman intensities in the SERRS spectrum display a higher enhancement factor for both molecules. Therefore, to achieve single molecule detection, the highest Raman enhancement of SERRS is needed

5.5.3 SERRS mapping and ensemble averaged spectra

In Raman microscopy, one can record extended Raman spectra or obtain Raman maps. For example, the average single point extended SERRS spectra of an LB sample with a 10:1 ratio of AA to TRITC deposited on SIF. In the latter case, the extended spectrum is the result of the scattering from an AA monolayer containing ca. 4×10^5 dye molecules/ μm^2 . Using a stage with high spatial resolution, one can also carry out point-by-point sampling, as line scanning, or area mappings of the surface sample. These experiments allow monitoring the uniformity and reproducibility of the surface sample with micrometer spatial resolution. Here, SERRS spectra from the LB films were recorded with 514.5 nm excitation using point-by-point area mapping. Raman intensity maps (TRITC in Figure 5.12.a and TEXAS in Figure 5.12.b) were generated based on the fundamental vibrational wavenumber at 1650 cm^{-1} , the strongest RRS band of the chromophore assigned to a ring stretching vibration. The bright coloration in the maps shows SERRS is observed at every point in the map, representing the ensemble SERRS spectra. To illustrate the results, individual spectra are reproduced in the figures from different point in the map. Each one of these spectra is the result of statistical averaging of as many as 4×10^5 dye molecules.

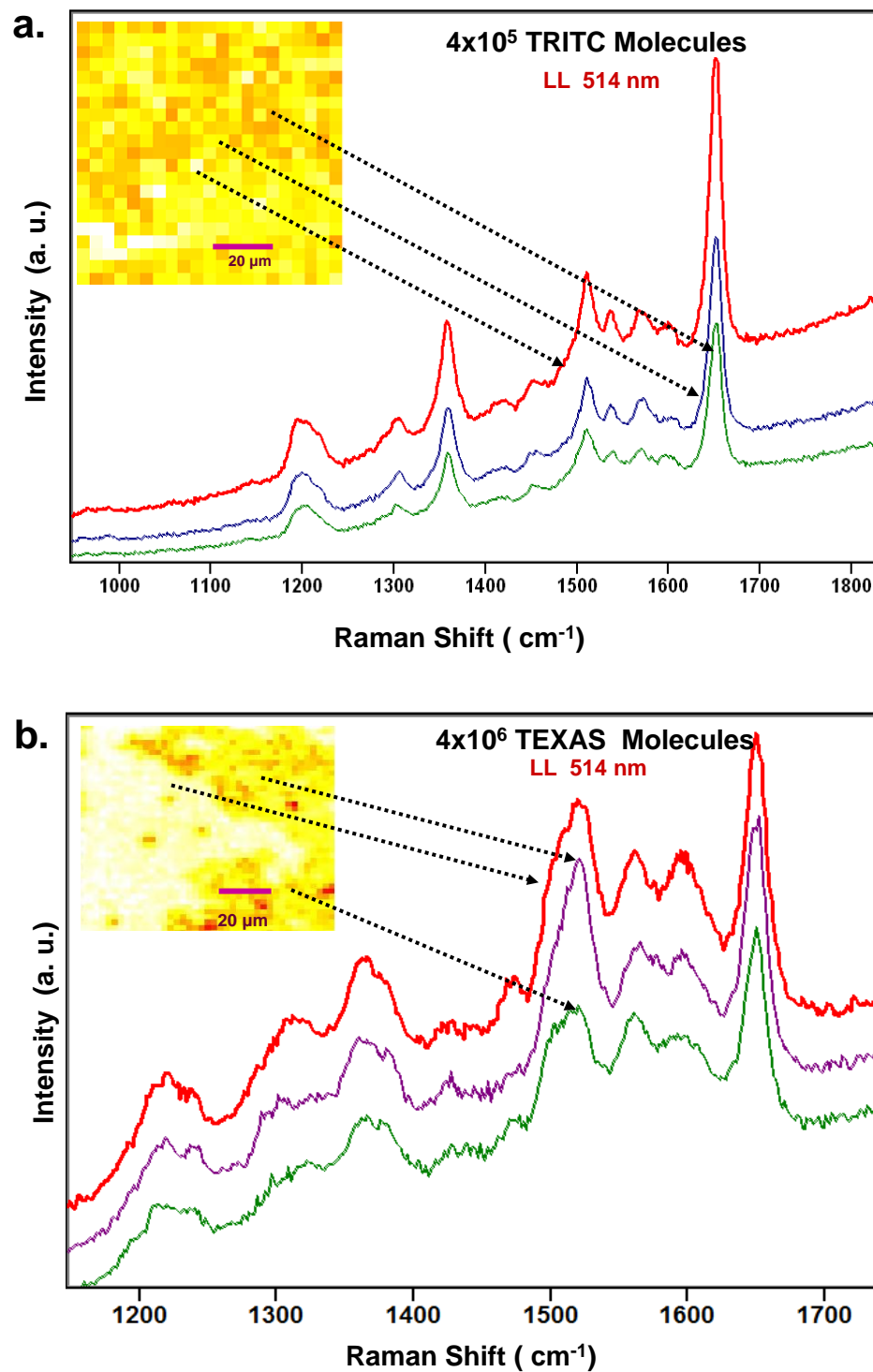


Figure 5.12: Ensemble SERRS map of LB film fabricated on SIF and excited at 514.5 nm and $\sim 20 \mu\text{W}$. Step sizes were $2 \mu\text{m} \times 2 \mu\text{m}$, and the map was constructed from 1651 collected spectra. An intensity map was generated from the integrated area of the 1650 cm^{-1} band. The inset shows the likely orientation of probe molecules with respect to the metal surface. a) TRITC and b) TEXAS RED.

The uniformity of the SERRS signals for TRITC and TEXAS would seem to indicate that the tagged phospholipids are thoroughly dispersed in the Langmuir film. One interesting note is the evidence that the SERRS spectra contain a background due to a fluorescence signal. A regular observance in the SERRS of fluorescent molecules is the quenching of the molecular fluorescence by an interaction with the metal surface. For this system, the most likely point of interaction of the phospholipids and the Ag surface is through the negatively charged phosphate group. As a result, TRITC and TEXAS could be oriented in such a way as to reduce contact with the silver surface and hence limit the efficiency of quenching experienced by TRITC and TEXAS. This fluorescent background, characteristic of the “average” LB-SERRS spectra, is in contrast to observations within the regime of statistical breakdown when single-molecule spectra are observed.

5.5.4 Trace detection with SERRS and the spectrum of the single molecule

To get hold of the spectral indication of statistical average breaking in SERRS spectra for TRITC and Texas Red, they were dispersed in the inert matrix, arachidic acid, forming mixed LB monolayers onto silver island films. For this purpose, different mixing ratios i.e. 1:10, 1:100, 1:1,000, 1:10,000 were prepared, so that mixed monolayer contains an average of 4×10^5 , 4×10^4 , 4×10^3 or 4×10^2 TRITC or Texas molecules/ μm^2 . The point by point SERRS mappings were run on all the LB films. One LB-SERRS spectrum from each of the acquired Raman maps (all of them based on band intensity at 1650 cm^{-1}) are shown in

Figure 5.13.a and 5.13.b for TRITC and TEXAS respectively. The Raman maps were taken using 514 nm laser excitation and a step size 2 μm , with power at the sample of 10-20 μW and exposure time 2 s.

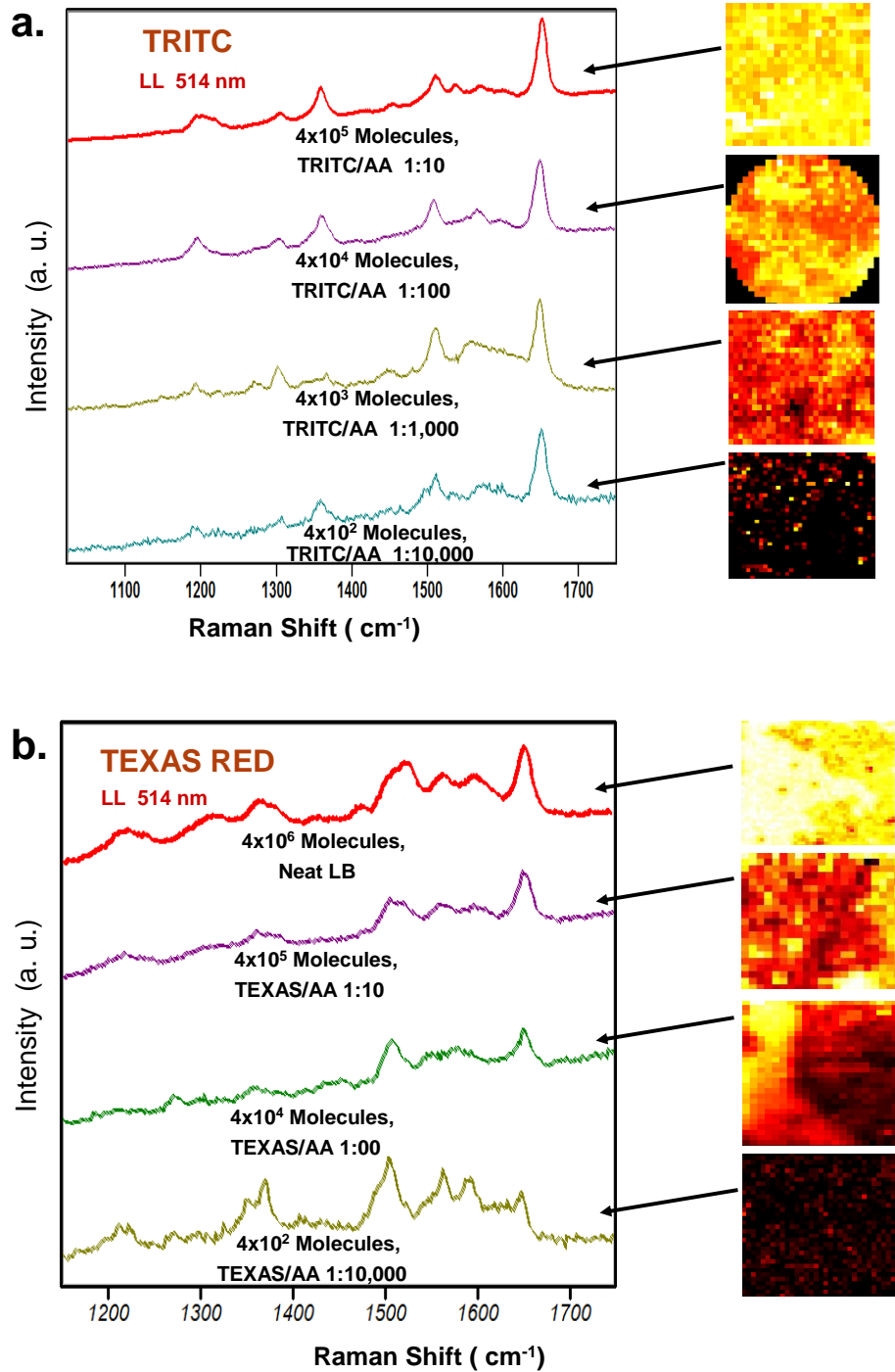


Figure 5.13: Ensemble average breaking in LB-SERRS spectra
a) TRITC and b) TEXAS RED

The statistical average and the statistical breakdown of the SERRS spectra clearly define two regimes of the experimental phenomena: detection and quantitative⁴¹ applications for “average SERS” and high sensitivity for qualitative trace detection. In average spectra, the measured parameters such as frequency, relative peak intensity, and bandwidth are constant and reproducible, which is shown in Figure 5.13. In figure 5.13, it is noticeable that the absolute Raman intensity decreases as the number of molecules per probe area decreases (top-down), which is recognized by reducing the brightness of the mapping images. The band width and frequencies also begin to fluctuate when the ensemble average spectra breaks down towards single molecule detection. These spectral variations are the signature of single molecule spectra.

5.5.5 *Single-molecule (SM) SERRS spectra*

The concentrations of the spreading solution for Langmuir film fabrication were calculated to achieve 10 molecules of the probe molecule (TRITC or TEXAS RED) per μm^2 of surface area in the AA monolayer. Raman maps were obtained for a single molecule LB monolayer containing 10 probe molecules/ μm^2 of surface area, fabricated on silver islands films with mass thicknesses of 9 nm used as SERS substrates. The results for TRITC and TEXAS RED are shown in Figure 5.14.a and 5.14.b respectively.

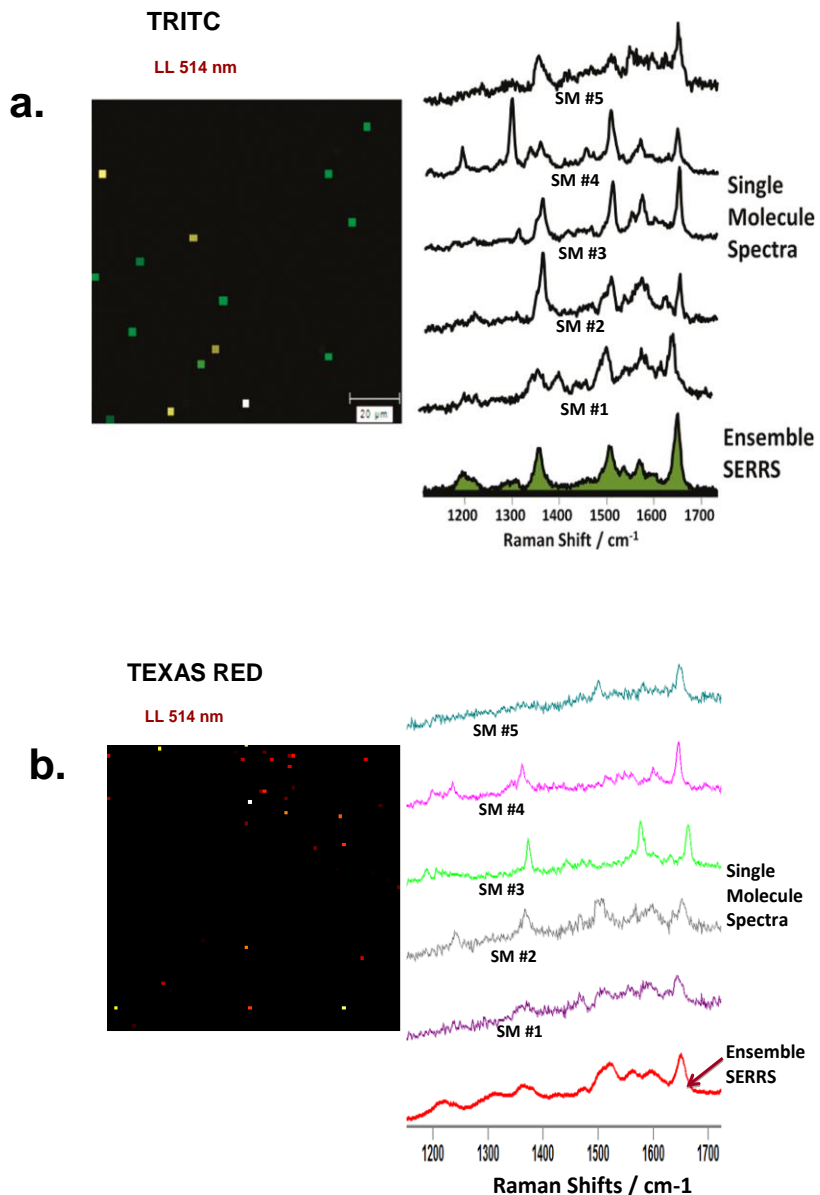


Figure 5.14: Single molecule LB-SERRS maps, excited at 514 nm with a step size $2 \mu\text{m} \times 2 \mu\text{m}$ and power $\sim 20 \mu\text{W}/\mu\text{m}^2$. The intensity map images were generated from correlation to the reference ensemble spectrum. a) TRITC and b) TEXAS RED

From previous studies with SM-SERRS and LB, it has been found that even at higher surface concentration, it is only SM events that are observed.³¹ At this surface coverage and because the chromophore is attached to a bulky phospholipid, it is very unlikely that anything but a monomer is the source of the measured Raman signal. Acquiring SM spectra has been possible by scanning

the sample surface using low laser power (10-20 $\mu\text{W}/\mu\text{m}^2$) to avoid photodegradation and collecting one spectrum every 2 μm to avoid any contribution from overlapping areas. The data set is analysed with the native Wire 3.0 software. Correlation maps are generated based on spectral matching to a representative spectrum for the target system. Only data points of highest coincidence based on the degree of correlation to the reference spectrum are distinguished. These correspond to the bright spots or pixels seen in the data maps shown in the Figure 5.14. After the data maps are generated, each highlighted spot is examined and its spectral character verified to attain a number of spectra that are very likely SM spectra for our molecular system and to eliminate false positives. For example, the map for TRITC shown in Figure 5.14.a, was generated from a total of 1651 spectra and for TEXAS shown in Figure 5.14.b, the map was generated from a total of 7021 spectra. In both cases, only spectra that have a good correlation with the reference spectra appear as highlighted spots, which, as can be seen from the map, is a very small percentage of the total spectra collected.

The single-molecule spectra exhibit several differences from those collected from the average SERRS samples. The variations in the properties of SM spectra have become one of the key indicators of SM detection with SERRS, which is due to the loss of ensemble averaging. These fluctuations have been observed regularly in SMD experiments, and can be considered as the signature of the SMD regime; such as deviation in the relative intensities of bands, band frequencies, narrowing of full width half maximum (FWHM). Concerning these

parameter fluctuations, a band at 1650 cm^{-1} has been analysed from the SM spectra of TRITC and TEXAS RED as shown in Figure 5.14 and the results are presented in Table 5.5. There is also absence of fluorescence background in SM spectra compare to the average spectra (shown in Figure 12). Single-molecule spectra are rare events in the mapping of the surface area. TRITC or TEXAS is closer to or in contact with the Ag surface, and the local electromagnetic enhancement is well above the average enhancement. These points of efficient coupling, most likely are areas in the nanostructures where the highest enhancement is provided by specific spatial locations, a hot spot.⁴²

Table 5.5: Observed band (1650 cm^{-1}) parameters in SM-SERRS spectra of TRITC and TEXAS RED in LB monolayer.

<u><i>Spectrum</i></u>	<u><i>Frequency</i></u>	<u><i>Height</i></u>	<u><i>FWHM</i></u>	<u><i>Area</i></u>
TRITC				
Average	1650	8159	21	178957
SM#1	1649	209	14	3164
SM#2	1654	218	13	3027
SM#3	1653	398	14	5627
SM#4	1645	259	13	3669
SM#5	1651	104	11	1136
TEXAS RED				
Average	1650	3178	19	64738
SM #1	1648	180	16	2890
SM #2	1651	119	12	1536
SM #3	1659	314	12	4036
SM #4	1644	331	10	3029
SM #5	1647	112	14	1636

The experiments show that SMD on SIF is a rare event involving coupling of the single molecule with the hot spot. At this moment, there is no analytical protocol to fabricate reproducible hot spots on a SERS substrate of at least $1\mu\text{m}^2$,

and hot spots are brought into being in aggregates nanostructures by its enhancing effect on a given target molecule. The variation of enhancement both in magnitude and distribution on the nanoparticles surface is irregular or inhomogeneous.

Slight differences in the frequency positions and widths of the Raman peaks from one spectrum to the other are the strongest hint of SM-SERRS. They are typically attributed to the slightly different chemical environments in which each molecule find itself and influenced by molecule-surface interactions. These sudden changes are often considered the results of thermally activated diffusion of the molecules into and out of the SERS active sites, structurally relaxation of these sites (possibly surface morphology changes through photo-reaction for example), photodesorption and photoinduced electron transfer processes. The other factor of SERRS fluctuations may due to changes in molecular orientation.

In summary, the various phenomena emerge in the SERS signals of single molecules identifications. The SERS signals of single molecules show fluctuations which are absent in the SERS of a great number of molecules due to ensemble average.^{11,13} These phenomena contain information on dynamics processes, interaction between the molecule and metallic surface, modification of molecular orientation and configuration, micro-environmental changes, etc.

5.6 Conclusions

LB-SERRS has been employed to achieve single-molecule detection of biological-relevant systems of dye-tagged (SERRS probes) phospholipids

dispersed in an LB monolayer coating silver nanostructures. The 2D mapping approach in Raman microscopy permits the acquisition and identification of SM spectra from targeted systems. The spectra attributed to a single molecule in the matrix of the fatty acid present the characteristic signature of single molecule detection: small variation of the wavenumbers for molecules on different sites, fluctuations in relative intensity and the FWHM, in contrast with the SERRS spectra of ensemble average. For future work, one of the major challenges to SM-SERS is to fabricate reproducible nanostructures with the highest possible enhancement factor, and accumulate experimental data allow to understand the variations in spectral parameters, so as to tap into the wealth of information that may carry. The examples presented here represent the initial steps towards developing SM-SERRS for biological applications.

REFERENCES

- (1) Tamarat, P.; Maali, A.; Lounis, B.; Orrit, M. *Journal of Physical Chemistry A* **2000**, *104*, 1-16.
- (2) Peterman, E. J. G.; Sosa, H.; Moerner, W. E. *Annual Review of Physical Chemistry* **2004**, *55*, 79-96.
- (3) Sako, Y.; Yanagida, T. *Nature Cell Biology* **2003**, SS1-SS5.
- (4) Haran, G. *Journal of Physics-Condensed Matter* **2003**, *15*, R1291-R1317.
- (5) Moerner, W. E.; Fromm, D. P. *Review of Scientific Instruments* **2003**, *74*, 3597-3619.

- (6) Kneipp, J.; Kneipp, H.; Kneipp, K. *Chemical Society Reviews* **2008**, *37*, 1052-1060.
- (7) Qian, X. M.; Nie, S. M. *Chemical Society Reviews* **2008**, *37*, 912-920.
- (8) Albrecht, M. G.; Creighton, J. A. *Journal of the American Chemical Society* **1977**, *99*, 5215-5217.
- (9) Fleischmann, M.; Hendra, P. J.; McQuillan, A. J. *Chemical Physics Letters* **1974**, *26*, 163-166.
- (10) Jeanmaire, D. L.; VanDuyne, R. P. *Journal of Electroanalytical Chemistry* **1977**, *84*, 1-20.
- (11) Nie, S. M.; Emery, S. R. *Science* **1997**, *275*, 1102-1106.
- (12) Eggeling, C.; Schaffer, J.; Seidel, C. A. M.; Korte, J.; Brehm, G.; Schneider, S.; Schrof, W. *The Journal of Physical Chemistry A* **2001**, *105*, 3673-3679.
- (13) Kneipp, K.; Wang, Y.; Kneipp, H.; Perelman, L. T.; Itzkan, I.; Dasari, R. R.; Feld, M. S. *Physical Review Letters* **1997**, *78*, 1667.
- (14) Kneipp, K.; Kneipp, H.; Itzkan, I.; Dasari, R. R.; Feld, M. S. *Chemical Physics* **1999**, *247*, 155-162.
- (15) Moskovits, M. *Reviews of Modern Physics* **1985**, *57*, 783-826.
- (16) Xu, H. X.; Aizpurua, J.; Kall, M.; Apell, P. *Physical Review E* **2000**, *62*, 4318-4324.
- (17) Xu, H.; Bjerneld, E. J.; Käll, M.; Börjesson, L. *Physical Review Letters* **1999**, *83*, 4357.
- (18) Kneipp, K.; Kneipp, H.; Kartha, V. B.; Manoharan, R.; Deinum, G.; Itzkan, I.; Dasari, R. R.; Feld, M. S. *Physical Review E* **1998**, *57*, R6281.

- (19) Aroca, R. *Canadian Journal of Analytical Sciences and Spectroscopy* **2004**, *49*, 114-120.
- (20) Pieczonka, N. P. W.; Moula, G.; Aroca, R. F. *Langmuir* **2009**, *25*, 11261-11264.
- (21) Aćimović, S. S.; Kreuzer, M. P.; González, M. U.; Quidant, R. *ACS Nano* **2009**, *3*, 1231-1237.
- (22) Hering, K.; Cialla, D.; Ackermann, K.; Dorfer, T.; Moller, R.; Schneidewind, H.; Mattheis, R.; Fritzsche, W.; Rosch, P.; Popp, J. *Analytical and Bioanalytical Chemistry* **2008**, *390*, 113-124.
- (23) Le Ru, E. C.; Meyer, M.; Etchegoin, P. G. *The Journal of Physical Chemistry B* **2006**, *110*, 1944-1948.
- (24) Zhang, W.; Yeo, B. S.; Schmid, T.; Zenobi, R. *The Journal of Physical Chemistry C* **2007**, *111*, 1733-1738.
- (25) Constantino, C. J. L.; Lemma, T.; Antunes, P. A.; Aroca, R. *Analytical Chemistry* **2001**, *73*, 3674-3678.
- (26) Weiss, A.; Haran, G. *The Journal of Physical Chemistry B* **2001**, *105*, 12348-12354.
- (27) Pieczonka, N. P. W.; Aroca, R. F. *Chemical Society Reviews* **2008**, *37*, 946-954.
- (28) Goulet, P. J. G.; Aroca, R. F. *Analytical Chemistry* **2007**, *79*, 2728-2734.
- (29) Constantino, C. J. L.; Lemma, T.; Antunes, P. A.; Goulet, P.; Aroca, R. *Applied Spectroscopy* **2003**, *57*, 649-654.
- (30) Goulet, P.; Pieczonka, N.; Aroca, R. *Canadian Journal of Analytical Sciences and Spectroscopy* **2003**, *48*, 146-152.

- (31) Goulet, P. J. G.; Pieczonka, N. P. W.; Aroca, R. F. *Journal of Raman Spectroscopy* **2005**, *36*, 574-580.
- (32) Mohwald, H. *Annual Review of Physical Chemistry* **2003**, *41*, 441-476.
- (33) Korchowiec, B.; Paluch, M.; Corvis, Y.; Rogalska, E. *Chemistry and Physics of Lipids* **2006**, *144*, 127-136.
- (34) Benda, A.; Fagul'ová, V.; Deyneka, A.; Enderlein, J.; Hof, M. *Langmuir* **2006**, *22*, 9580-9585.
- (35) Slaughter, B. D.; Unruh, J. R.; Price, E. S.; Huynh, J. L.; Urbauer, R. J. B.; Johnson, C. K. *Journal of the American Chemical Society* **2005**, *127*, 12107-12114.
- (36) Sabatte, G.; Keir, R.; Lawlor, M.; Black, M.; Graham, D.; Smith, W. E. *Analytical Chemistry* **2008**, *80*, 2351-2356.
- (37) Faulds, K.; McKenzie, F.; Smith, W. E.; Graham, D. *Angewandte Chemie-International Edition* **2007**, *46*, 1829-1831.
- (38) Jensen, L.; Schatz, G. C. *Journal of Physical Chemistry A* **2006**, *110*, 5973-5977.
- (39) Shorygin, P. P.; Krushinskij, L. L. *Journal of Raman Spectroscopy* **1997**, *28*, 383-388.
- (40) Aroca, R. *Surface-enhanced Vibrational Spectroscopy*; John Wiley & Sons: Chichester, 2006.
- (41) Graham, D.; Faulds, K. *Chem. Soc. Rev. FIELD Full Journal Title:Chemical Society Reviews* **2008**, *37*, 1042-1051.
- (42) Le Ru, E. C.; Etchegoin, P. G.; Meyer, M. *Journal of Chemical Physics* **2006**, *125*.

CHAPTER 6

CONTROLLED SURFACE PLASMON RESONANCES BY SELF- ASSEMBLY OF SILVER NANOPARTICLES ON SILANIZED SURFACES

6.1 Overview

Plasmons (or surface excitation of electron-hole pairs)- are simple the quanta of the oscillations of the surface charges produced by external electric field. Plasmon modes can be sustained in thin films, called surface plasmons (SPs), and in nanoparticles, called localized surface plasmon resonances (LSPR). The latter are currently being explored for surface-enhanced spectroscopy applications by a wide spectrum of scientists: physicists, chemists, materials scientists and biologists.¹⁻⁶ In particular, the localized surface plasmon resonance in Au, Ag nanoparticles greatly enhances the local electromagnetic field that extends a few nanometers above surface. Fabricating nanostructures for optical enhancement is now a rising field of research.

The rational development of SERS-active substrates depends critically on the homogeneity and intensity of surface plasmon resonances, the properties that are strongly dependent on both the morphology and dielectric properties of the metals and composite materials making up the SERS substrates. The search of appropriate substrates as platforms for the SERS ultrasensitive detection of molecules has led to an enormous activity with the proposal and test of a variety of different strategies with complementary performances.⁷ The driving forces behind these efforts are the fundamental understanding of the SERS process. Typically substrates with higher SERS amplification display lower reproducibility and control of the significant parameters.⁸⁻⁹ Conversely, substrates with better controlled and reproducible performance may present a smaller but still significant amplifying factor.¹⁰⁻¹¹ Calculations by Xu et al. have shown that

electromagnetic enhancements of 10^{10} are present between two nanosphere separated by 1 nm.¹² These results suggest that aggregates are better substrates for SERS applications than individual nanoparticles because large enhancements can be achieved at particle junctions of aggregates.¹³ In any case, if analytical applications are sought, and a good understanding of the SERS process is desired, it is clear that reproducible, homogeneous and stable-in-time substrates are better adapted for the task.

A great variety of surface-confined nanostructures, that allow the control of the plasmonic properties and improvement of the Raman signal enhancement, can be produced by numerous fabrication methods, including nanosphere lithography, electron-beam lithography, and colloidal immobilization by self assembly of nanoparticles. The conventional nanosphere lithography process begins with self-assembly of a nanosphere mask onto a substrate, followed by deposition of a material(s) through the mask. Nanosphere lithography is now being employed as an inexpensive, high-throughput, and materials general nanofabrication technique.¹⁴⁻¹⁵ The nanosphere diameters determine the size and interspacing distance of the NSL produced nanoparticles. Electron-beam lithography, although more time-consuming and expensive, offers the advantage of creating nanoparticles of arbitrary size, shape, and spacing. Here, an electron beam is used to write a deposition mask directly into a polymer film; metal is then deposited through this mask and the film washed away, leaving behind the desired pattern. Researchers have used this technique to study plasmonic coupling between nanoparticles of arbitrary shape with different inter-particle

spacing.¹⁵⁻¹⁸ Based on the consideration that the large enhancement factors can be obtained at the junctions of aggregated nanoparticles, colloidal nanoparticles of different sizes and shapes were immobilized by self assembly bottom-up technique on functionalized solid substrates and were found to be highly efficient SERS substrate (Baia et al. 2006d, Li et al, 2004; wang and Gu 2005, Orendoff et al. 2005). In this work, SERS substrates has been prepared by self assembly of colloidal Ag nanoparticles

6.2 Self assembly of Ag nanoparticles

Approaches within nanofabrication are manifold and typically classified as either “top-down” or “bottom-up” techniques. The electron-beam lithography (EBL) and self-assembly of nanoparticles are examples for top-down and bottom-up technique, respectively. However, the common disadvantage among some of these top-down methodologies is their high cost per fabricated sample. Furthermore, the extensive processing time needed in EBL for the fabrication of metal nanostructures over large areas makes the technique expensive, time-consuming, and in less accessible. Less expensive but still time-consuming alternative parallel top-down techniques include colloidal lithography and roughened metal surfaces.¹⁹ Alternatively, “bottom-up” techniques with comparably very low fabrication and time expenses per area, have advanced as an elegant and prevalent choice, to meet the demand for control of the dimensions of nanostructures on a large scale. The option considered here is the preparation of SERS substrates by the self-assembly of metallic nanoparticles

(bottom-up approach). The building blocks in this case are nanoparticles of different shapes and compositions.²⁰ The NPs are immobilized in a planar platform through either covalent²¹⁻²⁵ or non-covalent²⁶⁻³² interactions with linkers. The general choices of non-covalent self assembly linkers are commonly polymers³³ and polymer dendrimers,^{26,34} and proteins;^{31,29} and for covalent self assembly, the typical choices are organic silane²⁸ and dithiols^{21-23,25}. The preparation of positively charged Ag NPs³⁵ and their application in the multi-layer self-assembly of oppositely charged NPs as SERS substrates³⁶⁻³⁷ has also been reported. The bottom-up approach, however, commonly provides less spatial and sample-to-sample reproducibility than the nanolithographic methods.

In this work, a self-assembled substrate used for SERS, which is based on Ag NPs (colloidal silver citrate nanoparticles) as building blocks and amino functional silane (3-Amino propyl triethoxysilane) as linker or coupling agent for the NPs onto the microscopic glass slides. The colloidal silver made by the reduction of silver nitrate by trisodium citrate.^{36,38} The colloid is stable over long periods of time almost certainly because unoxidised citrate forms an outer layer on the surface of the particles.³⁹ This ensures a stable surface layer with a negatively charged surface and a stable colloid suspension. The silanization of glass surface and the deposition of negatively charged silver nanoparticles onto silanized glass surfaces are accomplished by electrostatic interaction using a dipping approach. Controlling the time span of deposition eventually control the extent of the nanoparticles aggregation, i.e. the particles come close each other when more particles are grown on the surface by a longer period of deposition.

The larger number of nanoparticles per unit surface area creates more inter-particle junctions and decreasing particle-to-particle distances; which provides an improved signal-to-noise ratio of the SERS signals. Consequently the number of hot spots increases, which endowed with a big enhancement in SERS signals and more possibility to trace detection.⁴⁰⁻⁵¹ It also opens the way to optimized SERS substrates with high sensitivity and reproducibility.

To assess the ultimate results of the SERS effects, mixed Langmuir-Blodgett monolayers of a dye “octadecyl rhodamine B chloride R18” with an inert matrix arachidic acid (AA) have been fabricated on self-assembled silver substrates, which are made from different time-span of nanoparticle deposition. This type of monolayer has significant importance in SERS spectroscopy to assess SERS results foundations.⁵²⁻⁵⁵ The mixed LB monolayer used for testing was in the ratio of 1:100 (R18 : AA), which grants a detection limit of $\sim 10^{-19}$ M.

6.3 Experimental

Silver nitrate (AgNO_3), trisodium citrate ($\text{Na}_3\text{C}_6\text{H}_5\text{O}_7$), nitric acid HNO_3 , hydrochloric acid (HCl), sulfuric acid (H_2SO_4), anhydrous acetone ($\text{C}_3\text{H}_6\text{O}$), 3-amino propyl triethoxysilane ($\text{C}_9\text{H}_{23}\text{NO}_3\text{Si}$), octadecyl rhodamine B chloride R18 ($\text{C}_{46}\text{H}_{67}\text{ClN}_2\text{O}_3$), arachidic acid ($\text{C}_{20}\text{H}_{40}\text{O}_2$) and dichloromethane (CH_2Cl_2) were obtained from Aldrich. All were used without any further purification.

Citrate silver colloid dispersion was prepared via reduction of silver in aqueous AgNO_3 solution with trisodium citrate. All glasswares used were thoroughly cleaned with aqua regia (three parts HCl and one part HNO_3). The

water used in the experiments was doubly-distilled, purified using a Milli-Q system from Millipore. The water resistivity was greater than 18.2 MΩ cm at 25⁰ C. In a 500 ml Erlenmeyer flask connected to a condenser, a volume of 200 ml 10⁻³ M AgNO₃ aqueous solution was brought to boiling point with constant stirring. Then 4 ml of 1% trisodium citrate (Na₃C₆H₅O₇) was added to the solution. The resulting solution is a citrate silver colloid dispersion with turbid grey color.⁵⁶ For surface silanization, the microscopic corning 2048 glass slides, size 75 cm x 25 cm, were placed, for cleaning, in aqueous solution of 50% H₂SO₄ for 3-4 hours, and then washed with Milli-Q water several times by sonication, and dried them at ambient condition in a dust free environment. The clean slides were then dipped into a solution of 2% 3-amino propyl triethoxy silane in acetone for about 10 minutes. After silanization, the glass slides were washed with Milli-Q water to remove excess silanes from the surface. The silanized glass slides were immersed into a citrate silver colloidal solution to start the deposition of silver nanoparticles by self assembly through the association between positively charged amine from silanized glass surface, and negatively charged silver colloids. The unbound silver particles are removed by washing in Mill Q water. A cartoon for the schematic of the silver nanoparticles deposition is shown in Figure 1. The immersion time of silanized substrates inside the colloidal solution permits control of nanoparticle density per unit surface area. By trial and error, several immersion times were explored. Here, we present the results in terms of the estimation of surface-enhanced Raman scattering for silanized slides after 2 hrs, 6 hrs, 10 hrs and 14 hrs of silver deposition.

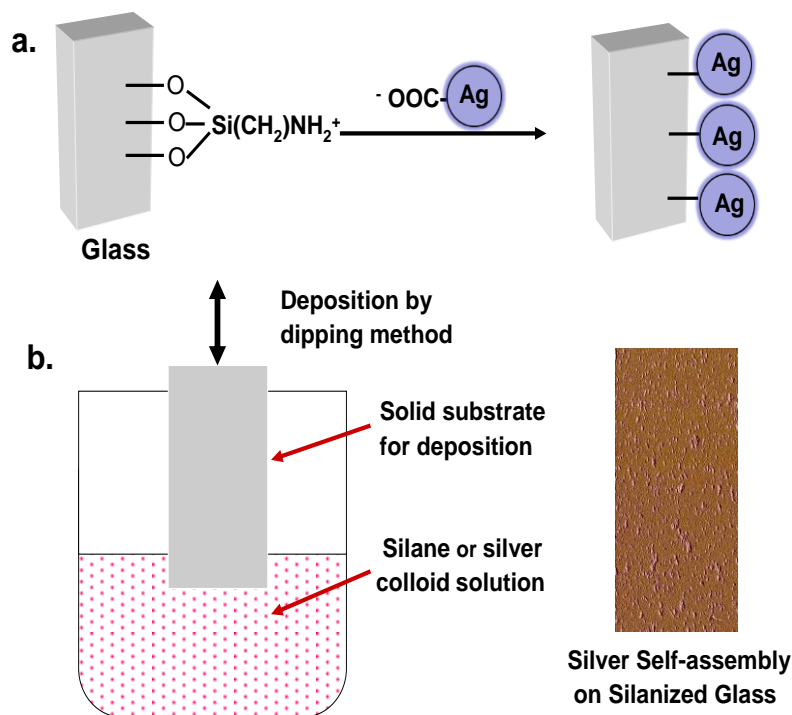


Figure 6.1: Surface silanization of glass and preparation of silver metal film by self-assembly of silver nanoparticle on silanized surface

Pure grade dichloromethane was used to make solutions of octadecyl rhodamine B chloride R18 ($\text{C}_{46}\text{H}_{67}\text{ClN}_2\text{O}_3$) and arachidic acid ($\text{C}_{20}\text{H}_{40}\text{O}_2$) for Langmuir monolayer formation. The mixed solution was spread drop to drop on the aqueous surface using a microsyringe held very close to the aqueous surface, and then the solvent was allowed to evaporate completely over a period of time at least 30 minutes. The subphase was ultrapure Milli-Q water ($18.2 \text{ M}\Omega \text{ cm}$) and a constant temperature of $25 \text{ }^\circ\text{C}$ of the subphase has been maintained. The monolayer was then compressed at a fixed barrier speed of $10 \text{ cm}^2/\text{min}$ to record the surface pressure.

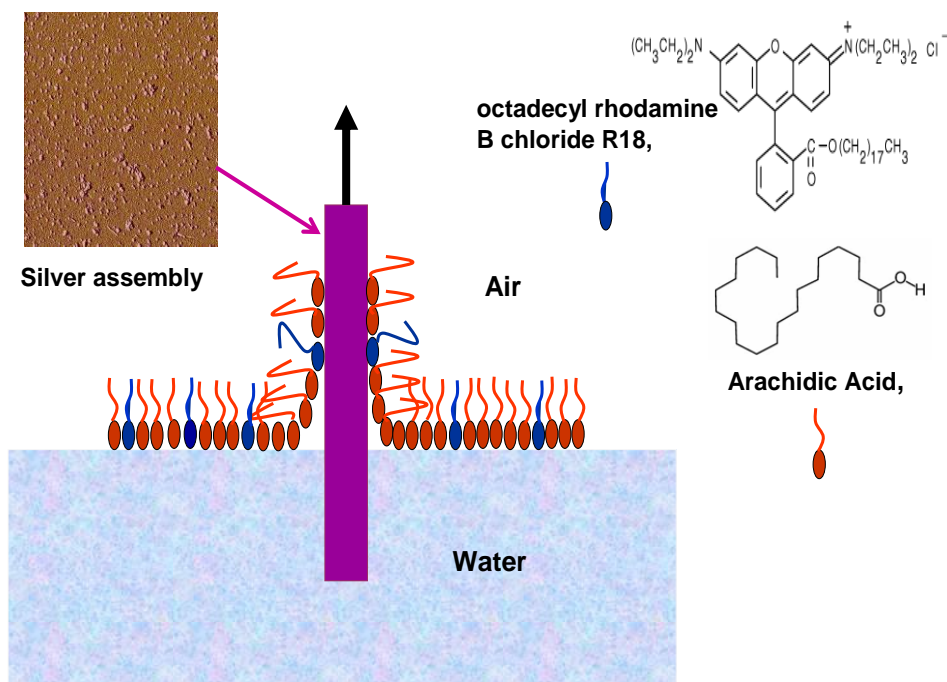


Figure 6.2: Experimental set up for LB monolayer deposition on silver metal film

The surface pressure (π) was measured by a Wilhelmy paper plate pressure sensor. The monolayer film transfer was carried out using Z-deposition with an electronically controlled dipping device at a constant surface pressure of $25 \text{ mN}\cdot\text{m}^{-1}$ and film transfer ratio close to unity. The experimental set-up for LB monolayer deposition is shown in Figure 6.2. Langmuir-Blodgett monolayers of octadecyl rhodamine B chloride R18 and arachidic acid at the ratio of 1:100 were then fabricated onto silver metal films.

Uv-visible absorption spectra were recorded for solution of octadecyl rhodamine B chloride R18, colloidal silver citrate dispersion and the silver metal films prepared by self assembly on silanized surfaces employing a Cary 50 scan UV-visible spectrometer. Atomic force microscopy (AFM) of silver metal films was carried out by using Digital Instruments NanoScope IV, operating in non-contact

tapping mode with a n⁺ silicon tip at a scan rate of 0.5 Hz with 512 sample line and 512 sample points per line. Topographical (height), error (amplitude) and phase images were used to analyze the surface morphology of the films. The data were collected under ambient conditions, and each scan was duplicated to ensure that any features observed were reproducible. All Raman scattering on the monolayer of mixed LB films were conducted with Renishaw InVia system using a laser excitation 514.5 nm (argon ion) with a powers of 10-20 μ W at the sample to avoid any possibility of photodegradation. All measurements were made in a backscattering geometry, using a 50x microscope objective with a numerical aperture value of 0.75, providing scattering areas of ca. 1 μ m². Single point spectra were recorded with 4 cm⁻¹ resolution and 10-second accumulation times unless noted otherwise. 2D SERS mapping experiments were carried out using the rastering of a computer-controlled two-axis (XY) motorized stage, with a step of 2 μ m.

6.4 Results and Discussions

6.4.1 Absorption

The plasmon absorption spectra of the silver citrate colloid dispersion used for the self assembly of silver nanoparticles on silanized glass surface and the 1.34x10⁻⁴ M solution of octadecyl rhodamine B chloride R18 are shown in Figure 6.3. The plasmon absorption shows a broad spectrum covering the visible range hinting a large distribution of particle sizes. The molecular absorption spectra, with a maximum centered at 557 nm, is also in resonance with the laser

excitation wavelength of 514 nm, which was used in this work to acquire Raman spectra.

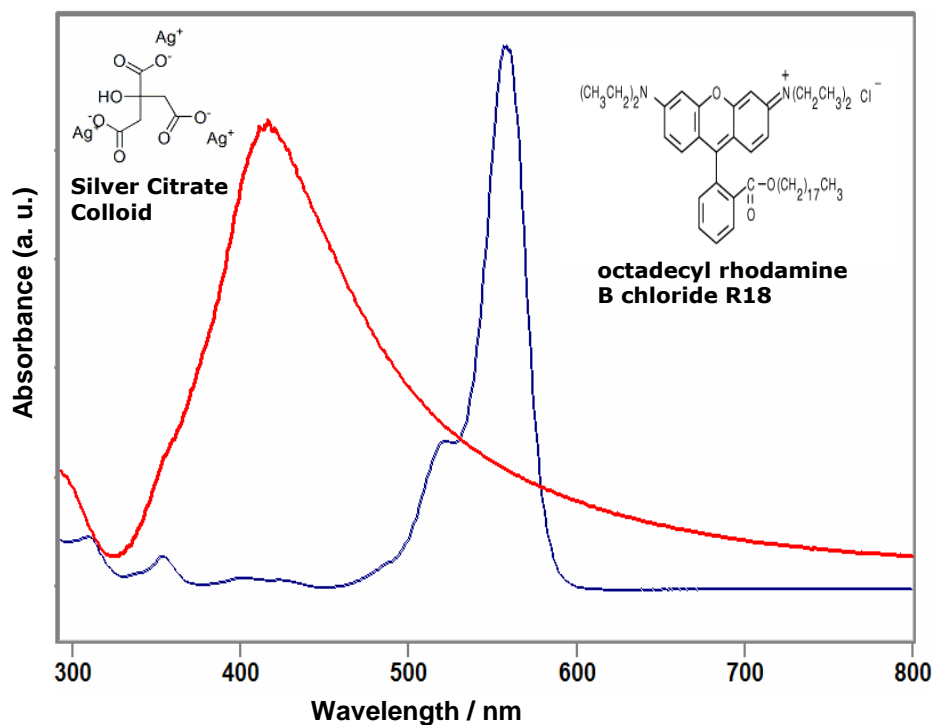


Figure 6.3: Surface plasmon absorption of citrate silver colloid dispersion and molecular absorption of 1.34×10^{-4} M octadecyl rhodamine B chloride R18.

The plasmon absorption spectra of the silver films made by self assembly on silanized glass surface using different immersion time periods: 2 hours, 6 hours, 10 hours and 14 hours, are shown in Figure 6.4. The inset of this figure shows the AFM images of 2 hrs and 14 hrs silver films, providing a glimpse on nanoparticle growth on the silanized surface. The density of silver nanoparticles increases with the extension of the deposition period and, consequently, the intensity and shape of the plasmon absorption is changing, in part due to additional plasmon coupling. These results also indicate that the glass surface

was fully silanized, permitting the increase in silver particle attachment with the immersion time. The corresponding SERS spectra are discussed in the following section.

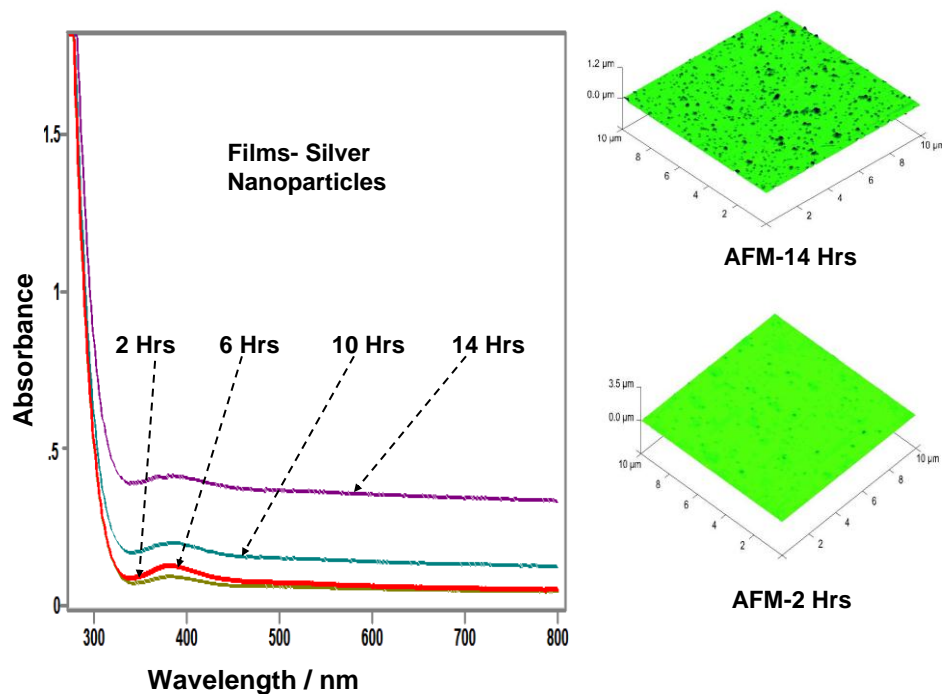


Figure 6.4: : Plasmon absorption spectra of silver films made by 2 hrs, 6 hrs, 10 hrs and 14 hrs of deposition

6.4.2 Reference and LB-SERRS spectra of R18

The sample for LB-SERRS experiment was a mixed LB film of octadecyl rhodamine B chloride R18 with an inert matrix arachidic acid (ratio 1 : 100). The reference SERRS spectra were obtained from mixed LB on a silver island film of 9 nm mass thicknesses (LB-SERRS spectra) and the reference resonance Raman spectra acquired on solid R18. Laser excitation of 514 nm with a power of 10-20 μ W to avoid photo degradation was used to record the spectra shown in

Figure 6.5. The background fluorescence is seen in both reference spectra, although the vibrational bands are in full agreement.

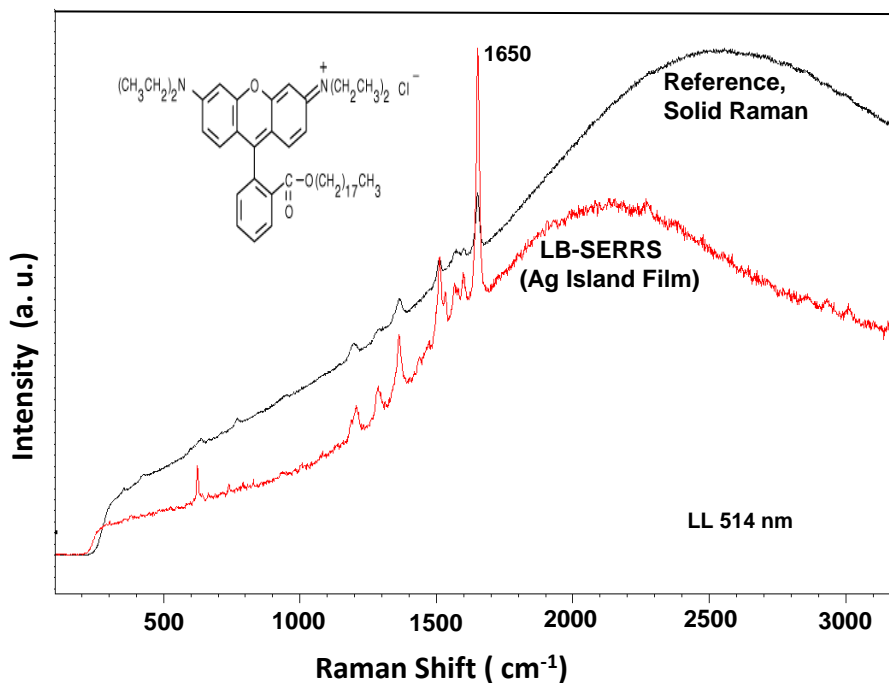


Figure 6.5: The LB-SERRS and reference resonance Raman (solid) spectrum of octadecyl rhodamine B chloride R18.

6.4.3 LB-SERRS substrate

The silver film substrates prepared with different immersion times: 2 hrs., 6 hrs., 10 hrs. and 14 hrs. of the silanized surface, were coated with a mixed LB of octadecyl rhodamine B chloride R18 and arachidic acid (ratio 1 : 100). The SERRS spectra on these LB films were obtained by a 2D mapping (raster scan) using a laser excitation of 514 nm with a power of 10-20 μ W to avoid photodegradation and step size of 2 μ m x 2 μ m to circumvent any contribution from overlapping areas. In all maps, a total of 1651 spectra were acquired on

each sample. The maps were produced based on the band intensity at frequency 1650 cm^{-1} using the native Wire 3.0 software. The AFM image of the Ag film, the mapping image of acquiring Raman spectra and representative spectra from the map of a mixed LB monolayer of octadecyl rhodamine B chloride R18 and arachidic acid (1:100), coated on the 2 hours deposited Ag film, are shown in Figure 6.6. The bright pixels correspond to the recorded LB-SERRS spectra; and the map provides a visualization of the spots in the film that are SERS active. Therefore, only a small number of active spots are observed here, since only a few silver nanoparticles are grown on the surface, and they seem to be well separated.

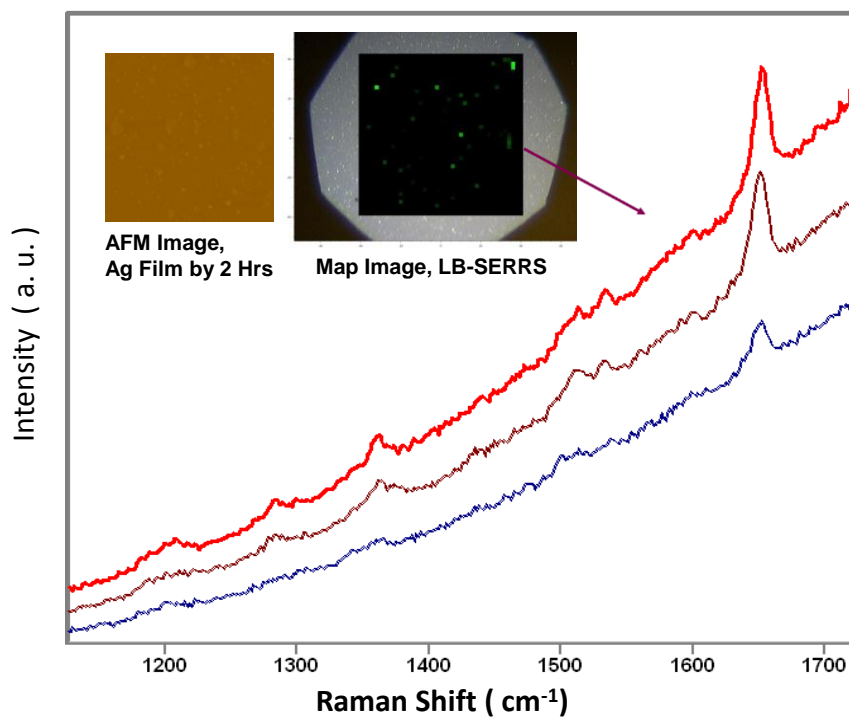


Figure 6.6: SERRS mapping spectra from a self assembly silver film made by 2 hrs deposition, mapping image and AFM image of the Ag

When the same mixed LB film is used to coat the Ag film resulting from 14 hours immersion time, the LB-SERRS results are quite different. The representative LB-SERRS spectra on that Ag film (14 hours), the map image and the AFM image of the Ag film are presented in Figure 6.7. Clearly, not only the higher number of bright pixels in the map is an indicator of higher SERS activity; but the absolute band intensity or pixel brightness, is much higher than that observed on the Ag film made in 2 hours. It could be argued that since there is a higher density of Ag nanoparticles on the SERS substrate, the chances are that the nanoparticles of close proximity may create more localized 'hot spots' with high enhancement factor.

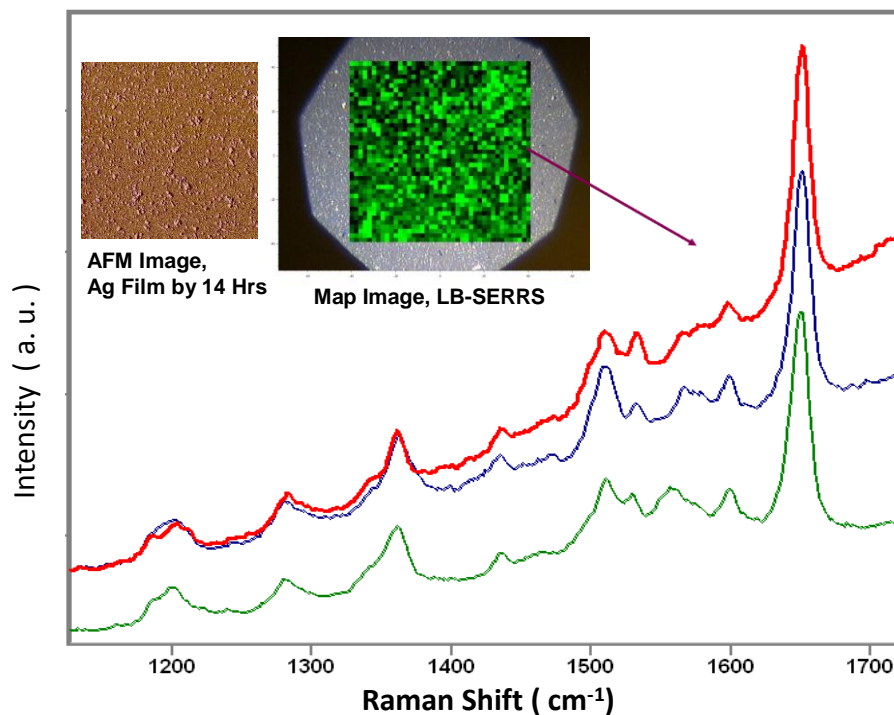


Figure 6.7: SERRS mapping spectra from a self assembly silver film made by 14 hrs deposition, mapping image and AFM image of the

The main objective in this section was to explore the LB-SERRS properties by controlling nanostructure formation using self assembly of Ag nanoparticles. Since the target molecular system can be made reproducibly (LB film), the LB-SERRS maps provide a clear visualization of the SERS activity of the fabricated SERS substrate. See, for example the accumulated results of LB-SERRS maps for the Ag films, made by 2 hours, 6 hours, 10 hours and 14 hours for immersion, are presented in Figure 6.8. One representative spectrum from each map for the comparison of Raman spectra is included in the figure. The increase density of bright pixels in the map images signifies the decrease in inter-particle distance and increase of aggregations, which results in large number of hot spots and higher absolute intensities as well.

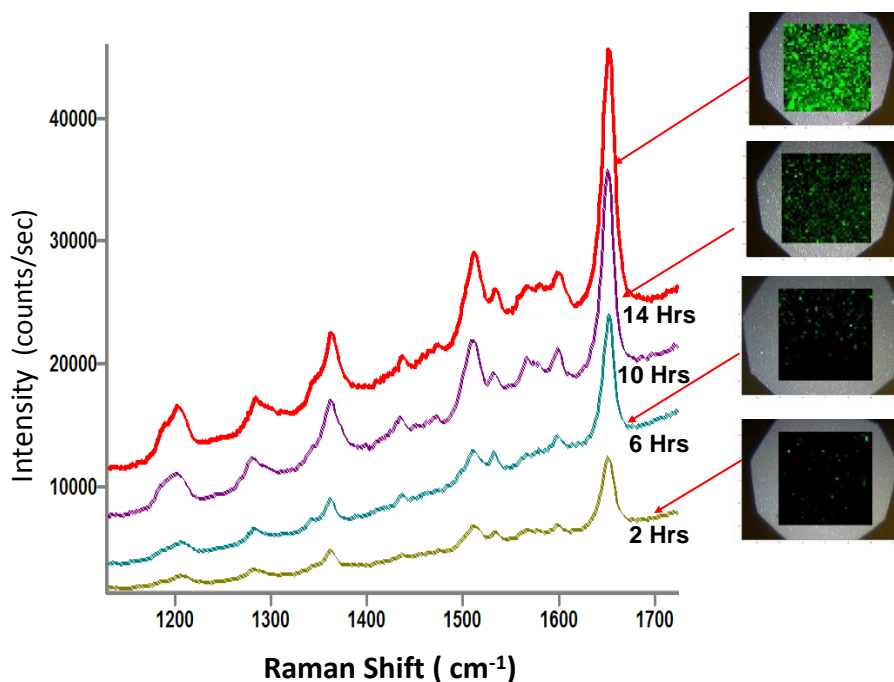


Figure 6.8: SERRS spectra and mapping images from self assembly silver films made by 2 hrs, 6 hrs, 10 hrs and 14 hrs deposition

6.5 Conclusions

In this work, the LB-SERRS results on the controlled surface activity of the substrate, prepared by silanization process are reported. Tuning of enhancement of the SERS substrate is achieved by increasing the time of self assembly of silver nanoparticles on the silanized glass surface. Ultra-low trace detection could be possible using this methodology of substrate surface preparation. The foremost important aspect in this work is the control of the target molecule (LB film), allowing to visualize the increase in surface activity with the resolution of the microscope objective.

The detection limits demonstrate here for the fabricated SERS substrates are well below 4×10^4 molecules (a zeptomole) that can be detected easily using plasmon enhancement in the nanostructures obtained in the surface silanization method. The detection limit is estimated from the illuminated area (possible 4×10^6 molecular sites) containing, on average a ratio of 100 molecules of arachidic acid for one dye molecule. The strong LB-SERRS signals were obtained, when the LB monolayer (ratio 100 :1) was on the silver films prepared by 14 hours immersion , reveals that much lower trace detection limits can be easily achieved; and single molecule detection is also possible by tuning this self assembly surface preparation.

References

- (1) Barnes, W. L.; Dereux, A.; Ebbesen, T. W. *Nature* **2003**, *424*, 824-830.
- (2) Kneipp, K.; Kneipp, H.; Kneipp, J. *Accounts of Chemical Research* **2006**, *39*, 443-450.
- (3) Maye, M. M.; Luo, J.; Han, L.; Zhong, C.-J. *Nano Letters* **2001**, *1*, 575-579.
- (4) Moskovits, M. *Reviews of Modern Physics* **1985**, *57*, 783-826.
- (5) Andrew, P.; Barnes, W. L. *Science* **2004**, *306*, 1002-1005.
- (6) Pinchuk, A. O.; Schatz, G. C. *Applied Physics B: Lasers and Optics* **2008**, *93*, 31-38.
- (7) Baker, G. A.; Moore, D. S. *Analytical and Bioanalytical Chemistry* **2005**, *382*, 1751-1770.
- (8) Maher, R. C.; Cohen, L. F.; Etchegoin, P. *Chemical Physics Letters* **2002**, *352*, 378-384.
- (9) Tognalli, N.; Fainstein, A.; Calvo, E.; Bonazzola, C.; Pietrasanta, L.; Campoy-Quiles, M.; Etchegoin, P. *Journal of Chemical Physics* **2005**, *123*.
- (10) Felidj, N.; Aubard, J.; Levi, G.; Krenn, J. R.; Salerno, M.; Schider, G.; Lamprecht, B.; Leitner, A.; Aussenegg, F. R. *Physical Review B* **2002**, *65*.
- (11) Jackson, J. B.; Westcott, S. L.; Hirsch, L. R.; West, J. L.; Halas, N. J. *Applied Physics Letters* **2003**, *82*, 257-259.
- (12) Xu, H.; Bjerneld, E. J.; Käll, M.; Börjesson, L. *Physical Review Letters* **1999**, *83*, 4357.

- (13) Kneipp, K.; Wang, Y.; Kneipp, H.; Perelman, L. T.; Itzkan, I.; Dasari, R.; Feld, M. *S. Physical Review Letters* **1997**, *78*, 1667-1670.
- (14) Hulteen, J. C.; Vanduyne, R. P. *Journal of Vacuum Science & Technology a- Vacuum Surfaces and Films* **1995**, *13*, 1553-1558.
- (15) Deckman, H. W.; Dunsmuir, J. H. *Applied Physics Letters* **1982**, *41*, 377-379.
- (16) Fromm, D. P.; Sundaramurthy, A.; Schuck, P. J.; Kino, G.; Moerner, W. E. *Nano Letters* **2004**, *4*, 957-961.
- (17) Hicks, E. M.; Zou, S. L.; Schatz, G. C.; Spears, K. G.; Van Duyne, R. P.; Gunnarsson, L.; Rindzevicius, T.; Kasemo, B.; Kall, M. *Nano Letters* **2005**, *5*, 1065-1070.
- (18) Lamprecht, B.; Schider, G.; Lechner, R. T.; Ditlbacher, H.; Krenn, J. R.; Leitner, A.; Aussenegg, F. R. *Physical Review Letters* **2000**, *84*, 4721-4724.
- (19) Jeanmaire, D. L.; Vanduyne, R. P. *Journal of Electroanalytical Chemistry* **1977**, *84*, 1-20.
- (20) Aroca, R. F.; Alvarez-Puebla, R. A.; Pieczonka, N.; Sanchez-Cortez, S.; Garcia-Ramos, J. V. *Advances in Colloid and Interface Science* **2005**, *116*, 45-61.
- (21) Addison, C. J.; Brolo, A. G. *Langmuir* **2006**, *22*, 8696-8702.
- (22) Fan, M. K.; Brolo, A. G. *Chemphyschem* **2008**, *9*, 1899-1907.
- (23) Freeman, R. G.; Grabar, K. C.; Allison, K. J.; Bright, R. M.; Davis, J. A.; Guthrie, A. P.; Hommer, M. B.; Jackson, M. A.; Smith, P. C.; Walter, D. G.; Natan, M. J. *Science* **1995**, *267*, 1629-1632.
- (24) Jackson, J. B.; Halas, N. J. *Proceedings of the National Academy of Sciences of the United States of America* **2004**, *101*, 17930-17935.

- (25) Musick, M. D.; Keating, C. D.; Lyon, L. A.; Botsko, S. L.; Pena, D. J.; Holliway, W. D.; McEvoy, T. M.; Richardson, J. N.; Natan, M. J. *Chemistry of Materials* **2000**, *12*, 2869-2881.
- (26) Aroca, R. F.; Goulet, P. J. G.; dos Santos, D. S.; Alvarez-Puebla, R. A.; Oliveira, O. N. *Analytical Chemistry* **2005**, *77*, 378-382.
- (27) Kho, K. W.; Shen, Z. X.; Zeng, H. C.; Soo, K. C.; Olivo, M. *Analytical Chemistry* **2005**, *77*, 7462-7471.
- (28) Peng, C.; Song, Y.; Wei, G.; Zhang, W.; Li, Z.; Dong, W. F. *Journal of Colloid and Interface Science* **2008**, *317*, 183-190.
- (29) Pieczonka, N. P. W.; Goulet, P. J. G.; Aroca, R. F. *Journal of the American Chemical Society* **2006**, *128*, 12626-12627.
- (30) Tao, A.; Kim, F.; Hess, C.; Goldberger, J.; He, R. R.; Sun, Y. G.; Xia, Y. N.; Yang, P. D. *Nano Letters* **2003**, *3*, 1229-1233.
- (31) Wei, G.; Wang, L.; Sun, L. L.; Song, Y. H.; Sun, Y. J.; Guo, C. L.; Yang, T.; Li, Z. A. *Journal of Physical Chemistry C* **2007**, *111*, 1976-1982.
- (32) Zhao, S.; Zhang, K.; An, J.; Sun, Y. Y.; Sun, C. Q. *Materials Letters* **2006**, *60*, 1215-1218.
- (33) Li, X. L.; Xu, W. Q.; Zhang, J. H.; Jia, H. Y.; Yang, B.; Zhao, B.; Li, B. F.; Ozaki, Y. *Langmuir* **2004**, *20*, 1298-1304.
- (34) Goulet, P. J. G.; dos Santos, D. S.; Alvarez-Puebla, R. A.; Oliveira, O. N.; Aroca, R. F. *Langmuir* **2005**, *21*, 5576-5581.
- (35) Tan, S.; Erol, M.; Attygalle, A.; Du, H.; Sukhishvili, S. *Langmuir* **2007**, *23*, 9836-9843.

- (36) Lee, P. C.; Meisel, D. *Journal of Physical Chemistry* **1982**, *86*, 3391-3395.
- (37) Tan, S.; Erol, M.; Sukhishvili, S.; Du, H. *Langmuir* **2008**, *24*, 4765-4771.
- (38) Munro, C. H.; Smith, W. E.; Garner, M.; Clarkson, J.; White, P. C. *Langmuir* **1995**, *11*, 3712-3720.
- (39) Siiman, O.; Bumm, L. A.; Callaghan, R.; Blatchford, C. G.; Kerker, M. *Journal of Physical Chemistry* **1983**, *87*, 1014-1023.
- (40) Chumanov, G.; Sokolov, K.; Gregory, B. W.; Cotton, T. M. *Journal of Physical Chemistry* **1995**, *99*, 9466-9471.
- (41) Fritzsche, W.; Sokolov, K.; Chumanov, G. D.; Cotton, T. M.; Henderson, E. *Journal of Vacuum Science & Technology a-Vacuum Surfaces and Films* **1996**, *14*, 1766-1769.
- (42) Froner, E.; Baschera, F.; Tessarolo, F.; Bettotti, P.; Pavesi, L.; Rossi, B.; Scarpa, M.; Mariotto, G.; Rigo, A. *Applied Surface Science* **2009**, *255*, 7652-7656.
- (43) Hajdukova, N.; Prochazka, M.; Stepanek, J.; Spirikova, M. *Colloids and Surfaces a-Physicochemical and Engineering Aspects* **2007**, *301*, 264-270.
- (44) Kim, K.; Lee, H. B.; Shin, K. S. *Langmuir* **2008**, *24*, 5893-5898.
- (45) Kreuzer, M. P.; Quidant, R.; Salvador, J. P.; Marco, M. P.; Badenes, G. *Analytical and Bioanalytical Chemistry* **2008**, *391*, 1813-1820.
- (46) Liang, Y. J.; Ozawa, M.; Krueger, A. *Acs Nano* **2009**, *3*, 2288-2296.
- (47) Nath, N.; Chilkoti, A. *Analytical Chemistry* **2004**, *76*, 5370-5378.
- (48) Olson, L. G.; Lo, Y. S.; Beebe, T. P.; Harris, J. M. *Analytical Chemistry* **2001**, *73*, 4268-4276.

- (49) Peron, O.; Rinnert, E.; Lehaitre, M.; Crassous, P.; Compere, C. *Talanta* **2009**, *79*, 199-204.
- (50) Szunerits, S.; Coffinier, Y.; Janel, S.; Boukherroub, R. *Langmuir* **2006**, *22*, 10716-10722.
- (51) Wang, J.; Zhu, T.; Song, J. Q.; Liu, Z. F. *Thin Solid Films* **1998**, *327*, 591-594.
- (52) Dynarowicz-Latka, P.; Dhanabalan, A.; Oliveira, O. N. *Advances in Colloid and Interface Science* **2001**, *91*, 221-293.
- (53) Mazloff, M. R.; Yang, J. *Langmuir* **2001**, *17*, 2727-2732.
- (54) Petrov, J. G.; Petrov, P. G. *Langmuir* **1998**, *14*, 2490-2496.
- (55) Takahashi, M.; Kobayashi, K.; Takaoka, K.; Takada, T.; Tajima, K. *Langmuir* **2000**, *16*, 6613-6621.
- (56) Saraiva, S. M.; Oliveira, J. F. *Journal of Dispersion Science and Technology* **2004**, *25*, 229-237.

CHAPTER 7

SINGLE MOLECULE DETECTION OF PERYLENE TETRACARBOXYLIC DERIVATIVES IN LANGMUIR-BLODGETT MONOLAYERS USING SURFACE ENHANCED RESONANCE RAMAN SCATTERING AND SHELL ISOLATED NANOPARTICLE ENHANCED FLUORESCENCE (SHINEF)

7.1 Overview

The objective of this section of the thesis was to explore, for the same molecular system and using the LB technique, the plasmon enhancement of emission and scattering down to single molecule detection. The enormous impact of single-molecule spectroscopy on physics and chemistry, and its application to biological problems is seen in the burst of activity and publications¹. The detection of a single quantum system may help the description and understanding of its interaction with light. In particular, fluorescence² and surface-enhanced fluorescence (SEF)³ are established and effective methods to achieve single-molecule detection (SMD). In the last thirteen years, SMD has also been achieved for many molecular systems using surface enhanced Raman scattering and surface-enhanced resonance Raman scattering⁴⁻⁵. The very large cross section of fluorescence permit SMD directly, and single-molecule fluorescence (SMF) is a growing field of research and the source of new analytical methods.⁶ SMF has progressed considerably in the visualization and localization of single molecules, and, for instance, it helps the development of powerful tools for the structural and functional characterization of protein complexes. In contrast, the information rich vibrational Raman scattering has very low molecular cross section and the optical signal needs the plasmon enhancement to achieve the sensitivity required for SMD.⁷⁻⁸ Fluorescence applications are rapidly becoming a leading methodology in medical diagnostics and biotechnology, primarily because of their versatility, potential for multiplexing, ease of use, and remarkable sensitivity. As has been discussed in previous

chapters, localized surface plasmon resonances in metallic nanoparticles (mainly silver and gold) can enhance the absorption (visible and IR radiation),⁹⁻¹¹ fluorescence emission,¹²⁻¹⁴ and Raman scattering from analytes¹⁴⁻¹⁵ residing on, or near the surface of the metal nanostructures. Here, we illustrate two plasmon enhanced spectroscopic techniques on well defined LB structures: surface-enhanced fluorescence and SERRS. The high sensitivity allows demonstrating the SMD using either technique.

Surface-enhanced fluorescence. Since this is the first extensive application of SEF in this thesis, a brief discussion of the SEF phenomenon is needed.

Two basic properties of the fluorophore are the absorption cross section and the quantum yield.

$$P_0^{fluo} = \kappa_0 I_0 Q_0 \quad [7.1]$$

Where, κ_0 is the absorption coefficient and I_0 is the photon flux impingent on the chromophore. Q_0 , is the quantum yield, a number between 0 and 1 that described the proportion of absorbed light that is detected as radiative decay.

For the isolated chromophore the quantum yield is given by the fraction of two competitive factors; the radiative decay, Γ_0 and the non-radiative decay, Γ_{nR}^{int} :

$$Q_0 = \frac{\Gamma_0}{\Gamma_0 + \Gamma_{nR}^{int}} \quad [7.2]$$

Chromophores on or near a metal nanostructure that can sustain localized surface plasmon resonances will see a substantial changes in both, their absorption coefficient and their decay rates. The absorption rate is modified because of the new local field near the nanostructure when its surface plasmons are excited¹⁶;

$$EF_{loc} = \frac{|E_{loc}|^2}{|E_0|^2} \quad [7.3]$$

Since I_0 is proportional to $|E_0|^2$, the absorption is enhanced by the factor EF_{loc} . However, an excited chromophore on a metal surface is strongly quenched¹⁷. Near a metal nanostructure sustaining surface plasmon excitations, both, the radiative decay and the non-radiative decay are affected. In fact, a new non-radiative decay channel is open by direct energy transfer to the metal.

$$Q = \frac{\Gamma_{rad}}{\Gamma_{rad} + \Gamma_{nR}^{metal} + \Gamma_{nR}^{Int}} \quad [7.4]$$

Assuming that near the metal nanostructure, $\Gamma_{rad} \neq \Gamma_0$, the enhancing and quenching will be depending on the magnitude of Γ_{rad} vs Γ_{nR}^{metal} . Here the competitive result of the two opposing effects will determine the outcome in either SEF or quenching. The net results is a function of the metal-molecule separation, and this distance dependence is the most important property of SEF.¹⁸⁻¹⁹

The theory predicts, and the experiments confirm, that for a chromophore located on an enhancing nanostructure, a continuous transition from fluorescence quenching to fluorescence enhancement should be observed by increasing the

thickness of the spacer layer (shell thickness) between the molecule and the metal surface^{14, 20-21}. The molecule-metal distance for observation of SEF varies in different reports from 2.5 nm¹⁸, to 5 nm²⁰, to 10 nm¹⁹ up to 30 nm²² and even 90 nm.²¹ At large metal-fluorophore separation, the enhancement effect progressively declines. Recently, we have developed a new approach to experimental SEF using shell-isolated nanoparticles (SHINs)²³, where the gold core is covered with silica coatings in the range of about 10 to 20 nm. The SEF demonstrated with these nanoparticles has been named SHINEF²⁴. Up to this point, SHINEF has been demonstrated, and can be attained with a good enhancement factor using coatings between 10 nm and 20 nm. Here, using the LB technique for sample preparation, mixed arachidic acid (AA) monolayer doped by perylene tetracarboxylic derivatives with variable concentrations of PTCDs (down to 10 molecule in the probed area of 1 μm^2 , that represents single molecule detection), were fabricated onto glass slides. In a typical SHINEF experiments, the LB monolayer is covered with shell-isolated nanoparticles (SHIN)²³. The expanded versatility²⁵ of this technique consists in spraying the substrate onto the target, rather than coating the substrate with the analyte. The importance of using the silica shell around the gold core is 3-folds: (1) silica layers offer the robustness, chemical inertness, and the versatility needed for the conjugation of biomolecules or fluorophores, (2) it protects the gold core from ions present in biological media, and (3) it allows easy application as 'smart dust' over the sample surface.²⁶⁻²⁷

The plasmonic origin of surface enhanced spectroscopy permits to focus on the experimental task of fabricating nanostructures (mainly silver and gold) that sustain localized surface plasmon resonances.²⁸ The attained electromagnetic enhancement factor,²⁹ EF_{loc} , at a given excitation frequency, depends on the dielectric function of the metal nanoparticles, their shape, size and packing of nanostructures. It is also affected by the dielectric constant of the surrounding medium that wraps the metal nanoparticles. In many cases, the spectral properties of the species adsorbed onto the metal nanoparticles may change on account of the “chemical or physical” interactions with the nanostructure, and, correspondingly, the electromagnetically enhanced spectrum will contain the information that shed light on these molecule-nanostructure interactions. In this work, silver island film (SIF) of 9 nm mass thickness was used in SERRS experiment and silica shell (> 10 nm) coated on gold core (~40 nm) was used in SHINEF.

The SERRS presented here is unique, since it shows the fundamentals vibrational wavenumbers of PTCDs; but also combinations and overtones (second and third harmonics) are demonstrated. The high harmonics can only be seen in the spectra when the excitation is in resonance with the absorption of the chromophore. Notably, the observation of overtone and combination bands is a rare event in Raman scattering. In addition, Perylene tetracarboxylic derivatives molecules are investigated due to unique electroactive and photo active properties with many potential applications in optoelectronics.³⁰ In particular, PTCDC materials are at the centre of a research effort intended to improve the n-

type electron transporting-conduction properties by introducing chemical groups into the main PTC backbone.³¹

7.2 Experimental

The molecules of two compounds were selected as targets for SMD in this study. Bis (ndodecyl imido)perylene ($C_{48}H_{58}N_2O_4$) and Bis-(3,4 dichloro benzylimido) perylene ($C_{40}H_{18}N_2O_4Cl_4$). These perylene tetracarboxylic derivatives (PTCD) were synthesized and purified at the Xerox Research Centre of Canada and used as provided. The other materials needed to carry on this investigation were arachidic acid (AA, $C_{20}H_{40}O_2$), dichloromethane ($CHCl_2$), ultra pure Ag shot (1-3 mm), potassium tetrachloroauric acid ($HAuCl_4$), sodium citrate ($C_6H_5NaO_7$), 3-aminopropyltriethoxysilane (APTES, $C_9H_{23}NO_3Si$), and sodium silicate (Na_2SiO_3) obtained from Aldrich, and all they were used without further purification.

All PTCD solutions were prepared using spectroscopic grade dichloromethane as the solvent. The insolubility of perylene derivatives in water and organic solvents is well-known. Thus, stock $\sim 10^{-4}$ M solution of the analyte was prepared using $\sim 10\%$ trifluoroacetic acid (TFA) and the remaining dichloromethane. TFA is necessary to increase the solubility of the PTCDs in conventional organic solvents. Silver nanostructured films of 9 nm mass thickness, used for SERRS, were vacuum evaporated onto corning 2048 microscope glass slides at a pressure of 10^{-6} Torr and keeping the temperature of the substrate at $100^\circ C$ (maintained for 1 h after evaporation) followed by 30 minutes cooling. Mass thickness was monitored using a quartz crystal balance.

In this work, arachidic acid Langmuir mixed monolayers, doped with PTCD derivatives each in varying concentrations were prepared at the air-water interface of Lauda Langmuir film balance. LB films with 4×10^5 , 10^3 or 10 molecules of the perylene molecules within $1 \mu\text{m}^2$ (the eventual area being probed for Raman scattering), were fabricated onto silver island films for the SMD investigation by LB-SERRS. The same LB film was also fabricated onto a clean corning 2048 microscope glass slides to be used as a reference. The same protocol was used to study SMD by SHINEF (see Figure 7.1).

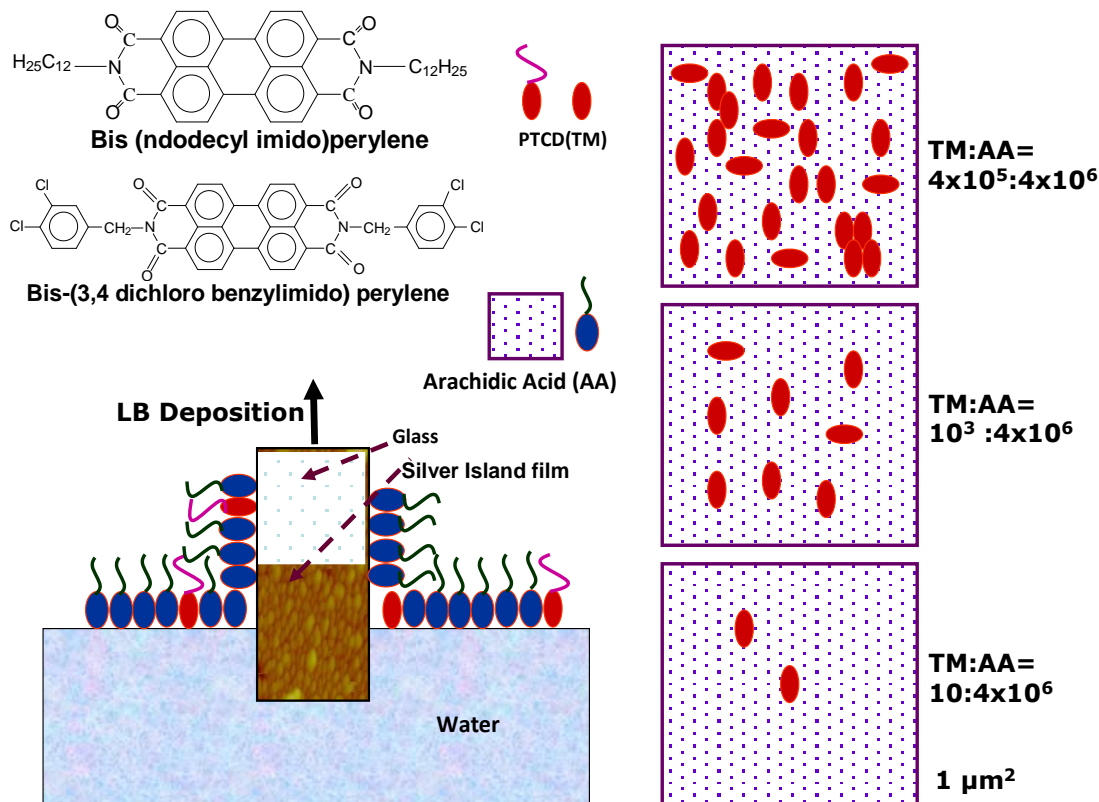


Figure 7.1: LB monolayers of arachidic acid mixed with PTCDs fabricated on SIF and glass for SMD by SERRS and SHINEF

Film transfer was carried out using Z-deposition with a Lauda Film Lift FL-1 electronically controlled dipping device at a constant surface pressure of 25 mN

m^{-1} , corresponding with the condensed phase of the Langmuir monolayer, and consistently resulted in transfer ratios near unity. Pure water ($18.2 \text{ M}\Omega \text{ cm}$) as subphase in the LB trough (containing small amounts of CdCl_2 , $2.5 \times 10^{-4} \text{ M}$), was maintained at a constant temperature of 25° C , for the preparation of all Langmuir monolayers.

Silica coated gold particles were synthesized adapting the method described by Li et al.²³ The gold core was synthesized by gold citrate reduction of tetrachloroauric acid (HAuCl_4) by adapting the existing protocol.³²⁻³³ A 50 ml of 0.01% HAuCl_4 solution was brought to boiling and a solution of 1% sodium citrate ($667 \mu\text{L}$) was then added. Boiling was continued for 15 minutes and then removed from heat, with persisting stirring for 15 minutes. After, to the solution, 3 mL of a 1 mM of 3-aminopropyltriethoxysilane (APTES), was added under vigorous stirring, and allowed to stand. Then the resulting solution was heated in a water bath to a temperature between $90\text{-}95^\circ\text{C}$; then, we added 9 mL of 0.54% sodium silicate solution to obtain the silica coating, keeping the solution at this temperature for 2 hours. The final solution was centrifuged at 4000 rpm for 4 minutes, recovering the supernatant, and later filtered using $0.20 \mu\text{m}$ pore polyethersulfone filters (Sarstedt). The concentrated SHIN particle solution was then used to drop coat using $5 \mu\text{L}$, on the PTCB LB-monolayer fabricated on bare glass slide (shown in Figure 7.2) and dried at ambient atmosphere for ~ 16 hours to make ready for the SHINEF measurements using a Renishaw InVia system.

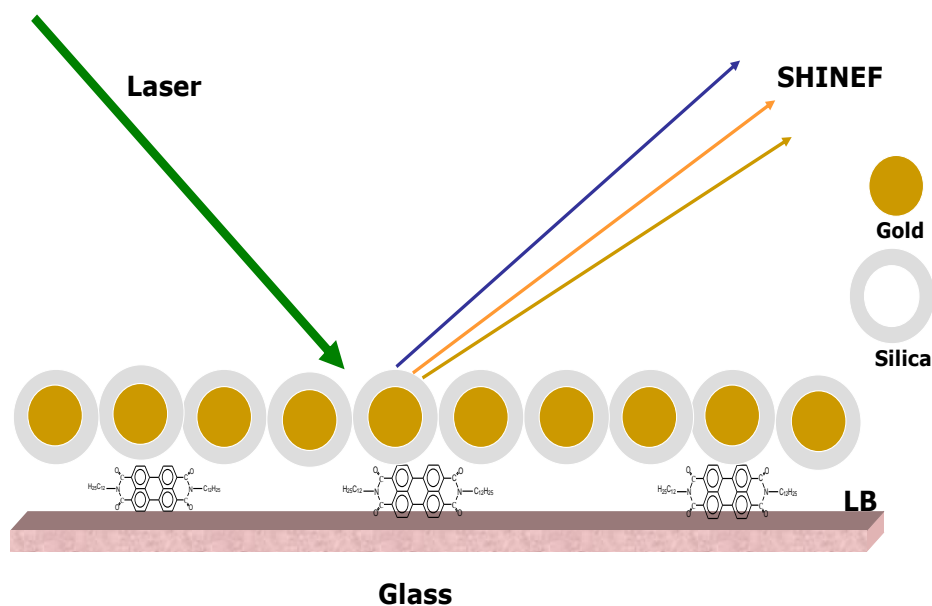


Figure 7.2: Schematic of coating the LB monolayers on glass by SHIN particles and experimental for SHINEF

UV-visible absorption spectra were recorded for all PTCD solutions and 9 nm nanostructured Ag films employing a Cary 50 scan UV-visible spectrophotometer. Atomic force microscopy (AFM) images were recorded using a Digital Instruments NanoScope IV, operating in noncontact tapping mode with an n^+ silicon tip. All images were collected with high resolution (512 lines/scan) at a scan rate of 0.5 Hz. Topographical (height), error (amplitude), and phase images were used for analysis of the surface morphology of the films. The data were collected under ambient conditions, and each scan was duplicated to ensure that any features observed were reproducible. All micro-Raman scattering experiments were conducted using a Renishaw InVia system, with laser excitation at 514.5 nm, and powers of 10-20 μW at the sample. All

measurements were made in a backscattering geometry, using a 50x microscope objective with a numerical aperture value of 0.75, and scattering areas of $\sim 1 \mu\text{m}^2$. Single-point Raman spectra were recorded with 4 cm^{-1} resolution and 10 s accumulation times; while 2D SERRS and SHINEF extended mapping results were collected through the rastering of a computer-controlled, three-axis encoded (XYZ) motorized stage, with a step size of $5 \mu\text{m}$ to avoid photoinduced effects, and with a single 10s accumulation time at each spot. Data acquisition and analysis were carried out using the WIRE software for windows and Galactic Industries GRAMS™ C software.

7.3 Results and Discussion

7.3.1 Absorption and resonance Raman scattering

The absorption spectra of neat PTCD solutions and the plasmon absorption of Ag island film are shown in Figure 7.3. Both PTCDs, Bis (ndodecyl imido) perylene in dichloromethane ($\sim 10^{-4} \text{ M}$) and Bis (3, 4 dichloro benzyimido) perylene in dichloromethane ($\sim 10^{-5} \text{ M}$), absorbed in the visible region of the spectrum. The observed visible absorption spectra usually are due to the $\pi - \pi^*$ electronic transition of the PTCD moiety from the ground electronic state to any of the excited vibrational states with the corresponding vibronic structure.³⁴

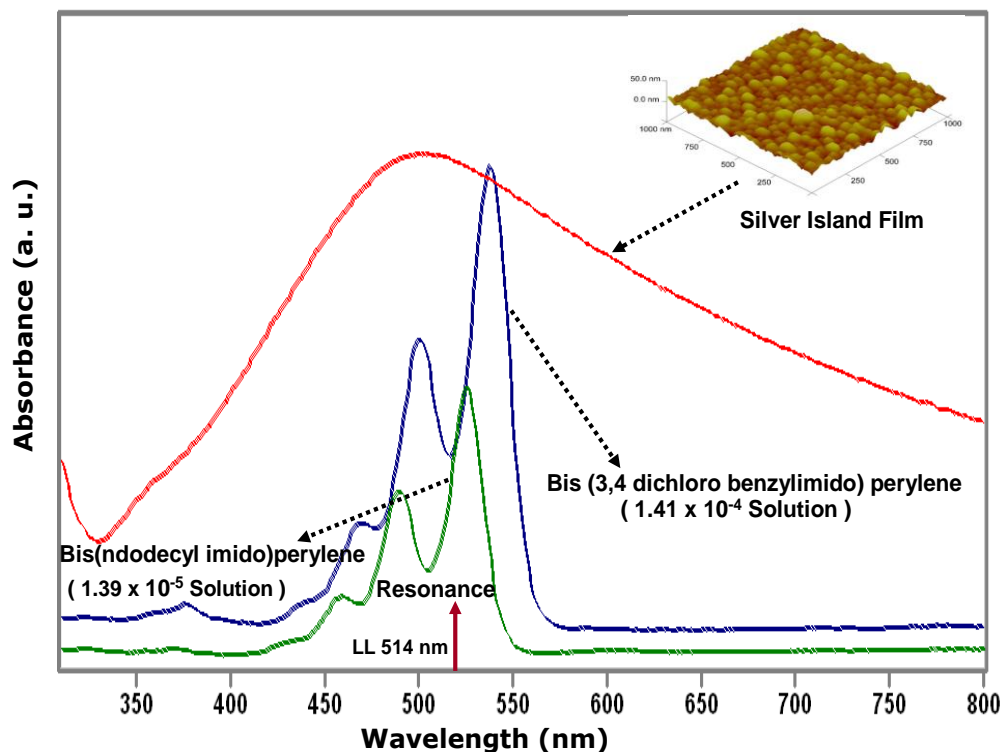


Figure 7.3: Schematic of coating the LB monolayers on glass by SHIN particles and experimental for SHINEF

The 0-0 transition bands appear at 527 nm with a vibronic structure at 490 and 458 nm for Bis (ndodecyl imido) perylene; and in Bis (3, 4 dichloro benzylimido) perylene, the 0-0 transition band shows at 540 nm with a vibronic structure at 504 and 468 nm. The silver island film absorption, with its maxima at 503 nm, shows a broad extinction spectrum which covers the entire visible region-to-near IR, indicating a wide distribution of particle geometries and particle-particle interactions. The typical image of a $1 \mu\text{m}^2$ area of the Ag film, acquired by tapping mode atomic force microscopy (TM-AFM), is shown in an inset of Figure 7.3; which reveals the Ag particles morphology and their inhomogeneous distribution of particle sizes in agreement with the broad surface plasmon

absorption. It can also be noticed that the 514.5 nm laser excitation in Raman experiments is resonant with the surface plasmon absorption of the Ag nanostructured film as well as molecular absorption of the PTCDs, which effectively fulfill the double resonance condition of SERRS.

7.3.2 Ensemble average SERRS spectra

The LB-mixed monolayer of AA doped with PTCD in ratio 10:1, fabricated on Ag island film, was used to obtain ensemble average SERRS spectra. The concentration of the PTCD at this stage was $\sim 10^5$ molecules per μm^2 , and ca. 10^6 AA molecules per μm^2 on the Ag films. The excitation laser line 514.5 nm was used to acquire LB-SERRS spectra using extended scanning. A wide scanning range of (4000 cm^{-1} or ca. 134 nm) was set in order to observe the fundamental vibrational wavenumbers, as well overtones and combinations. The average spectra are shown in Figure 7.4.a for Bis (ndodecyl imido) perylene and in Figure 7.4.b shown the same for Bis (3,4 dichloro benzylimido) perylene. The LB-SERRS shows fundamentals, combinations and overtones characteristic of the three fundamental stretching ring vibrations of the PTCD chromophore, which are mainly from the perylene chromophore

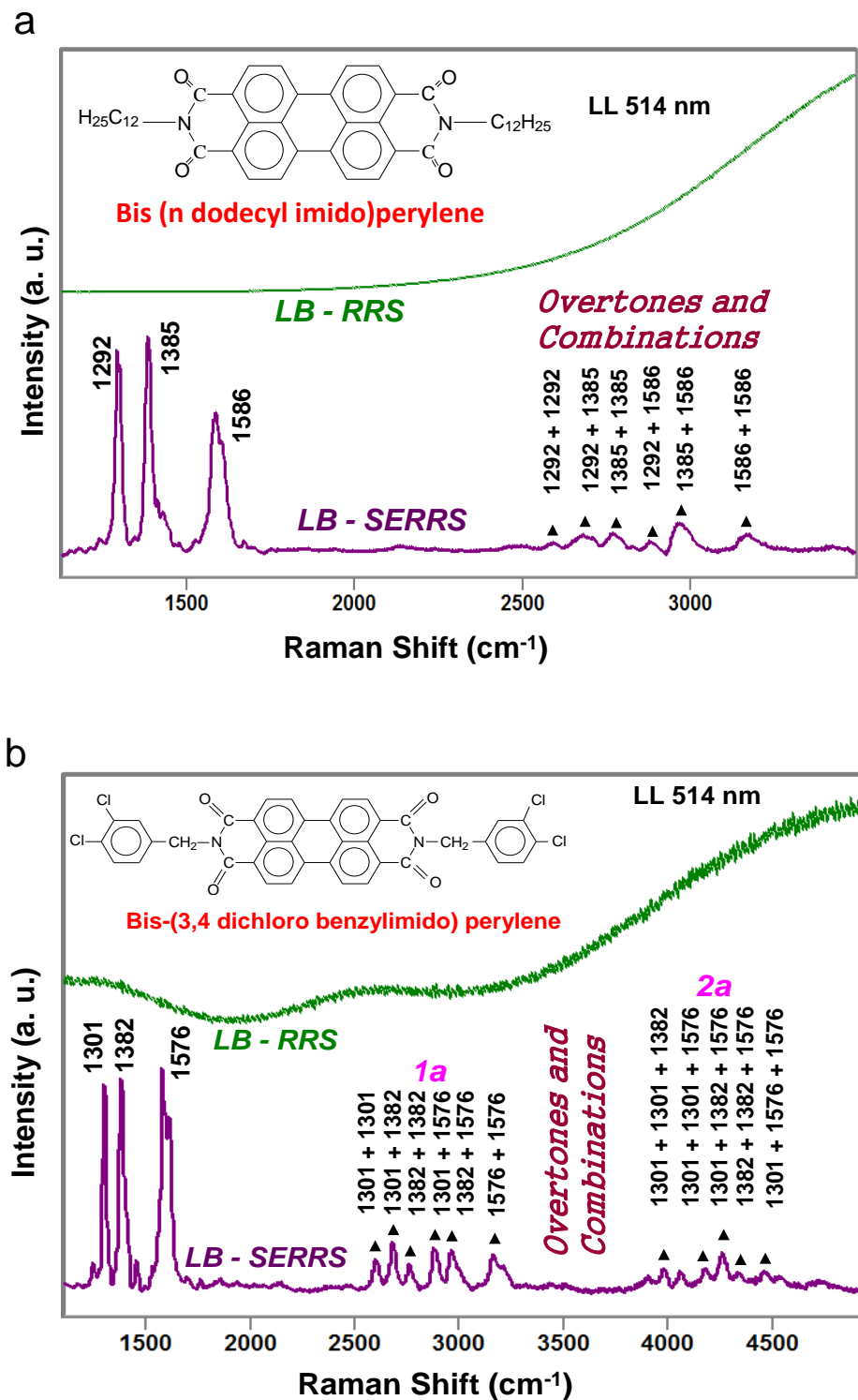


Figure 7.4: The ensemble average spectra, SERRS and RRS, of PTCDs at laser excitation of 514 nm and power 10-20 μW . a) Bis (ndodecyl imido) perylene and b) Bis (3,4 dichloro benzylimido) perylene

In Figure 7.4.a, the fundamentals of perylene ring (planar PTCD chromophore) vibrational modes are: 1292 cm^{-1} , 1385 cm^{-1} and 1586 cm^{-1} for the Bis (ndodecyl imido) perylene molecules, are observed along with their first set of overtones and combinations, which are labeled in the spectrum. In case of Bis (3, 4 dichloro benzylimido) perylene shown in Figure 7.4.b, first and second set of overtones and combinations as stated in the spectrum are seen for the fundamental vibrational modes: at 1301 cm^{-1} , 1382 cm^{-1} and 1576 cm^{-1} . The resonance Raman spectra (RRS) for these PTCDs were also collected for the same LBs are fabricated on bare glass slides. The RRS spectra are not observed, and only the fluorescence can be seen.

7.3.3 The spectrum of the single molecule

To approach single molecule detection using SERRS, the concentration of the spreading solution for Langmuir film fabrication were calculated to achieve, on average, 1000 and 10 molecules of PTCD per μm^2 of surface area in the mixed AA monolayer. The fabricated LBs were investigated by 2D mapping of Raman spectra collected point-by-point. A laser of 514.5 nm excitation was used to acquire these Raman spectra with an extended mode and a single accumulation of 10s exposure time. About 300 spectra were recorded for these maps in both PTCD LB films. The resulting data sets are analyzed with the native Wire 3.0 software and correlation maps are generated on the basis on one of the fundamental band intensity, 1292 cm^{-1} for Bis (ndodecyl imido) perylene and 1301 cm^{-1} for Bis (3, 4 dichloro benzylimido) perylene correspondingly.

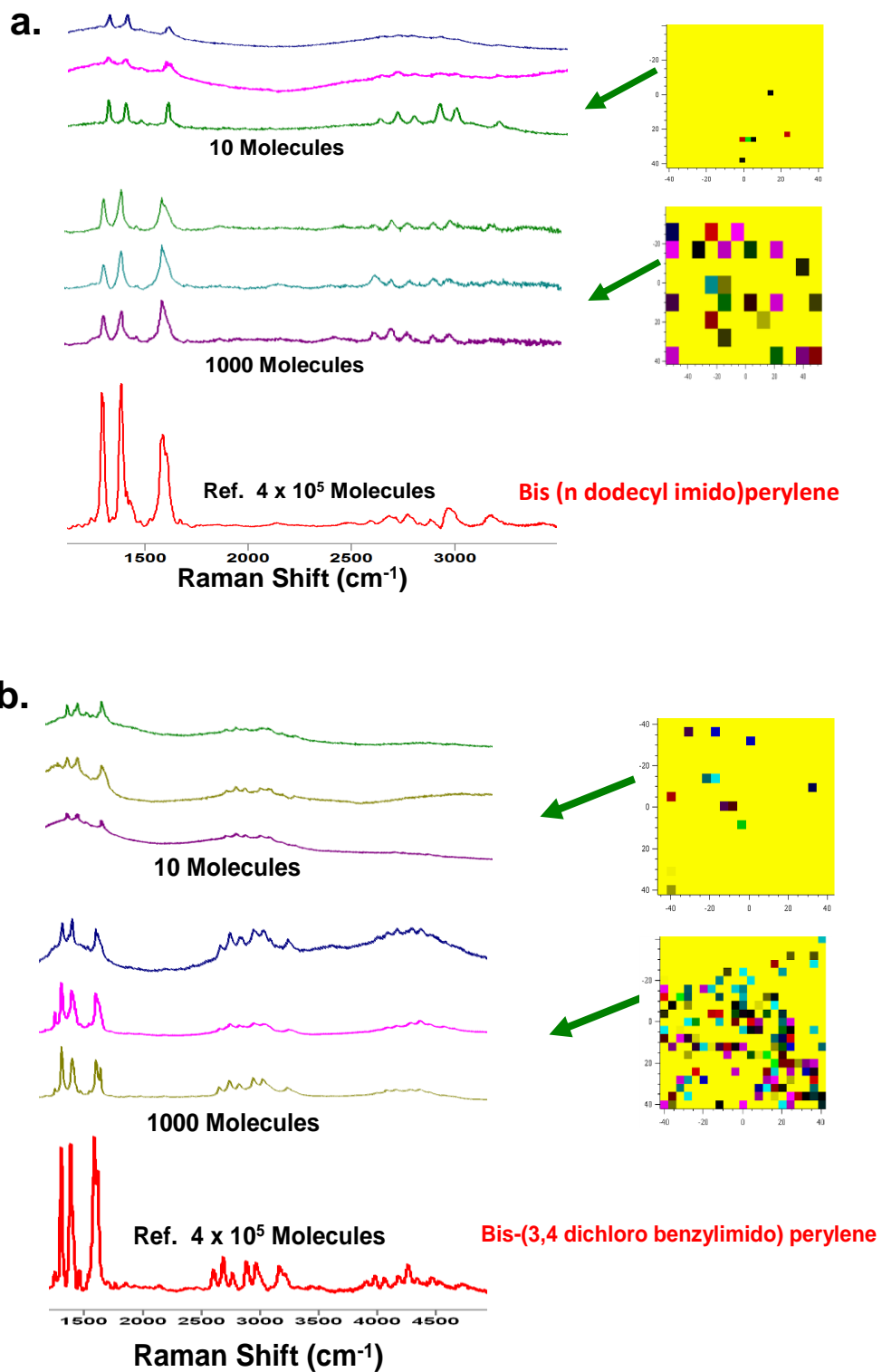


Figure 7.5: SMD in LB-SERRS of PTCDs. laser excitation of 514.5 nm and power 10-20 μW . a) Bis (ndodecyl imido) perylene and b) Bis (3,4 dichloro benzylimido) perylene

Selected spectra of the map are shown in Figure 7.5, and the reference ensemble LB-SERRS spectrum presented at the bottom. The pixels are in different colors to display the highest observed intensity. The selected spectra of both PTCDs correspond to LB films of 1000 molecules and 10 molecules in the field of view, respectively. It is outstanding that the first overtones and combinations are also clearly observed in the single molecule SERRS spectra for both PTCDs. However, the second set of overtones and combinations of Bis (3, 4 dichloro benzylimido) perylene are distinguished in 1000 molecules and hardly noticeable in 10 molecules. Since, detecting the spectrum of the single molecule is a rare event, it is reasonable to state that at a surface concentration of 10 molecules per μm^2 , only SM events are observed.³⁵ Only a few points on the LB surface produce the spectrum of the single molecule (out of ~300 spectra) coupling, most likely, the molecule with a specific spatial locations in the nanostructure, the hot spots.²⁹ In addition, at this surface coverage and because the chromophore is bulky, it is very unlikely that anything but a monomer is the source of the measured Raman signal. A monolayer composed of PTC D molecules in a matrix laid upon a nanostructured silver surface is not static, and at room temperature, the fluctuation of signals may be attributed to the movement of physically adsorbed molecule under constant laser illumination.

Relative Intensity variations observed when single molecule regime is approached

Fluctuations in the spectral parameters are the most important and defining features in the spectra of single molecule. In addition to these intrinsic

properties, there is a unique evidence of the role of plasmonic in the observed spectra of isolated target molecules; the variation of the observed intensities in different spatial regions of a silver island film, due to the fact that different plasmons are involved in the enhanced signal. In a recent report from our group,³⁶ the signature for different plasmons in diverse spatial regions of the films was demonstrated using spin coating of the dye onto SIF. A more control dispersion of the dye onto the SIF is attained using the LB technique, and it was the objective of this particular work to validate the previous findings using LB monolayers containing a few target dye molecules to see the plasmon signatures. It is important to point out that it is necessary to scan large section of the Stokes region in the Raman spectrum, large enough to be much wider than the average full width at half maximum of the plasmon. For instance, in this work Stokes Raman scattering was recorded from the 514.5 nm excitation line, which is 19436 cm^{-1} down to 14436 cm^{-1} . The latter correspond to a span of 178 nm, that is wider than any plasmon of silver nanostructures commonly found in the silver island film. Experimentally, variation in the relative intensity in different section of the film is clearly observed that are assigned to be the result of different plasmon contribution, or simple different enhancement at different localities in the film. The effect is illustrated here with the LB-SERRS Raman spectra given in Figure 7.6. The extended Raman spectra were acquired using mapping technique at different points of the SIF coated with mixed LB films of Bis (3, 4 dichloride benzylimido) perylene at a concentration of 10 molecules / μm^2 .

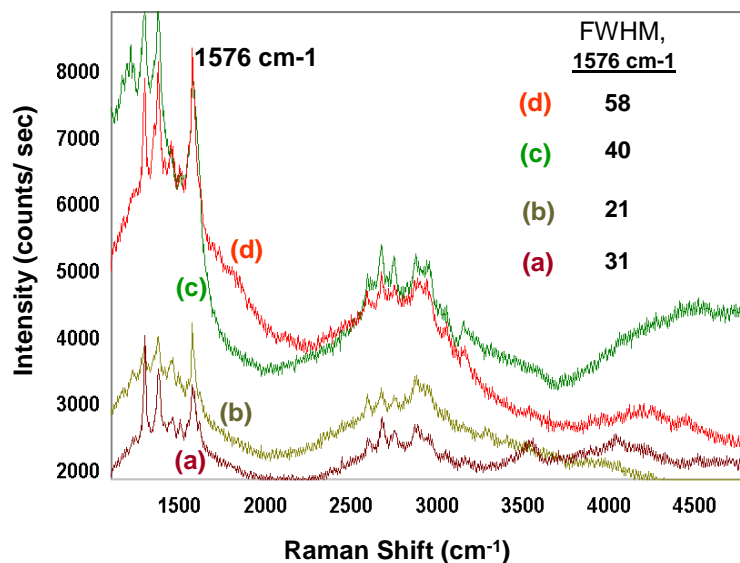


Figure 7.6: SMD spectra (LB-SERRS) of Bis (3,4 dichloro benzylimido) perylene acquired at different spots by mapping with a laser excitation of 514.5 nm and power 10-20 μ W.

The spectra (a), (b), (c) and (d) are obtained from different spots of the LB film and correspondingly from different locations of the silver island film coated by the mixed LB film. For the comparison of disproportion in band relative intensity and FWHM, a band at 1576 cm^{-1} used; intensities are clearly observed in Figure 7.6, and the FWHM values are given in the same Figure. These results represent the difference in plasmon excitation on the spatial locations of the silver island film. Notably, most SERS reports will span a very small section of the Stokes Raman spectrum ($\sim 1700 \text{ cm}^{-1}$), and this may not allow to observed the spatial variations in silver island films. In particular, the overtones and combinations of the PTCD present a unique opportunity to unravel the plasmon properties in the inhomogeneous SIF, which is due to of variation in the nanoparticles size, shape and aggregation

7.3.4 Fluorescence of LB stock solutions

The fluorescence spectra of stock solutions used in the Langmuir monolayer formation were recorded with the 514.5 nm laser excitation. The

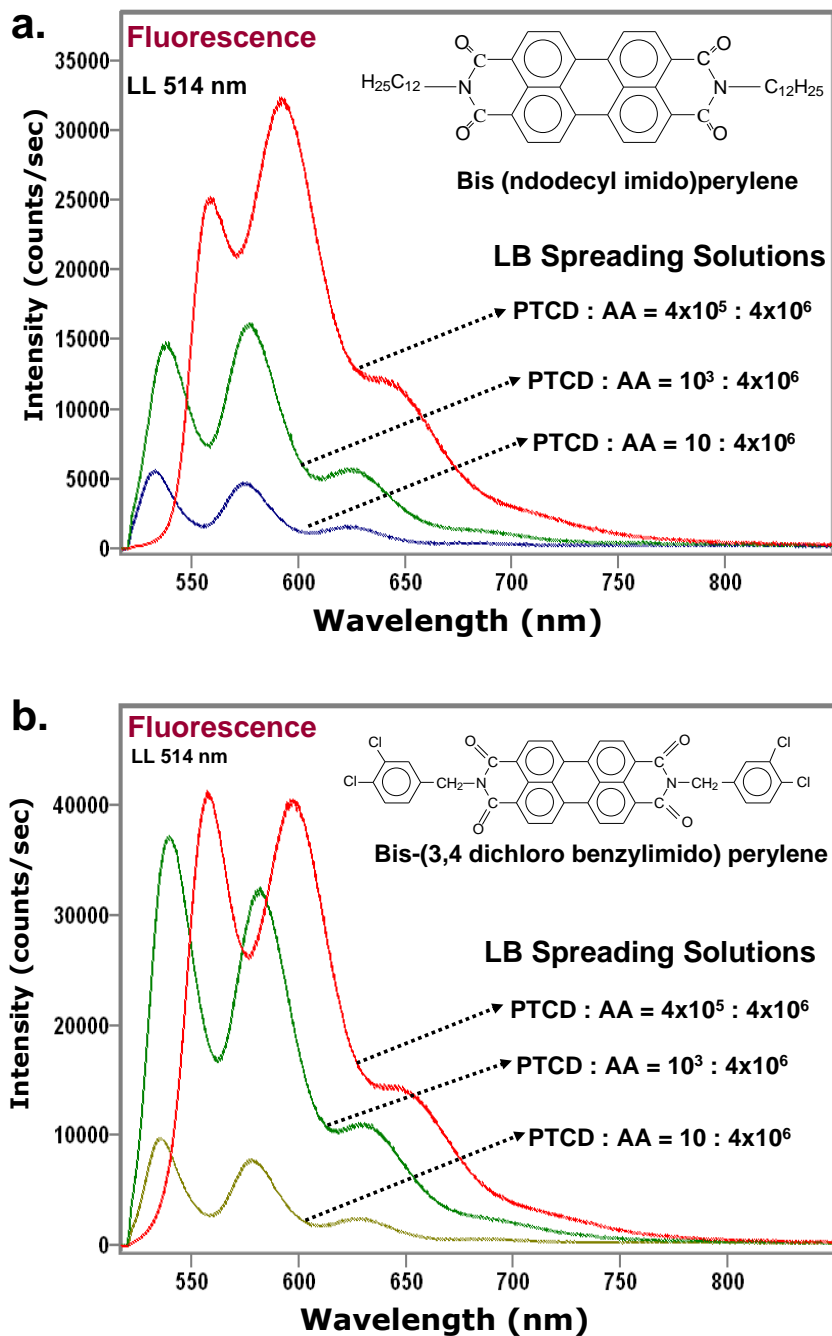


Figure 7.7: The solution fluorescence spectra of PTCDs mixed with AA excited at 514 nm a) Bis (ndodecyl imido) perylene and b) Bis (3,4 dichloro benzylimido)

solutions were prepared with molar ratio: PTCD : AA as $4 \times 10^5 : 4 \times 10^6$, $10^3 : 4 \times 10^6$ and $10 : 4 \times 10^6$. The fluorescence spectra of these solutions are shown in Figure 7.7.a for Bis (ndodecyl imido) perylene and Figure 7.7.b for Bis (3, 4 dichloro benzylimido) perylene.

It can be observed that the fluorescence spectra in both PTCDs are the mirror images of absorption as shown in Figure 7.3. However, the fluorescence is red shifted with increase in solution concentration due to formation of dimmers, trimers or higher aggregates. The fluorescence spectrum of the lowest concentration, PTCD: AA = $10 : 4 \times 10^6$, most likely a monomer emission, is used as reference in the studies of single molecule detection in one LB monolayer by SHINEF.

7.3.5 SHINEF in concentrated LB films

Fluorescence enhancement from a Langmuir-Blodgett (LB) monolayers of both PTCDs covered with shell isolated nanoparticles was observed. The competitive relaxation effect due to radiationless energy transfer from the excited molecules to the nearby metallic surface is controlled by using the silica shell (coating of the gold particles); and plasmon enhancement arises from the gold nanostructures. In this work, a concentrated mixed LB of AA doped by PTCD with a molar ratio of 10:1 deposited on bare corning 2048 glass, was used in the SHINEF experiments. Therefore, an average 4×10^5 PTCD molecules, covered by SHIN nanoparticles, were illuminated using a 514.5 nm laser excitation to attain the enhance fluorescence. Fluorescence spectra of the same LB monolayer, in

the absence of SHIN nanoparticles, were also acquired to be used as a reference, and compare the effect of fluorescence enhancement.

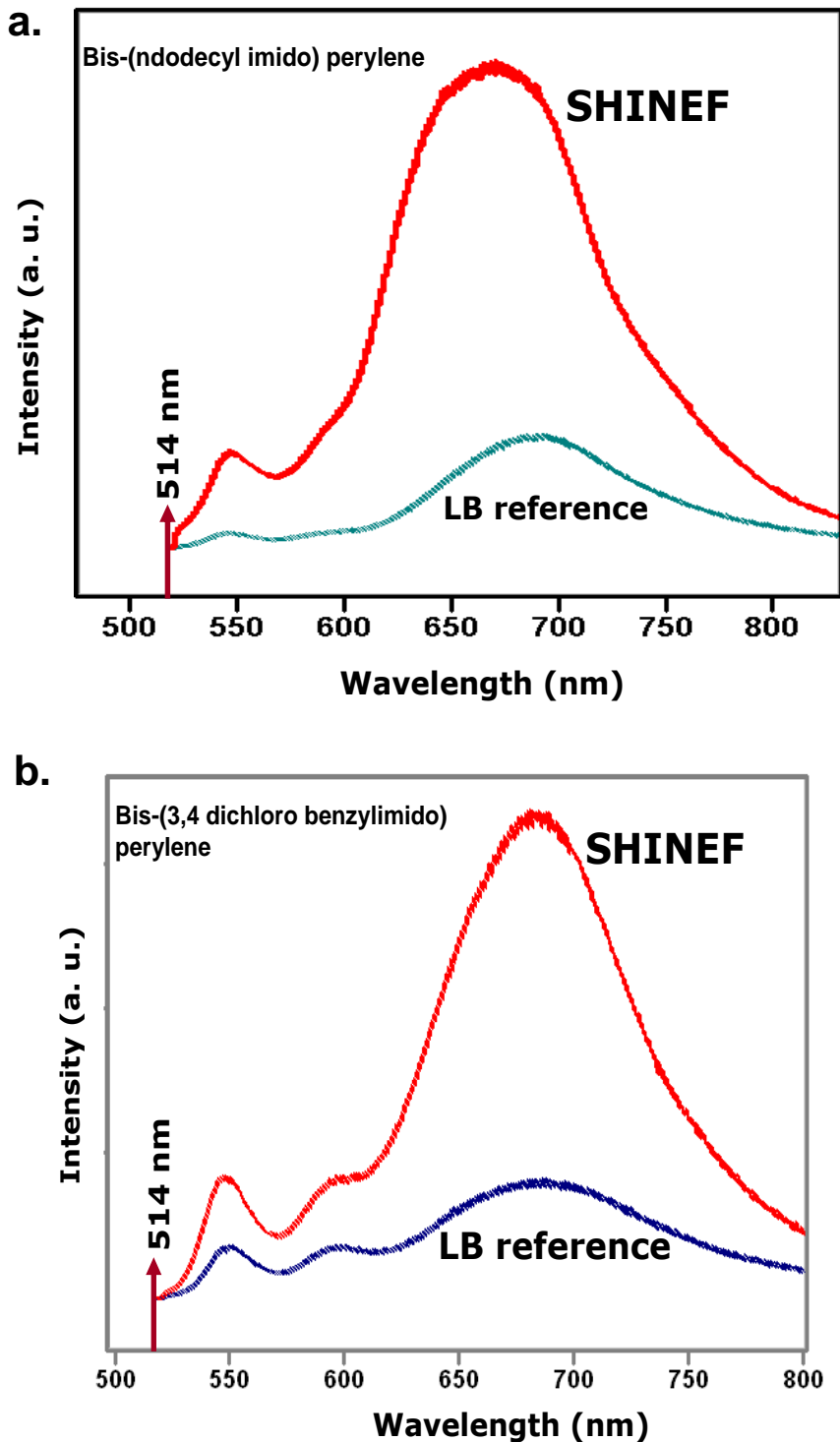


Figure 7.8: Fluorescence and SHINEF spectra of concentrated LB-PTCDs at 514.5 nm excitation a) Bis (ndodecyl imido) perylene and Bis (3,4 dichloro benzyimido) perylene

The reference fluorescence and SHINEF spectra of both PTCDs are presented in Figure 7.8, where Figure 7.8.a represents Bis (ndodecyl imido) perylene and Figure 7.8.b for Bis (3, 4 dichloro benzylimido) perylene.

In both cases, a robust fluorescence enhancement was achieved utilizing the SHINEF technique. In this case the enhanced fluorescence corresponds to excimer fluorescence. The excimer formation is characteristic of the PTCDs in thin solid films or any other state of aggregation.

7.3.6 Single-molecule detection by SHINEF

In this study, a mixed LB of concentration, PTCD: AA = 10: 4×10^6 i.e. 10 molecules per μm^2 of surface coverage, was used. The LB films then covered by SHIN particles to examine single molecule detection by SHINEF. Two dimensional maps were created, by acquiring the spectral data using the micro-Raman system, to record the emission from SHIN coated LB films excited with the 514.5 nm laser line. Notably, in these SHINEF spectra, only the emission spectra of the monomer are observed, as shown in Figure 7.9. Selected single molecule spectra resulting from these maps are displayed in Figure 7.9.a for Bis (ndodecyl imido) perylene and Figure 7.9.b for Bis (3, 4 dichloro benzylimido) perylene.

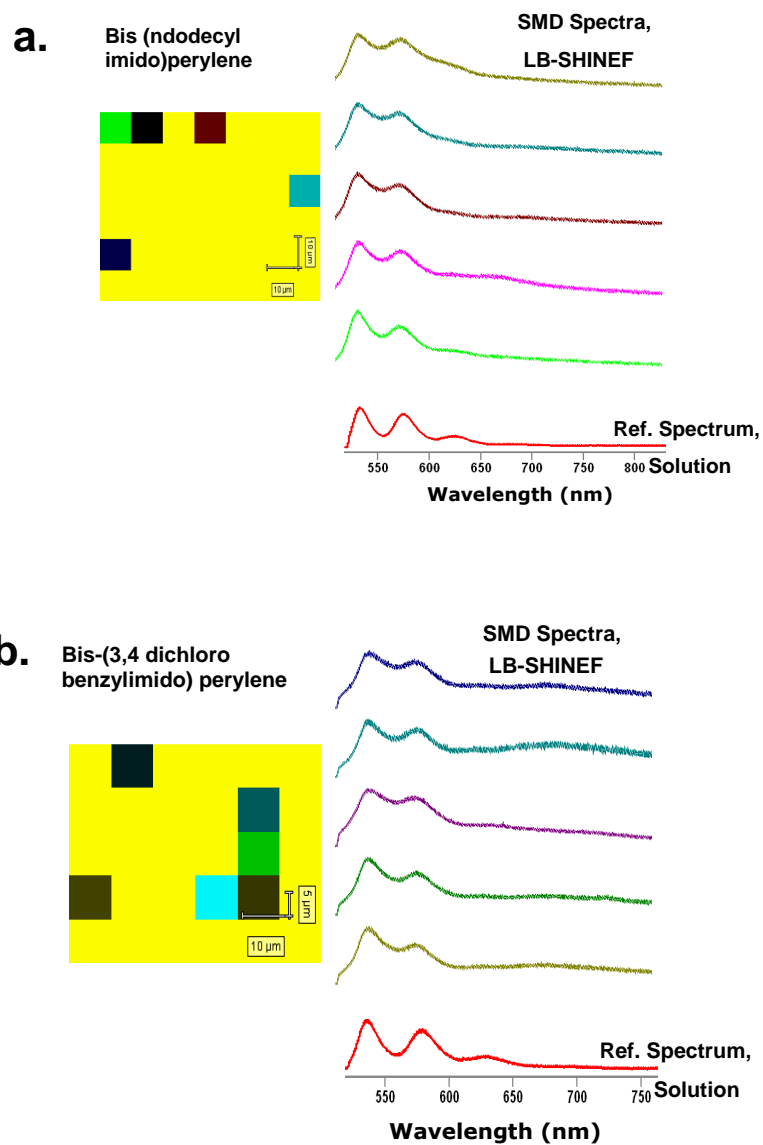


Figure 7.9: Single molecule - SHINEF spectra of LB-PTCDs at laser 514.5 nm excitation a) Bis (ndodecyl imido) perylene and b) Bis (3,4 dichloro benzylimido) perylene

A fluorescence spectrum of the same concentration stock solution (used in LB deposition) is included in this figure as a reference. A total of ~200 spectra were acquired to create the maps; but only a few single molecule spectra are detected.

7.4 Conclusions

Two important ultra-sensitive analytical techniques, LB-SERRS and LB-SHINEF, have been exploited in this work to detect single molecule which is the ultimate objective for analysis in chemistry, biology or biomedical science. The success of these techniques is based on plasmonics, i.e. plasmon enhancement of the optical signal. The most striking difference between SERRS and SHINEF is the distance dependence from the metal nanostructures. The SHINEF is a versatile technique, since it is easily applicable to any sample without sample preparation. The LB technique used for fabrication of the molecular monolayers on solid surfaces is an effective method that can be used for single molecule detection. For both LB-SERRS and LB-SHINEF, it is necessary to create high resolution maps, from where we can extract spectra corresponding to the rare event of SMD. It can be said that, the constructed maps bring to light the spatial location of hot spots in the silver film, although the rarity of coincidence between hot spots and single isolated molecules, may be a sign that there are many more sites with high enhancement that are not exposed. Consequently, variation of the ratio of the two components in mixed dye–fatty acid LB films, followed by 2D mapping measurements, can be employed to study the enhancement activity of the silver or gold films, and also the degree of coupling of different dyes introduced in monolayer architectures with metal nanostructures.

Reference

- (1) Moerner, W. E. *Springer Series in Chemical Physics* **2001**, 67(Single Molecule Spectroscopy), 32-61.
- (2) Cornish Peter, V.; Ha, T. *ACS Chem Biol* **2007**, 2(1), 53-61.
- (3) Lakowicz, J. R. *Analytical Biochemistry* **2001**, 298(1), 1-24.
- (4) Kneipp, K.; Wang, Y.; Kneipp, H.; Perelman, L. T.; Itzkan, I.; Dasari, R.; Feld, M. *S. Physical Review Letters* **1997**, 78(9), 1667-1670.
- (5) Nie, S. M.; Emery, S. R. *Science* **1997**, 275(5303), 1102-1106.
- (6) Peters, R. *Annual Review of Biophysics and Biomolecular Structure* **2007**, 36, 371-394.
- (7) Moskovits, M. *Reviews of Modern Physics* **1985**, 57, 783-826.
- (8) Moskovits, M. *J Chem Phys* **1978**, 69(9), 4159-4161.
- (9) Garoff, S.; Weitz, D. A.; Gramila, T. J.; Hanson, C. D. *Optics Letters* **1981**, 6(5), 245-247.
- (10) Glass, A. M.; Liao, P. F.; Bergman, J. G.; Olson, D. H. *Optics Letters* **1980**, 5(9), 368-370.
- (11) Osawa, M. *Bulletin of the Chemical Society of Japan* **1997**, 70(12), 2861-2880.
- (12) Aroca, R.; Kovacs, G. J.; Jennings, C. A.; Loutfy, R. O.; Vincett, P. S. *Langmuir* **1988**, 4(3), 518-521.
- (13) Geddes, C. D.; Cao, H.; Gryczynski, I.; Gryczynski, Z.; Fang, J.; Lakowicz, J. R. *J Phys Chem A* **2003**, 107(18), 3443-3449.
- (14) Wokaun, A.; Lutz, H. P.; King, A. P.; Wild, U. P.; Ernst, R. R. *J Chem Phys* **1983**, 79(1), 509-514.

- (15) Vo-Dinh, T. *TrAC, Trends Anal Chem* **1998**, 17(8+9), 557-582.
- (16) Gersten, J.; Nitzan, A. *Journal of Chemical Physics* **1981**, 75(3), 1139-1152.
- (17) Chance, R. R.; Prock, A.; Silbey, R. *Advances in Chemical Physics* **1978**, 37, 1-65.
- (18) Wokaun, A.; Lutz, H. P.; King, A. P.; Wild, U. P.; Ernst, R. R. *Journal of Chemical Physics* **1983**, 79(1), 509-514.
- (19) Aroca, R.; Kovacs, G. J.; Jennings, C. A.; Loutfy, R. O.; Vincett, P. S. *Langmuir* **1988**, 4(3), 518-521.
- (20) Anger, P.; Bharadwaj, P.; Novotny, L. *Phys Rev Lett* **2006**, 96(11), 113002-113001 to 113002-113004.
- (21) Ray, K.; Badugu, R.; Lakowicz, J. R. *Langmuir* **2006**, 22(20), 8374-8378.
- (22) Ray, K.; Badugu, R.; Lakowicz, J. R. *Chemistry of Materials* **2007**, 19(24), 5902-5909.
- (23) Li, J. F.; Huang, Y. F.; Ding, Y.; Yang, Z. L.; Li, S. B.; Zhou, X. S.; Fan, F. R.; Zhang, W.; Zhou, Z. Y.; Wu, D. Y.; Ren, B.; Wang, Z. L.; Tian, Z. Q. *Nature* **2010**, 464(7287), 392-395.
- (24) Guerrero, A. R.; Aroca, R. F. *Angewandte Chemie* **2010**(Manuscript number: anie.201004806).
- (25) Moskovits, M. *Nature* **2010**, 464(7287), 357-357.
- (26) Aslan, K.; Leonenko, Z.; Lakowicz, J. R.; Geddes, C. D. *Journal of Fluorescence* **2005**, 15(5), 643-654.
- (27) Geddes, C. D.; Aslan, K.; Gryczynski, I.; Malicka, J.; Lakowicz, J. R. *Rev Fluoresc* **2004**, 1, 365-401.

- (28) Willems, K. A.; Van Duyne, R. P. *Annual Review of Physical Chemistry* **2007**, 58, 267-297.
- (29) Le Ru, E. C.; Etchegoin, P. G.; Meyer, M. *J Chem Phys* **2006**, 125(20).
- (30) Lam, J. F.; Forrest, S. R.; Tangonan, G. L. *Physical Review Letters* **1991**, 66(12), 1614-1617.
- (31) Horowitz, G.; Kouki, F.; Spearman, P.; Fichou, D.; Nogues, C.; Pan, X.; Garnier, F. *Advanced Materials* **1996**, 8(3), 242-&.
- (32) Frens, G. *Nature-Physical Science* **1973**, 241(105), 20-22.
- (33) Grabar, K. C.; Freeman, R. G.; Hommer, M. B.; Natan, M. J. *Analytical Chemistry* **1995**, 67(4), 735-743.
- (34) Michalet, X.; Pinaud, F.; Lacoste, T. D.; Dahan, M.; Bruchez, M. P.; Alivisatos, A. P.; Weiss, S. *Single Molecules* **2001**, 2(4), 261-276.
- (35) Goulet, P. J. G.; Pieczonka, N. P. W.; Aroca, R. F. *Journal of Raman Spectroscopy* **2005**, 36(6-7), 574-580.

CHAPTER 8

CONCLUSIONS

8.1 Conclusions

The work presented in this thesis demonstrates the advantages and potential applications of the Langmuir-Blodgett technique in the fabrication of samples for spectroscopic analysis using surface-enhanced Raman scattering (SERS), surface-enhanced resonance Raman scattering (SERRS) and shell isolated nanoparticle enhanced fluorescence (SHINEF). The results of these studies may help the understanding and the development of analytical techniques to be used in several areas of chemistry, biology or material science. An important part of the work is dedicated to substrate development for SERS/SERRS, including fabrication and characterization. Notably, the synergy of the Langmuir-Blodgett monolayer technique and nanostructured metal surfaces (mainly Ag and Au) permits the detection of the spectrum of the single molecule.

In chapter 3, the fabrication of SERS substrates (Ag or Au island films) by vacuum evaporation technique and their characterization by AFM and UV-Vis absorption are discussed. The SERS effect is demonstrated using a well known organic molecule; benzene thiol. Since SERS is a plasmonic phenomenon, tuning the localized surface plasmon absorption to be in resonance with the laser lines of the Raman excitation is important. The latter is achieved experimentally by controlling the metal film thickness or the temperature of the substrate during deposition of Ag, Au or mixed Ag/Au. Section 3.4 introduced the Langmuir-Blodgett (LB) technique as an advanced method of handling the analyte molecule(s) on the SERS substrates (solid).

In an attempt to study phospholipids' bilayers, which mimics the lipid bilayers of cell membrane, SERS results of LB phospholipids' monolayer, bilayers and trilayers coated on Ag island films are discussed in chapter 4. Two phospholipids (1,2-Dipalmitoyl-sn glycerol-3-phosphocholine - DPPC and 1,2-dimyristoyl-sn-glycerol-3-phosphocholine-DMPC) of similar chemical structure have been used in this examination. Both phospholipids in LB-bilayers SERS give the reproducible results shown in section 4.3, which could direct to the model study of cell membrane. LB-SERS in the phospholipid monolayer was not reproducible due to photo dissociation on the Ag nanostructure. The trilayers LB-SERS of the phospholipids didn't show further enhancement for the limitation of near field effects of the localized surface plasmon. Similar experiments were carried out on Au island films. However, no SERS was observed (section 4.3.5), probably due to lower enhancement factor on Au, and the fact that the phospholipids have an intrinsic very poor scattering cross section.

In chapter 5, the LB-SERRS results of two dye tagged phospholipids, TRITC-DHPE and TEXAS RED, were discussed. Silver island films were used in this study to attain highest SERRS enhancement that is the prerequisite for single molecule detection (SMD). The breakdown of the ensemble average and the observation of single molecule spectra are presented in section 5.5. The high scattering cross section attained in SERRS measurements, exploiting resonance effects, is the only approach to single molecule detection of the target chromophore. Mixed LB monolayer of inert matrix, arachidic acid (fatty acid), doped with target molecule, TRITC or TEXAS, so as to disperse them in the LB

sample, and to have in average about 1 molecule in $1\mu\text{m}^2$ (micro-Raman probe area) of coated metal island film. It is assumed that the SMD is observed only at special spatial locations of particularly high enhancement factor or hot spots. Since the latter is a rare event, 2D mapping of Raman measurements is carried out throughout the surface of the LB monolayer hunting for the rare match between hot spot and the molecule. The single molecule spectra of TRITC and TEXAS are presented in section 5.5.4, which shows their characteristic fluctuations of wavenumber, full width at half maximum (FWHM) and relative intensity. When a large number of molecules are present in the probed area of the micro-Raman, an average spectrum is observed (shown in section 5.5.3), where the wavenumber at the center of the Raman band, the FWHM and the relative intensity, all have a constant and reproducible value. The average SERS/SERRS regime allows for quantitative applications. On the other hand, SMD offers the studies of molecular dynamics of the molecule and its surroundings.

There is no analytical protocol to fabricate reproducible hot spots on a SERS/SERRS substrate, and hot spots are found in aggregates nanostructures by its enhancing effect on a given target molecule. In metal island films, exact control of the growth of nanoparticles and their aggregates is not possible. In an effort to control the nanostructures and fabricate a metal film, nanoparticles were grown on a flat surface. The self assembly of silver nanoparticles from negatively charged silver citrate colloidal nanoparticles onto a positively charged silanized glass surface was done. The time of assembly or deposition was the key factor

for the growth of the nanoparticles, which are discussed in chapter 6. The SERRS spectra in a mixed LB monolayer of octadecyl rhodamine B chloride R18 doped with fatty acid (ratio 1:100) and fabricated on the self assembly metal films (time of assembly 2 hrs, 6 hrs, 10 hrs and 14 hrs), are presented in section 6.3. Nanoparticle density on the glass surface was proportional to deposition time. Again 2D mapping was used here to find the source of SERRS spectra. Films with higher nanoparticle density on the surface produced highly enhanced SERRS spectra, probably due to the formation of aggregates and hot spots.

Finally, using perylene tetracarboxylic (*PTCD*) derivatives as target molecules in mixed LB samples, single molecule detection is achieved with silica shell isolated nanoparticle enhanced fluorescence (SHINEF) and surface-enhanced resonance Raman scattering (SERRS). All the results of SHINEF and SERRS for Bis (n dodecyl imido) perylene and Bis-(3,4 dichloro benzylimido) perylene are presented in chapter 7. The SERRS data include not only the Raman vibrational wavenumbers; but also combinations and overtones. The unique property of SHINEF is in the way it is applied: substrate to analyte. The observation of single molecule fluorescence using doped LB films is reported here for the first time.

8.2 Future Work

This thesis has explored the applications of surface enhanced Raman scattering and surface enhanced resonance Raman scattering (SERS/SERRS), in conjunction with the Langmuir-Blodgett (LB) technique in pursuit of single

molecule detection (SMD). Vibrational Raman spectroscopy is unique due to its ability to detect functional groups and its interactions; open problems like understanding the dynamics of macromolecules at cellular level, optical properties of nanosystems, etc. can be addressed with greater accuracy. In particular, the exceptional SERS/SEERS sensitivity together with chemical imaging capabilities can be exploited to address interesting problems which are not viable with any other techniques.

Single molecule detection using SERS/SEERS on nanostructures is yet an early phase of scientific development and holding enormous wealth for potential applications of biomedical science. In chapter 5, single molecule studies of two dye tagged phospholipids exploiting double resonance of SEERS and LB were presented. The preparation of Ag nanostructured film by vacuum evaporation was successful for the plasmonic needed in this work. The same metal films were used in LB-SERS examination of similar phospholipids as a model of cell membrane as discussed in chapter 4. These investigations opens the windows of future studies of biological systems in dynamic behaviours, molecular interactions, environmental influences etc. using LB-SERS/LB-SEERS.

With an experimental point of view, there are various issues in SERS which have to be addressed in future, particularly, the rational design of metal nanostructures to achieve hot-spots in a regular pattern on the nanostructured metal surface and adsorption of molecules onto this surface in a well organized manner. The LB technique is one choice, which was used in this work and

attained successful results in SMD-SERRS. An approach was made in controlling the surface plasmon using a simple technique by growing Ag colloidal nanoparticles on the silanized glass surface and varying the time of deposition as its key parameter. The effective SERRS results on this work were presented in chapter 6. A similar kind of approach may be addressed in future which is simple, economic and easy accessible.

Single molecule studies using silica coated shell isolated nanoparticle enhanced fluorescence (SHINEF) is an advanced analytical tool in terms of its easy application on any samples only by spreading and avoid toxic effects on the sample. In chapter 7, such investigations were presented on Perylene tetracarboxylic (*PTCD*) derivatives. This technique is very valuable when sample toxicities are a big concern and identification of chemical structure is not mandatory. This technique may offer a broad application in biology or biomedical science.

This thesis has provided answers to some of the questions posed in the full understanding of the SERS/SERRS processes. There are, of course, many questions still to be answered, such as how does the orientations of LB molecules influenced SERS, if Raman probe could be synchronized on LB monolayer, how experiments could be conducted under conditions of environmental control, how a specific order of hot spot could be generated on metal nanostructure films and more. These aspects could be considered in the future SERS studies.

VITA AUCTORIS

Golam Moula was born in 1960 in Naogaon, Bangladesh. He received his Bachelor in Chemical Engineering and Master of Chemical Engineering, in 1984 and 1992 respectively, from the Bangladesh University of Engineering and Technology, Dhaka, Bangladesh. Upon completion of Bachelor in Chemical Engineering, he was employed as a Manager in Research and Development in a chemical company, The Security Printing Corporation (Bangladesh) Ltd., and worked there from July 1985 to March 2000.

He moved to Canada by immigration in 2000. He started another graduate study in Master of Science in Polymer Chemistry enrolling at the University of Eastern Michigan, Michigan, USA in September 2003 and obtained his graduation in August 2005. Then he took admission in a Ph. D. program in Chemistry and Biochemistry at the University of Windsor, Windsor, Canada in September 2006. Since then he has been working in the Material and Surface Science Group at the University of Windsor headed for completion his doctoral degree.

PUBLICATIONS

1. **G. Moula**; R. F. Aroca "Plasmon enhanced resonance Raman scattering and Fluorescence in Langmuir-Blodgett Monolayers" *Journal of Analytical Chemistry*, December, 2010.
2. **G. Moula**; R. F. Aroca "Surface-Enhanced Raman Scattering (SERS) of Phospholipids in Langmuir-Blodgett Films" *Journal of Physical Chemistry*, 2010 (In review)
3. A. Merlen ; V. Chevallier ; J. C. Valmalette; L. Patrone; P. Torchio; S. Vedraine ; F.Flory; **G. Moula** "Surface Enhanced Spectroscopy with gold nanostructures on silicon and glass substrates " *International Journal of Nanotechnology*, June 2010 (Submitted).
4. T. K. A. Hoang; A. Hamdaed; **G. Moula**; R. F. Aroca; M. Trudeau; D. M. Antonelli "Kubas-Type Hydrogen Storage in Novel V(III) Polymers Using Tri- and Tetrahedron Bridging Ligands" Plasmon enhanced resonance Raman scattering and fluorescence in Langmuir-Blodgett Monolayers" *Journal of the American Chemical Society*, Nov. 2010 (Submitted).
5. Ahmad Hamaed; Tuan K. A. Hoang; **G. Moula**; Ricardo Aroca; Michel Trudeau; David M. Antonelli "Hydride-induced Amplification of Performance and Binding Enthalpies in Alkylchromium (II) Hydrazide Gels for Kubas-type Hydrogen Storage" *Journal of Nature Chemistry*, Dec., 2010 (Submitted).
6. N.P.W. Pieczonka; **G. Moula**; R. F. Aroca "SERRS for Single-Molecule Detection of Dye Labeled Phospholipids in Langmuir-Blodgett Monolayer, *Langmuir*, 2009, 25, 11261.

7. Nicholas P.W. Pieczonka; **G. Moula**; Adam R. Skarbek; Ricardo F. Aroca
"Single Molecule and Trace Detection by SERS", Surface Enhanced Raman Spectroscopy; Analytical, Biophysical and Life Science Applications, Chap 4, *Wiley Publishers*, 2010.

Manuscripts in Preparation

1. **G. Moula**; R. F. Aroca "LB-SERS on Self-assembled Silver Nanoparticles on Silanized Surfaces".
2. **G. Moula**; R. F. Aroca "Single-Molecule Detection in Langmuir- Blodgett Monolayers with SERRS and SHINEF"

CONFERENCES

1. **G. Moula**; R. F. Aroca "Langmuir-Blodgett Monolayers of Phospholipids. Surface Enhanced Raman Scattering on Nanostructured Silver Films" 92nd Canadian Chemistry Conference and Exhibition, Toronto, Ontario, Canada, 2010.
2. R. F. Aroca; **G. Moula**; A. Guerrero "Plasmonic, Surface-Enhanced Raman Scattering, Surface-Enhanced Fluorescence and Single Molecule Detection" 92nd Canadian Chemistry Conference and Exhibition, Toronto, Ontario, Canada, 2010.
3. **G. Moula**; N. P. W. Pieczonka; R. F. Aroca "SERS and SERRS imaging in Langmuir – Blodgett monolayers. Single molecule detection and hot spot

- statistics” PacificChem 2010 Congress, Hawaii, USA, 2010.
4. A. Guerrero; **G. Moula**; R. F. Aroca “Plasmon enhanced spectroscopy with nanostructures and the reproducibility of Surface-Enhanced Raman Scattering of biomolecules” International Nanotechnology Exhibition and Conference , Mexico, 2010.
 5. **G. Moula**; N. P. W. Pieczonka; R. F. Aroca “Surface Enhanced Resonance Raman Scattering-SERRS for Single-Molecule Detection in Langmuir Blodgett Monolayer on Nanostructured Metallic Films” 92nd Canadian Chemistry Conference and Exhibition, Hamilton, Ontario, Canada, 2009 .
 6. **G. Moula**; N. P. W. Pieczonka; R. F. Aroca “ SERS and SERRS for group Identification and Single-Molecule Detection in Langmuir-Blodgett Monolayers” Proceedings of the XXIst International Conference of Raman Spectroscopy, London, UK”. 2008.